



저작자표시-비영리-변경금지 2.0 대한민국

이용자는 아래의 조건을 따르는 경우에 한하여 자유롭게

- 이 저작물을 복제, 배포, 전송, 전시, 공연 및 방송할 수 있습니다.

다음과 같은 조건을 따라야 합니다:



저작자표시. 귀하는 원저작자를 표시하여야 합니다.



비영리. 귀하는 이 저작물을 영리 목적으로 이용할 수 없습니다.



변경금지. 귀하는 이 저작물을 개작, 변형 또는 가공할 수 없습니다.

- 귀하는, 이 저작물의 재이용이나 배포의 경우, 이 저작물에 적용된 이용허락조건을 명확하게 나타내어야 합니다.
- 저작권자로부터 별도의 허가를 받으면 이러한 조건들은 적용되지 않습니다.

저작권법에 따른 이용자의 권리는 위의 내용에 의하여 영향을 받지 않습니다.

이것은 [이용허락규약\(Legal Code\)](#)을 이해하기 쉽게 요약한 것입니다.

[Disclaimer](#)

Doctor of Philosophy

**A Numerical Study on the Effect of Flow Channel Modification
on Temperature Profiles, Mass Transport Characteristics, and
Performance of PEM Fuel Cell**

**The Graduate School
of the University of Ulsan
Department of Mechanical Engineering
Binyamin**

**A Numerical Study on the Effect of Flow Channel Modification
on Temperature Profiles, Mass Transport Characteristics, and
Performance of PEM Fuel Cell**

Supervisor: Prof. Ocktaeck Lim

A Dissertation

Submitted to

the Graduate School of the University of Ulsan

In partial Fulfillment of the Requirements

for the Degree of

Doctor of Philosophy

by

Binyamin

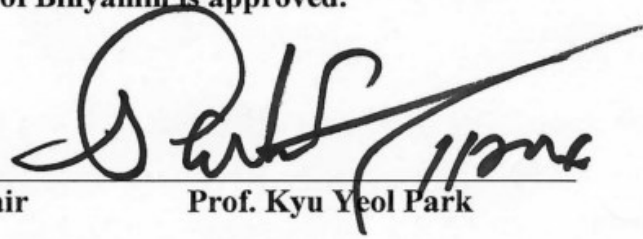
Department of Mechanical Engineering

University of Ulsan, Republic of Korea

June 2024

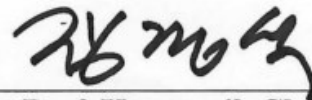
**A Numerical Study on the Effect of Flow Channel
Modification on Temperature Profiles, Mass Transport
Characteristics, and Performance of PEM Fuel Cell**

This certifies that the dissertation
of Binyamin is approved.



Committee Chair

Prof. Kyu Yeol Park



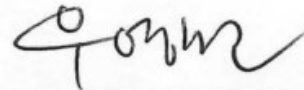
Committee Member

Assoc. Prof. Kyoungsik Chang



Committee Member

Asst. Prof. Yoon Ho Lee



Committee Member

Dr. Youngmin Woo



Committee Member

Prof. Ocktaeck Lim

**Department of Mechanical Engineering
University of Ulsan, Republic of Korea**

June 2024



ABSTRACT

A Numerical Study on the Effect of Flow Channel Modification on Temperature Profiles, Mass Transport Characteristics, and Performance of PEM Fuel Cell

Department of Mechanical Engineering
Binyamin

This study investigates innovative design approaches to enhance mass transport, the performance, and temperature profiles of proton exchange membrane fuel cells (PEMFCs) by employing tapered flow field (TFF) models and streamlined imitated water drop blocks (WDBs) configuration of flow channels with considering porous medium thickness (PMT), thermal contact resistance (TCR), interface contact resistance (ICR), and GDL face permeability variations. A three-dimensional multiphase fuel cell model in ANSYS Fluent using SIMPLE solver was utilized to quantify the impact on oxygen mass transport, water removal, and overall cell performance by experimental data validation combined with an artificial neural network-genetic algorithm (ANN-GA). By employing the tapered flow field (TFF) models, results demonstrate superior performance to conventional FFCs, with a 68.74% reduction in pressure drop, a 7.57% increase in current density, and a 12.63% improvement in power density. Meanwhile, the streamlined imitated water-drop blocks (WDBs) model, considering suitable ICR and GDL face permeability, outperforms the conventional model by achieving higher current density (6.94%), power density (12.27%) and improved water removal (7.18%) at 0.4 V. The additional findings highlight the necessity of considering TCR and GDL face permeability to optimize temperature distribution and cell efficiency. The proposed combined artificial neural network-genetic algorithm (ANN-GA) method effectively identifies optimal operating conditions and predicts fuel cell performance. Overall, these innovative design strategies provide insights into optimizing PEMFC performance, guiding future developments in low-temperature PEMFC design.

Keywords: PEM fuel cell, thermal contact resistance, tapered flow field configurations, imitated water-drop block, ANN-GA.

ACKNOWLEDGEMENT

I am sincerely grateful to my advisor, Professor Ocktaeck Lim, for allowing me to study in the Smart Powertrain Laboratory and for his continuous guidance on my research. And also for his patience, motivation, and insightful feedback to help me sharpen my thinking and take my work to the next level. Without his support and encouragement, I would not have been able to complete this dissertation. I am grateful to the Graduate School of Mechanical and Automotive Engineering, University of Ulsan, and Universitas Muhammadiyah Kalimantan Timur for giving me the opportunity, approval, and support to pursue my Ph.D. program.

I feel very fortunate to be a member of the Smart Powertrain Laboratory at University of Ulsan. I would like to thank all my current and former colleagues – Dr. Yanuandri Putrasari, Dr. Bambang Wahono, Dr. Muhammad Khristamto Aditya Wardana, Dr. Cahyani Windarto, Ardhika Setiawan, Bernike Febriana Samosir, Ahmad Adib Rosyadi, Ali, Warsita Wayan, I Komang Gede Tryas Agameru Putra and all laboratory members for the many fond memories we have spent together and their valuable support during my research. This work could only be realized thanks to their unconditional help and honest feedback.

I would like to thank the research sponsors: National Research Foundation of Korea, Regional Innovation Strategy (RIS), Hyundai Heavy Industries Co., Ltd., and the University of Ulsan.

My special thanks go to my parents, who have passed away, my beloved wife, Aniq Hudiayah Bil Haq, S.Psi., M.A., and my beautiful daughters (Syakira Alifa Rasyadani and Latiefa El Hebron). Without their unwavering support, I would not have been able to complete this important journey in my life. This dissertation is dedicated to them.

Finally, I would like to thank the members of my dissertation committee for their time and valuable comments on improving the quality of this work.

This dissertation contains all of the research conducted during the doctoral studies. The entire content of this thesis was written to partially fulfill the requirements of the PhD of Science in Mechanical and Automotive Engineering at the University of Ulsan.

Binyamin

TABLE OF CONTENTS

ABSTRACT	iii
ACKNOWLEDGEMENT	iv
TABLE OF CONTENTS	v
LIST OF FIGURES	viii
LIST OF TABLES	xiv
NOMENCLATURES AND ABBREVIATION	xv
1. INTRODUCTION.....	1
1.1. Background.....	1
1.2. Challenges and Strategies for mass transport and cell performance improvement on PEMFC.....	6
1.3. Objectives of the study	8
1.4. Scope of the study	9
1.5. Thesis outline.....	10
2. LITERATURE REVIEW	12
2.1. Introduction	12
2.2. PEM Fuel cell	12
2.2.1. PEM Fuel cell layout and operation	13
2.2.2. PEM Fuel cell electrochemistry	15
2.2.3. Membrane Electrode Assembly (MEA).....	16
2.2.4. PEM Fuel cell bipolar plates	19
2.3. Review of previous studies on flow field configurations at bipolar plate effect on mass transport and performance	20
2.4. Review of previous studies on PEM fuel cell performance predictions	25
2.5. Summary.....	28
3. RESEARCH METHODOLOGY	29
3.1. Numerical model	29
3.1.1. PEMFC models development.....	29
3.1.2. Material Properties of the PEM Fuel Cell Components	34

3.1.3.	Boundary condition, initial condition, assumption, and numerical procedure	37
3.1.4.	Governing equations.....	45
3.2.	Grid-independent verification and model validation.....	49
3.3.	Summary.....	53
4.	EFFECT OF GDL FACE PERMEABILITY AND THERMAL CONTACT RESISTANCE ON TEMPERATURE DISTRIBUTION, MASS TRANSPORT, AND PERFORMANCE OF PEM FUEL CELL	54
4.1.	Thermal contact resistance (TCR) and GDL face permeability affect cell performance and temperature profiles.	54
4.2.	Implementation of artificial neural network (ANN) and Genetic algorithm (GA) optimization on cell performance	63
4.3.	Oxygen mass fraction	66
4.4.	Hydrogen mass fraction.....	68
4.5.	Water mass fraction.....	70
4.6.	Velocity magnitude and cathode pressure drop.....	73
4.7.	Summary.....	75
5.	TAPERED FLOW FIELD CONFIGURATION TO IMPROVE MASS TRANSPORT AND PERFORMANCE OF PROTON EXCHANGE MEMBRANE FUEL CELL.....	77
5.1.	Effect of tapered PEM fuel cell model on overall cell performance.....	77
5.2.	Temperature distributions with varying tapered flow field configuration	79
5.3.	Oxygen mass fraction and hydrogen mass fraction.....	81
5.4.	Water mass fraction and osmotic drag coefficient	86
5.5.	Current density, velocity magnitude, and pressure drop	91
5.6.	Summary.....	96
6.	EFFECTS OF WATER DROP BLOCK CONFIGURATIONS ON TEMPERATURE PROFILES, MASS TRANSPORT CHARACTERISTICS, AND PERFORMANCE IN PEM FUEL CELL	98
6.1.	The influence of WDB models, considering interfacial contact resistance (ICR) and GDL face permeability on the temperature profiles and the cell performances	98
6.2.	Oxygen mass fraction distribution.....	105
6.3.	Hydrogen mass fraction distribution	107

6.4.	Water mass fraction distribution.....	110
6.5.	Flow velocity and pressure drops	112
6.6.	Summary.....	118
7.	CONCLUSIONS AND CONTRIBUTION	120
	REFERENCES.....	123
	APPENDICES.....	138

LIST OF FIGURES

Fig. 1.1 Oil consumption worldwide from 1970 to 2022 (in million metric tons).....	2
Fig. 1.2 Annual global greenhouse gas (GHG) emissions by sector from 1990 to 2022 (in a million metric tons of carbon dioxide equivalent)	2
Fig. 1.3 Estimate shared of CO ₂ emissions in the transportation sector worldwide in 2022 by transport type.....	3
Fig. 1.4. Mass transport and performance strategies on PEM fuel cell: (a) Baffle blocks computational domain, (b) Polarization curves of PEMFC without and with 6 two-block structures under different cathode RHs.	7
Fig. 1.5. Flowcharts of the potential strategies to enhance mass transport and PEM fuel cell performance.....	9
Fig. 2.1. Schematics of a PEM fuel cell	13
Fig. 2.2. Polarization curve of proton exchange membrane (PEM) fuel cell.....	14
Fig. 2.3. A pictorial illustration of Nafion Membrane.....	16
Fig. 2.4. Membrane Transport Phenomena	17
Fig. 2.5. Transport pathways in a cathodic catalyst layer	18
Fig. 2.6. Gas diffusion layer (GDL) unit cell	19
Fig. 2.7. Bipolar plate of PEM fuel cell.....	20
Fig. 3.1. Schematic of the straight flow field of PEM Fuel Cell (a) and its operating principle (b).	30
Fig. 3.2. PEM fuel cell with six different flow field channel models	32
Fig. 3.3. Imitated water drop model description and operating principle of PEMFC.	33
Fig. 3.4. Detail and schematic representation of WDB channel and their model structures.	34
Fig. 3.5. Material properties setup for bipolar plats/current collectors.	35
Fig. 3.6. Material properties setup for gas diffusion layers (GDLs).	35
Fig. 3.7. Material properties setup for catalyst layers (CLs).	36
Fig. 3.8. Material properties setup for electrolyte/membrane (PEM).	36

Fig. 3.9. Graphical user interface (GUI) Setup of ANSYS Fluent with Fuel Cell and Electrolysis (PEMFC) Model	40
Fig. 3.10. Detailed flowchart for solving a multiphysics problem for a straight and currently developed PEM fuel cell model.	41
Fig. 3.11. The Parameters Tab of the Fuel Cell and Electrolysis Models Dialog Box	42
Fig. 3.12. Operating Condition Dialox Box	43
Fig. 3.13. Boundary conditions tab for current collector (Tab-C) with electric potential 0.6V.	43
Fig. 3.14. Residual graph for convergence condition of PEM fuel cell simulation	44
Fig. 3.15. Console window of average current density report at cell voltage 0.6V	44
Fig. 3.16. Plot window of average current density report (0.6841 A/cm ²) at cell voltage 0.6V and 250 iteration.	45
Fig. 3.17. A diagram depicting the model geometry, structure, and computational domains of straight and parallel tapered flow fields for PEM fuel cell.....	50
Fig. 3.18. A schematic describing PEM Fuel Cel's computational domains and meshes of difference flow field structures (Straight and Water Drop Blocks).	51
Fig. 3.19. (a) Grid independency verification for the current density at V = 0.60V, (b) comparison of the polarization curves between the current computational study with experiment results for straight channel model with different pressure and temperature operations.	52
Fig. 4.1. Temperature distributions on XY-plane (40mm from origin of Z-axis) at various cell voltages without considering TCR (operating pressure, P = 1 atm; operating temperature, T = 70°C; cathode gas: oxygen; anode gas: hydrogen).....	56
Fig. 4.2. Temperature distributions on XY-plane (40mm from origin of Z-axis) at various cell voltages with considering TCR (1.00E-01 m ² •K/W) and GDL face permeability (3.50E12 m ⁻²) (operating pressure, P = 1 atm; operating temperature, T = 70°C; cathode gas: oxygen; anode gas: hydrogen).....	57
Fig. 4.3. Distributions of temperature at iso view with various cell voltages (a) 0.4V, (b) 0.5V, (c) 0.6V, (d) 0.7V, (e) 0.8V, and (f) 0.9V ignoring TCR (operating pressure, P = 1 atm; operating temperature, T = 70°C; cathode gas: oxygen; anode gas: hydrogen).	59

Fig. 4.4. Current and power densities of various cases (operating pressure = 1 atm; operating temperature, $T = 70^{\circ}\text{C}$ (343.15K)).	61
Fig. 4.5. Profiles of temperature toward the Y-axis with various cell output voltages: (a) without (b) with TCR ($1.00\text{E-}01 \text{ m}^2 \text{ K/W}$).	61
Fig. 4.6. (a) Current density and (b) power density curves with distinct cases (operating temperature, $T = 70^{\circ}\text{C}$ (343.15K); operating pressure = 1 atm).	62
Fig. 4.7. Combined ANN and GA optimization using 3D multiphysics simulation.	65
Fig. 4.8. (a) Current density and (b) power density curves with ANN-GA optimization models in different cases (operating temperature $T = 70^{\circ}\text{C}$ (343.15K); operating pressure = 1 atm).	65
Fig. 4.9. The distribution of oxygen mass fraction in the x-y planes of the fuel cell through the z direction (gas flow) for six different cases at 0.4V cell voltage.	67
Fig. 4.10. The mass fraction of O_2 on the centerline of the interface between CGDL and CCL is examined for six cases at 0.4 V of a cell voltage.	68
Fig. 4.11. The contours of H_2 mass fraction at the x-y planes inside the fuel cell through the z (gas flow) at 0.4 V cell voltage for six various scenarios.	69
Fig. 4.12. Mass fraction of H_2 along the centerline of the interface between the ACL and the AGDL in the anode channel at 0.4 V of cell voltage for six cases.	70
Fig. 4.13. For six difference cases, the contours of water mass fraction at the x-y planes inside the fuel cell at 0.4 V cell voltage along the z (gas flow).	71
Fig. 4.14. The mass fraction of H_2O on the centerline of the interface between CGDL and CFC across the cathode channel is examined for numerous scenarios at a cell voltage of 0.4V.	72
Fig. 4.15. The velocity of oxygen at the centerline of the interface between CGDL and CFC through the cathode channel is examined for distinct scenarios at a cell voltage of 0.4 V.	73
Fig. 4.16. The pressure distributions at the x-y planes inside the fuel cell through the z-axis representing gas flow) are examined at a cell voltage of 0.4 V for six cases.	74
Fig. 4.17. The pressure on the centerline of the interface between CGDL and CFC along the cathode channel is examined for different scenarios at 0.4 V of a cell voltage.	75
Fig. 5.1. Polarization curves for various tapered parallel FFC models.	78
Fig. 5.2. Power density versus current density for various tapered parallel FFC models.	79

Fig. 5.3. The temperature distribution at left (inlet side), middle PEMFC (YZ-Plane), and right (outlet side) views along the CH for various cases at cell voltage 0.4 V.	80
Fig. 5.4. Oxygen mass fraction distribution at the x-y planes within the fuel cell along the z (gas flow) direction for various cases at cell voltage 0.4 V.	81
Fig. 5.5. Oxygen mass fraction on the centerline of the interface between CCL and CGDL along the cathode channel for various cases at a cell voltage of 0.4V.	82
Fig. 5.6. O ₂ mass fraction profiles at the interface between CCL and CGDL along the CH for various cases at cell voltage 0.4 V.	83
Fig. 5.7. For six distinct cases, the distributions of hydrogen mass fraction at the x-y planes within the fuel cell along the z (gas flow) at 0.4 V cell voltage.	84
Fig. 5.8. H ₂ mass fraction on the centerline of the interface between ACL and AGDL along the anode channel for various scenarios at a cell voltage of 0.4 V.	85
Fig. 5.9. H ₂ O mass fraction distribution at the interface between CCL and CGDL along the CH for various cases at cell voltage 0.4 V.	86
Fig. 5.10. For various cases, H ₂ O mass fraction distribution at X-Y planes within the fuel cell along the channel at cell voltage 0.4 V.	87
Fig. 5.11. H ₂ O mass fraction on the centerline of the interface between the CCL and CGDL along the cathode channel for various cases at a cell voltage of 0.4 V.	88
Fig. 5.12. Osmotic drag coefficient profiles at X-Y planes of the middle of the PEM fuel cell for various cases at cell voltage 0.4 V.	89
Fig. 5.13. Current density profiles at the middle cross-section of the CCL along the channel for various cases at cell voltage 0.4 V.	91
Fig. 5.14. Velocity profiles at X-Y planes within the fuel cell along the channel for various cases at cell voltage 0.4 V.	93
Fig. 5.15. Velocity on the centerline of the interface between CCL and CGDL along the cathode channel for various cases at a cell voltage of 0.4 V.	94
Fig. 5.16. Pressure distribution at X-Y planes along the channel for various cases at a cell voltage of 0.4 V.	95
Fig. 5.17. Pressure drop on the centerline of the interface between CFC and CGDL along the cathode channel for various cases at a cell voltage of 0.4 V.	96
Fig. 6.1. Profiles of temperature distributions in the Z-Y planes through the fuel cell channel's midsection at 0.4 V cell voltage under various scenarios.	99

Fig. 6.2. Temperature distributions at XY-plane (38 mm from origin of Z-axis) with different cases at 0.4 V cell voltage (operating temperature, $T = 70^{\circ}\text{C}$; operating pressure, $P = 1 \text{ atm}$).....	101
Fig. 6.3. Temperature distributions at the centerline of xy-plane (38 mm from origin of Z-axis) with different cases at 0.4 V cell voltage (operating temperature, $T = 70^{\circ}\text{C}$; operating pressure, $P = 1 \text{ atm}$).	102
Fig. 6.4. (a) Polarization and (b) power density curves with different cases (operating pressure = 1 atm; operating temperature, $T = 70^{\circ}\text{C}$ (343.15K)).....	103
Fig. 6.5. Average current density and power density with six different cases of PEM fuel cell.....	103
Fig. 6.6. O_2 mass fraction contours for various cases between the cathode CL/GDL interface through the channel at 0.4 V of cell voltage.	105
Fig. 6.7. Mass fraction of oxygen on the centerline between cathode GDL/CL interface through the cathode channel for distinct scenarios at 0.4V of a cell voltage....	106
Fig. 6.8. H_2 mass fraction distribution for various cases at the anode GDL/CL interface along the channel at cell voltage 0.4 V.	108
Fig. 6.9. Mass fraction of hydrogen on the centerline at the anode GDL/CL interface through the channel for six different scenarios at a cell voltage of 0.4 V.....	109
Fig. 6.10. For various cases, H_2O mass fraction profiles at the cathode GDL/CL interface throughout the channel at 0.4 V of cell voltage.	110
Fig. 6.11. For six cases, H_2O mass fraction comparison on the centerline within the CL/GDL interface throughout the channel at 0.4 V of cell voltage.	111
Fig. 6.12. Patterns of the velocity magnitudes at ZY planes on the center cross-section of the fuel cell passing through the channel for distinct scenarios with a 0.4 V cell voltage.....	113
Fig. 6.13. Comparison of velocity magnitude on the center-line between cathode GDL/CL interface through the cathode channel at a cell voltage of 0.4 V for six cases.	114
Fig. 6.14. For various cases, the pressure distributions were compared at Z-Y planes on the center cross-section of the fuel cell through the channel at 0.4 V of cell voltage.	116

Fig. 6.15. Comparison of pressure on the middle-line of the interface between cathode GDL/FC throughout the cathode channel from inlet to outlet for various cases at a cell voltage of 0.4 V..... 117

Fig. 6.16. The pressure drop comparison across the cathode channel was measured for six scenarios at a cell voltage of 0.4 V. 118

LIST OF TABLES

Table 1.1. Thesis consists of seven chapters organized into four main sections.....	11
Table 3.1. PEMFC geometric parameters for the straight channel model	31
Table 3.2. Material properties of the PEMFC components.....	34
Table 3.3. Description of the simulated cases regarding the various GDL face permeability and TCR.....	37
Table 3.4. For ordinary parallel and other tapered parallel FFCs, TCR dan PMT between BPs and GDLs.....	38
Table 3.5. Description of the simulated cases regarding the distinct WDB models, ICR, and GDL face permeability.....	38
Table 3.6. Operating parameters for validation.....	39
Table 3.7. Source terms of governing equations.	48
Table 4.1. Description of the simulated cases regarding the various GDL face permeability and TCR.....	55

NOMENCLATURES AND ABBREVIATION

Nomenclature

A	: area, (m^2)
A_{act}	: activation area, (m^2)
a	: water activity
A_{in}	: inlet area, (m^2)
A_s	: a specific area of the catalyst layer, (m^{-1})
C_i	: gas molar concentration, ($\text{mol}\cdot\text{m}^{-3}$)
C_p	: specific heat capacity, ($\text{J}\cdot\text{mol}^{-1}\cdot\text{K}^{-1}$)
D	: coefficient of diffusion, ($\text{m}^2\cdot\text{s}^{-1}$)
D_i^{eff}	: effective gas species diffusion coefficient, ($\text{m}^2\cdot\text{s}^{-1}$)
E_r	: reversible voltage
EW	: equivalent weight of PEM
F	: Faraday's number 96,487 ($\text{C}\cdot\text{mol}^{-1}$) or mass flux ($\text{kg}\cdot\text{m}^2\cdot\text{s}^{-1}$)
h	: coefficient of heat transfer
I^{ref}	: reference current density, ($\text{A}\cdot\text{m}^{-2}$)
J	: electrochemical reaction rate, ($\text{A}\cdot\text{m}^{-3}$)
J_{ion}	: ionic current density, ($\text{A}\cdot\text{m}^{-2}$)
$J_{0,a}^{ref}$: anode reference exchange current density, ($\text{A}\cdot\text{m}^{-3}$)
$J_{0,c}^{ref}$: cathode reference exchange current density, ($\text{A}\cdot\text{m}^{-3}$)
K	: intrinsic permeability, (m^2)
k	: relative permeability
k^{eff}	: effective thermal conductivity, ($\text{W}\cdot\text{m}^{-1}\cdot\text{K}^{-1}$)
m	: mass flow rate, ($\text{kg}\cdot\text{s}^{-1}$)
n_d	: electro-osmotic drag coefficient
P	: pressure (Pa) or power density, ($\text{W}\cdot\text{cm}^{-2}$)

p^{sat}	: water saturation pressure, (Pa)
P_c	: capillary pressure, (Pa)
R	: universal gas constant, $8.314 \text{ (J}\cdot\text{mol}^{-1}\cdot\text{K}^{-1})$
RH	: relative humidity
S	: source term of governing equations, $(\text{kg}\cdot\text{m}^{-3}\cdot\text{s}^{-1})$
s	: liquid water saturation
T	: temperature, (K)
t	: time, (s)
v	: velocity, $(\text{m}\cdot\text{s}^{-1})$
V	: voltage, (V)
V_{out}	: output voltage, (V)
Y_i	: gas species mass fraction

Greek letters

α	: transfer coefficient phase volume fraction
γ	: phase change rate, (s^{-1})
ε	: porosity
η	: overpotential, (V)
ϕ	: potential, (V)
ϕ_e	: electric potential, (V)
ϕ_{ion}	: ionic potential, (V)
λ	: membrane water content
σ	: surface tension coefficient, $(\text{N}\cdot\text{m}^{-1})$
ζ	: stoichiometric flow ratio
μ	: dynamic viscosity, $(\text{N}\cdot\text{s}\cdot\text{m}^{-2})$
ω	: ionomer volume fraction

Abbreviations

3D	: three-dimensional
ABP	: anode bipolar plate
ACL	: anode catalyst layer
AGDL	: anode gas diffusion layer

AFC	: anode flow channel
CBP	: cathode bipolar plate
CCL	: cathode catalyst layer
CFC	: cathode flow channel
CFD	: computational fluid dynamics
CGDL	: cathode gas diffusion layer
EOD	: electro-osmotic drag
HTC	: heat transfer coefficient
MEA	: membrane electrode assembly
MEM	: membrane
PEMFC	: proton exchange membrane fuel cell
TCR	: thermal contact resistance
UDF	: user-defined function

Subscripts and superscripts

a	: anode
c	: cathode, capillary
ch	: channel
d	: dissolved
d-v	: membrane water to water vapor
e	: state of equilibrium
eff	: effective
eq	: equilibrium state
g	: gas phase
H ₂	: hydrogen
H ₂ O	: water vapor
i	: gas species
in	: inlet
ion	: ionic
l	: liquid phase
mem	: membrane
mw	: membrane water

N₂ : nitrogen
O₂ : oxygen
OC : open circuit
out : outlet
p : pressure
ref : reference state
sat : saturation state
v-l : water vapor to liquid

1. INTRODUCTION

Proton Exchange Membrane Fuel Cells (PEMFCs) have emerged as promising electrochemical devices for clean and efficient energy conversion. By directly converting the chemical energy of hydrogen and oxygen into electrical energy, PEMFCs offer significant potential for addressing global energy challenges, including reducing greenhouse gas emissions, mitigating climate change, and enhancing energy security. In this chapter, the research background of the work undertaken is introduced. An overview of the trends and challenges of PEM fuel cell research on flow field configurations is produced by correlating the relevant literature and the recent progress of the author's laboratory. The research objectives and scope are presented at the end of this chapter, followed by the organization of the thesis.

1.1. Background

Over the past few years, there has been a significant increase in the quantity of depletion that has taken place due to the extraction and usage of fossil fuels. One of the most prominent strategies for solving this dilemma is the development of new energy technologies, which have emerged as a consequence. The automobile industry, small-scale portable power generation, and power generation distribution are only some of the businesses that have used fuel cells, a cutting-edge energy technology that has been employed in a range of industries [1]. Oil consumption has been continuously increasing over the previous three decades, as shown in Fig. 1.1. This trend has been seen with increasing frequency. As of 2022, it is anticipated to reach 4.39 billion metric tonnes, which is an increase from the 4.26 billion tonnes it reached in 2021 [2]. From the financial crisis that occurred in 2008-2009 until the coronavirus pandemic that occurred in 2020, this drop was an isolated occurrence between those two events. Throughout the past few years, there has been a consistent rise in the price of crude oil.

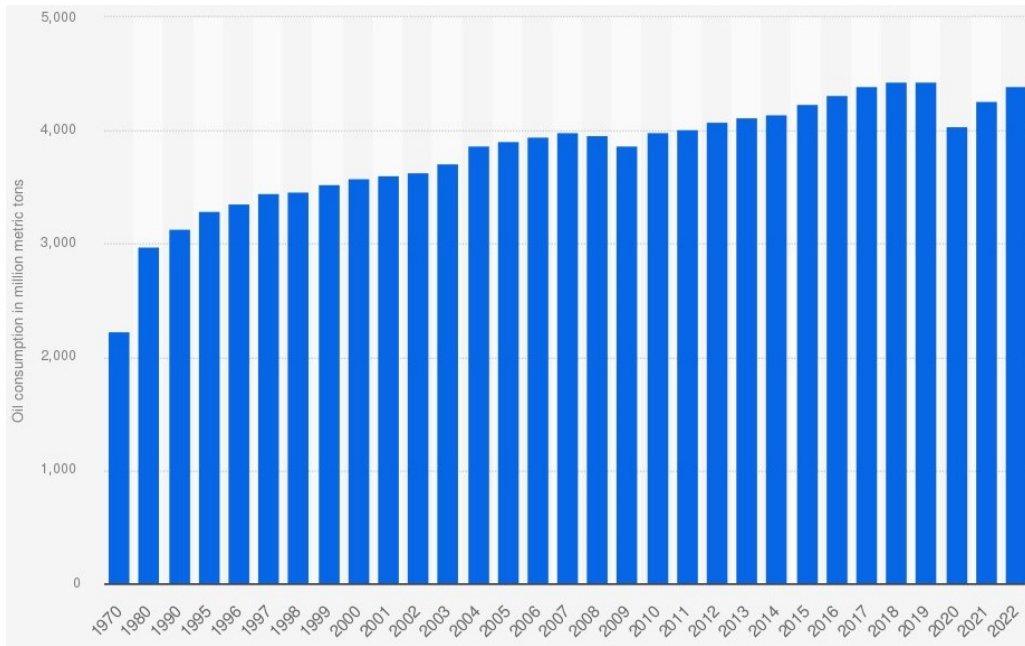


Fig. 1.1 Oil consumption worldwide from 1970 to 2022 (in million metric tons)
(Adapted from ref. [2])

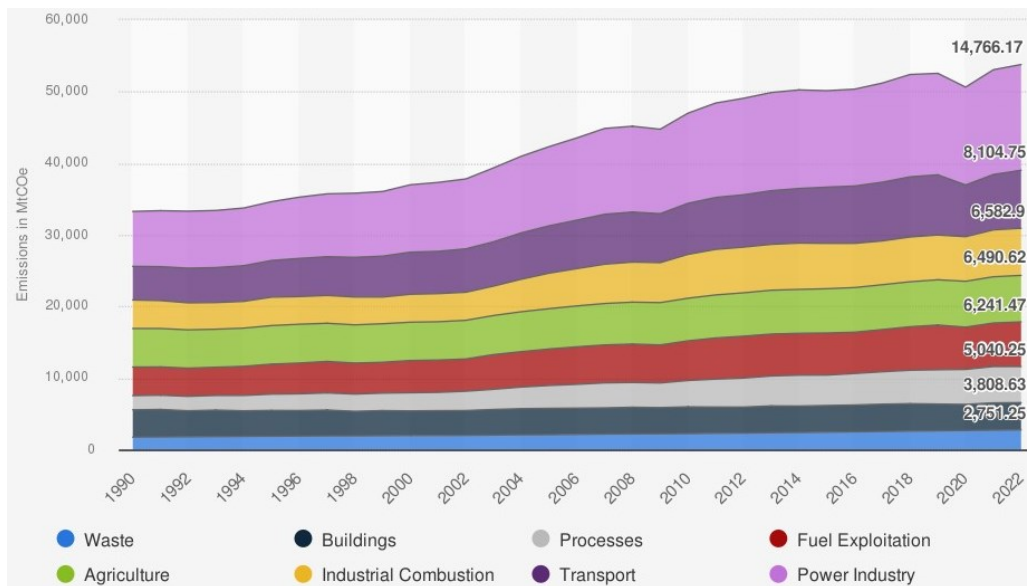


Fig. 1.2 Annual global greenhouse gas (GHG) emissions by sector from 1990 to 2022 (in a million metric tons of carbon dioxide equivalent) (Adapted from ref. [3])

Fig. 1.2 illustrates the progression of worldwide greenhouse gas (GHG) emissions from 1990 to 2022. The emission patterns for the primary sectors of activity, such as the power industry, industrial combustion and processes, transport, buildings, agriculture, waste, and fuel extraction, are also shown. The COVID-19 pandemic led to a substantial reduction in global emissions in 2020, in contrast to the previous year, so interrupting a long-standing trend of

consistent growth over the past decade. Global greenhouse gas (GHG) emissions increased in 2022 after the COVID-19 pandemic, reaching a level of 53.8 gigatonnes of carbon dioxide equivalent (Gt CO₂eq). That signifies a 2.3% surge compared to the Fig. 1.2 from 2019 and a 1.4% growth compared to the numbers from 2021.

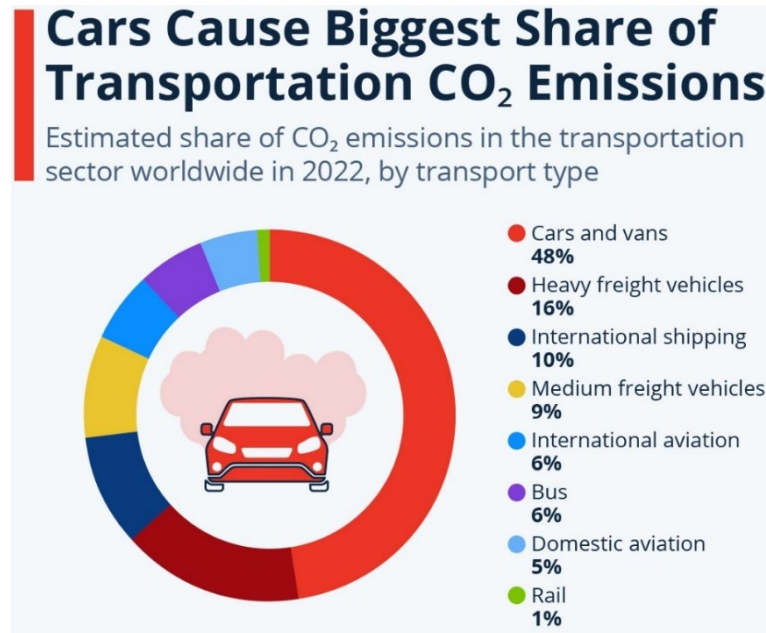


Fig. 1.3 Estimate shared of CO₂ emissions in the transportation sector worldwide in 2022 by transport type (adapted from [4])

Fig. 1.3 displays the projected distribution of CO₂ emissions in the global transportation sector in 2022, categorized by different modes of transport. Statista analyzed International Energy Agency statistics to find that cars and vans accounted for 48% of worldwide transport carbon dioxide emissions in 2022 [4]. The subsector was the most polluting mode of transport worldwide. The accompanying infographic demonstrates that vehicle and van emissions were four times more than international shipping (10%) and air travel (11%). Despite being a smaller share of vehicles, medium and heavy freight vehicles accounted for 25% of transportation emissions last year. The transportation sector emits almost seven billion metric tons of CO₂ annually.

The PEM fuel cells represent a cutting-edge advancement in sustainable energy technology, marking the fifth generation of fuel cells [5]. The device is compact, operates at a low temperature, and is highly portable. Due to its ability to transfer the chemical energy of the reactants directly into electrical energy, the PEM fuel cell eliminates the requirement for the Carnot cycle. It uses hydrogen as fuel and oxygen as oxidizer, leading to negligible

environmental consequences. The byproducts of this process are only water and a small amount of heat [5]–[7]. Integrating fuel cells with photovoltaic arrays and grid-connected technologies has the potential to improve energy management [8], [9]. Given the environmental impact, the long-term viability of urban areas, and the restrictions on renewable energy sources. PEM fuel cells have become a promising alternative for tackling these difficulties, providing a clean and efficient source of energy. However, the PEM fuel cell has faced challenges in terms of durability and cost, which have slowed its widespread adoption and commercialization [10].

The flow channel's geometry significantly impacts the transport of reaction gases in PEM fuel cells. The flow field's precise arrangement enhances reactants' effective movement in the active region, facilitating increased involvement of surplus reactants. Optimize the power density of the Proton Exchange Membrane Fuel Cell (PEMFC) by precisely adjusting the use of reaction gases. Uncover the enigmas of optimizing flow channel configuration through meticulous scientific inquiry. In their work, Wang et al. [11] examined the impact of a staggered trapezoid block on the flow channel. In their research, Song et al. [12] presented a dedicated multi-passages cooling plate designed for PEM fuel cells. The findings demonstrated that the design had the highest level of efficiency in gas distribution. Tardy et al. [13] did a study on a novel sinusoidal channel that integrates various input temperatures in order to enhance the power density of cells. Shen et al. [14] examined the optimal spacing between square blocks within a channel. Yang et al. [15] developed a numerical model to calculate the dimensions of the elliptical bulge in the M-shaped flow passage. In their research study, Liu et al. [16] utilized a multi-objective evolutionary algorithm to improve energy efficiency and output power. This was achieved by optimizing operating circumstances, channel input, and outlet height. In a previous study conducted by Zeng et al. [17], a genetic algorithm was utilized to determine the optimal cross-section channel. Based on a thorough analysis, it was determined that the area maximizing of a trapezoidal channel is influenced by two main factors: a bottom edge width of 1.2874 mm and a top edge width of 0.8886 mm. In their study, Chen et al. [18] conducted a numerical analysis of the porous-blocked baffles in a PEMFC. The baffles were positioned at a vertical displacement of 1.125mm from the reference point and sloped at an angle of 60 degrees. By incorporating baffles, the channel had a significant 90% enhancement in the optimum net power, as compared to a passage without baffles.

Ding et al. [19] conducted a study to evaluate the criteria used to quantify the flow channel in PEM fuel cells, focusing particularly on entropy generation. The study demonstrated that the current density reaches its peak value with a wavelength of 2 mm and an amplitude of 0.4 mm, resulting in a 10.40% enhancement against to the waveless design. Xu et al. [20] examined the impact of wave-shaped flow passages and grooved models in the Gas Diffusion Layer (GDL) of Proton Exchange Membrane (PEM) fuel cells. The results suggest that the flow field containing a groove in the GDL has remarkable efficiency due to its wave-shaped design. The ideal flow channel exhibits a sinusoidal pattern with an amplitude of 0.643 mm and undergoes 9 undulating cycles. The groove is positioned at a location of 9.5 mm and has a depth of 0.05 mm. Moreover, the net power density can be enhanced by 2.64%. In their investigation, Liu et al. [21] implemented the serpentine flow field (SFF) and the parallel flow field (PFF) to enhance the mass transport of PEM fuel cells. The findings demonstrated a significant improvement in the distribution of oxygen in the PFF with a variable diameter (PFF@VD), leading to a noteworthy 26% increase in peak power. Park et al. [22] examined the mass transfer characteristics of a metallic Bipolar Plate (BP) for stationary applications in a PEM fuel cell by studying the flow field and Gas Diffusion Layer (GDL). The study revealed that the flow characteristics of the metal foam resulted in a 6.55% enhancement in water drainage. The fuel cell's performance experienced a notable enhancement, resulting in a 9.33% rise. The fuel cell's efficiency was greatly improved by a gas diffusion layer with a high porosity and permeability level, resulting in a significant improvement of 14.67%. In their study, Wan et al. [23] utilized a metal foam flow field to effectively regulate the dissipation of heat and retention of water. Upon comparing the parallel flow fields of varied widths (case 1, case 3, and case 5), it was seen that case 6 significantly improved net output performance and reduced compression work. The net output performance of case 6 showed a corresponding rise of 3.4%, 8.8%, and 55.1%, while the compression work decreased by 69.7%, 38.3%, and 64.4%, all at a specific temperature of 50°C.

In the mentioned studies, many researchers conducted numerically, and some experimentally investigated the flow field configurations at bipolar plates. However, very few researchers have investigated the effect of modification of flow field designs without considering variations of porous medium thickness (PMT), thermal contact resistance (TCR), interface contact resistance (ICR), GDL face permeabilities, GDL properties on temperature profiles,

mass transport and performances of PEM fuel cell. Moreover, a single PEM fuel cell contains very small flow fields of bipolar plates, making it more difficult to visualize and analyze experimentally. Because of this, a comprehensive inquiry to enhance comprehension of the flow features, temperature profiles, and performances mainly based on the modification of flow channel configurations and variations of porous medium thickness (PMT), thermal contact resistance (TCR), interface contact resistance (ICR), GDL face permeabilities, GDL properties on bipolar plates of PEM fuel cell is needed. Lastly, this work is expected to act as a basis for visualization of bipolar plate flow field and optimizing mass transport and performance of proton exchange membrane fuel cell.

1.2. Challenges and Strategies for mass transport and cell performance improvement on PEMFC

To achieve the highest possible levels of efficiency and reliability with this technology, it is vital to have a solid understanding of the strategies that may be utilized to optimize mass transfer and improve cell performance in proton exchange membrane fuel cells (PEMFCs). It is essential to identify innovative methods to overcome these challenges, as it has been acknowledged that restrictions in mass movement are a significant element that affects the performance of PEMFCs [24]. PEMFCs have been the subject of extensive study, highlighting the significance of fine-tuning flow field patterns to maximize mass transfer efficiency and overall cell performance [25]. Both the performance of PEMFCs and the transport of reactants are improved when flow channels with baffles are incorporated into the design [26], as seen in Fig. 1.4.

Addressing the challenges and implementing effective strategies to increase mass transport and enhance cell performance in Proton Exchange Membrane Fuel Cells (PEMFCs) are critical focal points of current research. Identifying mass transfer limitations is crucial in understanding the performance challenges faced by PEMFCs [24]. It is essential to address these limitations to maximize fuel cell systems' efficiency and reliability. Research has emphasized the significance of flow field patterns in addressing mass transport limitations and enhancing the performance of PEM fuel cells [25]. Optimizing flow field design is a crucial strategy that significantly impacts mass transfer within PEMFCs, enhancing cell performance [27].

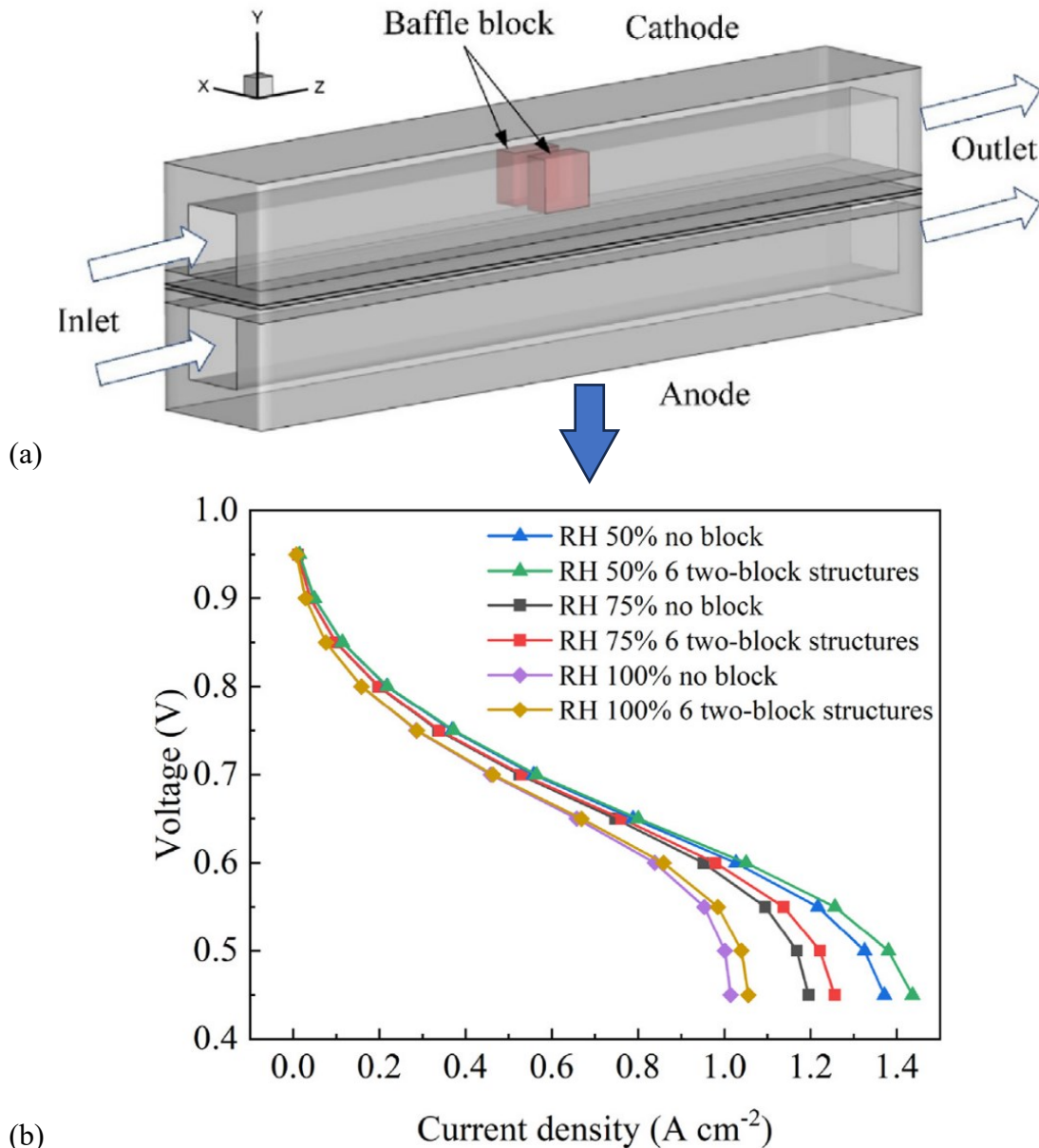


Fig. 1.4. Mass transport and performance strategies on PEM fuel cell: (a) Baffle blocks computational domain, (b) Polarization curves of PEMFC without and with 6 two-block structures under different cathode RHs (Adapted from ref. [26]).

In addition, researchers have explored using a traveling-wave flow field to enhance the performance of PEMFCs by enhancing mass transport efficiency [28]. This novel approach shows great potential in addressing the obstacles associated with mass transfer limitations in fuel cell systems. In addition, optimizing flow channels by incorporating features such as baffles has demonstrated promising results in improving reactant transfer and enhancing the overall performance of PEM fuel cells [29]. Strategies that aim to enhance cell performance

by focusing on transient mass transport have been extensively studied to ensure a sufficient oxygen supply for fuel cells [30]. These strategies focus on tackling the ever-changing challenges of mass transport under different operating conditions, which ultimately leads to enhanced efficiency and stability in PEMFC operation.

Ultimately, researchers are tirelessly working to find new ways to address the obstacles related to mass transport limitations and increase the overall efficiency of Proton Exchange Membrane Fuel Cells. Through optimizing flow field design, exploring innovative flow field patterns, and examining transient mass transport dynamics, researchers strive to unleash the complete potential of PEMFC technology for sustainable energy applications.

1.3. Objectives of the study

This study focuses on the combination of both simulation and experimental validation literature methods to investigate the flow field configurations that take into account variation of porous medium thickness (PMT) thermal contact resistance (TCR), interface contact resistance (ICR), GDL porosity, and GDL face permeability effect on mass transport and cell performance of PEM fuel cell. The objectives of this study are given below:

- (i) Set up a single PEM fuel cell based on ANSYS Fluent Fuel Cell and Electrolysis Model to simulate the PEM fuel cell mass transport characteristics and cell performance with various flow field channels.
- (ii) To investigate the influence of tapered flow field configurations on improving PEM fuel cells' mass transport and cell performance. The primary data are polarization curves, temperature distributions, mass fractions (oxygen, hydrogen, and water), mass transport distribution, gas velocity, and pressure drops.
- (iii) To investigate the consideration of porous medium thickness (PMT), thermal contact resistance (TCR), interface contact resistance (ICR), and GDL face permeability on mass transport and cell performance.
- (iv) To optimize the operating parameters of voltage, GDL face permeability, and thermal contact resistance on cell performance.
- (v) To investigate the influence of water-block drop models on bipolar plate flow fields on mass transport characteristics, temperature profiles, and cell performances.

A brief explanation of the flowchart strategy is seen in Fig. 1.5 to obtain the above targets.

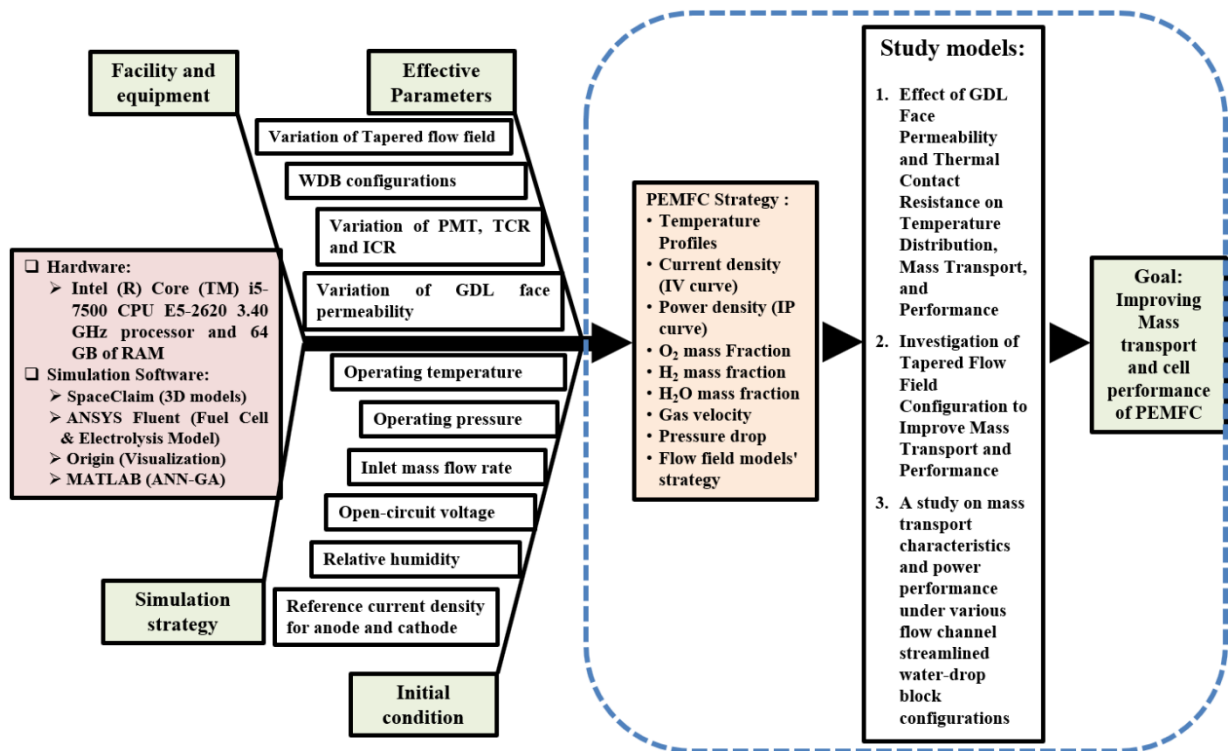


Fig. 1.5. Flowcharts of the potential strategies to enhance mass transport and PEM fuel cell performance.

1.4. Scope of the study

The thesis will mainly focus on modeling and simulating a PEM fuel cell with a single flow field on both the anode and cathode sides to provide a specific good accuracy method to determine optimal numerical modeling of flow field design of PEM fuel cell on mass transport and cell performance.

The scopes of the study include:

1. The ANSYS Fluent Fuel Cell and Electrolysis Model has been exclusively used to run the simulations.
2. Flow field models used are parallel, tapered ($L_{i/o}0.7$; $L_{i/o}0.8$; $L_{i/o}0.9$; $L_{i/o}1.0$; $L_{i/o}1.1$; $L_{i/o}1.2$), and five models of imitated water drop block configurations.
3. The single flow field of bipolar plates is used on both the cathode and anode sides for numerical simulation.
4. Applicable element numbers were used for the grid independence verification study, ranging from 496,000 to 592,000.
5. The utilization of the SIMPLE algorithm is prevalent in the pressure-velocity coupling, and the component is Least Squares Cell-based.

6. The simulation validation of the polarization curve is taken from the experimental results of the literature.
7. The parameters used for validation are operating pressure 1 atm, operating temperature 70°C, open-circuit voltage 0.95V, and other parameters in Table 3.6.
8. Analysis results of current density (polarization curve), power density, temperature profiles, mass transport characteristics (oxygen, hydrogen, and water mass fractions), velocity magnitude, and pressure drops.

1.5. Thesis outline

The thesis comprises seven chapters organized into four main sections, as illustrated in Table 1.1. The first consists of Chapter 1 and Section 2. Chapter 1 gives a brief introduction of the thesis, a general topic area of the flow field configuration effect on mass transport and cell performance, an explanation of how vital flow field configuration can influence the mass transport and performance of PEM fuel cells, a brief introduction the efficacious solution which researches specific objectives and scopes of the research. Meanwhile, Chapter 2 gives a short literature review of the research objectives most closely related to the work, such as the arrangement of three-dimensional flow fields (parallel, serpentine, and irregular models) effect on mass transport distribution, temperature distribution, gas flow rate, current density distribution and output performance of various PEM fuel cells. A brief review of previous research related to this area has been done. Highlight the gap in the study on the flow field structures, which considers thermal and interface contact resistances, GDL porosities, and permeability variation that has not been researched or solved. This thesis work will fill up the gap.

The second section is Chapter 3, which describes the research methodology, PEMFC model development, material properties, boundary conditions, initial condition, governing equations for the analysis, grid-independent verification, and model validation.

The third section consists of Chapter 4 and Chapter 5. Chapter 4 presents the results and discussion of temperature distribution, mass transport, and cell performance, emphasizing GDL face permeability and thermal contact resistance (TCR) parameters with a combined artificial neural network algorithm (ANN-GA) method to identify the optimum powers and their operating conditions in six cases in PEM fuel cells. Chapter 5 presents the tapered flow field numerical results and discusses mass transport distribution and cell performance of

PEM fuel cells in detail. This chapter will comprehensively study the effect of tapered flow field structures considering porous medium thickness (PMT) and thermal contact resistance (TCR) variation on mass transport distribution, temperature distribution, velocity distribution, and cell performance.

The fourth section, Chapter 6, presents results and discussion of various flow channel streamlined water-drop block configurations that influence mass transport characteristics and PEM fuel cells' power performance.

The final section of this thesis is Chapter 7, which comprises the summary of this research, the contribution to the research field, and the additional information in the references and appendices.

Table 1.1. Thesis consists of seven chapters organized into four main sections

Research objectives and literature review	<p>Chapter 1. INTRODUCTION Key point: background, challenges, objectives, scope</p> <p>Chapter 2. LITERATURE REVIEW Key point: flow field designs, mass transport, cell performances</p>
Research platform	<p>Chapter 3. RESEARCH METHODOLOGY Key point: models development, governing equations, numerical model, and model validation</p>
Research on mass transport characteristics, cell performance, and optimization operating parameters	<p>Chapter 4. EFFECT OF GDL FACE PERMEABILITY AND THERMAL CONTACT RESISTANCE ON TEMPERATURE DISTRIBUTION, MASS TRANSPORT, AND PERFORMANCE OF PEM FUEL CELL Key point: porous medium thickness, thermal contact resistance, ANN-GA optimization</p> <p>Chapter 5. EFFECT OF TAPERED FLOW FIELD CONFIGURATION TO IMPROVE MASS TRANSPORT AND PERFORMANCE OF PROTON EXCHANGE MEMBRANE FUEL CELL Key point: tapered flow field, porous medium thickness, thermal contact resistance</p> <p>Chapter 6. EFFECTS OF WATER DROP BLOCK CONFIGURATIONS ON TEMPERATURE PROFILES, MASS TRANSPORT CHARACTERISTICS, AND PERFORMANCE IN PEM FUEL CELL Key point: water-drop block, mass transport, temperature profiles, cell performances</p>
Research outcomes	<p>Chapter 7. CONCLUSION AND CONTRIBUTION Key point: conclusion, contribution</p>

2. LITERATURE REVIEW

2.1. Introduction

This chapter comprehensively explains the previous research endeavors relevant to the current investigation. Additionally, a comprehensive summary of additional pertinent research studies is also included. This review is organized chronologically to provide an understanding of how previous research endeavors have established the basis for subsequent studies, including the current research effort. This review offers a comprehensive analysis to inform the design of future research efforts by including the existing body of literature and considering the scope and direction of this study. The initial section will elucidate the fundamental principles of a PEM fuel cell, while the subsequent segment will delve into the design aspects of bipolar plate flow fields. This chapter also provides a detailed discussion of mass transport characteristics within a PEM fuel cell. At the conclusion of this chapter, detailed explanations are provided for some of the reviews undertaken by past researchers that are relevant to this study.

2.2. PEM Fuel cell

A proton exchange membrane (PEM) fuel cell is an electrochemical cell that utilizes an electrochemical reaction to transform the chemical energy from hydrogen and oxygen into electrical energy. PEM fuel cells possess notable attributes such as superior power density, low operational temperatures (60~80°C), rapid starting durations, and very few emissions [31]. Consequently, they have great potential for a wide range of applications, including automobile vehicles, stationary power production, and portable electronics. Recent developments in PEM fuel cell technology have prioritized enhancing crucial performance factors, including efficiency, durability, cost-effectiveness, and operational flexibility. Research has focused on creating new materials for catalysts, membranes, and electrode architectures in order to improve cell performance and lower expenses. Furthermore, researchers have explored novel system designs and control methodologies to enhance the efficiency of fuel cell operation in different circumstances and address challenges such as water management, fuel crossover, and catalyst degradation.

2.2.1. PEM Fuel cell layout and operation

A PEM fuel cell is composed of a proton exchange membrane (PEM) that is positioned between two electrodes, namely the anode and the cathode. Hydrogen gas is introduced to the anode, where it performs electrochemical redox reactions to generate protons and electrons. The protons migrate through the Proton Exchange Membrane (PEM) towards the cathode, whereas the electrons traverse an external circuit, producing electrical power. At the cathode, the oxygen present in the air reacts with the protons and electrons, resulting in the formation of water, which is the sole consequence of this process. Fig. 2.1 depicts the PEM fuel cell's specific structure adapted from the ANSYS Fluent Fuel Cell and Electrolysis Model [32]. There are three primary justifications for utilizing hydrogen. Out of all the many types of fuels, such as methanol, ethanol, and formic acid, hydrogen fuel has the highest weight-based energy density, measuring 33.3 Wh/g. Furthermore, of all the available fuels (including fluidized solids, liquids, vapors, and gases), hydrogen exhibits the highest ease of oxidation under temperature and pressure conditions close to the surrounding environment. One additional factor is that if the cathode utilizes air, particularly oxygen, in the air, the fuel cell process can be emission-free (without greenhouse gases or pollution) as the only byproducts are electricity, heat, and water. PEM fuel cells may only be considered zero-emission if there is no hydrocarbon consumption during the entire process or if an equal amount of hydrocarbon production balances off the consumption.

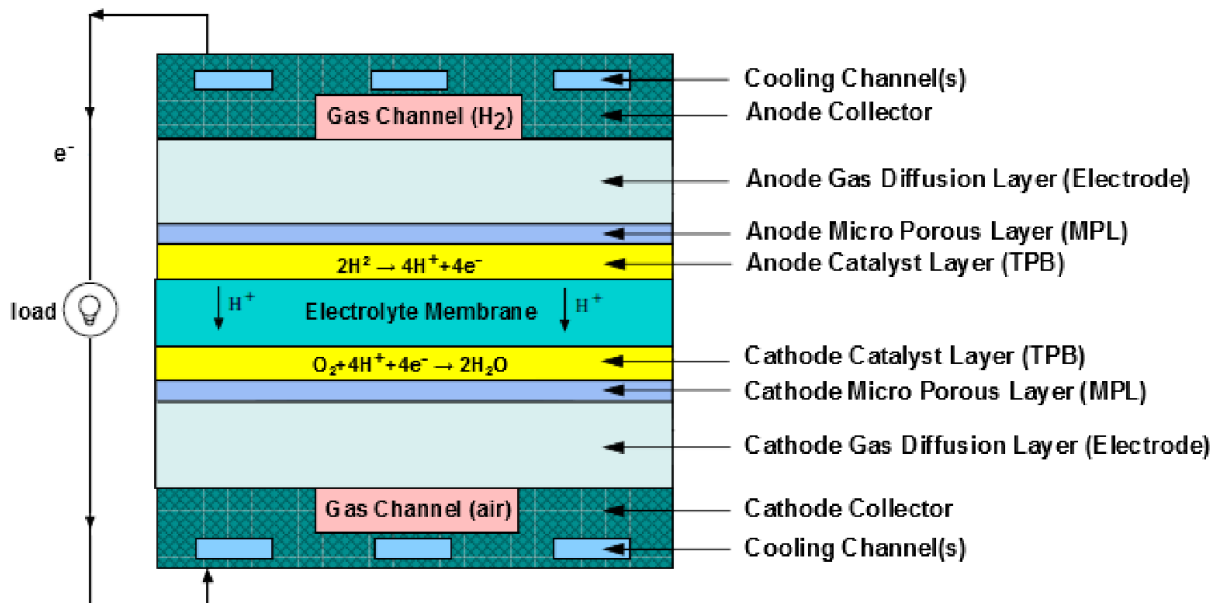


Fig. 2.1. Schematics of a PEM fuel cell (Adapted from ref. [32])

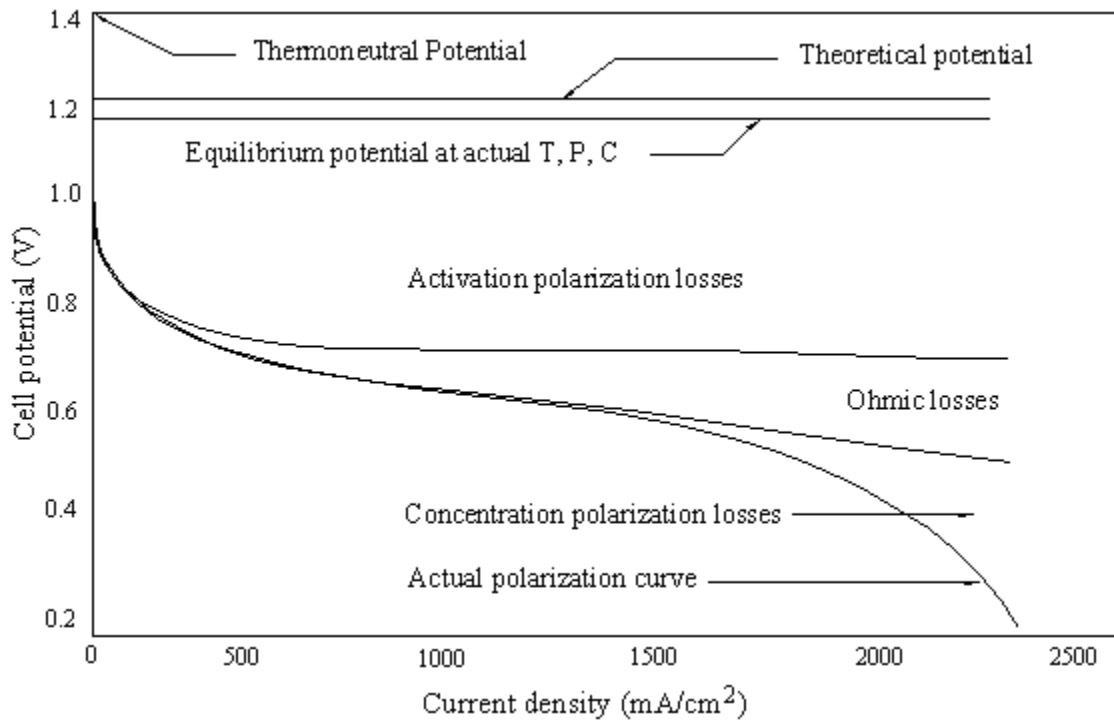


Fig. 2.2. Polarization curve of proton exchange membrane (PEM) fuel cell (Adapted from ref. [122]).

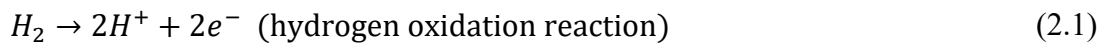
Three types of voltage losses can occur in fuel cells. These include activation loss, also known as activation polarization. Ohmic loss, also known as ohmic polarization, and finally, concentration losses, also known as concentration polarization. At low levels of electric current, the area where the cell voltage decreases owing to activation polarization experiences a significant drop. This dip is mostly caused by the slow kinetics of the oxygen reduction reaction (ORR), as depicted in Fig. 2.2. Ohmic resistance refers to the resistance encountered by protons flowing through the electrolyte and electrons flowing through the electrode, resulting in voltage losses at intermediate current densities in the ohmic polarisation area. The cell's performance significantly declines in the concentration polarisation zone because the mass movement of the reactant gas is restricted across the gas diffusion layer, pore structure, and catalyst layer. This restriction leads to the creation of gradients of concentration at the reactive sites.

2.2.2. PEM Fuel cell electrochemistry

The proton-exchange membrane fuel cell, sometimes called a PEM fuel cell, can produce electricity through an electrochemical process between hydrogen and oxygens. These are the most essential electrochemical processes:

1. Reaction at the Anode

At the anode, hydrogen gas undergoes a catalytic process that results in the separation of protons and electrons [33]:

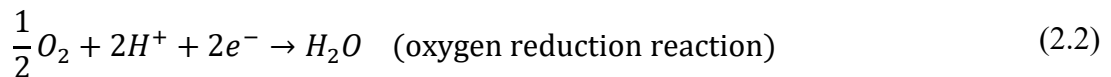


2. Membrane

In order to generate an electrical current, the protons (H^+) go through the polymer electrolyte membrane and arrive at the cathode side. Meanwhile, the electrons move through an external circuit to generate voltage.

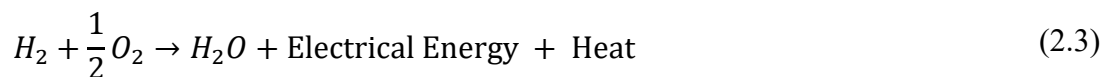
3. Reaction at the Cathode

At the cathode, oxygen from the air undergoes a reaction with the protons and electrons, which results in the formation of water [33]:



4. Overall Reaction

The total electrochemical reaction can be described as follows [33]:



Hydrogen gas (H_2) combined with half oxygen (O_2) results in the formation of water (H_2O), electrical energy, and heat. The reactions take place at the triple-phase boundaries, which are the points of intersection of the electrolyte, the catalyst (usually platinum), and the reactant gases.

In recent years, researchers [33]–[36] have been concentrating on lowering platinum loading, enhancing membrane conductivity, optimizing electrode topologies, and inventing long-

lasting catalysts made of non-precious metals to achieve improved energy efficiency and cost-effectiveness. The polymer electrolyte membrane, which carries protons while insulating electrons, and the catalyst layers on each side of the membrane, which accelerate the electrode reactions, are the essential components that make electrochemistry possible.

2.2.3. Membrane Electrode Assembly (MEA)

The Membrane Electrode Assembly (MEA) is the core component of a proton exchange membrane fuel cell (PEMFC), comprising a proton exchange membrane (PEM), catalyst layers (CLs), and gas diffusion layers (GDLs). The PEM acts as an electrolyte, facilitating the passage of protons while impeding the movement of electrons. The CLs comprise catalyst particles facilitating hydrogen oxidation and oxygen reduction electrochemical processes. The GDLs serve as conduits for gas transfer and electron conduction while providing mechanical support for the system.

Components:

- a. Proton Exchange Membrane (PEM): The PEM is a semipermeable membrane that facilitates the movement of protons while inhibiting the flow of electrons. Usually, it consists of perfluorosulfonic acid polymers (see Fig. 2.3), such as Nafion or similar substances, because of their excellent proton conductivity and chemical stability.

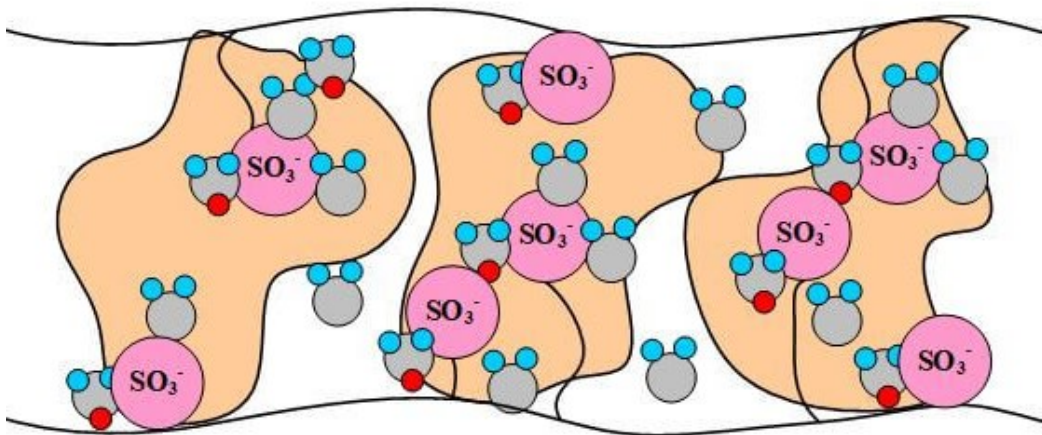


Fig. 2.3. A pictorial illustration of Nafion Membrane (Adapted from ref. [37])

The proton-conducting membrane typically has a polymer backbone based on PTFE, to which sulfonic acid groups are affixed. The proton-conducting membrane is effective for fuel cell applications due to the efficient movement of H^+ ions from one SO_3 site to another

within the material. The H^+ ions pass through the membrane and appear on the opposite side. In order for the membrane to conduct protons, it must maintain a sufficient level of hydration. The working temperature of PEMFCs is restricted to a level below the boiling point of water, which necessitates a focus on water management in the development of PEMFCs. Fig. 2.3 depicts the locations of the SO_3 spots within the Nafion membrane.

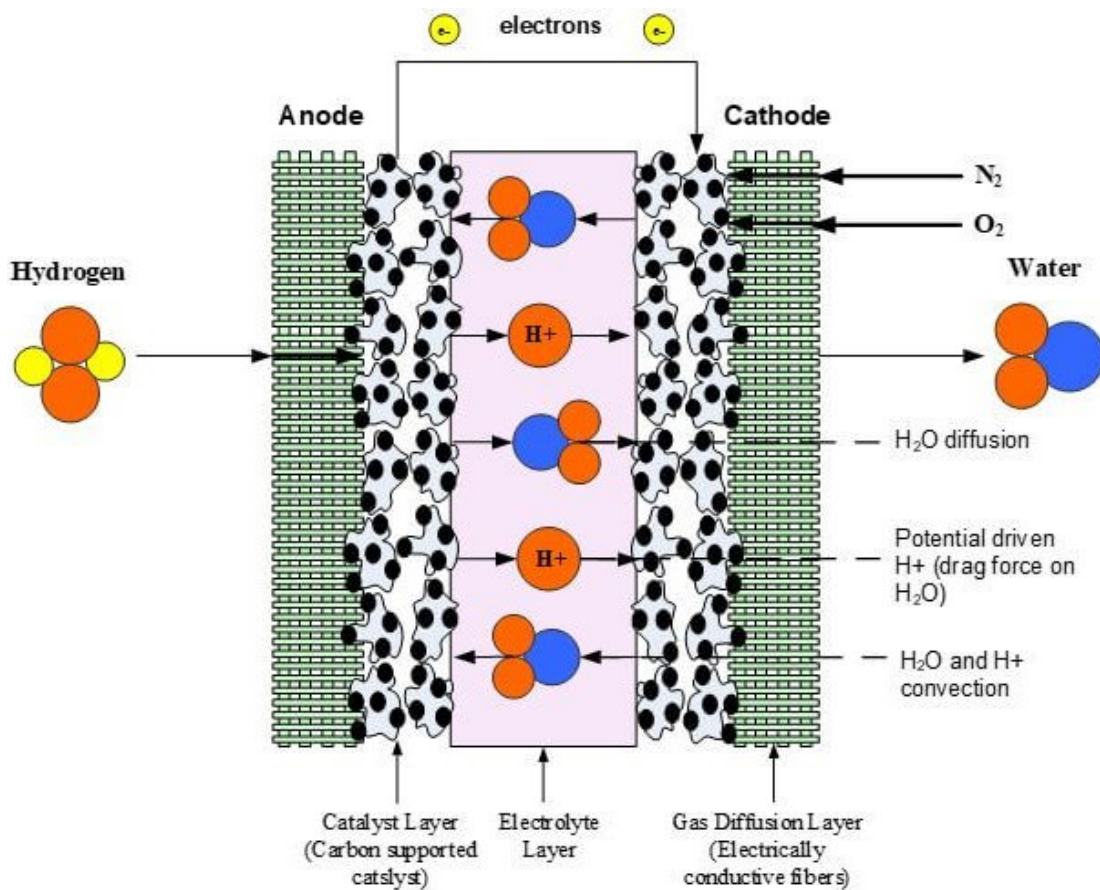


Fig. 2.4. Membrane Transport Phenomena (Adapted from ref. [37])

The phenomena examined within the membrane include energy transfer, potential conservation, and the transport of water and protons. Modeling water transport can be challenging due to the involvement of many forces, including convection, osmosis (i.e., diffusion), and electricity. The forces acting within the membrane arise from a difference in pressure, a difference in concentration, and the movement of protons from the anode to the cathode, which in turn affects the dipole water molecules. Proton transport can be defined as the movement of protons, which includes both a protonic current caused by the protons themselves and a convective flux caused by the flow of water in the membrane driven by pressure. Fig. 2.4 depicts the transport processes of protons occurring within the membrane.

- b. Catalyst Layers (CLs): CLs are located on both sides of the PEM and consist of catalyst particles distributed on a conductive substrate, usually carbon black. These catalysts, frequently composed of platinum, promote the electrochemical processes of hydrogen oxidation at the anode and oxygen reduction at the cathode, as shown in Fig. 2.5.

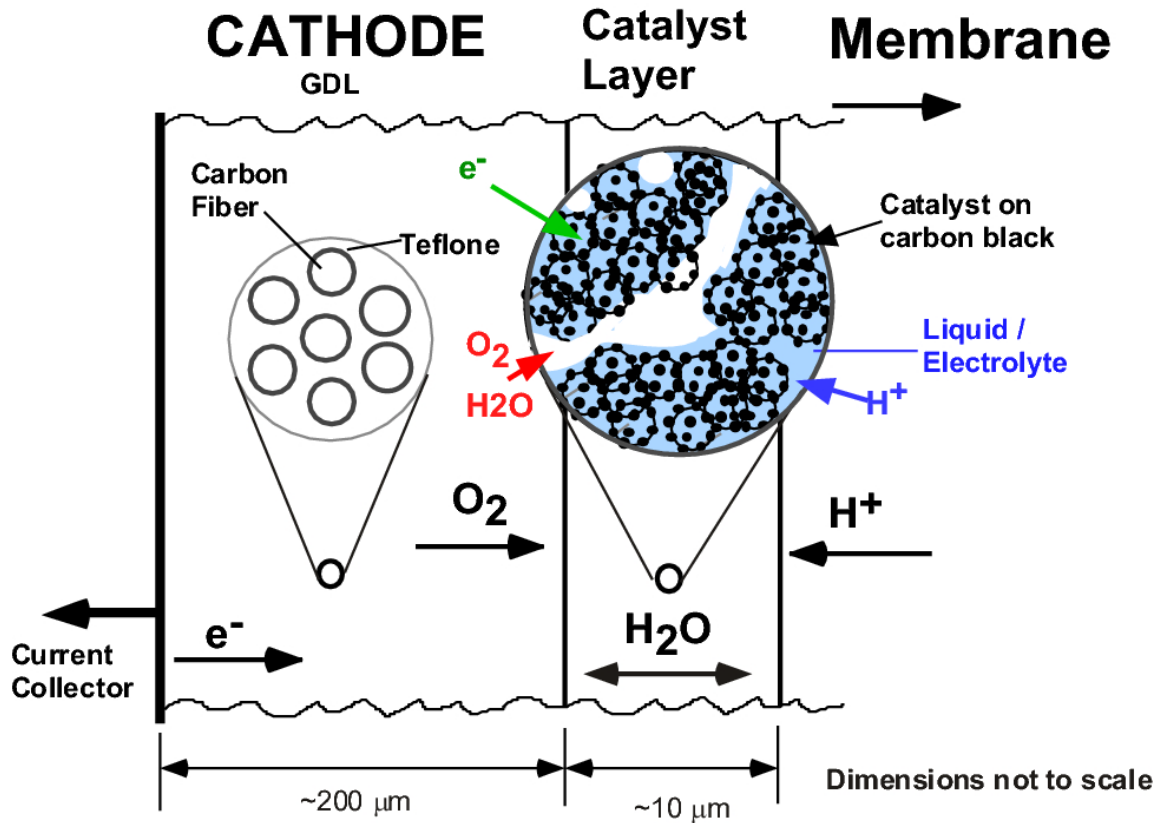


Fig. 2.5. Transport pathways in a cathodic catalyst layer (Adapted from ref. [34])

- c. Gas Diffusion Layers (GDLs): GDLs are permeable conductive substances positioned next to the CLs, facilitating the movement of gases (hydrogen and oxygen) and the conduction of electrons. Additionally, they play a vital function in water management by allowing water extraction from the cell, for more detail can be seen in Fig. 2.6.

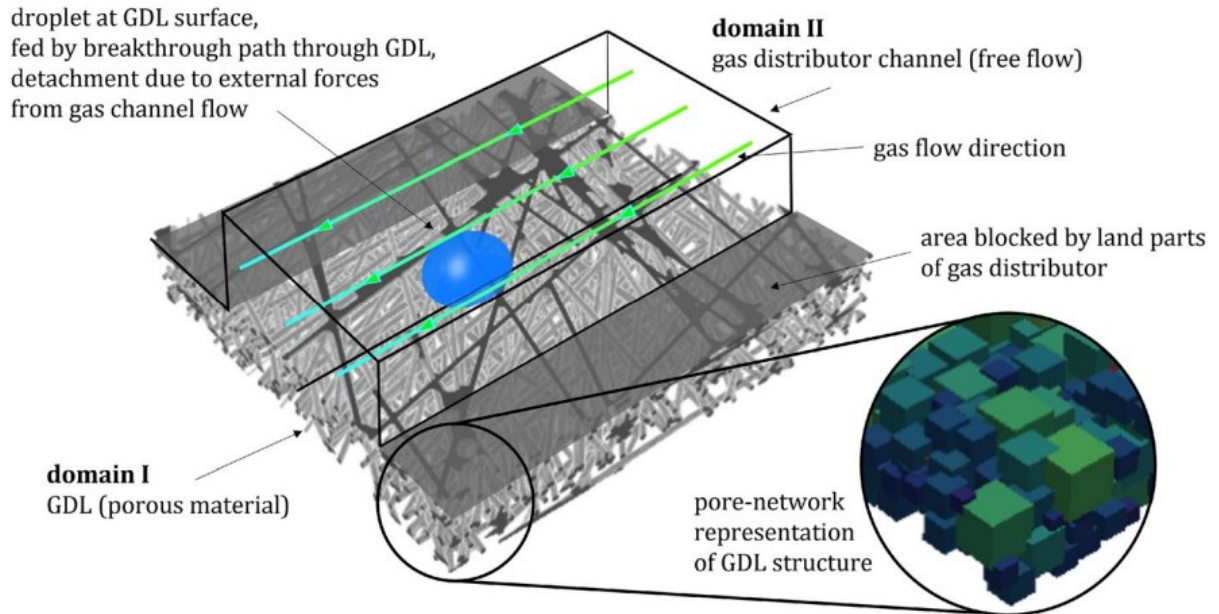


Fig. 2.6. Gas diffusion layer (GDL) unit cell (Adapted from ref. [38])

2.2.4. PEM Fuel cell bipolar plates

A hydrogen fuel cell is a device that produces electrical energy through the chemical reaction between hydrogen and oxygen. The bipolar plate shown in Fig. 2.7 is a crucial structural component in a hydrogen fuel cell. The bipolar plate efficiently transports hydrogen and oxygen to the reaction zone of the cathode and anode, respectively, while effectively isolating the reaction gases in each chamber. Within the reaction zone, hydrogen on the cathode undergoes decomposition into protons (positively charged hydrogen ions) and electrons (negatively charged) with the assistance of a catalyst. The protons can reach the cathode by passing through a polymer electrolyte membrane (PEM), while the electrons can flow to the anode through an external circuit. At the anode, oxygen reacts with protons and electrons, facilitated by a catalyst, to produce water and generate electrical energy.

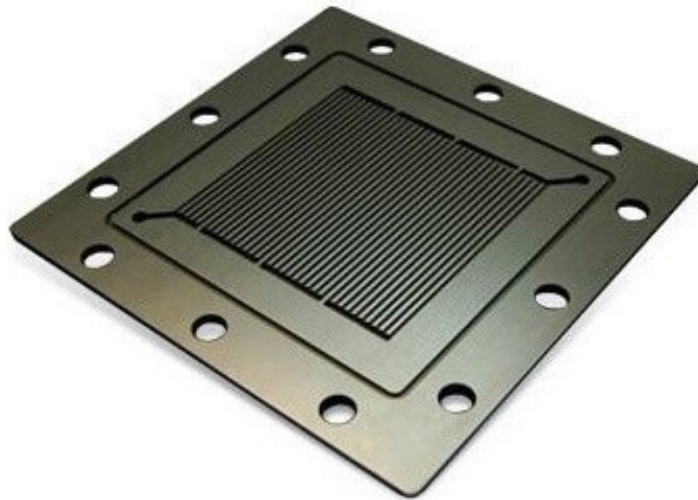


Fig. 2.7. Bipolar plate of PEM fuel cell (Adapted from ref. [39])

2.3. Review of previous studies on flow field configurations at bipolar plate effect on mass transport and performance

This sub-chapter summarizes prior and current studies on flow field design structures on mass transport characteristics, temperature profiles, and cell performance of PEM fuel cells. The review focuses on the bipolar plate design based on flow field structure configurations.

The construction of renewable energy resources is imperative, prompted by the exhaustion of traditional energy sources and the environmental obstacles associated with the utilization of fossil fuels. In recent years, there has been an increasing worldwide fascination with the remarkable power density and low emissions of PEM fuel cells. PEMFC is environmentally benign as it solely generates heat and water. PEMFC applications encompass a range of uses, with the most prevalent ones being hybrid automobiles, portable power sources, and distributed power generation [1–3].

The flow field's geometry considerably impacts the transportation of reaction gases in the PEM fuel cell. The complex configuration of the flow field can enhance the movement of the reactants inside the active region, facilitating increased involvement of surplus reactants. Optimize the power density of the PEMFC by precisely adjusting the use of the reaction gas. Explore the complexities of flow field configuration optimization through comprehensive research. In their study, Wang et al. [11] examined the impact of a staggered trapezoid block on the flow channel. Song et al. [12] presented a multi-channel cooling plate designed for

PEM fuel cells. The results demonstrated that the model attained the utmost level of gas distribution efficiency. Tardy et al. [13] examined a novel sinusoidal channel by adjusting input temperatures to improve cell power density. Shen et al. [14] examined the optimal spacing between square blocks in a channel. Yang et al. [15] developed a mathematical model to calculate the dimensions of the circular bulge in the M-shaped flow channel. In their study, Liu et al. [16] utilized a multi-objective evolutionary algorithm to improve energy efficiency and output power by optimizing the operational state, channel input, and outlet height. In a previous study conducted by Zeng et al. [17], a genetic algorithm was utilized to determine the optimal cross-sectional channel. The researchers discovered that the most effective proportions for a trapezoidal channel to maximize a specific area were a bottom edge width of 1.2874 mm and a top edge width of 0.8886 mm. Chen et al. [18] performed computational research to examine the influence of porous-blocked baffles on a PEM fuel cell. The baffles were positioned at a height of 1.125mm and tilted at a 60-degree angle. The addition of baffles led to a significant 90% enhancement in the channel's net power output compared to a channel without baffles.

By utilizing more efficient PEM fuel cells, the diffusion of reactants into the catalyst layer during the electrochemical process is projected to improve significantly [26, 27]. Building traditional flow channels is relatively straightforward; however, there is potential for boosting their effectiveness in transporting mass. One way to accomplish this is by optimizing the flow's input and exit areas, altering the ribs' width, or integrating blocks of varying sizes. Straight-flow channels are frequently employed in production due to their simplicity [28, 29]. In addition, bionic design has been utilized to optimize flow channels, going beyond the unique flow fields mentioned earlier. Scientists have explored new ideas from nature to create flow fields with distinct characteristics. The previous discussion included examples that demonstrated the characteristics of artificial lungs [30], flow channels resembling bionic leaves that adhere to Murray's law regarding branching widths, and squid fins [30–32].

PEM fuel cells can efficiently convert the chemical energy of fuel into electricity, unlike heat engines. Due to its distinctive attributes, it is capable of producing power with an efficiency ranging from 40 to 60% [31]. Creating a model to accurately predict the overall performance of PEM fuel cells is essential for successfully implementing these cells in

commercial applications [41]. After evaluating the performance of PEMFCs, scholars can apply targeted modifications to improve performance in different operating parameters [29], [48], [49]. Nevertheless, a disadvantage of conventional modeling is that fuel cells encompass numerous physical processes. A comprehensive comprehension of the fuel cell process parameters and the fundamental physical processes is required in order to properly employ traditional fuel cell modeling methodologies, including analytical and mechanistic models [50].

The flow block improved the transport efficiency of reactants within the Gas Diffusion Layer (GDL). Chen et al. [51] suggested using channels with a wavelength of 2 millimeters and a depth of 0.45 millimeters to improve current density and mass transmission. Yan et al. [52] constructed a model that accurately represented the geometric characteristics of a canal with an undulating slope. Oxygen concentration was significantly augmented upon transitioning from the flow field to the catalyst layer (CL). As a result, there was an increase in the concentrations in the natural environment and a decrease in the polarization of the concentration. Dong et al. [53] conducted an analysis that found that the use of geometric flow blocks led to a substantial enhancement in the efficiency of fuel cells. It was observed that these blocks had a significant effect on the nozzle. The utilization of a trapezium block was found to improve both the flow of reactants and the efficiency of water distribution, as discovered by He et al. [54]. In their research, Li et al. [55] used a genetics-based methodology to determine the optimal height and number of blocks for the straight flow field. As a result, they achieved the utmost precision in obtaining the outcome. The flow block tended to increase progressively instead of remaining at a constant height over time. Yin and colleagues [56] conducted a study to examine how the angle of the trapezoid block inside the channel affects its overall performance. According to the investigation's findings, it was concluded that the best oxygen transfer performance was attained by generating a 45-degree angle between the front and back surfaces.

In their study, Vaisala et al. [57] conducted research to determine how the presence of serpentine flow fields in three different channels affected the productivity of PEM fuel cells in their field of study. The performance of a single channel is optimum, according to research that relies on both computational and experimental methods. Increasing the cross-sectional area of the channel will result in a more significant fraction of the surface area of the reactant

coming into direct contact with the Gas Diffusion Layer (GDL) for the first time. Ghasabehi et al. [58] conducted a study where they investigated several designs aimed at enhancing electrochemical performance and minimizing power loss. The study examined various configurations, including a conical block placed at the manifold, a conical flow field, and a straight flow field [59]. The researchers examined how the height, width, and aspect ratio of the flow channel affect the performance of PEM fuel cells. Zhang et al. [60] conducted a study that produced four separate serpentine flow patterns. The flow fields displayed a variety of curvatures and flow directions for their components.

Cai et al. [61] integrated bionic squid fins into the flow block and utilized neural algorithms to precisely adjust the amplitude and frequency of the waveform center. They successfully attained the most favorable outcomes for their research. Upon thorough examination, it was determined that the optimal values for the center amplitude and wave cycle are 0.305 mm and 3.52 mm, respectively. The bionic flow channel demonstrated exceptional gas distribution uniformity by using a structure and design inspired by nature. Suo et al. [62] conducted a thorough analysis of the transportation of oxygen in metal foam flow fields using a three-dimensional multi-species lattice Boltzmann model. The results suggest that using a metal foam flow field improves the efficiency of oxygen mass transfer to the catalyst layer and facilitates a more even distribution of oxygen. They were increasing the density of pores in the metal foam, and the compression ratio resulted in a higher oxygen mass transfer rate. This effect gets more pronounced as the velocity of the inflow increases. Zhang et al. [63] conducted a study to investigate the influence of the metal foam flow field on the transport phenomena. The study revealed that the metal foam architecture significantly improves fuel cell performance under high current density conditions. Although the collection area at the GDL surface is smaller in the metal foam flow field, the increase in Ohmic loss will not be considerable. The enhanced conductivity is attributed to the metal foam's intricate pore structure, facilitating improved physical contact.

Some interesting flow fields are shedding light on the subject. The study conducted by Yin et al. [64] investigated the implementation of unique wavy flow fields in the metallic bipolar plate, using an inverse phase for both the anode and cathode. The researchers discovered that the coolant channels, which are arranged in two layers and crisscrossed, improve the movement of heat by convection. This leads to the formation of secondary flow between the

layers, with a velocity that is 25% of the primary flow. Tan et al. [65] proposed a novel flow field based on the design principles of Murray's Law, as revealed in their investigation. The researchers discovered that utilizing this new flow field resulted in an average increase of 1.35 percent in the output power density of the PEMFC Wang et al. [66] improved the performance of PEMFC by optimizing the flow field structure through the implementation of a design that includes serial impediments in the channel. The addition of barriers was shown to enhance the movement of reactant gas toward the Gas Diffusion Layer (GDL) and broaden the range of current density at which the system can operate. Huang et al. [67] introduced a serpentine flow field with a gradually decreasing slope and assessed its effectiveness using visualization tests. The data clearly demonstrate that the design of the U-shaped corner in the tapered-slope serpentine flow field is essential in maintaining the shape of droplets, reducing splashing, and limiting droplet breakage resulting from contacts with the channel wall. Consequently, the time required for the drainage process was lowered by a substantial 62.3% when compared to a traditional serpentine flow field.

In addition, there is ongoing research on bionic flow fields. Huang et al. [68] created an innovative bionic flow field that was influenced by the anatomical characteristics of the higher mesenteric artery and its branches in the human body. Their study revealed that the implementation of the bionic flow field significantly improves the transmission properties of droplets, reduces droplet aggregation at bends, shortens the duration of droplets within the flow field, and increases the droplet removal rate by 36.3%. Hie et al. [69] conducted a comparative analysis of several flow field configurations. It was discovered that the ginkgo flow field had a slightly lower maximum power density compared to the serpentine flow field but was substantially more significant than the parallel flow field. Nevertheless, the ginkgo tree only required a minimal 3% of the air-feeding capacity that the serpentine tree needed. Badduri et al. [70] performed an experimental study investigating the influence of flow field designs inspired by natural structures, like lungs and leaves, on bipolar plates. The leaf channel design was found to have the highest power density output among the various flow channel designs that were investigated. The power density of the Proton Exchange Membrane Fuel Cell (PEMFC) utilizing the interdigitated leaf channel design showed a 6.72 percent increase compared to the non-interdigitated leaf channel structure. Liu et al. [71] assessed the performance of fuel cells by examining the impact of two bionic flow channels with different orientations. The results suggest that the performance of PEMFC with a bionic

flow field is significantly influenced by gravity. There are significant differences in PEMFC performance when comparing symmetrical and asymmetric bionic flow channels. PEMFCs with asymmetric bionic flow channels demonstrate superior performance when oriented perpendicularly.

Optimizing the structure of baffles can improve the performance of PEMFC. Through numerical analysis, Guo et al. [72] found that different baffled flow channels affect mass transport and cell performance in PEMFC. The study revealed that the rectangular baffle had the most significant improvement in reactant transfer and cell performance. However, it also resulted in the highest power loss among the baffled flow channels. Zhang et al. [73] introduced a single-channel PEMFC with wedge-shaped fins in the cathode channel. They measured the effects of different fin parameters, including volume, number, and porosity, on the GDL. It was found that using wedge-shaped fins significantly improved the performance of PEMFCs. As the fin volume increased, there was a noticeable decrease in the distributions of oxygen mass fraction in the cathode channel output area. Heidary et al. [74] conducted a numerical analysis of the effects of different blockage arrangements in a parallel flow field. The results show that the staggered layout significantly boosts maximum net power, considerably surpassing the base case and the in-line scenario. In the staggered design, the pressure loss is reduced by 70% compared to the in-line instance due to over-rib convection, which is not present in the design. In their study, Huang et al. [75] examined five different flow channel architectures with baffles. They utilized a CFD approach to analyze and compare the mass transport and cell performance of PEMFCs with these various baffled channels. Based on the data, it is evident that the PEMFC with a cylinder-cutting baffle showcases the most impressive performance, with an output current density of 1.82 A/m^2 and a voltage of 0.4 V. Optimizing the design of baffles can enhance the efficiency of gas transport and increase the concentration in the channel.

2.4. Review of previous studies on PEM fuel cell performance predictions

An artificial neural network (ANN), which draws inspiration from the biological networks of neurons, is renowned for efficiently solving. The artificial neural network (ANN) structure, resembling the human brain, allows replicating the brain's ability to process information in parallel. This establishes complex and highly nonlinear relationships between input and output data [67, 68]. An accurately trained artificial neural network (ANN) can

serve as an approximation representation of a sophisticated physics-based model capable of handling arbitrary functions [78]. The Genetic Algorithm (GA) is a selection algorithm based on Darwin's principle of natural survival [79]. Optimization problems can be effectively addressed using this method, as it avoids the common issue of becoming stuck at local minima, which can cause other conventional search methods to fail unless they are well handled. This algorithm demonstrates the principle of natural selection, in which the most adapted chromosomes are selected to generate their progeny. The process of natural inheritance involves three operations: selection, crossover, and mutation [79]. These activities entail the exchange of traits between parents and successfully transferring these characteristics to their offspring through crossover. Mutations will introduce additional characteristics to the offspring. Through this method, certain offspring are anticipated to possess a superior fitness score compared to their parents, and these offspring will be chosen to generate the subsequent generation. The chromosome with the highest fitness value will be identified over a series of iterations.

Multiple endeavours have been undertaken to suggest artificial neural network (ANN) models as substitutes for intricate three-dimensional multiphysics models in analyzing proton exchange membrane (PEM) fuel cells. Pang and Wang [80] utilized a Convolutional Neural Network (CNN) to examine neutron radiography images to detect spatial variations in water distribution under various operational settings. Additionally, they investigated the spatial inconsistencies in fuel cell segments 5 and 10. The findings indicate that picture pre-processing significantly enhances the accuracy of convolutional neural networks, resulting in a remarkable 96.6% success rate. At a relative humidity of 50%, liquid water becomes visible downstream at a rate of 55%. However, when the humidity reaches 100%, the entire cell undergoes a two-phase flow. The accuracy of the convolutional neural network findings is 91.8%, which is consistent with the data obtained from pixelation image processing. Wang et al. [81] conducted research on optimizing deformed GDLs in PEM fuel cells using a combination of multi-physics and machine-learning surrogate modeling. They compared the usage of Response Surface Machine (RSM) with artificial neural network-based machine learning. The utilization of M5 greatly enhances the effectiveness and efficiency of GDL optimization. The current density and standard deviation of oxygen distribution experienced a respective increase of 20.8% and 74.6% at a voltage of 0.4 V. The Pareto front optimizes the trade-off between cell efficiency and the uniformity of oxygen distribution. Increasing

the standard deviation of oxygen distribution by 26.0% results in a 20.5% increase in current density. Mehrpooya et al. [82] developed an Artificial Neural Network (ANN) consisting of two hidden layers. The ANN was trained and validated using 400 data points, while 60 data points were reserved for testing. Measurements were conducted experimentally using different inlet humidities, temperatures, and oxygen and hydrogen flow rates. The training and testing data exhibited strong correlation values (R^2) of 0.982 and 0.972, respectively. Kheirandish et al. [79] constructed an Artificial Neural Network (ANN) with two hidden layers to forecast the efficiency of a Proton Exchange Membrane (PEM) fuel cell bicycle. The first hidden layer comprised 17 neurons, while the second layer included four neurons. The inputs comprised five parameters: relative humidity, stack current oxygen flow rate, stack temperature, hydrogen flow rate, and voltage output. On the other hand, the outputs were limited to two: voltage output and efficiency. Following the training, the mean square errors for voltage and efficiency were decreased to 0.0118 and 0.0314, respectively.

Numerous studies have utilized GA optimization to determine the most favourable parameters for PEM fuel cells. Lan et al. [83] created an artificial neural network (ANN) surrogate model to simulate high-temperature PEM fuel cells. They then validated this model using an isothermal physical model. A genetic algorithm (GA) was utilized to optimize the shape of the flow channel, resulting in a 10.54% increase in current density and a 3.93% gain in power. Wang et al. [84] employed a support vector machine (SVM) based surrogate model in conjunction with Genetic Algorithm (GA) to determine the ideal composition of the catalyst layer for achieving the highest power output. The optimal results yielded a maximum power output of 1.2647 (W/cm²), deviating by 1.4% from the prediction made by their physical model. Li et al. [55] utilized a combined genetic algorithm (GA) and three-dimensional (3D) physical model to optimize the design of a blocked channel for proton exchange membrane (PEM) fuel cells, including blocked channels resulted in a significant increase of around 10.9% in the maximum power output compared to channels without blocks. Furthermore, the results obtained from the GA analysis indicated that the cell voltage and power exhibited an initial increase till reaching the maximum power output, followed by a subsequent reduction as the block number grew. The peak power output was achieved by introducing 16 blocks into the flow channels. Zhang et al. [36] utilized a support vector machine (SVM)-based surrogate model to enhance the efficiency of designing a 3D mesh porous media flow field, encompassing the mesh spacing and rod dimensions. A 3D physical

model was utilized to generate the data for support vector machine (SVM) training and subsequently validate the findings obtained from the Genetic Algorithm (GA).

2.5. Summary

This chapter gives an introduction to PEM fuel cells and a literature review regarding bipolar plate flow field configuration's effects on mass transport characteristics and performance of PEM fuel cells. All previous studies have focused on modified bipolar plate flow channels' influence on mass transport characteristics and performances of PEM fuel cells.

Using non-carbon fuels such as hydrogen is a promising way to reduce oil consumption and greenhouse gases produced by conventional internal combustion engine vehicles. In order to minimize these problems, the utility of fuel cells such as PEM fuel cells is one appropriate strategy. Previous studies have demonstrated that creating modified flow channel configurations affects the amount of mass transfer to the gas diffusion layer (GDL) and performance in PEM fuel cells. Besides that, there are still challenges to modified flow field channels and a lack of consideration for other parameters.

Therefore, this study examines novel design strategies to improve the efficiency and temperature distribution of proton exchange membrane fuel cells (PEMFCs) by analyzing tapered flow field configurations (FFCs), streamlined water block configurations, and different baffle shapes in the flow channels. The investigation takes into account variations in parameters such as porous medium thickness (PMT), thermal contact resistance (TCR), interface contact resistance (ICR), and GDL face permeability. A three-dimensional multiphysics fuel cell model utilizing the SIMPLE solver was employed in ANSYS Fluent. The purpose was to assess the effects on mass transport (specifically oxygen and hydrogen mass fractions), water removal, velocity flow, pressure drops, and overall cell performance. This assessment was achieved through a combination of literature experimental validation and the application of an artificial neural network-genetic algorithm (ANN-GA) in PEM fuel cells.

3. RESEARCH METHODOLOGY

3.1. Numerical model

The other goal of this study is to conduct numerical simulations for the bipolar plate flow field structures on mass transport characteristics (oxygen, hydrogen, and water mass fraction), temperature profiles, gas velocity, pressure drops, and PEM fuel cell performance. Computing bipolar plate flow field configuration requires a detailed mathematical description of all significant properties of the process utilizing solving some algebraic equations. Using computational fluid dynamics (CFD) and multiphysics software such as ANSYS-Fluent for studying modeling PEM fuel cell consists of geometry creating (SpaceClaim), mesh generation, setting up physical sub-models, solving algebraic equations, and post-processing resulting data.

3.1.1. PEMFC models development

This work constructed a three-dimensional computer model to simulate the unobstructed flow of a single PEM fuel cell. The channel dimensions were as follows: length of 40 mm, width of 1 mm, height of 1 mm, and rib width of 1 mm. For further information, please refer to Table 3.1. This study will consist of three sequential parts. Initially, the bipolar plate of a PEM fuel cell with a straight channel design will be examined. Furthermore, the flow channels of bipolar plates can be altered by adjusting the angles and block form models. Finally, other parameter modifications, including porous medium thickness (PMT), thermal contact resistance (TCR), interface contact resistance (ICR), GDL faces permeability and GDL porosity, were incorporated into the simulated instances. Fig. 3.1 (a) displays a PEM fuel cell schematic with a straight flow channel model. This model comprises bipolar plates for the anode and cathode, flow channels for the anode and cathode, gas diffusion layers for the anode and cathode, catalyst layers for the anode and cathode, and a membrane.

Fig. 3.1 (b) transforms the chemical energy produced by the electrochemical process between hydrogen and oxygen into electrical energy instead of directly burning hydrogen and oxygen gasses to generate heat energy. The anodic component of the membrane electrode assembly (MEA) is continuously supplied with a hydrogen flow. At the anode, the material undergoes catalytic dissociation into protons and electrons. The protons that were just produced disperse throughout the polymer electrolyte membrane and go toward the

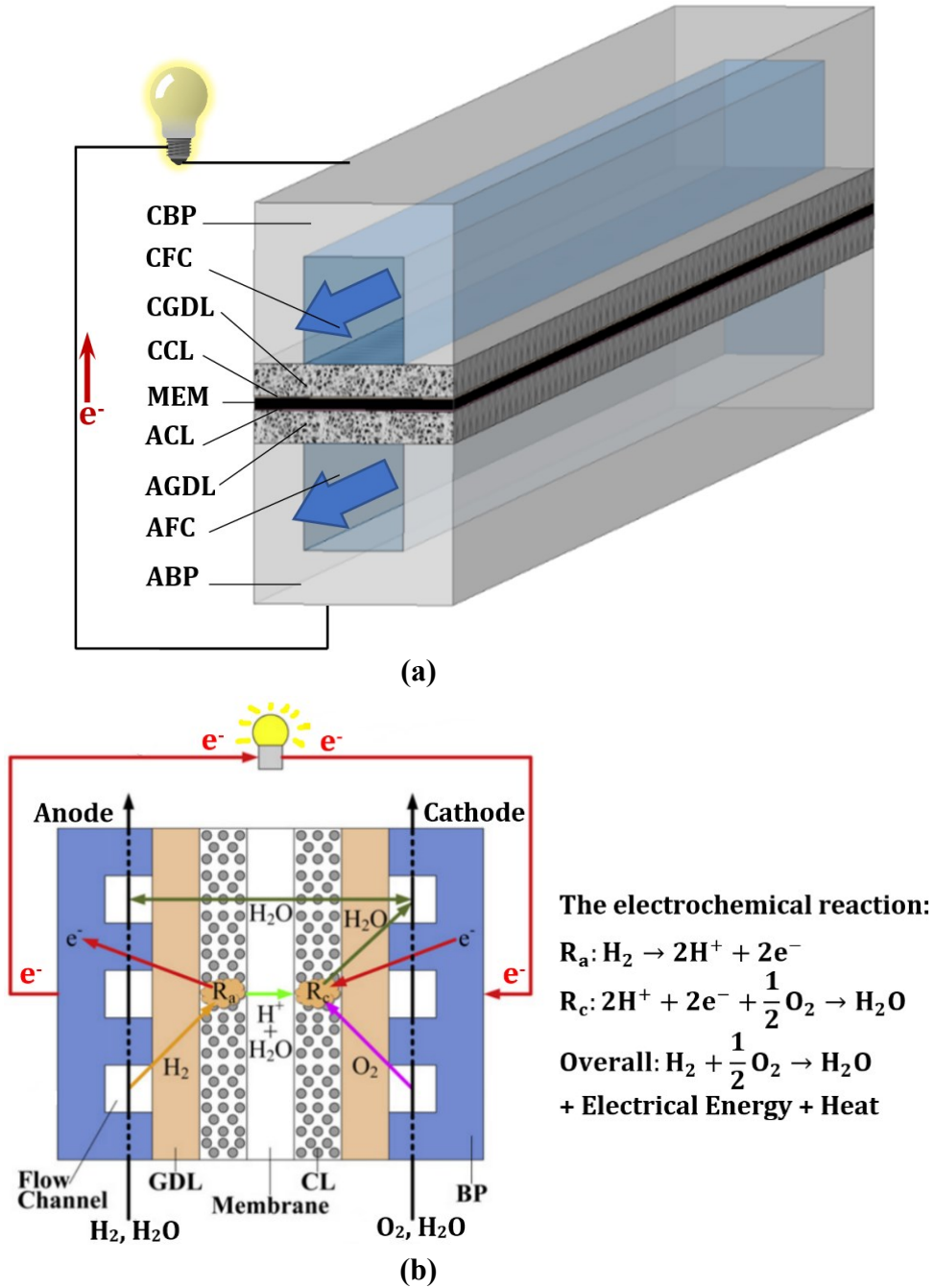


Fig. 3.1. Schematic of the straight flow field of PEM Fuel Cell (a) and its operating principle (b).

cathodic area. A current output is produced by the fuel cell as a result of electron flow that occurs through an external load circuit and towards the cathode side of the membrane electrode assembly (MEA). The cathodic region of the membrane electrode assembly (MEA) receives a steady flow of oxygen simultaneously for maximum efficiency. When oxygen molecules combine with protons that travel through the polymer electrolyte membrane and

electrons that come through the external circuit, water molecules are produced at the cathode. This reaction takes place at the cathode site.

Table 3.1. PEMFC geometric parameters for the straight channel model
(adapted from Li et al. [31])

No.	Parameters	Value	Unit
1	Channel length	40.0	mm
2	Channel height	1.0	mm
3	Channel width	1.0	mm
4	Rib width	1.0	mm
5	Cell width	2.0	mm
6	GDL thickness	0.3	mm
7	CL thickness	0.0129	mm
8	Membrane thickness	0.108	mm

The flow-field channels (FFCs) of PEM fuel cells that are tapered parallel are depicted in Fig. 3.2. These fuel cells are shown in schematic form. Electrodes at the anode and cathode, bipolar plates (BPs), gas diffusion layers (GDLs), catalyst layers (CLs), a membrane (MEM), and channels (CHs) are some of the components that make up the Proton Exchange Membrane (PEM) fuel cell. All of these components work together to form the fuel cell. There is a relationship between the tapered form of tapered parallel FFCs and the anode electrode and the cathode electrode. Within the scope of this work, seven distinct variants of tapered FFCs are developed. Each of these variants has a ratio of the intake side's length to the output side's size that is different from the other variants. A numerical investigation into six distinct varieties of tapered parallel FFCs will be carried out as part of this computational research within the project's scope. $L_{I/O}$ 0.7, $L_{I/O}$ 0.8, $L_{I/O}$ 0.9, $L_{I/O}$ 1.0, $L_{I/O}$ 1.1, and $L_{I/O}$ 1.2 are some available options. There is no need to be surprised that the contact surfaces between BPs and GDLs will vary substantially based on the tapered parallel FFCs that are utilized.

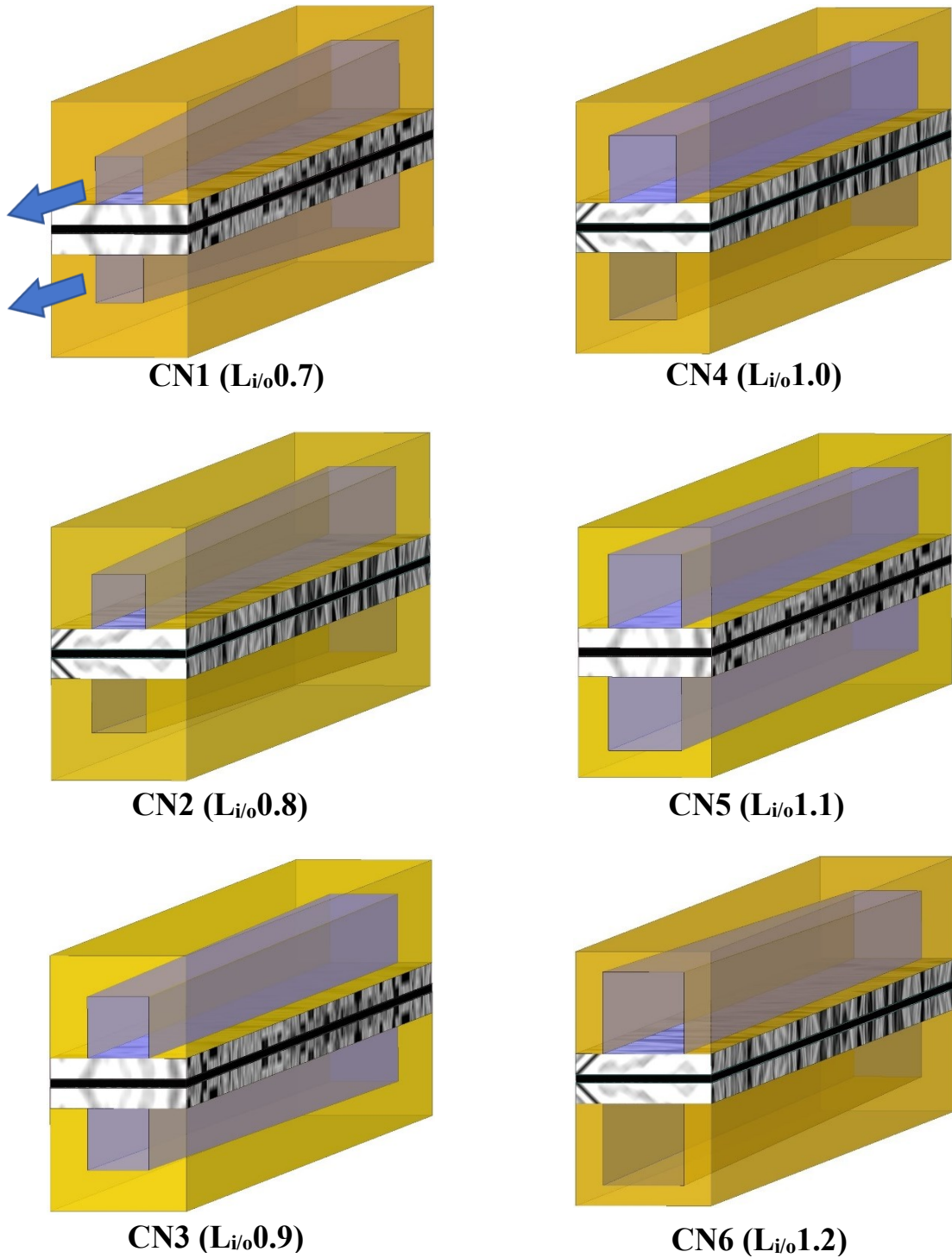


Fig. 3.2. PEM fuel cell with six different flow field channel models

In the field of aerodynamics, the term "streamline" refers to the structural configuration of objects that are distinguished by their sleek surfaces and contours. Consequently, this model has the ability to decrease the resistance that the gas experiences during its flow. Fig. 3.3 illustrates the PEM fuel cell's specific structure and operating principle with a water drop

block design. The study introduces five different iterations of water-drop blocks (WDB) that include streamlined characteristics, labeled as WDB I (case 2), WDB II (case 3), WDB III (case 4), WDB IV (case 5), and WDB V (case 6). The 3D, top, and right views depicted in Fig. 3.4 showcase the unique geometries of water droplet blocks. The basic construction of the Model I and Model II blocks comprises a hemispherical form and a hemispherical water droplet shape. The fundamental design of the WDB III, WDB IV, and WDB V models consists of semi-elliptical, isosceles triangular, and spliced semi-elliptical geometries, respectively. The diameters of the semicircle, the side length of the triangle, and the minor axis of the ellipse are equal. The process of generating the WDB I, WDB II, and WDB III include implementing rotational modification to the fundamental shape.

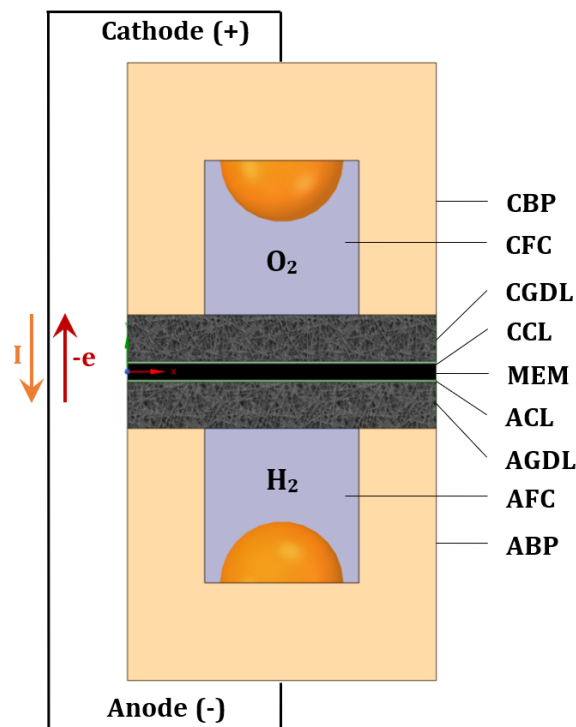


Fig. 3.3. Imitated water drop model description and operating principle of PEMFC.

Additionally, the WDB IV and WDB V blocks are obtained through the utilization of extending techniques. The WDB has an inter-block spacing of 4.0 millimeters, which is symbolized by the letter L. The flow channel being considered is designed with a mandated spacing of 2.0 millimeters between the intake and the junction of the block nearest to it, as stated in a reference that was quoted [14]. This distance corresponds to the distance that was measured at the outflow. A comprehensive analysis of the simulated situations of the various

WDB models that take into consideration both ICR and GDL face permeability is presented in Table 3.5.

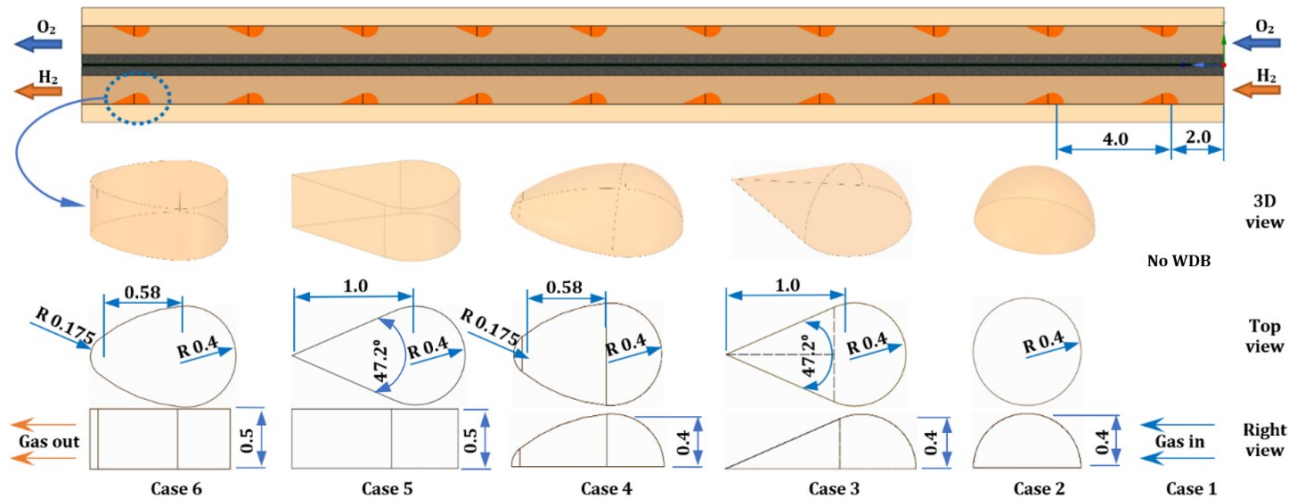


Fig. 3.4. Detail and schematic representation of WDB channel and their model structures.

3.1.2. Material Properties of the PEM Fuel Cell Components

The values of the material properties, such as density, elastic modulus, electrical conductivity, thermal conductivity, coefficient of thermal expansion, and specific heat for detail, are available in Table 3.2.

Table 3.2. Material properties of the PEMFC components, adapted from refs. [85],[86].

Parameters	Unit	BP	GDL	CL	PEM
Density	kg•m ⁻³	7930	1000	1000	1980
Elastic Modulus	MPa	193,000	6.3	249	232
Electrical conductivity	S•m ⁻¹	1.45x10 ⁶	300	300	9825
Thermal conductivity	W/m•K	16.2	1	1	0.95
Coefficient of thermal expansion (20-100°C)	K ⁻¹	16.3x10 ⁻⁶	2.5x10 ⁻⁶	3.7x10 ⁻⁵	1.23x10 ⁻⁴
Specific heat (0-100°C)	J/kg•K	500	568	3300	833

In order to ensure that the simulated and experimental polarisation curves are a good match, the research that was carried out is utilized to construct a comprehensive and step-by-step approach for calibrating the model for the first time. In addition, the ANSYS Fuel Cell and Electrolysis Model is used to analyze the material properties of the PEM fuel cell current

models. As can be shown in Fig. 3.5, Fig. 3.6, Fig. 3.7, and Fig. 3.8, the processes that are utilized to establish the material properties of bipolar plates (BPs), gas diffusion layers (GDL), catalyst layers (CLs), and electrolyte (membranes), respectively, are as follows.

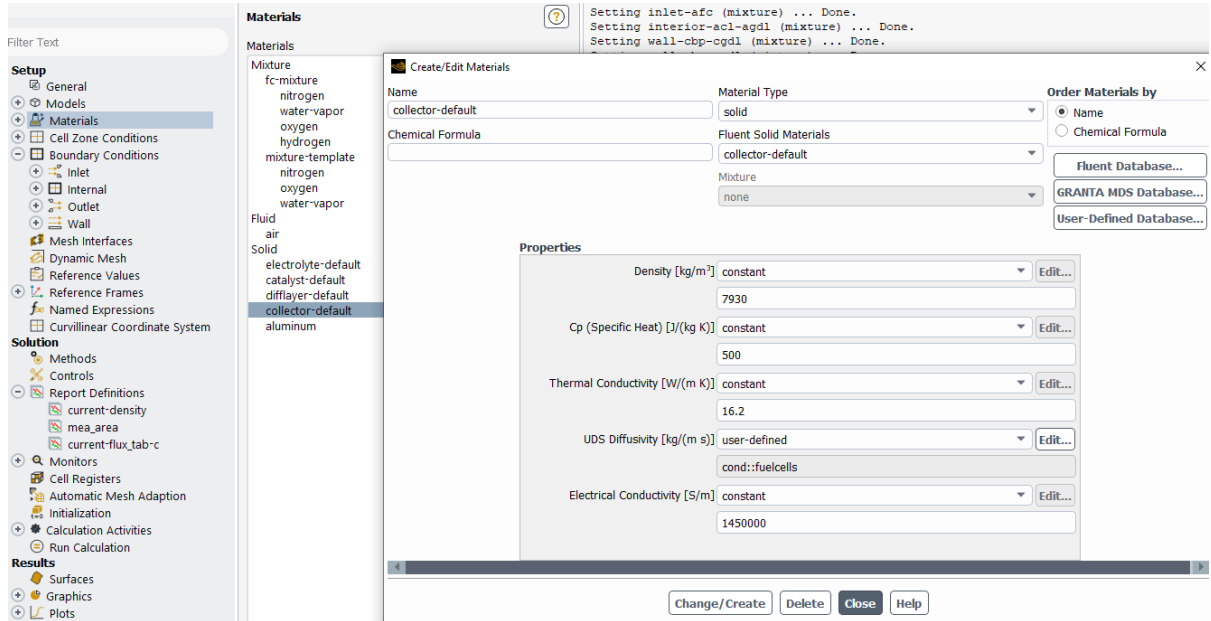


Fig. 3.5. Material properties setup for bipolar plats/current collectors.

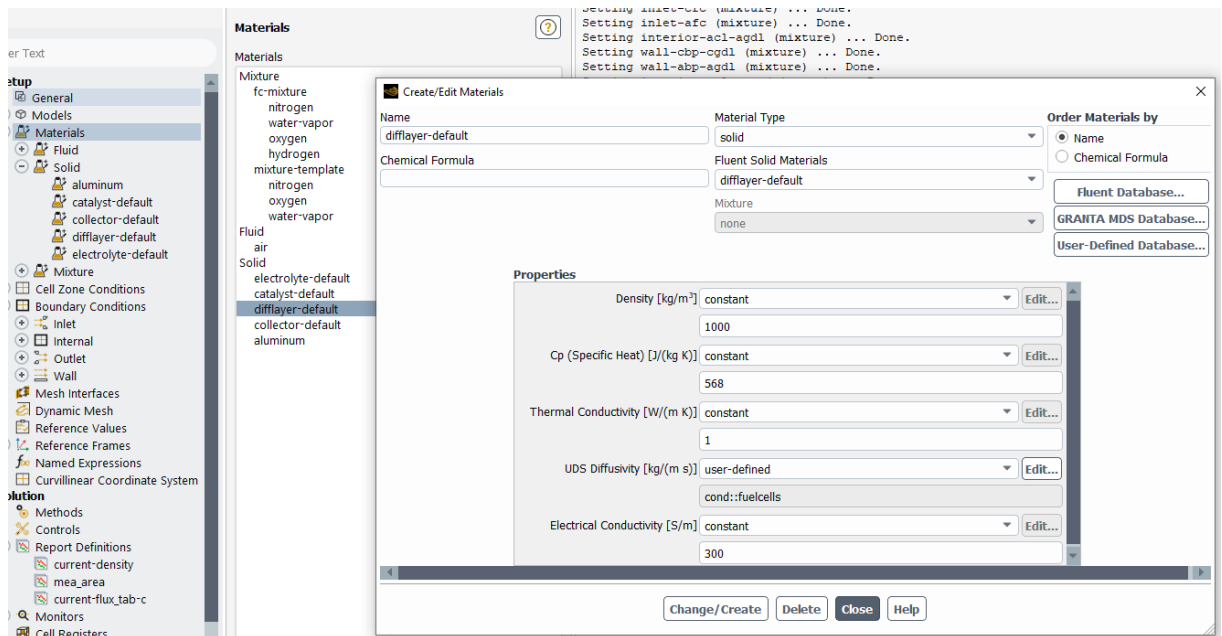


Fig. 3.6. Material properties setup for gas diffusion layers (GDLs).

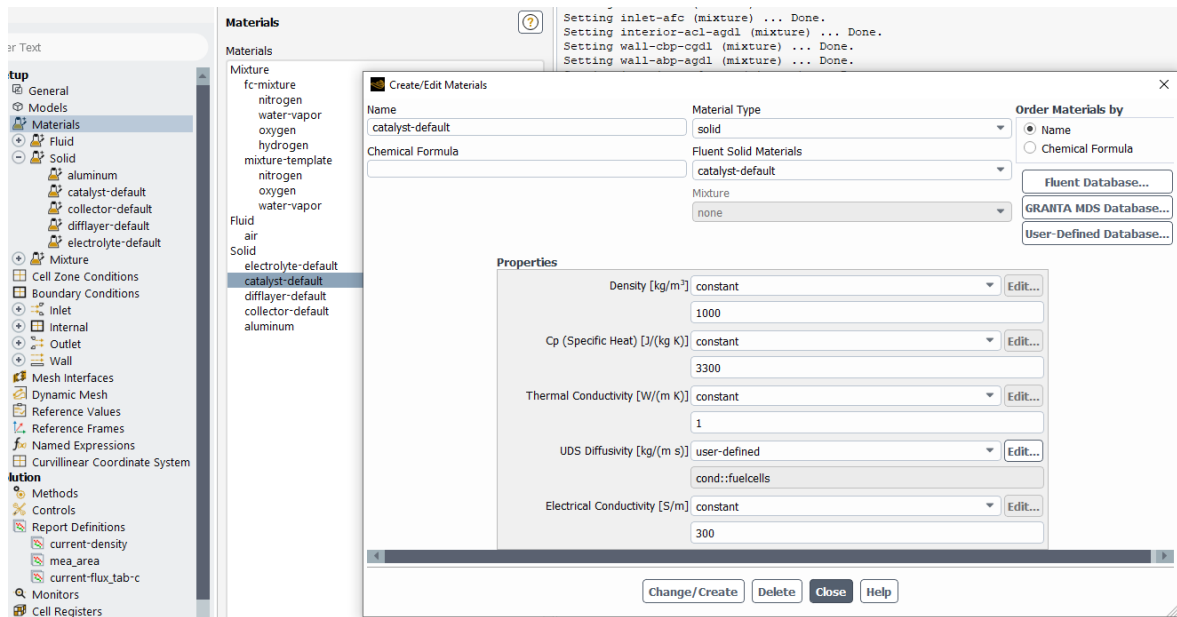


Fig. 3.7. Material properties setup for catalyst layers (CLs).

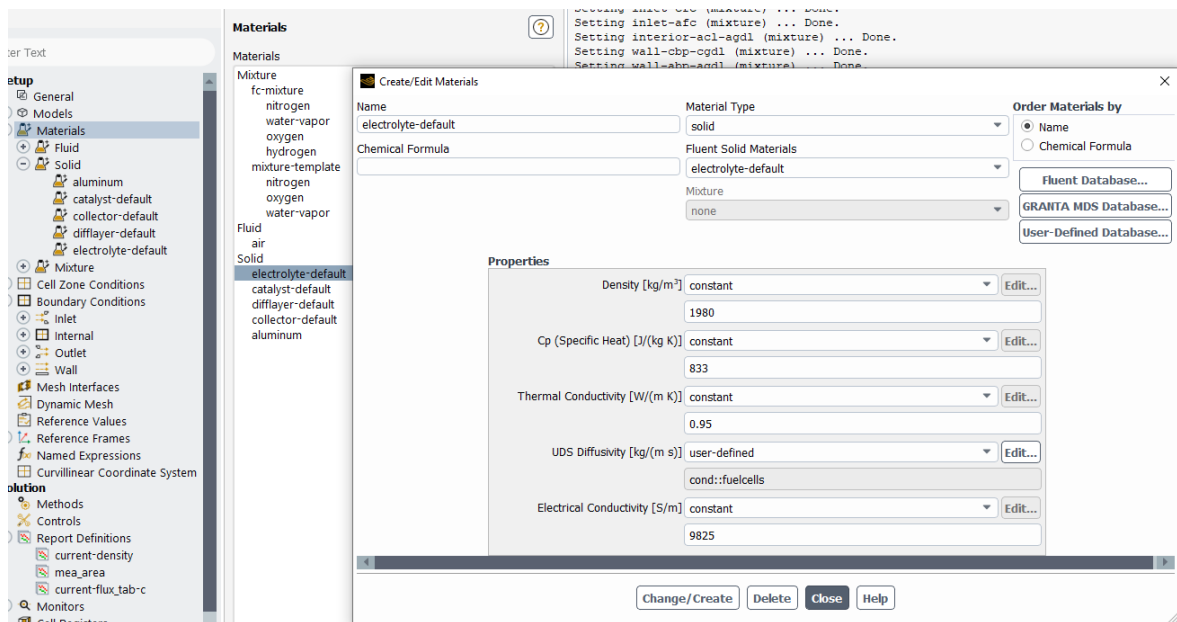


Fig. 3.8. Material properties setup for electrolyte/membrane (PEM).

3.1.3. Boundary condition, initial condition, assumption, and numerical procedure

The scenarios used in calculating GDL face permeability and TCR between BPs and GDLS are displayed in Table 3.3. These descriptions were utilized in the computation. The authors' application applies to every simulated situation concerning the various GDL face permeability and TCR on the PEM fuel cell.

Table 3.3. Description of the simulated cases regarding the various GDL face permeability and TCR.

Case No.	GDL face permeability (m ²)	TCR (m ² •K/W)
1	1.76E11	0
2	1.50E12	1.00E-04
3	2.25E12	2.50E-03
4	2.50E12	5.00E-03
5	3.25E12	7.50E-02
6	3.50E12	1.00E-01

Within the scope of this computational research, a numerical investigation will be conducted into six different types of tapered parallel FFCs. These include $L_{I/O}$ 0.7, $L_{I/O}$ 0.8, $L_{I/O}$ 0.9, $L_{I/O}$ 1.0, $L_{I/O}$ 1.1, and $L_{I/O}$ 1.2. It should come as expected that the contact surfaces between BPs and GDLS will vary greatly depending on the tapered parallel FFCs that are used. There have been a few studies [39, 40] that have discovered that TCR has a direct connection to the contact area. As a consequence of this, it is necessary to take into account the variation in TCRs for various tapered parallel FFC structures. In general, the TCR between BPs and GDLS can be determined by applying the correlation that is shown in the following phrase [89].

$$R_{TC} = \frac{\Delta T}{q} \quad (3.1)$$

where R_{TC} is the total interfacial TCR, ΔT is the temperature gradient, and q is the thermal flux, respectively. The computed PMT and TCR between BPs and GDLS for numerous tapered parallel FFCs and conventional parallel FFCs are shown in Table 3.4. Meanwhile,

Table 3.5 describes the simulated scenarios pertaining to the different WDB models, ICR, and GDL face permeability.

Table 3.4. For ordinary parallel and other tapered parallel FFCs, TCR dan PMT between BPs and GDLs.

Case No.	Description	Inlet side width (mm)	Outlet side width (mm)	PMT (m)	TCR (W/m ² K)
1	L _{VO} 0.7	1.0	0.7	0.0	0.0
2	L _{VO} 0.8	1.0	0.8	1.50E-06	1.00E-04
3	L _{VO} 0.9	1.0	0.9	2.00E-06	2.50E-03
4	L _{VO} 1.0	1.0	1.0	2.50E-06	5.00E-03
5	L _{VO} 1.1	1.0	1.1	3.00E-06	7.50E-02
6	L _{VO} 1.2	1.0	1.2	3.50E-06	1.00E-02

Table 3.5. Description of the simulated cases regarding the distinct WDB models, ICR, and GDL face permeability.





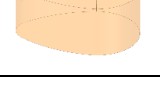
Case No.	WDB models	ICR (ohm.m ²)	GDL face permeability (m ²)
1	No WDB	4.50E-06	1.76E-11
2		4.00E-06	1.50E-12
3		3.50E-06	2.00E-12
4		3.00E-06	2.50E-12
5		2.50E-06	3.00E-12
6		2.00E-06	3.50E-12

Table 3.6. Operating parameters for validation (adapted from ref. [31], [78], [90]).

No.	Parameters	Value
1	Operating pressure	1, 2, and 3 atm
2	Operating temperature	60°C and 70°C
3	Open-circuit voltage	0.95 V
4	Reference current density for cathode	5210 A•m ⁻²
5	Reference current density for anode	9 x 10 ⁸ A•m ⁻²
6	Relative humidity of inlet gases	100%
7	GDL porosity	0.4
8	CL porosity	0.5
9	Anodic transfer coefficient at the anode	0.5
10	Cathodic transfer coefficient at the anode	0.5
11	Anodic transfer coefficient at the cathode	2
12	Cathodic transfer coefficient at the cathode	2
13	Anode concentration exponent	0.5
14	Cathode concentration exponent	1
15	Reference concentration of H ₂	54.7 mol•m ⁻³
16	Reference concentration of O ₂	3.39 mol•m ⁻³
17	H ₂ reference diffusivity	3.9 x 10 ⁻⁵ m ² •s ⁻¹
18	O ₂ reference diffusivity	2.275 x 10 ⁻⁵ m ² •s ⁻¹
19	H ₂ O reference diffusivity	3.9 x 10 ⁻⁵ m ² •s ⁻¹
20	Other species reference diffusivity	5.2 x 10 ⁻⁵ m ² •s ⁻¹
21	H ₂ mass flow rate	2.78 x 10 ⁻⁶ kg•s ⁻¹
22	O ₂ mass flow rate	1.15 x 10 ⁻⁵ kg•s ⁻¹
23	Anode fuel	H ₂ (60%) and H ₂ O (40%)
24	Cathode fuel	O ₂ (18.5%) and H ₂ O (22%)

Several conditions and activities can influence the performance and characteristics of a fuel cell. A fuel cell is a complex apparatus that operates utilizing electrochemical reactions. The performance and characteristics of a fuel cell can be modified by many variables and external factors in its environment. A fuel cell is a complex apparatus that participates in electrochemical reactions. Some assumptions have been formulated for the model to

streamline the equation for simulation analysis. All of these assumptions are delineated subsequently:

1. The fuel cells operate in a steady-state configuration.
2. There is an incompressible flow characteristic in gases.
3. The general consensus is that all gases are ideal gases.
4. Laminar behavior is a defining characteristic of fuel cell flow.
5. The system is affected by gravity in a direction opposite to that of Y.
6. The porosity and isotropy of the GDL textures are constant.
7. Only the surfaces of the gas diffusion layer have interface and thermal contact resistance.

To run a numerical simulation of multiphysics models in ANSYS Fluent. Fig. 3.9 depicts the Graphic User Interface (GUI) of ANSYS Fluent Setup to compute numerical models already imported as meshing formats. This GUI consists of tabs such as Setup, Solution, Results, Parameters & Customization, and Simulation Report. The SETUP tab consists of MODEL, which is defined as fuel cell and electrolysis (PEMFC) models in current work. Besides, there are Materials, Cell Zone Conditions, and Boundary Conditions. The SOLUTION tab comprises METHODS, Controls, Report Definitions, Monitors, Initialization, and Run calculation. The RESULTS tab comprises Surfaces, Graphics, Plots, Animation, and Reports. More detail regarding this Graphics User Interface can be seen in Fig. 3.9.

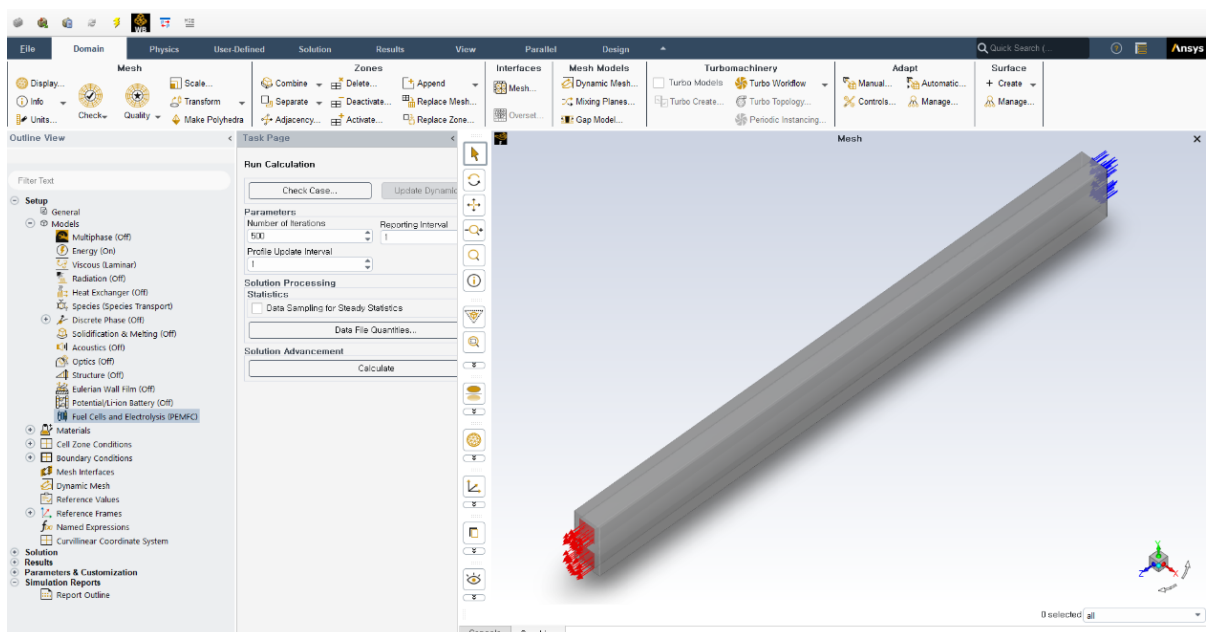


Fig. 3.9. Graphical user interface (GUI) Setup of ANSYS Fluent with Fuel Cell and Electrolysis (PEMFC) Model

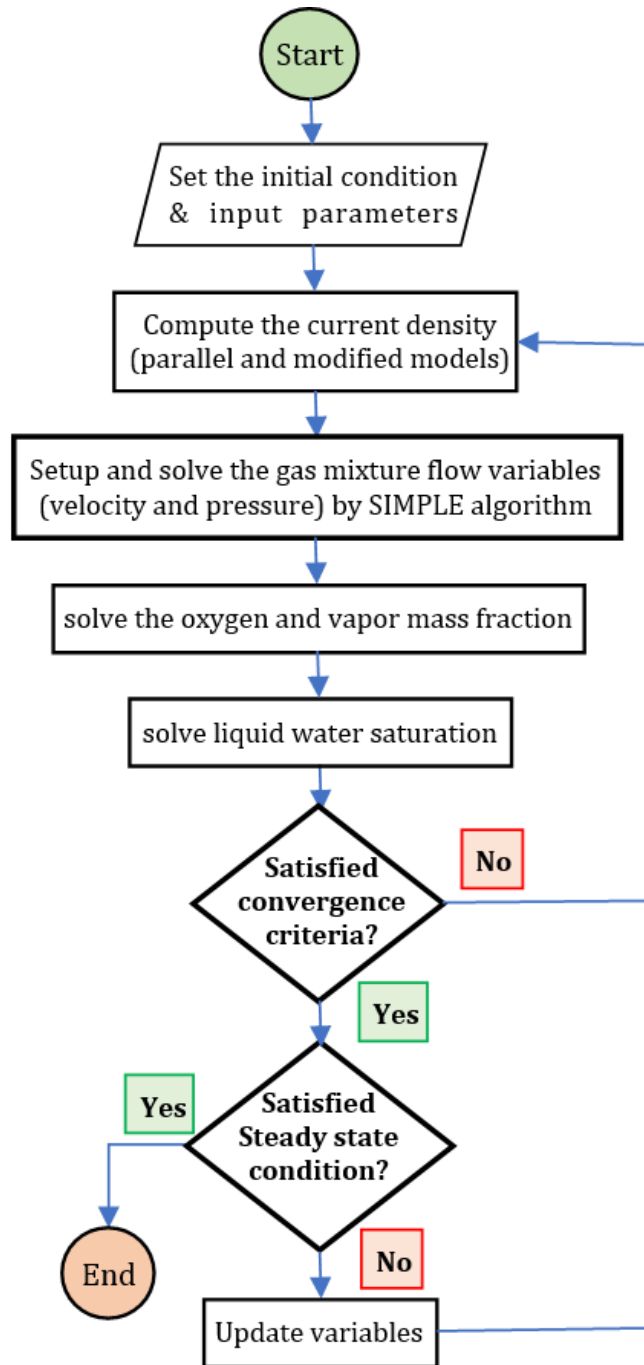


Fig. 3.10. Detailed flowchart for solving a multiphysics problem for a straight and currently developed PEM fuel cell model.

When the velocity field has reached a point of convergence, the equations pertaining to energy and electricity are coupled to the other equations and solved in order to arrive at the final solutions. In each and every CFD problem, the primary procedures that are involved are pre-processing, solution, and post-processing. Fig. 3.10 is a comprehensive flowchart that illustrates the actions that need to be taken in order to address a current computational

fluid dynamics (CFD) problem. Not only should the geometry be specified during the pre-processing phase, but the necessary physics in each domain and border also needs to be determined. Once the geometry was finished, it ought to have had the appropriate amount of elements and the appropriate size. In addition to this, it is crucial to evaluate the mesh and, if changes are required, to make improvements. The mesh structure that has been prepared can be used by the solver to begin using the predefined geometry and physics conditions. It is necessary to define the necessary model and boundary conditions, which are outlined in Table 3.6, at this phase in order to carry out the simulations. After the principal equations and the findings have been brought together, the data will be obtained in order to start the post-processing.

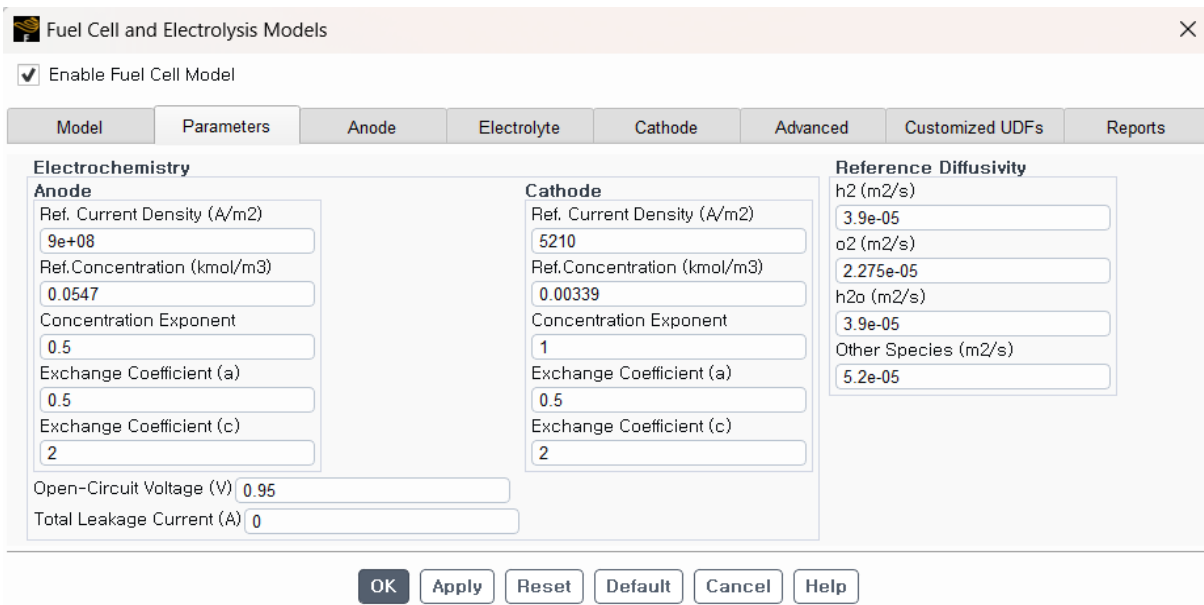


Fig. 3.11. The Parameters Tab of the Fuel Cell and Electrolysis Models Dialog Box

While resolving a fuel cell issue, the Model tab of the Fuel Cell and Electrolysis Models dialog box provides the ability to activate or deactivate a number of different options. Enabling the PEMFC option in the simulate tab is necessary to simulate the PEM fuel cell, as demonstrated in Fig. 3.11. It can provide the electrochemistry parameters for the Fuel Cell and Electrolysis Model by using the Parameters tab of the Fuel Cell and Electrolysis Models dialog box. This tab allows us to specify reference diffusivities for the reactants and other model characteristics.

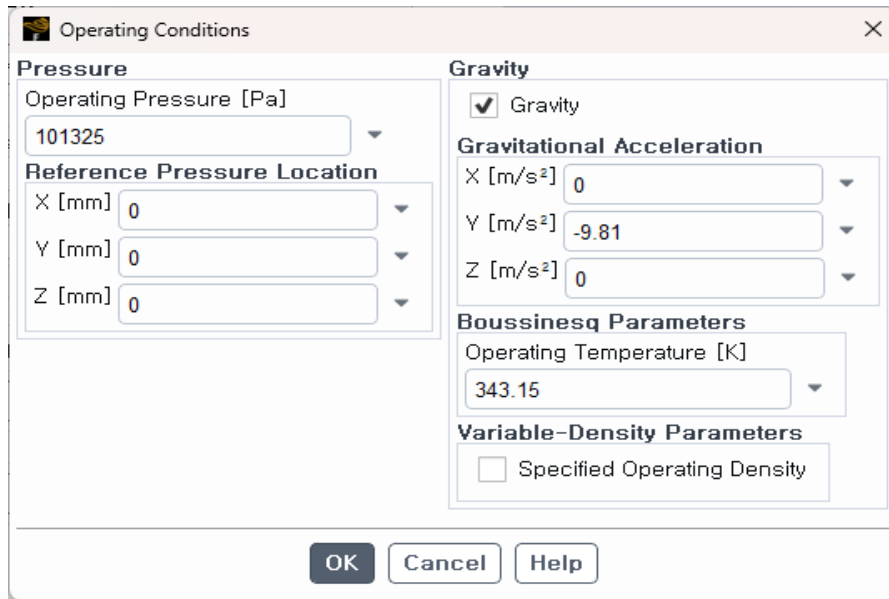


Fig. 3.12. Operating Condition Dialog Box

Physical operating conditions can be set up using the Operating Conditions Dialog Box (as shown in Fig. 3.12). For example, to set up operating pressure at 101,325 Pa, Gravitational Acceleration at Y -9.81 m/s², and operating temperature 343.15K (70°C) in current work models. In boundary conditions at the wall of cathode bipolar plate for getting the polarization curves based on relevant references [31], [90]. The authors would be shown a sample point of electric potential that should be set at 0.6 V at Tab-C, as depicted in Fig. 3.13. To be shorted, after all, initial and boundary conditions are set up completely. The next step to the Solution tab is to define SOLVER, such as utilizing Semi-Implicit Method for

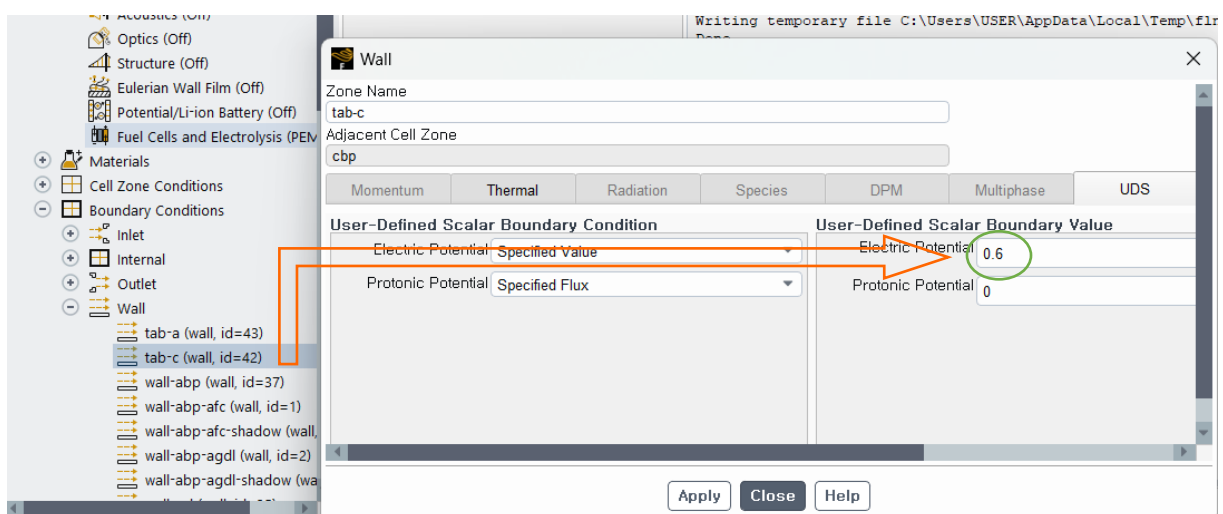


Fig. 3.13. Boundary conditions tab for current collector (Tab-C) with electric potential 0.6V.

Pressure-Linked Equations (SIMPLE) algorithm, which is prevalent in the pressure-velocity coupling, and the component is Least Squares Cell-based.

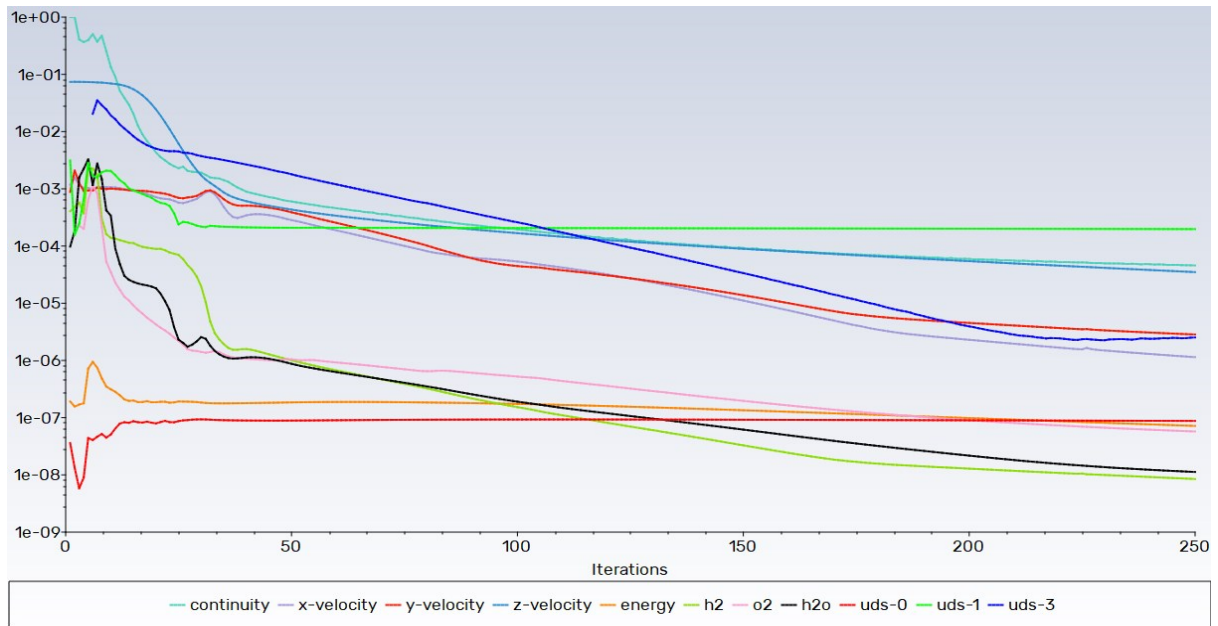


Fig. 3.14. Residual graph for convergence condition of PEM fuel cell simulation

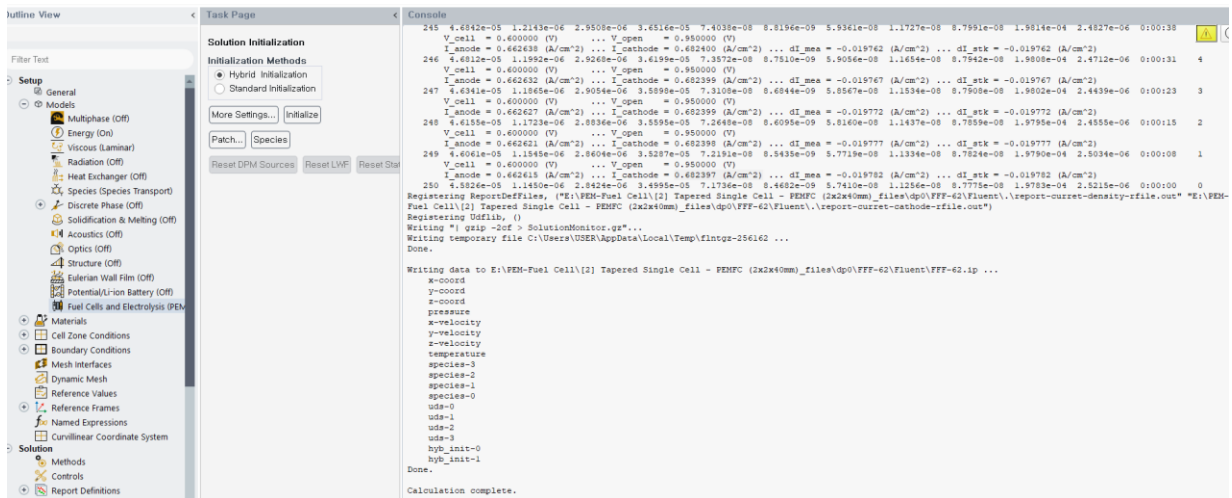


Fig. 3.15. Console window of average current density report at cell voltage 0.6V

The interpolation functions are frequently utilized in conjunction with the second-order upwind technique to determine a wide range of physical parameters. This is done in order to achieve accurate results. Composition, pressure, density, momentum, energy, proton potential, electric potential, water content, and water saturation are some of the qualities that are included in this category. The bi-conjugate gradient stabilized (BCGSTAB) method is the approach that is recommended to be applied in order to improve the accuracy of the

computation. This is because the BCGSTAB method is the stable method. Convergence conditions $10E-6$ are applied to the energy equation, and the F-cycle is selected as the type of cycle computation to be performed. In accordance with the illustration in Fig. 3.14, the remaining equations are subject to a convergence criterion of $10E-3$.

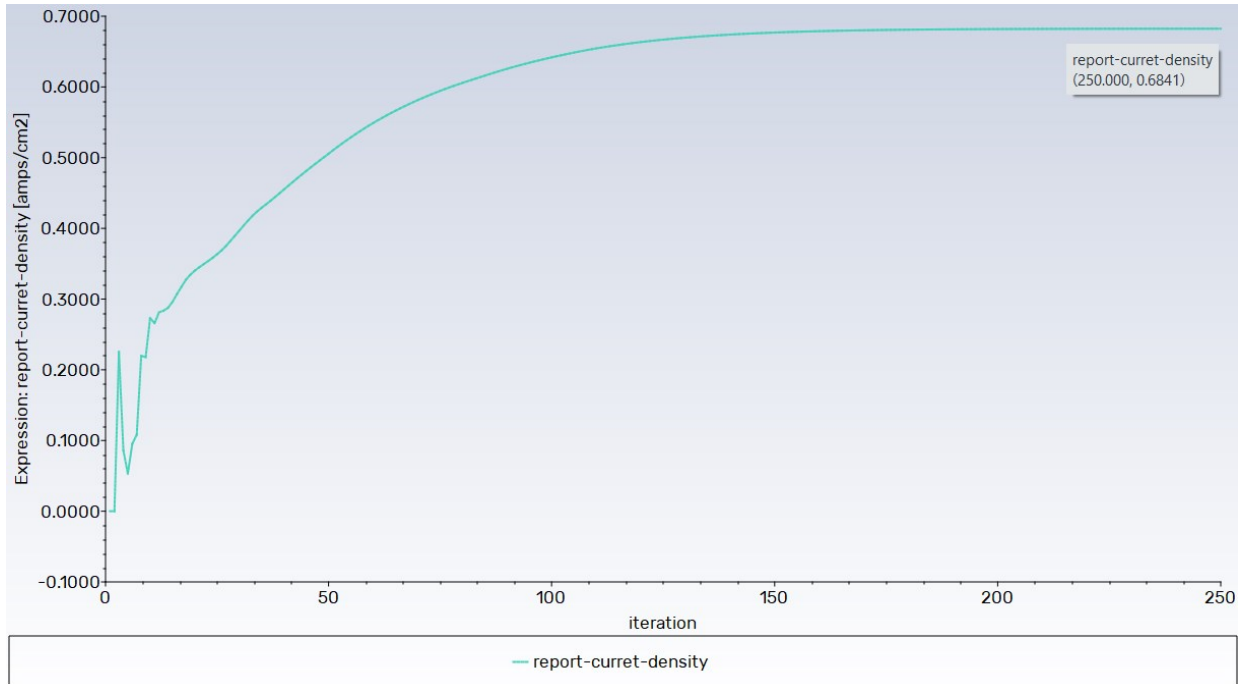


Fig. 3.16. Plot window of average current density report (0.6841 A/cm^2) at cell voltage 0.6V and 250 iteration.

Furthermore, Due to the convergence criteria accepted from Fig. 3.14, Its mean computational value for average current densities flow through the current collector at cell voltage 0.6 V has good results until the computational process is done in the last iteration as shown in the console window Fig. 3.15. In addition, this result can be strengthened by plotting window of average current density report at cell voltage 0.6 V has a stable value after 150 iterations are 0.6841 A/cm^2 (see Fig. Fig. 3.16), which has a similar value with the comparable polarization curve from Li et al. [31] and Wang et al. [90]. That means this computational work is acceptable and reliable compared to other numerical and experimental works.

3.1.4. Governing equations

The numerical modeling of a PEM fuel cell requires the utilization of several equations, including those pertaining to energy, momentum, continuity, species conservation, and

charge conservation, as well as those about the creation and transportation of liquid water. Following is a list of the fundamental equations that regulate the system [92].

Continuity equations

$$\nabla \cdot (\varepsilon \rho_g \vec{u}_g) = S_m \quad (3.2)$$

Momentum conservation expression

$$\nabla \cdot (\varepsilon \rho_g \vec{u}_g \vec{u}_g) = -\varepsilon \nabla P_g + \nabla \cdot (\varepsilon \vec{\tau}) S_{mom} \quad (3.3)$$

From Eq. (3.3), $\vec{\tau}$ represents the viscous stress tensor, which can be conveyed in the following equation:

$$\vec{\tau} = \mu_g \left(\nabla \vec{u}_g + \nabla \vec{\mu}_g^T \right) - \frac{2}{3} \mu_g \left(\nabla \cdot \vec{u}_g \right) I \quad (3.4)$$

Energy conservation expression

$$\nabla \cdot (\varepsilon \rho_{fl} C_p \vec{u} T) = \nabla \cdot (k_{eff} \nabla T) + S_E \quad (3.5)$$

C_p represents specific heat capacity at stable pressure in Eq. (3.5). S_E describes the energy source term, while k_{eff} represents the effective thermal conductivity.

Species conservation equation

$$\nabla \cdot (\varepsilon \rho_g \vec{u}_g \omega_i) + \nabla \cdot J_i = S_{mj} \quad (3.6)$$

where $J_i = -\rho_g D_i^{eff} \nabla \omega_i$, D_i^{eff} is the coefficient of gas diffusion:

$$D_i^{eff} = \varepsilon^{1.5} (1-s)^{2.5} D_i^0 \left(\frac{101325}{P} \right) \left(\frac{T}{300} \right)^{1.5} \quad (3.7)$$

The variable s represents the liquid water saturation, whereas S_{mj} denotes that the source term component is zero in the membrane, CL, GDL, flow channel, and current collector.

Expression of charge conservation

$$\nabla \cdot (\sigma_{ele} \nabla \varphi_{ele}) + S_{ele} = 0 \quad (3.8)$$

$$\nabla \cdot (\sigma_{ion} \nabla \varphi_{ion}) + S_{ion} = 0 \quad (3.9)$$

Table 3.7 provides a summary of the source terms. The symbol σ represents the conductivity, while φ_{ion} and φ_{ele} denote membrane phase potentials and the solid phase, respectively. The ion current source terms and electron current source, denoted as S_{ion} and S_{ele} , respectively, are defined within the anode and cathode catalyst layers as follows [93]:

$$S_{ion} = -S_{ele} = j_{ad} \quad (3.10)$$

in the layer of cathode catalyst:

$$S_{ele} = -S_{ion} = j_{cd} \quad (3.11)$$

The current density transfer, denoted as j , can be determined by employing the Butler-Volmer formula.

$$j_{ad} = (1 - s)j_{ad,ref} \left(\frac{C_{H_2}}{C_{H_2}^{ref}} \right)^{\gamma_{ad}} \left[\exp \left(\frac{\alpha_{ad} F \eta_{ad}}{RT} \right) - \exp \left(-\frac{\alpha_{cd} F \eta_{ad}}{RT} \right) \right] \quad (3.12)$$

$$j_{cd} = (1 - s)j_{cd,ref} \left(\frac{C_{O_2}}{C_{O_2}^{ref}} \right)^{\gamma_{cd}} \left[\exp \left(\frac{\alpha_{cd} F \eta_{cd}}{RT} \right) - \exp \left(-\frac{\alpha_{ad} F \eta_{cd}}{RT} \right) \right] \quad (3.13)$$

where $1 - s$ indicates the specific active surface area; γ is the concentration exponent; R is the universal gas constant of $8.314 \text{ J mol}^{-1}\text{K}$; F is the Faraday's constant of $96,487 \text{ C}\cdot\text{mol}^{-1}$; η represents the overpotential; j_{ref} is the exchange current density, and α denotes the transfer coefficient. Where η is stated by the following expression:

$$\eta_{ad} = \varphi_{ele} - \varphi_{ion} \quad (3.14)$$

$$\eta_{cd} = \varphi_{ele} - \varphi_{ion} - E_0 \quad (3.15)$$

where E_0 is the battery's open circuit voltage or the battery voltage theoretically in the open circuit state. E_0 is related to the temperature of a single battery and can be determined using the following expression:

$$E_0 = 1.23 - 0.9 \times 10^{-3}(T - 298) \quad (3.16)$$

Generation of liquid water and transport expression

$$\nabla \cdot (\rho_l \vec{u}_l s) = r_w \quad (3.17)$$

In Eq. (3.17), the rate of condensation r_w is reserved by the subsequent expression:

$$r_w = 100s^{-1} \max \left(\left[(1 - s) \frac{P_{wv} - P_{sat}}{RT} M_{H_2O} \right], [-S\rho_l] \right) \quad (3.18)$$

where P_{wv} represents water vapor pressure, P_{sat} is the pressure of water vapor saturation, a variable that relies on temperature.:

$$\begin{aligned} \log_{10} P_{sat} = & -2.1794 + 2.95 \times 10^{-2}(T - 273.15) \\ & - 9.1837 \times 10^{-5}(T - 273.15)^2 \\ & + 1.4454 \times 10^{-7}(T - 273.15)^3 \end{aligned} \quad (3.19)$$

Table 3.7 presents the complementary governing equations that are used to find the source term in each of the different regions.

Table 3.7. Source terms of governing equations (adapted from ref. [93],[94]).

Governing equations	Expression	Components
Conservation of mass	$S_m = -\frac{M_{H_2}}{2F}j_{ad} - \frac{\eta_d M_{H_2O}}{2F}j_{ad}$	Anode CL
	$S_m = \frac{M_{H_2O}}{2F}j_{cd} - \frac{M_{O_2}}{4F}j_{cd} + \frac{\eta_d M_{H_2O}}{F}j_{cd}$	Cathode CL
Conservation of momentum	$S_m = 0$	Other domains
	$S_{mom} = 0$	All domains
	$S_{mom} = -\frac{\mu}{K}\varepsilon^2\vec{u}$	GDLs/CLs
Conservation of energy	$S_E = h_{react} + j_{ad,cd}\eta_{ad,cd} + I^2R_{ohm} + r_w h_l$	All domains
Conservation of species	$S_{m,H_2} = -\frac{j_{ad}}{2F}M_{H_2}$	Anode CL
	$S_{m,O_2} = -\frac{j_{cd}}{4F}M_{O_2}, S_{m,H_2O} = \frac{j_{cd}}{2F}M_{H_2O}$	Cathode CL
Conservation of charge	$S_{ion} = -S_{ele} = j_{ad}$	Anode CL
	$S_{ele} = -S_{ion} = j_{cd}$	Cathode CL
	$S_{ion} = 0, S_{ele} = 0$	Other domains

The water distribution within the membrane for the cathode and anode flow channel is facilitated by implementing an inlet and outflow on the same side. Within the field of engineering, it is common to utilize the mass flow rate as the inlet boundary condition, rather than relying on velocity or pressure. The subsequent step is determining the mass flow rate using the provided equation [55]:

$$m_{ad,in} = \frac{\xi_{ad} I_{ref} \rho_{g,ad} A_{PEM}}{2F C_{H_2,in}} \quad (3.20)$$

$$m_{cd,in} = \frac{\xi_{cd} I_{ref} \rho_{g,cd} A_{PEM}}{4F C_{O_2,in}} \quad (3.21)$$

$$C_{H_2,in} = \frac{P_{ad,in} - RH_{ad} P_{sat}}{RT_{in}} \quad (3.22)$$

$$C_{O_2,in} = \frac{0.21(P_{cd,in} - RH_{cd} P_{sat})}{RT_{in}} \quad (3.23)$$

The stoichiometric flow ratio, denoted by ξ , is a crucial parameter in mixed gases. The variable ρ represents the density of the mixed gas. Additionally, it is essential to note that the current reference density, I_{ref} , requires manual specification. The symbol F denotes Faraday's constant, while A_{PEM} represents the proton exchange membrane cross-sectional area. RH refers to relative humidity, $C_{H_2,in}$, and $C_{O_2,in}$ which denote hydrogen and oxygen mass fractions, respectively.

3.2. Grid-independent verification and model validation

An algorithm for a personal computer that makes use of the finite volume method is utilized in order to effectively solve the problem. Because of the large difference in thickness that can be observed between the various layers, the utilization of hexahedral grids for straight/parallel channels in the Z direction is justified. As an alternative, uniform hexahedral grids are utilized for straight channels in both the X and Y directions, as can be seen in Fig. 3.17. As can be seen in Fig. 3.18, water-drop block (WDB) model configurations feature a preponderance of hexahedral grids and a limited number of tetrahedral grids at the surface of BPs. A framework consisting of two phases is utilized in the construction of the models. This framework incorporates the mechanisms of isotropic transport in gas diffusion layers. The idea proposes that the cell keeps its pressure and temperature settings at a constant level while the gas flows in a laminar fashion. In the gas mixture, it is hypothesized that the reactive gases exhibit behavior that is representative of ideal conditions. As an additional benefit, the rapid velocity that is observed in the flow channel makes it possible to overlook the liquid saturation that is present in the gas channel. Five different grid configurations were utilized in order to carry out the evaluation of grid independence. Fig. 3.19 (a) shows that the five grids correspond to 496,000, 512,000, 544,000, 560,000, and 592,000 values. The ongoing work employs a grid system that takes into account the equilibrium between accuracy and cost-effectiveness. Consequently, after the grid numbers reach 544,000, the results of the calculations become more stable. The Semi-Implicit Method for Pressure-Linked Equations (SIMPLE) algorithm is widespread in coupling pressure and velocity, and the component is based on the Least Squares Cell method.

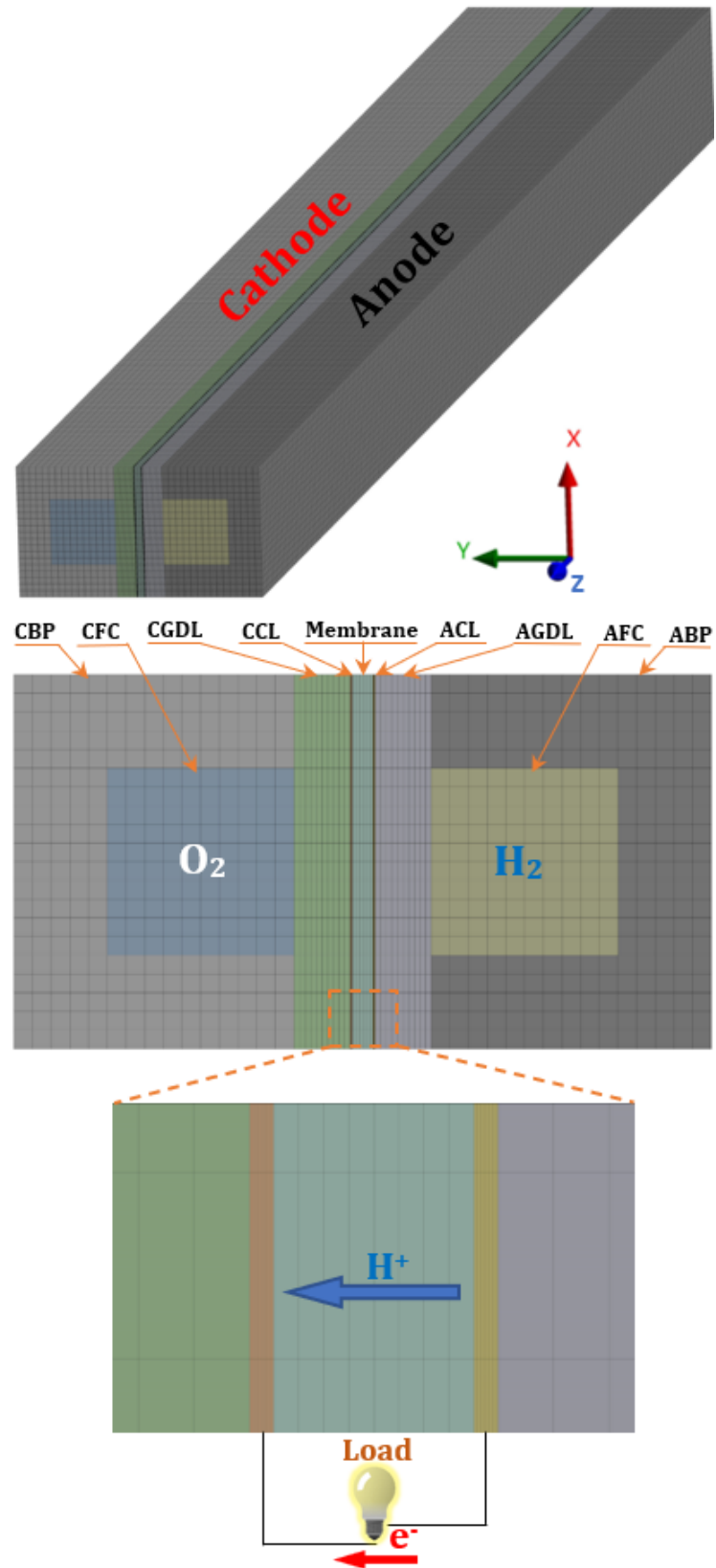


Fig. 3.17. A diagram depicting the model geometry, structure, and computational domains of straight and parallel tapered flow fields for PEM fuel cell.

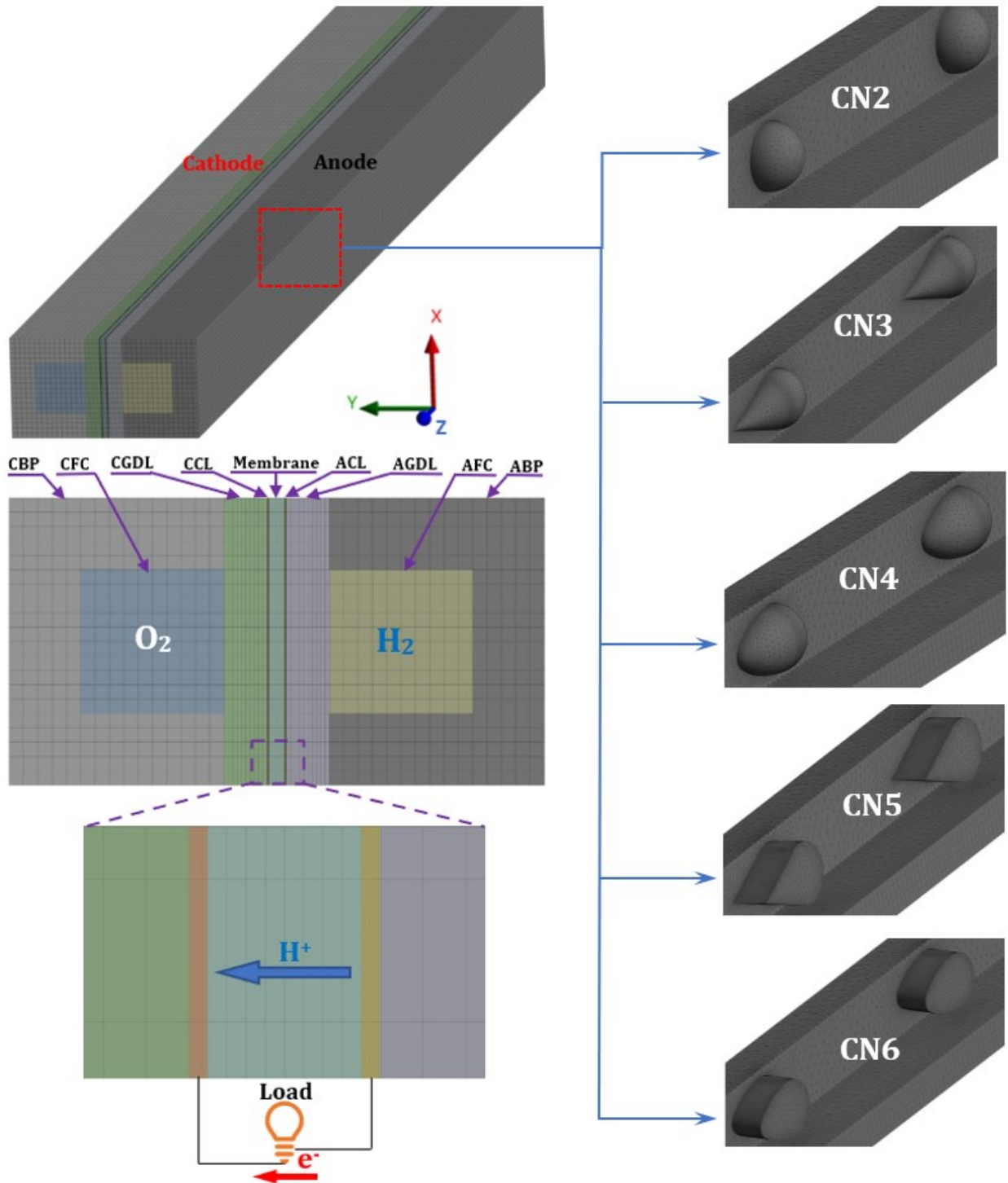


Fig. 3.18. A schematic describing PEM Fuel Cell's computational domains and meshes of difference flow field structures (Straight and Water Drop Blocks).

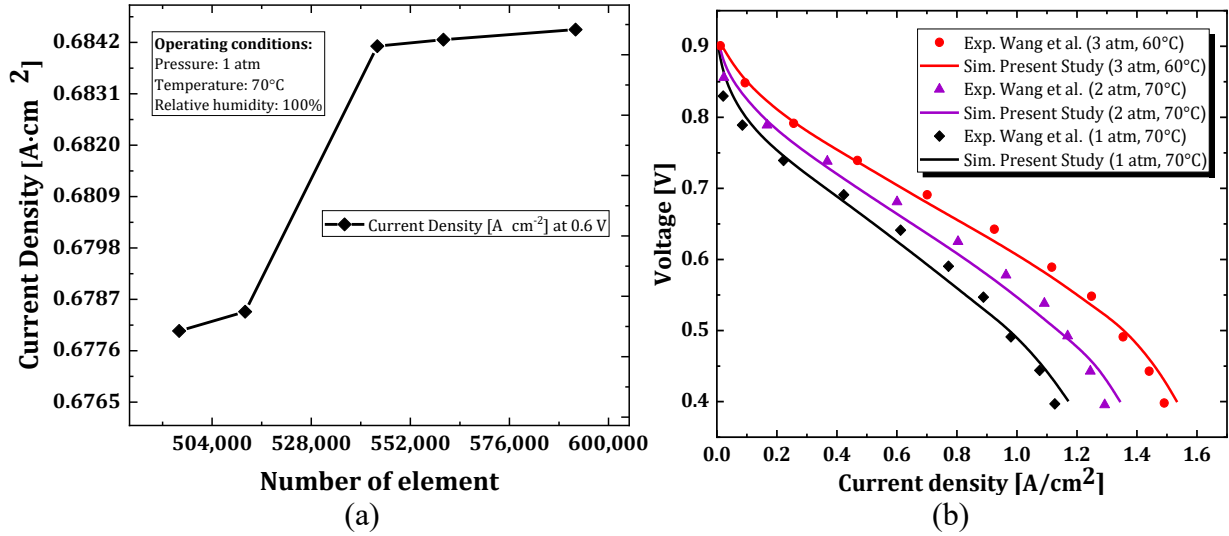


Fig. 3.19. (a) Grid independency verification for the current density at $V = 0.60\text{V}$, (b) comparison of the polarization curves between the current computational study with experiment results for straight channel model with different pressure and temperature operations.

In the meantime, the interpolation functions are widely used in conjunction with the second-order upwind approach to compute various physical values. These properties include composition, pressure, density, momentum, energy, proton potential, electric potential, water content, and water saturation. It is recommended that the bi-conjugate gradient stabilized (BCGSTAB) method be utilized as the stable method to achieve the high level of precision desired in the computation. Convergence conditions $10\text{E-}6$ are applied to the energy equation, and the F-cycle is selected as the sort of cycle calculation procedure to be used. A convergence condition of $10\text{E-}3$ is imposed on the equations still existing. For the purpose of providing a concise summary of the operational concepts that underlie numerical validation, Fig. 3.19 (b) was adapted from studies of relevant experimental literature [90].

The results of the current multiphysics computational model are validated by comparing the simulated polarization curves to the experimental value acquired from Wang et al. [90]. This comparison is done in order to ensure that the results of the model are accurate. Fig. 3.19 (b) provides a visual representation of this contrast. Several experimental situations, such as particular temperatures and pressures, are utilized in order to appraise the numerical models. Earlier, in Table 3.6, we gave the supplementary operational factors that were used in the process of constructing the polarization curves. While validating the model, it is necessary to evaluate the degree of concordance between the two polarization curves obtained under

various operating conditions and the corresponding experimental data. This is done to ensure that the curves fall within the permissible range. The multiphysics model performs significantly better than the experiments when the conditions are high in terms of current density.

3.3. Summary

This chapter provides an explanation of the simulation modeling setup based on the ANSYS-Fluent Fuel Cell and Electrolysis Model. The simulation's validity is established by comparing the simulation's findings with the results of the experiments found in the literature concerning the polarisation curve (I-V curve). The research of the influence of variation of bipolar plate flow fields (parallel, tapered, and water drop block models) on mass transport characteristics and cell performances of PEM fuel cells might be carried out using a simulated technique. This would involve taking into consideration some variable parameters. In chapters 4, 5, and 6, all of the specifics of optimizing mass transport and cell performance will be studied and described in greater detail.

4. EFFECT OF GDL FACE PERMEABILITY AND THERMAL CONTACT RESISTANCE ON TEMPERATURE DISTRIBUTION, MASS TRANSPORT, AND PERFORMANCE OF PEM FUEL CELL

This chapter analyzed the impact of TCR and GDL face permeability on the temperature profiles, mass transport, and cell performance of a single PEM fuel cell. The analysis was conducted using a three-dimensional, non-isothermal computational model with an isotropic gas diffusion layer (GDL). This model determines the optimal thermal contact resistance by comparing the anticipated temperature difference between the plate and cathode electrodes to the literature's existing computational and experimental data. The combined Artificial Neural Network-Genetic Algorithm (ANN-GA) method is utilized to determine the optimal power levels and their corresponding operating circumstances in six different scenarios. As shown by theoretical research, it is essential to consider thermal contact resistance (TCR) and proper GDL face permeability to improve temperature distribution and cell performance.

4.1. Thermal contact resistance (TCR) and GDL face permeability affect cell performance and temperature profiles.

The temperature of the PEM fuel cell may not always be optimized under real operating conditions. This could be attributed to limitations in heat management or specialized operational procedures, such as starting procedures. The increase in temperature from ambient temperature to the optimal operating temperature of a fuel cell exemplifies the ignition process. The temperature of a small fuel cell without an active thermal management component is mainly influenced by the temperature of its surrounding environment and the pace at which waste is produced. In order to effectively control and develop fuel cell systems, it is crucial to comprehend the maximum power that can be attained at different temperatures, as temperature dramatically influences the functioning of fuel cells. Both the correlation between temperature and maximum power and the identification of suitable operating conditions need to be examined. The methodology for determining GDL face permeability and TCR between BPs and GDLS is outlined in Table 4.1. The authors apply this methodology to all the simulated instances involving different GDL face permeability and TCR on the PEM fuel cell.

Table 4.1. Description of the simulated cases regarding the various GDL face permeability and TCR

Case No.	GDL face permeability (m^{-2})	TCR ($\text{m}^2\cdot\text{K}/\text{W}$)
1	1.76E11	0
2	1.50E12	1.00E-04
3	2.25E12	2.50E-03
4	2.50E12	5.00E-03
5	3.25E12	7.50E-02
6	3.50E12	1.00E-01

The interface between the contact surfaces of the different components of a fully functioning PEM fuel cell (PEMFC) is characterized by thermal contact resistance and GDL face permeability. This is because the PEMFC consists of several separate components. The Proton Exchange Membrane Fuel Cell (PEMFC) performs efficiently, hence elucidating its usefulness. The utilization of a hot press technique during the production of the membrane electrode assembly (MEA) leads to the general perception that the contact resistance between the cathode catalyst layer (CCL) and the gas diffusion layer (GDL) is typically deemed insignificant. This is because contact resistance is anticipated to be unimportant. This is because the MEA is produced using this specific technique.

On the other hand, the authors are solely concerned with examining the thermal contact resistance and the GDL face permeability between the collector and the gas diffusion layer (GDL). The thermal contact resistance between the graphite collector and the gas diffusion layer (GDL) demonstrates variability that ranges from $0.3 \times 10^{-4} \text{ m}^2\cdot\text{K}\cdot\text{W}^{-1}$ to $2.5 \times 10^{-4} \text{ m}^2\cdot\text{K}\cdot\text{W}^{-1}$, depending on the compression pressure that is applied, as a result of the findings that were presented by Nitta et al. [95]. The thermal contact resistance between the BP and the GDL can range anywhere from $1.0 \times 10^{-4} \text{ m}^2\cdot\text{K}\cdot\text{W}^{-1}$ to $8.0 \times 10^{-4} \text{ m}^2\cdot\text{K}\cdot\text{W}^{-1}$, as determined by Sadeghifar et al. [96]. This range is dependent on the particular type of GDL that is utilized as well as the degree of compression that is applied.

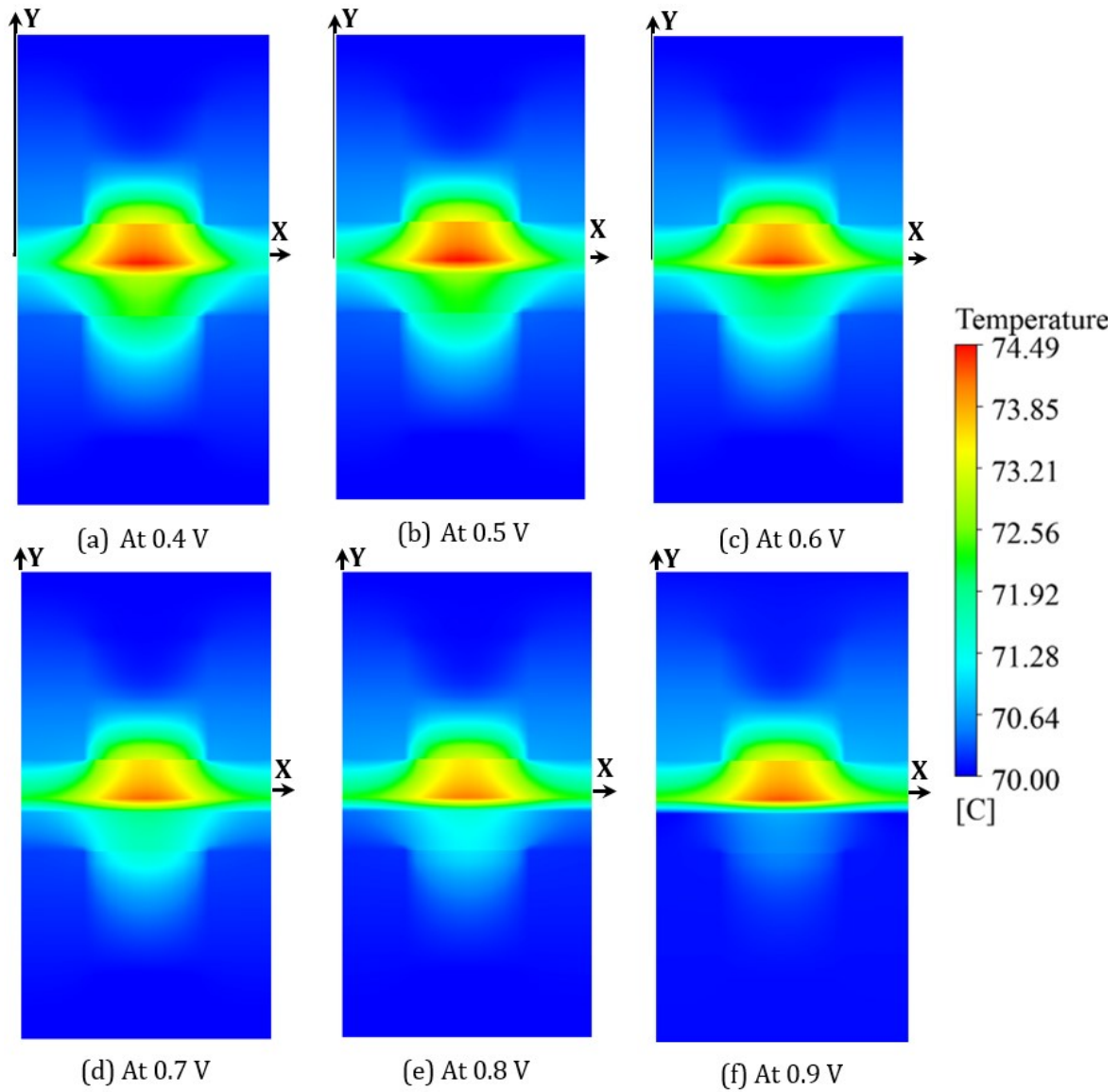


Fig. 4.1. Temperature distributions on XY-plane (40mm from origin of Z-axis) at various cell voltages without considering TCR (operating pressure, $P = 1$ atm; operating temperature, $T = 70^{\circ}\text{C}$; cathode gas: oxygen; anode gas: hydrogen).

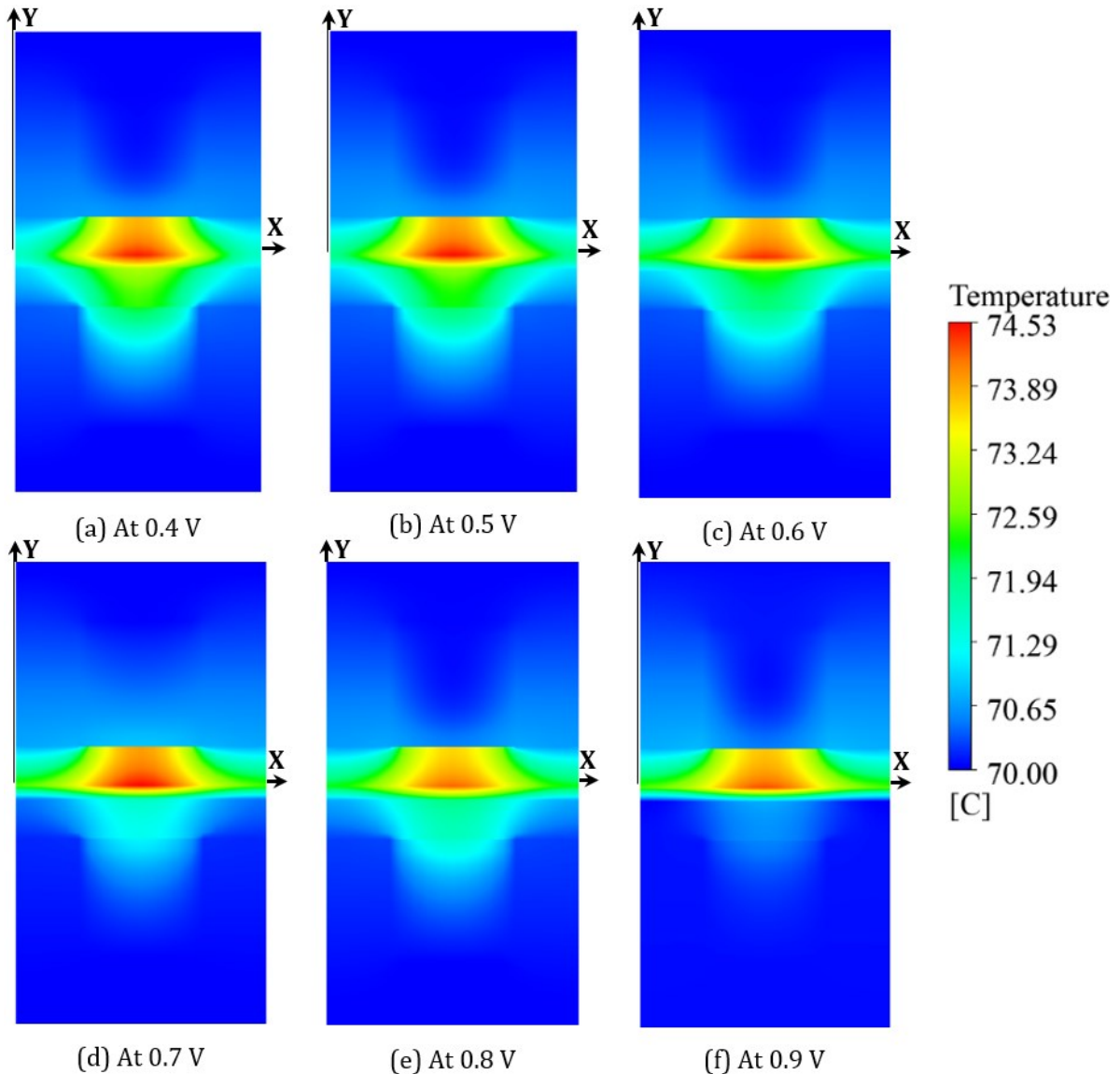


Fig. 4.2. Temperature distributions on XY-plane (40mm from origin of Z-axis) at various cell voltages with considering TCR ($1.00\text{E-}01 \text{ m}^2\cdot\text{K/W}$) and GDL face permeability ($3.50\text{E}12 \text{ m}^{-2}$) (operating pressure, $P = 1 \text{ atm}$; operating temperature, $T = 70^\circ\text{C}$; cathode gas: oxygen; anode gas: hydrogen).

This investigation demonstrates that the GDL face permeability and the TCR between the current collector and GDL vary from $1.76\text{E}11 \text{ m}^{-2}$ to $3.50\text{E}12 \text{ m}^{-2}$ and 0 to $1.00\text{E-}01 \text{ m}^2 \text{ KW-}1$, respectively. For more detailed information, please refer to Table 4.1. Fig. 4.1 displays the temperature distributions without the presence of a porous medium thickness and thermal contact resistances. Fig. 4.2., on the other hand, shows the temperature distributions with the inclusion of these factors. The output voltages considered in the analysis range from 0.4 to 0.9 V. A temperature gradient exists between the current collector (rib) and channel areas,

with the rib exhibiting lower temperature and the channel exhibiting higher temperature as one advances away from it. Given the low velocity in the porous GDL, it can be deduced that the rib region is primarily responsible for conducting most of the heat released by the electrode. Moreover, it has been found that there is a direct correlation between the increase in permeability values of TCR and GDL and the corresponding increase in the optimal cell temperature. The existence of GDL face permeability, and TCR between the collector rib and the GDL leads to an increase in heat transfer resistance and complicates heat dissipation within the porous electrode. Furthermore, both the GDL face permeability and the TCR hinder the disposal of heat.

Fig. 4.1 depicts temperature profiles that do not take into account the permeability of the gas diffusion layer (GDL) face and the thermal contact resistance (TCR) along the XY-Plane in the Z-Axis direction. The highest temperature is found in the cathode catalyst layer since the oxygen reduction process generates the majority of the heat. When the output cell voltage decreases, the heat produced in the cell increases, leading to an increase in the maximum temperature. By comparing Fig. 4.2., one can observe the influence of the gas diffusion layer (GDL) face permeability and thermal contact resistance (TCR) on the temperature distribution within the proton exchange membrane fuel cell (PEMFC). Ohmic heating occurs as a result of the resistance caused by the flow of electricity through the electrolyte membrane and the electrodes. Temperature fluctuations can occur within the MEA, with elevated temperatures commonly found in regions of greater current density. In addition, it is crucial to efficiently transfer and disperse the heat created within the MEA in order to maintain a uniform temperature distribution. Temperature fluctuations can occur due to differences in heat transmission rates and cooling processes across the MEA. Heat dissipation can be influenced by factors such as thermal contact resistances and the thickness of the porous medium of the materials being used. Ignoring the permeability of the TCR and GDL surfaces can result in underestimating the overall temperature of the MEA. The temperature results obtained without considering GDL face permeability and TCR are significantly lower than the temperature results obtained when considering GDL face permeability and TCR. For example, the optimal temperature gradient between these two cases is approximately 1.5°C when the output cell voltage is 0.4 V, and the average temperature increase across all cell voltage conditions is 0.5°C.

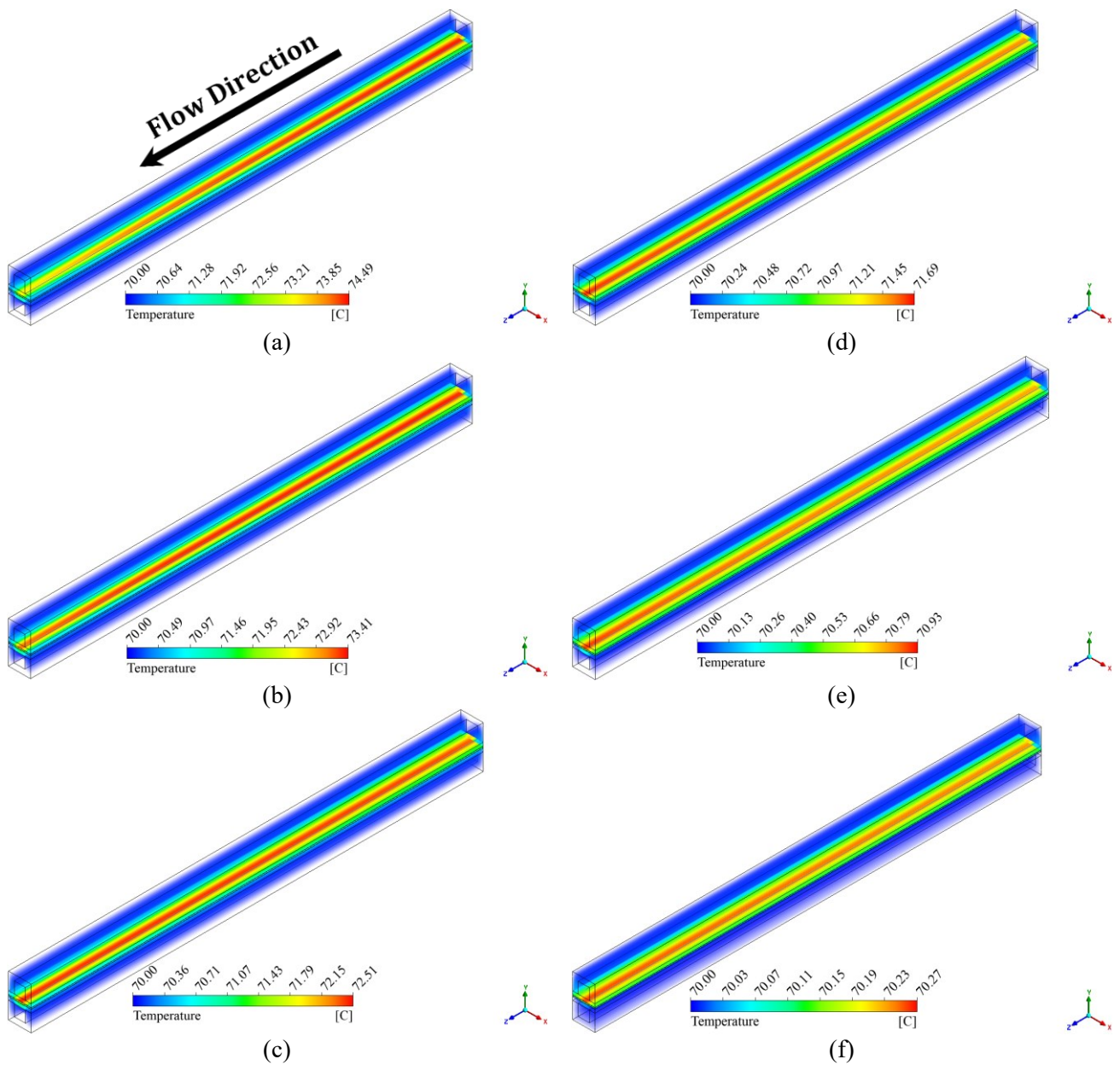


Fig. 4.3. Distributions of temperature at iso view with various cell voltages (a) 0.4V, (b) 0.5V, (c) 0.6V, (d) 0.7V, (e) 0.8V, and (f) 0.9V ignoring TCR (operating pressure, $P = 1$ atm; operating temperature, $T = 70^{\circ}\text{C}$; cathode gas: oxygen; anode gas: hydrogen).

In addition, Fig. 4.3 illustrates the temperature distribution at a constant volume for different cell voltages (ranging from 0.4 V to 0.9 V) without taking into account the effects of thermal contact resistance (TCR) and gas diffusion layer (GDL) face permeability. The maximum temperature primarily originates from the center of the MEA, with the highest temperature

occurring at a cell voltage of 0.4 V and the lowest temperature at a cell voltage of 0.9 V. Fig. 4.4. illustrates the relationship between the polarization curve, power density, and current density under certain operating circumstances in six different scenarios. The relationship between power density and current density is clearly demonstrated to rise with case number. This increase is attributed to the higher GDL face permeability and TCR, which aligns with findings in recent research [97]. The temperature patterns in the MEA vary between Fig. 4.5. (a) and Fig. 4.5. (b). The temperature patterns seen in MEA exhibit a "Λ" form in both Fig. 4.5. (a) and Fig. 4.5. (b). The temperature phenomena are attributed solely to the TCR and the permeability of the GDL face between the current collector (rib) and GDL. Put simply, the permeability of the gas diffusion layer (GDL) and the thermal contact resistance (TCR) between the bipolar plate (BP) and the GDL hinder the dissipation of heat, resulting in an increase in the temperature of the membrane electrode assembly (MEA). This finding aligns with the previous research conducted by Cao et al. [97]. Fig. 4.5. demonstrates that the porous electrode experiences more significant heating in TCR and GDL face permeability cases. A decrease in the condensation of water vapour into liquid form occurs as the temperature of the electrode rises. This is because the pressure at which water becomes saturated with vapor likewise rises as the temperature of the electrode rises. One possible explanation for this is that the permeability of the TCR and GDL faces has increased to a lower saturation level. While this is happening, the electrochemical process and oxygen transport to the reaction sites by the gas diffusion layer (GDL) are improved by increasing the temperature. In a similar manner, lowering the liquid water saturation in the GDL face permeability and operating under thermal contact resistance (TCR) conditions both make it easier for oxygen to be transported. The results of the GDL face permeability and TCR testing show that the performance of the cells is greatly improved under these conditions.

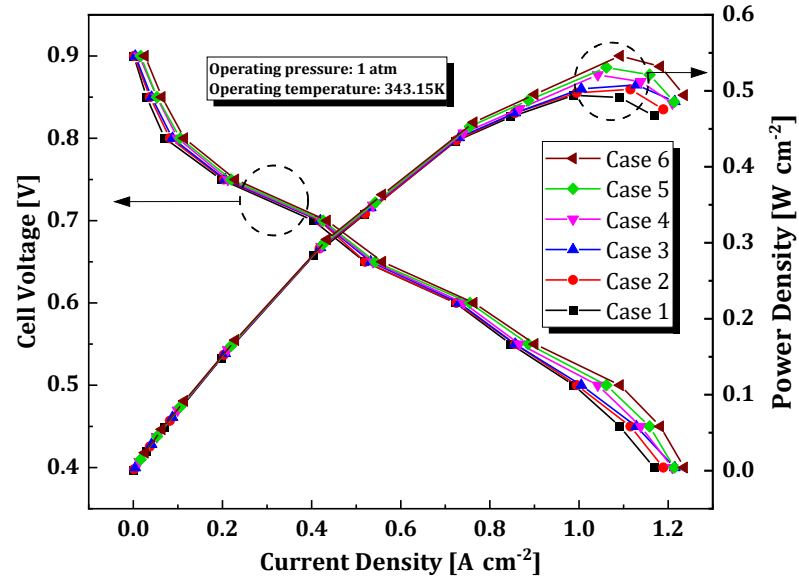


Fig. 4.4. Current and power densities of various cases (operating pressure = 1 atm; operating temperature, $T = 70^{\circ}\text{C}$ (343.15K)).

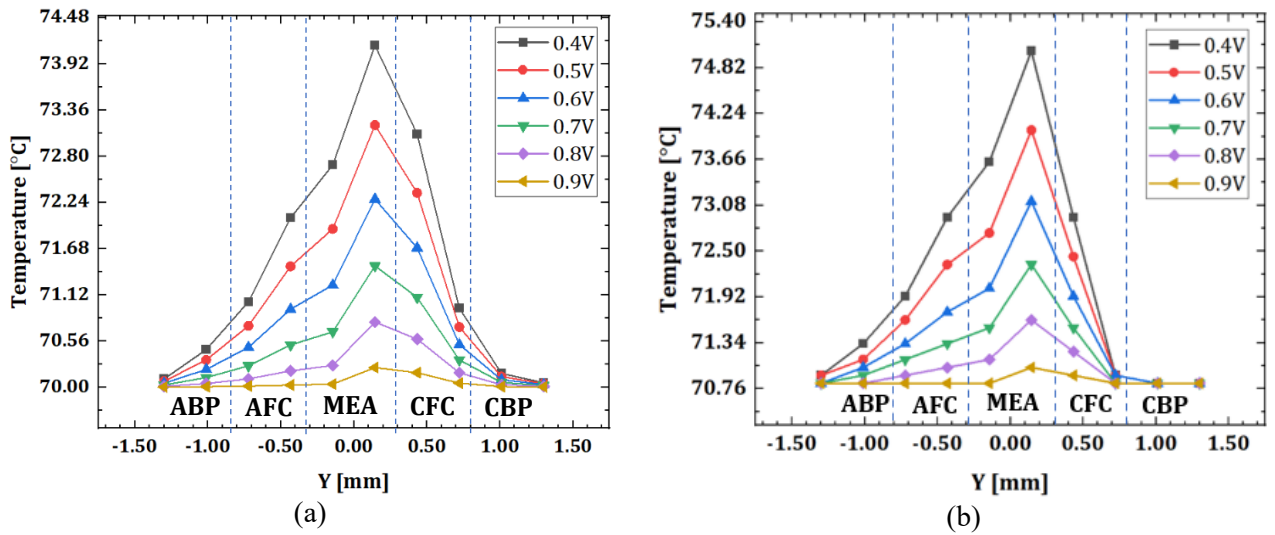


Fig. 4.5. Profiles of temperature toward the Y-axis with various cell output voltages: (a) without (b) with TCR ($1.00\text{E}-01 \text{ m}^2 \text{ K/W}$).

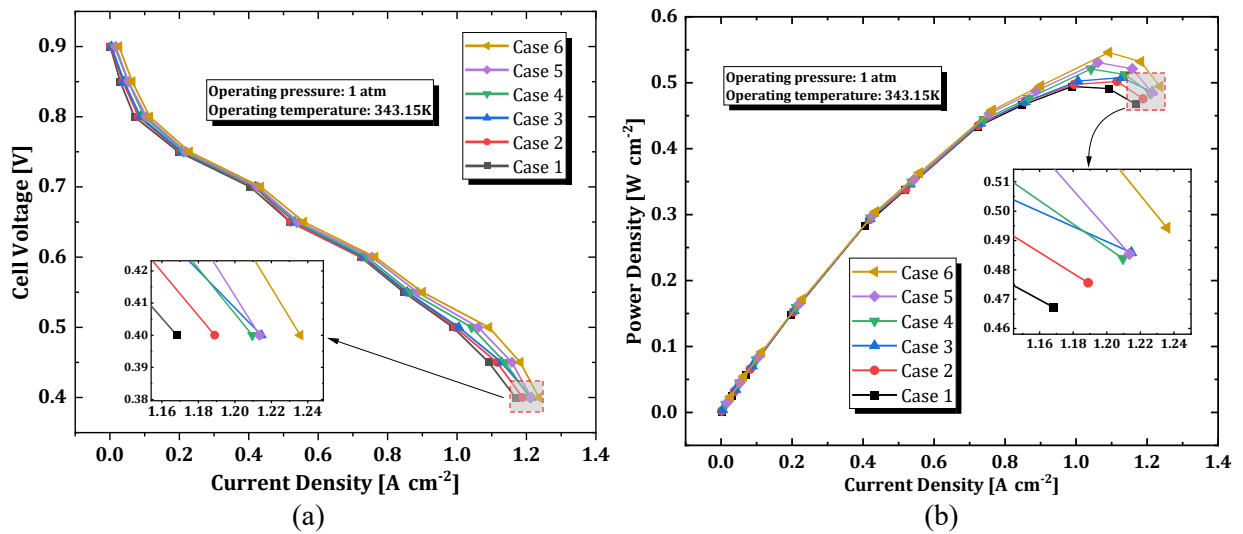


Fig. 4.6. (a) Current density and (b) power density curves with distinct cases (operating temperature, $T = 70^{\circ}\text{C}$ (343.15K); operating pressure = 1 atm.

This particular illustration of the polarization curve is shown in Fig. 4.6. (a), which illustrates the simulation results of the three-dimensional multiphysics model. Moreover, the power density curves for six alternative situations are displayed in Fig. 4.6. (b), each of which is distinguished by a unique set of particulars. Fig. 4.6. (a) demonstrates that there is only a slight difference in the current density between the several scenarios that are beyond the threshold of 1.15 A/cm^2 . The differences in current density between the various scenarios show a gradual increase as the operational voltages continue to decrease. On the other hand, when compared to all of the other cases, case 1 has the lowest current density, which is 1.168 A/cm^2 . Case 6, on the other hand, exhibits the highest current density, with a measurement of 1.236 A/cm^2 in its current density. At a voltage of 0.4 V , this number is higher than the one for case 1 by 0.068 A/cm^2 , which is equivalent to a relative increase of 6.8% . A further illustration of the power density curve is shown in Fig. 4.6. (b), which displays six different scenarios. 0.494 W/cm^2 is the smallest peak power density witnessed in case 1, according to the data that has been supplied. On the other hand, the most significant peak power density measured in case 6 was 0.546 W/cm^2 , which indicates a difference of 0.052 W/cm^2 relative to case 1 (comparable to an increase of 8.72%). Based on this finding, it appears that taking into account both the appropriate GDL face permeability and the thermal contact resistance (TCR) between the gas diffusion layer and the current collector can imp the performance of the PEM fuel cell.

4.2. Implementation of artificial neural network (ANN) and Genetic algorithm (GA) optimization on cell performance

The study employed an artificial neural network (ANN) with a multi-layer feedforward structure consisting of two hidden layers. Two outputs are meant to be provided by the network, which is designed to handle four input parameters independently. The three inputs include a number of operating parameters, such as the thermal contact resistance (TCR), the face permeability of the gas diffusion layer (GDL), and the output voltage (V). In addition, the first hidden layer is made up of eight neurons, while the second hidden layer is made up of an additional four neurons. The Levenberg-Marquardt algorithm, a training method for feedforward networks, is selected for its efficacy in tackling non-linear problems and training networks of modest to moderate dimensions. The hyperbolic tangent (tanh) function is employed as the activation function in the hidden layers, whereas the output layer uses the pure linear transfer function (purelin) [98]. The inherent correlation between the input and output parameters can be expressed as follows:

$$j = F(TCR, GDL \text{ face permeability}, V) \quad (4.1)$$

The design of the genetic algorithm (GA) frequently includes multiple common components [81]. The fundamental elements of this genetic algorithm framework comprise: 1. A collection of chromosomes that represent the population; 2. A fitness function employed to assess the chromosomes; 3. The procedure of selecting parents from the initial group of chromosomes, and 4. The implementation of crossover and mutation operations to produce offspring. A "chromosome" is a set of numerical parameters representing a possible optimization solution using Genetic Algorithms (GA). A chromosome's expression in n dimensions is commonly depicted in the following manner.

$$\text{chromosome} = [p_1, p_2, p_3, \dots, p_i] \quad (4.2)$$

where p_i represents the value of the i -th parameter, this study explicitly examines four actual variables; the components of the ANN-GA method include TCR, GDL face permeability, and V. The primary objective of this optimization technique is to maximize the current density (I) and power density (P). The fitness function is a numerical measure used to estimate a chromosome's reproductive success and survival capability. The

implementation of this function utilises a trained Artificial Neural Network (ANN) model as shown below:

$$P = jV = F(TCR, GDL \text{ face permeability}, V) * V \quad (4.3)$$

The selection of parent chromosomes for the purpose of reproducing the next generation is determined by the fitness values of the chromosomes. Chromosomes with greater fitness values are more likely to be selected for reproduction [99]. One possible occurrence of the phenomenon is the ability of chromosomes to demonstrate the maximum power output, which may be stated in the following manner:

$$C(TCR_{P_{max}}, GDL \text{ face permeability}_{P_{max}}, V_{P_{max}}) = \frac{P(TCR_{P_{max}}, GDL \text{ face permeability}_{P_{max}}, V_{P_{max}})}{\sum_1^N P(TCR, GDL \text{ face permeability}, V)} \quad (4.4)$$

The crossover operation is a biological recombination process that occurs between a pair of parent chromosomes. It involves the exchange of traits and leads to the generation of two offspring. N represents the total count of parent chromosomes. The mutation is usually applied to the elements of the child generation with a low likelihood in order to minimize any potential negative impact on the features of the chromosome.

MATLAB is used to build the artificial neural network (ANN) and the genetic algorithm (GA) by utilizing the Deep Learning Toolbox and the Genetic Algorithm Optimisation Toolbox (GAOT). The Artificial Neural Network (ANN) training phase is used to learn data points. The distribution of data points for training, validation, and testing is carried out randomly. 70% of the data points are allotted for training, 15% for validation, and the remaining 15% for testing. After completing adequate training, the Artificial Neural Network (ANN) is utilized as the fitness function to optimize the Genetic Algorithm (GA). The ANN is then provided with the predicted operating state, which is stated in terms of current density and power density after the GA optimization algorithm has completed its calculations.

Hence, the forecasts generated by the genetic algorithm (GA) could be vulnerable to random errors. Fig. 4.7 illustrates the flow chart of the Artificial Neural Network-Genetic Algorithm (ANN-GA) approach for training and prediction. After sufficient training, the Artificial Neural Network (ANN) can efficiently perform each Genetic Algorithm (GA) optimization

to determine the maximum power and its related operating state in less than one second on a single node. This node is outfitted with an Intel (R) Core (TM) i5-7500 CPU E5-2620 3.40 GHz processor and 64 GB of RAM. Its high computing efficiency makes it ideal for rapidly controlling PEM fuel cells in real-world applications.

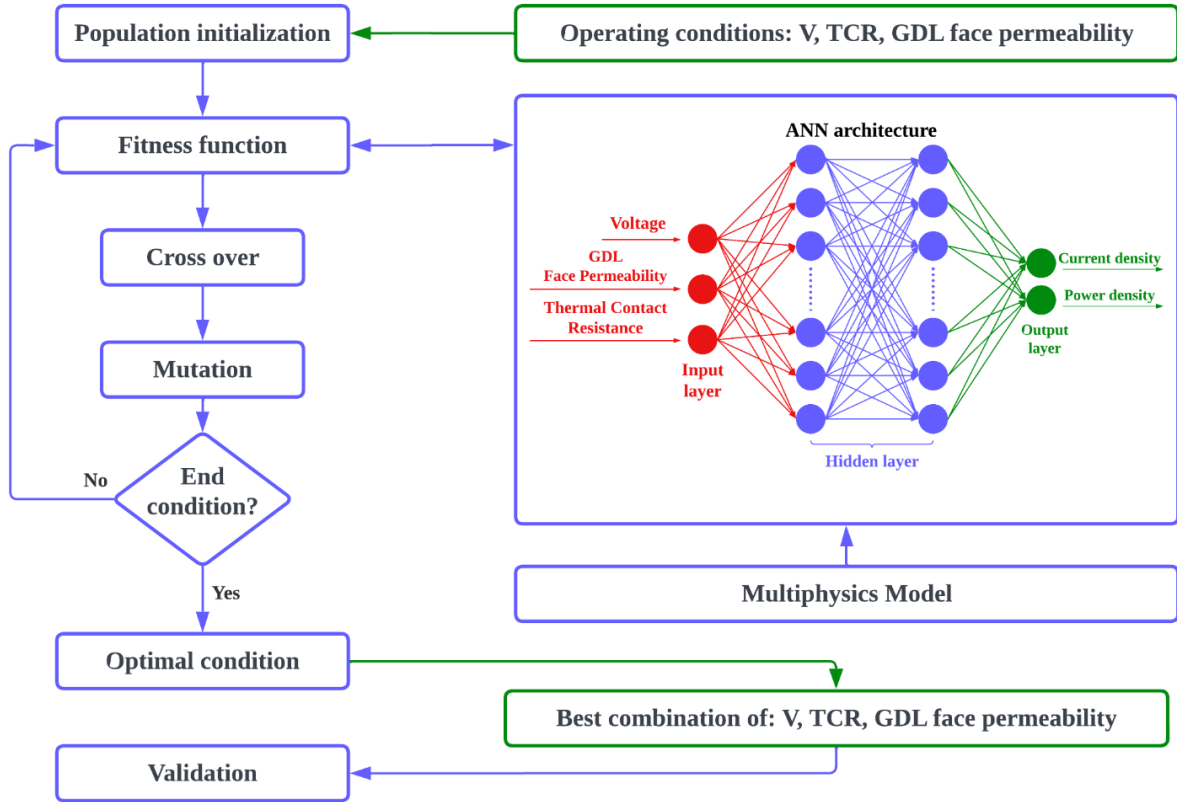


Fig. 4.7. Combined ANN and GA optimization using 3D multiphysics simulation.

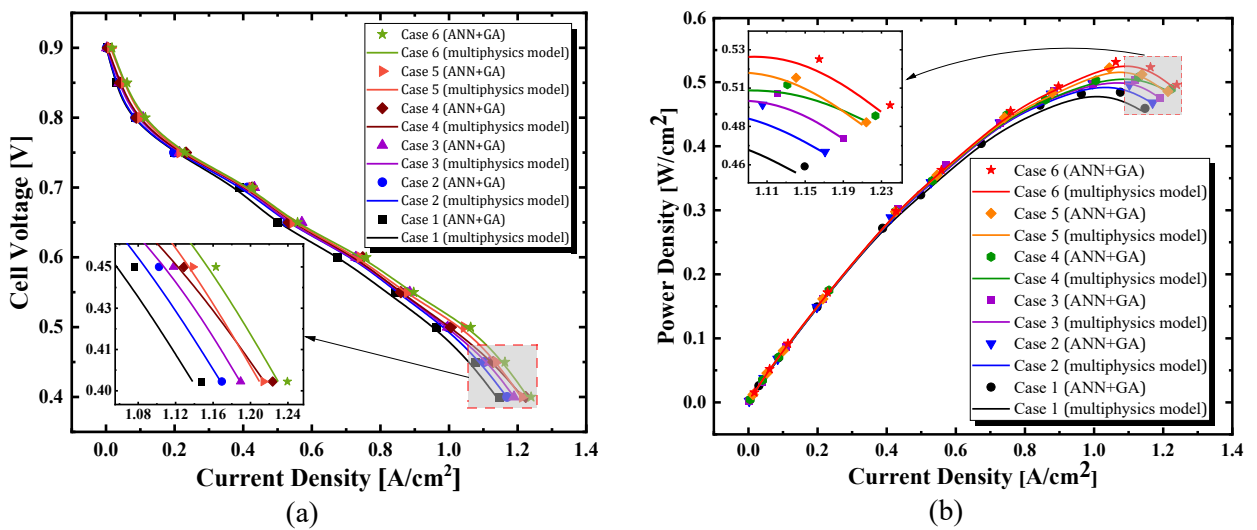


Fig. 4.8. (a) Current density and (b) power density curves with ANN-GA optimization models in different cases (operating temperature $T = 70^{\circ}\text{C}$ (343.15K); operating pressure = 1 atm).

To verify the accuracy of the findings achieved by the Artificial Neural Network-Genetic Algorithm (ANN-GA) method, the simulation outcomes of the 3D multiphysics model are displayed in Fig. 4.8. (a-b). Fig. 4.8. (a) shows the curves representing the current density, whereas Fig. 4.8. (b) presents a comparison of the power density curves for six different scenarios, all conducted using the provided parameters. The alignment between the two forecasts is apparent as it involves achieving the maximum achievable power in both systems. The proposed ANN-GA method provides a quick reference for determining the maximum power and optimal operating conditions in the design of real PEM fuel cell systems. This method takes into account both the appropriate thermal contact resistance (TCR) and gas diffusion layer (GDL) face permeability which results are in line with the prior study conducted by Wang et al. [81]. The maximum power is of great significance in numerous applications.

4.3. Oxygen mass fraction

At a cell voltage of 0.4 V, the contour of the oxygen mass fraction at the x-y planes inside the fuel cell is depicted in Fig. 4.9. This contour is shown through the z-axis, which represents the gas flow for six different combinations of conditions. At the x-y planes of the fuel cell, the oxygen mass fraction decreases in the z-direction (the cathode flow channel) until it reaches the outflow of the flow channel in every single scenario that was investigated. Additionally, the oxygen mass fraction is depicted along the centerline of the interface between the cathode catalyst layer and the cathode gas diffusion layer within the cathode channel in Fig. 4.10 at a cell voltage of 0.4 V was used to measure this depiction, which corresponds to six different cases. Up until around 5 millimeters of channel length, the oxygen mass fraction at the inlet is quite comparable for all cases. After that point, the variances become more clearly apparent. Because of the oxygen consumption that is brought about by the oxygen reduction reaction (ORR) that occurs within the CCL, the oxygen mass fraction gradually decreases until it reaches the end of the flow channel. Previous research carried out by Zhang et al. [47] is in agreement with the outcomes of these results. It is also possible that this indicates that the inclusion of GDL face permeability and TCR for all cases (with the exception of case 1) has a beneficial impact on the charger transfer and ORR rate increase of the CCL. The case 1 scenario, on the other hand, is the one that has the lowest O₂ mass fraction and the GDL face permeability, and it does not take into account TCR. In

light of this, the oxygen mass fraction is improved by 6.58 percent in comparison to case 1 (original model).

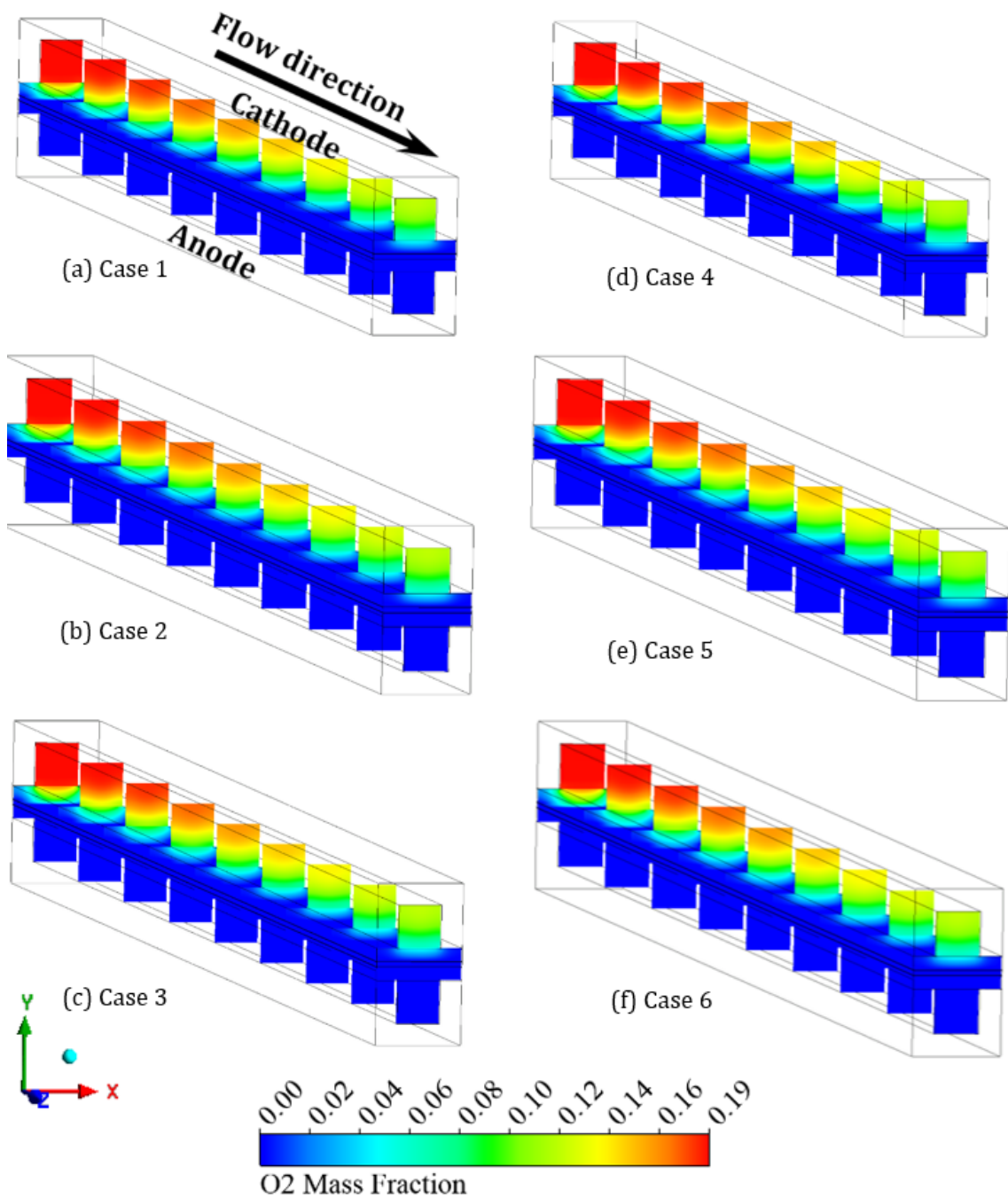


Fig. 4.9. The distribution of oxygen mass fraction in the x-y planes of the fuel cell through the z direction (gas flow) for six different cases at 0.4V cell voltage.

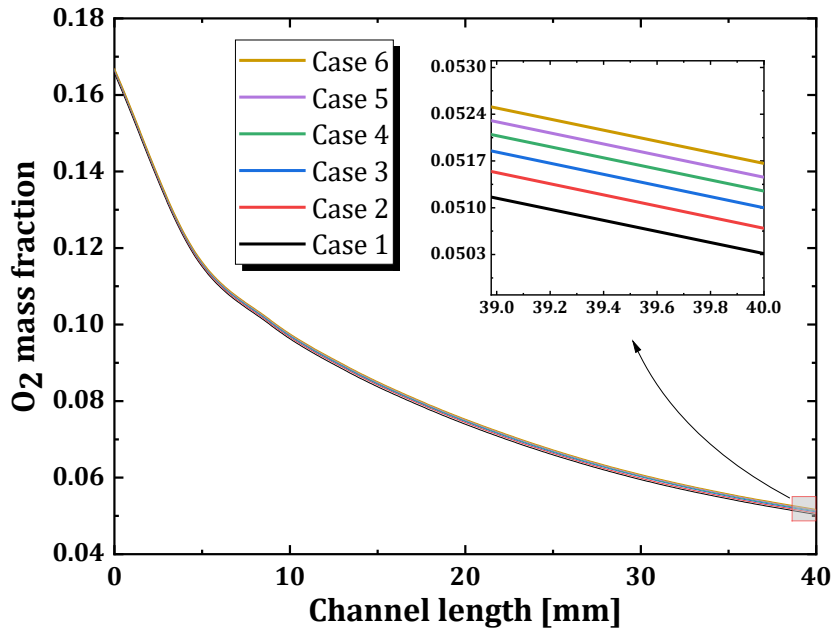


Fig. 4.10. The mass fraction of O_2 on the centerline of the interface between CGDL and CCL is examined for six cases at 0.4 V of a cell voltage.

4.4. Hydrogen mass fraction

Fig. 4.11. (a-f) illustrates the distribution of hydrogen mass fraction in the anode flow channel for six different scenarios at a cell voltage of 0.4 V. The hydrogen is introduced into the anode through the lower part and departs through the lower part of the anode flow channel. It is evident that the hydrogen mass fraction exhibits a progressive increase, indicating a corresponding gradual increase in the rate of hydrogen consumption for the electrochemical reaction. Furthermore, Fig. 4.12 illustrates the proportion of hydrogen mass along the central axis of the interface between ACL and AGDL in six different situations at a cell voltage of 0.4 V. The consumption of hydrogen caused by the hydrogen oxidation reaction (HOR) in the ACL and AGDL downstream of AFC leads to a gradual decrease in hydrogen mass fractions along the channel length (z-direction). This trend is consistent with the findings of a previous study [100]. Initially, the hydrogen mass fractions in the channel exhibit slight variations, with values below 0.27. Subsequently, there is a significant surge in the disparity values as a result of hydrogen consumption, and the impacts of gas diffusion layer (GDL) face permeability and thermal contact resistance (TCR) are taken into account. Among all situations when GDL face permeability and TCR are not included, Case 1 exhibits the lowest value of hydrogen mass fraction, while Case 6 has the highest value. This can be interpreted as a significant increase in GDL face permeability and TCR values, which are

being used to enhance hydrogen consumption and reduce excess fuel (hydrogen) in fuel cell electrodes.

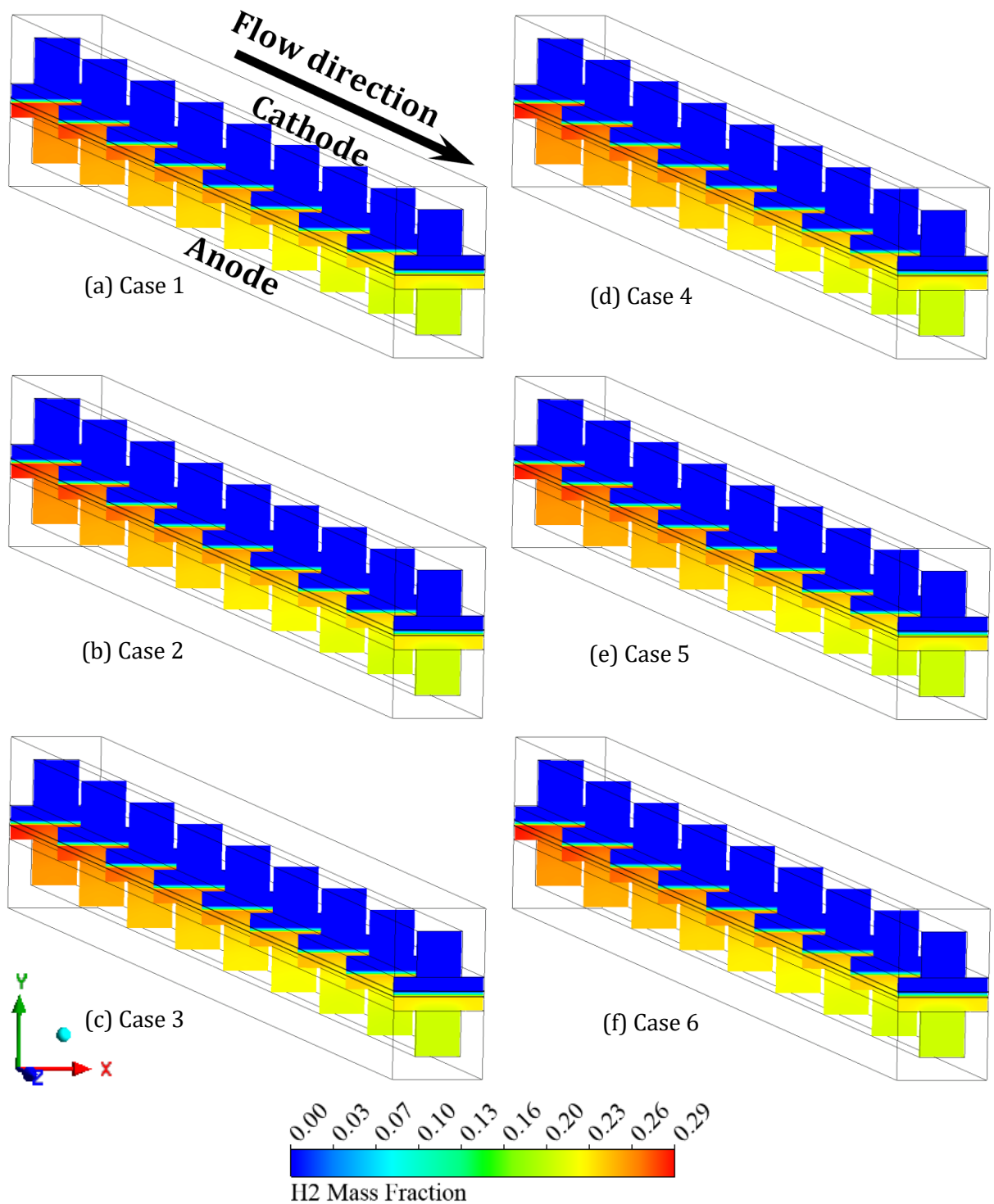


Fig. 4.11. The contours of H₂ mass fraction at the x-y planes inside the fuel cell through the z (gas flow) at 0.4 V cell voltage for six various scenarios.

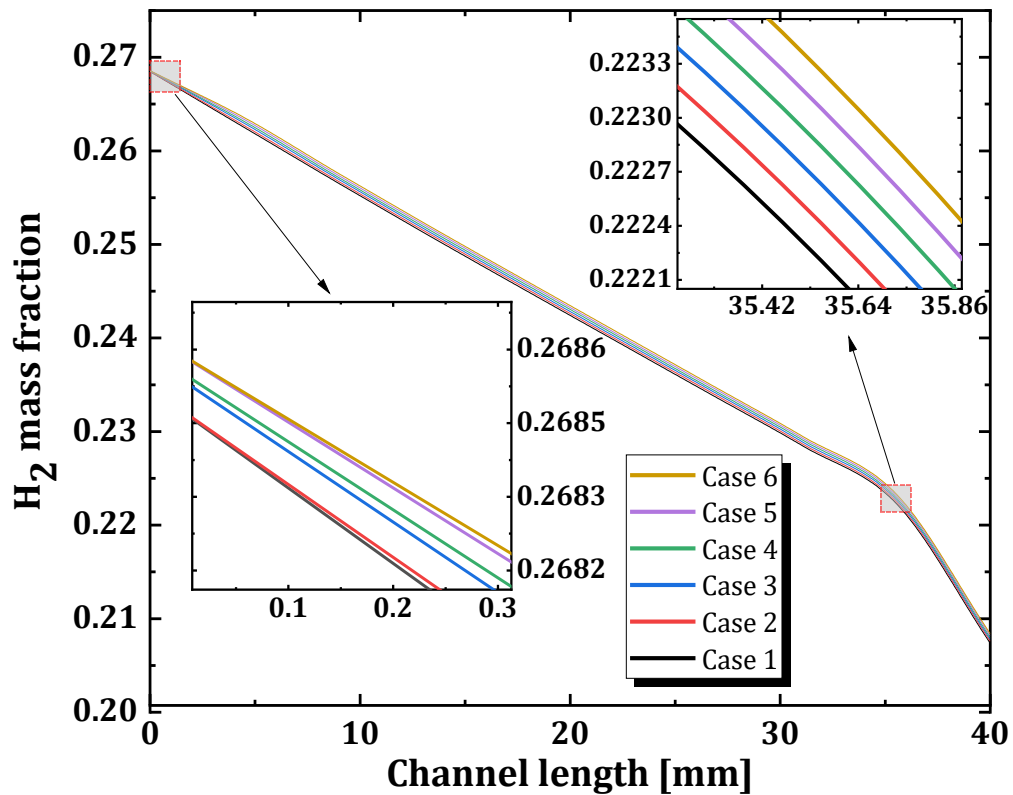


Fig. 4.12. Mass fraction of H₂ along the centerline of the interface between the ACL and the AGDL in the anode channel at 0.4 V of cell voltage for six cases.

4.5. Water mass fraction

The transportation of liquid water in the Gas Diffusion Layer (GDL) is mainly affected by capillary pressure and the strong adherence of the solid structures to liquid water, as opposed to the migration of water vapor [101]. The Leverett-J equation can be used to determine the local capillary pressure in the Gas Diffusion Layer (GDL) related to the local water saturation. An increase in water saturation levels in hydrophobic gas diffusion layers (GDLs) leads to a rise in capillary pressure. This phenomenon enables liquid water to flow from areas with greater saturation levels to areas with lower saturation levels. Darcy's law considers both of these adhesion mechanisms. Nevertheless, liquid water can be affected by the resistance caused by the movement of gas, the consequences of water vapor changing

from one phase to another, as well as its inertia and viscosity, all in line with the concept of continuity.

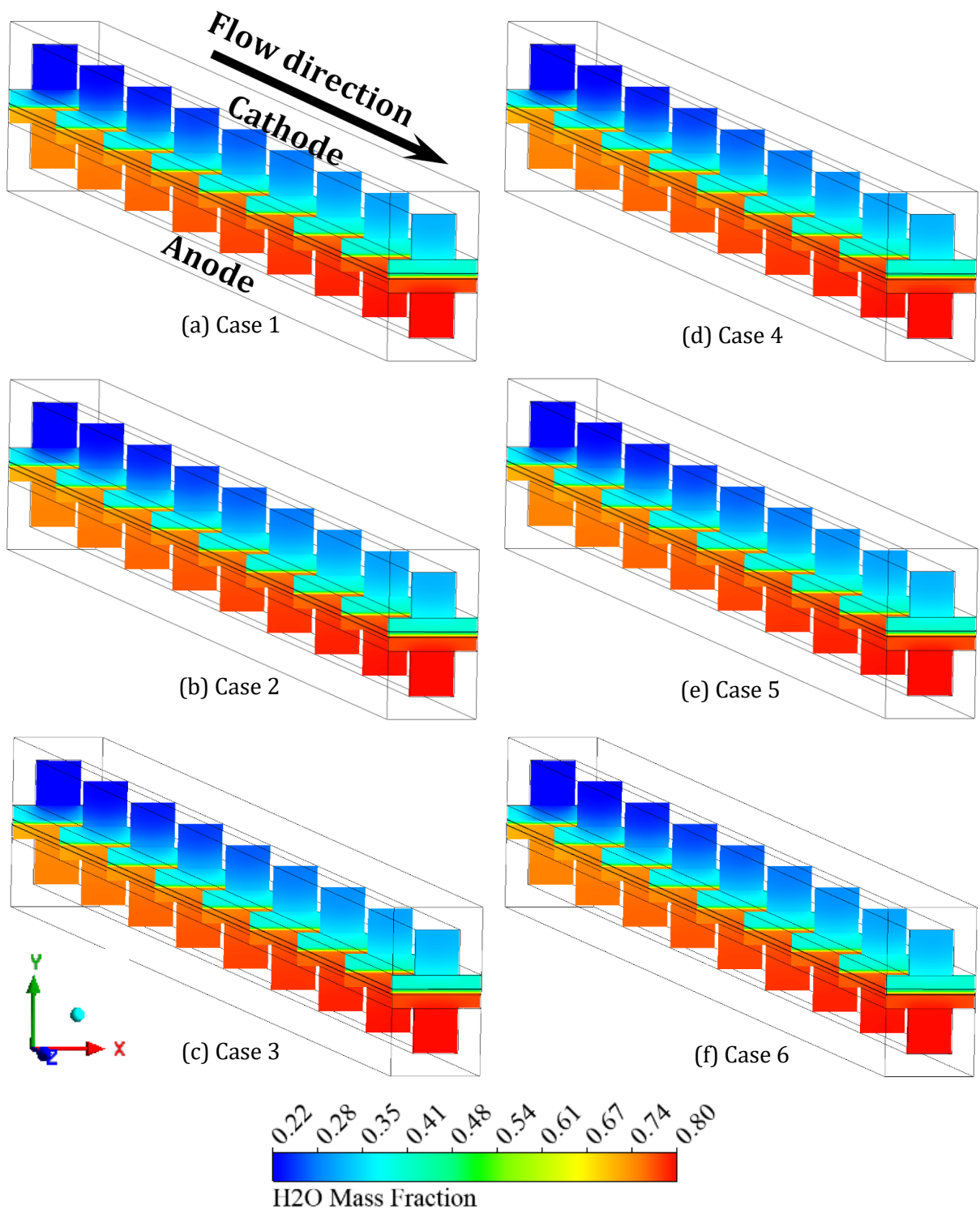


Fig. 4.13. For six different cases, the contours of water mass fraction at the x-y planes inside the fuel cell at 0.4 V cell voltage along the z (gas flow).

Fig. 4.13. depicts the contours of water mass fraction on the x-y planes within the fuel cell along the z-axis, which represents gas flow. The figure shows six different situations at a cell voltage of 0.4 V. The measured trend shows a consistent rise in the proportion of water in the channel. This is caused by the reaction between oxygen and hydrogen at the CCL and CGDL interface. Moreover, Fig. 4.14 illustrates the proportion of H₂O on the center axis of the interface between CFC and CGDL across the cathode channel for different scenarios at a cell voltage of 0.4 V. The accumulation of water mass fraction at the interfaces of the gas diffusion layer (CGDL) and the cathode catalyst layer (CCL) in the downstream region of the flow channel is caused by the gas flow within the flow channel [102]. Introducing the Forchheimer inertial coefficient has led to a new effect in the non-linear wave motion of multiphase deformable porous media. As a result, the water mass fraction in the inlet channel increases steadily from 0.24 to 0.29 over a distance of 5 mm. Then, it increases exponentially to approximately 0.38 for the rest of the channel.

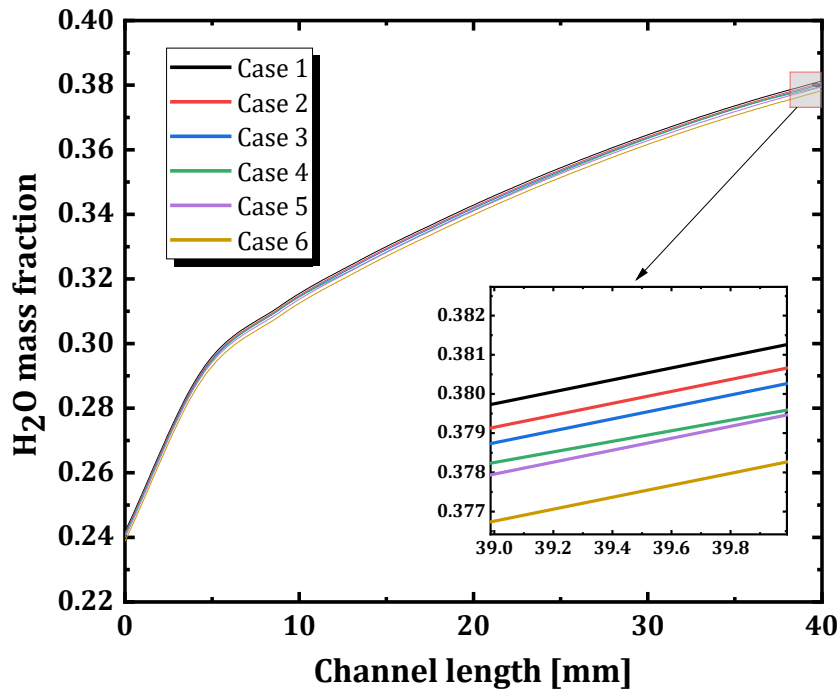


Fig. 4.14. The mass fraction of H₂O on the centerline of the interface between CGDL and CFC across the cathode channel is examined for numerous scenarios at a cell voltage of 0.4V.

When taking into account both thermal contact resistance and GDL face permeability, it becomes clear that they can reduce the water mass fraction. This is demonstrated in Fig. 4.14, where cases 2 through 6 exhibit lower values compared to case 1. Thus, the combination of

GDL face permeability and TCR efficiently reduces water formation. Simultaneously, the surplus oxygen in the cathode flow channel decreases due to the consumption of reactants in the electrochemical reaction, which helps prevent flooding in the CGDL.

4.6. Velocity magnitude and cathode pressure drop

This section examines the velocity and pressure of oxygen at the interface between CGDL and CFC in the cathode channel for six cases, with a cell voltage of 0.4 V. The corresponding figures, Fig. 4.15 and Fig. 4.17 provide visual representations of the data. As depicted in Fig. 4.15, the velocity of oxygen diffusion experiences a significant increase as it moves along the channel, reaching its peak at 5 mm of the channel length, which is approximately $2.7\text{E-}3 \text{ m}\cdot\text{s}^{-1}$. After reaching this point, it stabilizes and decreases as oxygen becomes more involved in a chemical reaction. This causes the oxygen to remain in the diffusion layer along the channel length until it reaches the end. This trend is supported by a previous study [93]. Overall, the GDL face permeability and TCR for case 2 to case 6 exhibit higher velocity values compared to case 1, resulting in a partial improvement in performance.

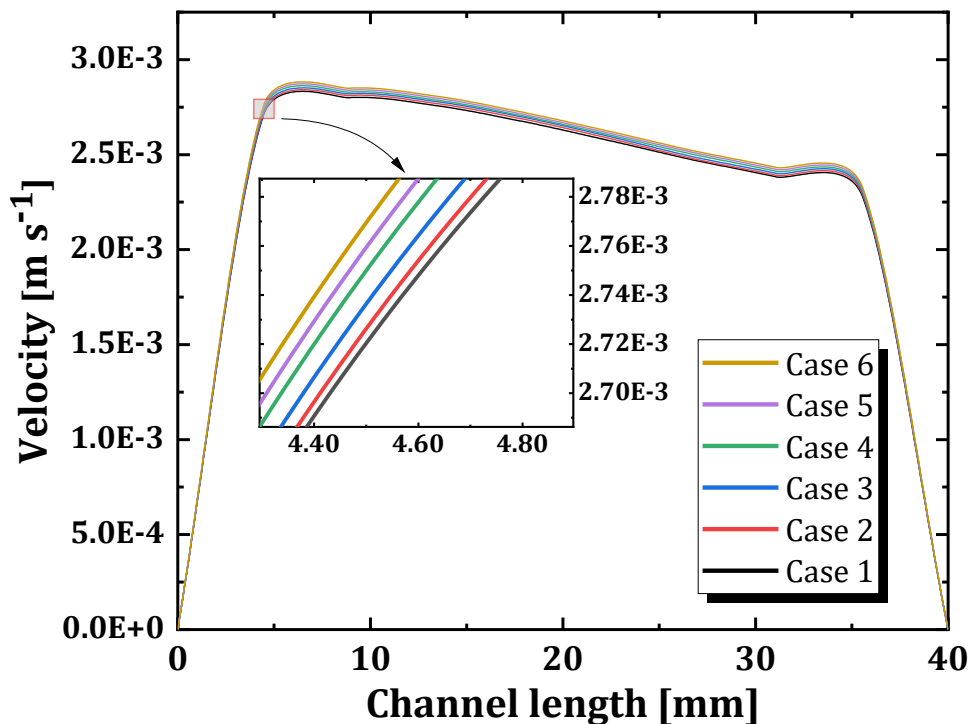


Fig. 4.15. The velocity of oxygen at the centerline of the interface between CGDL and CFC through the cathode channel is examined for distinct scenarios at a cell voltage of 0.4

V.

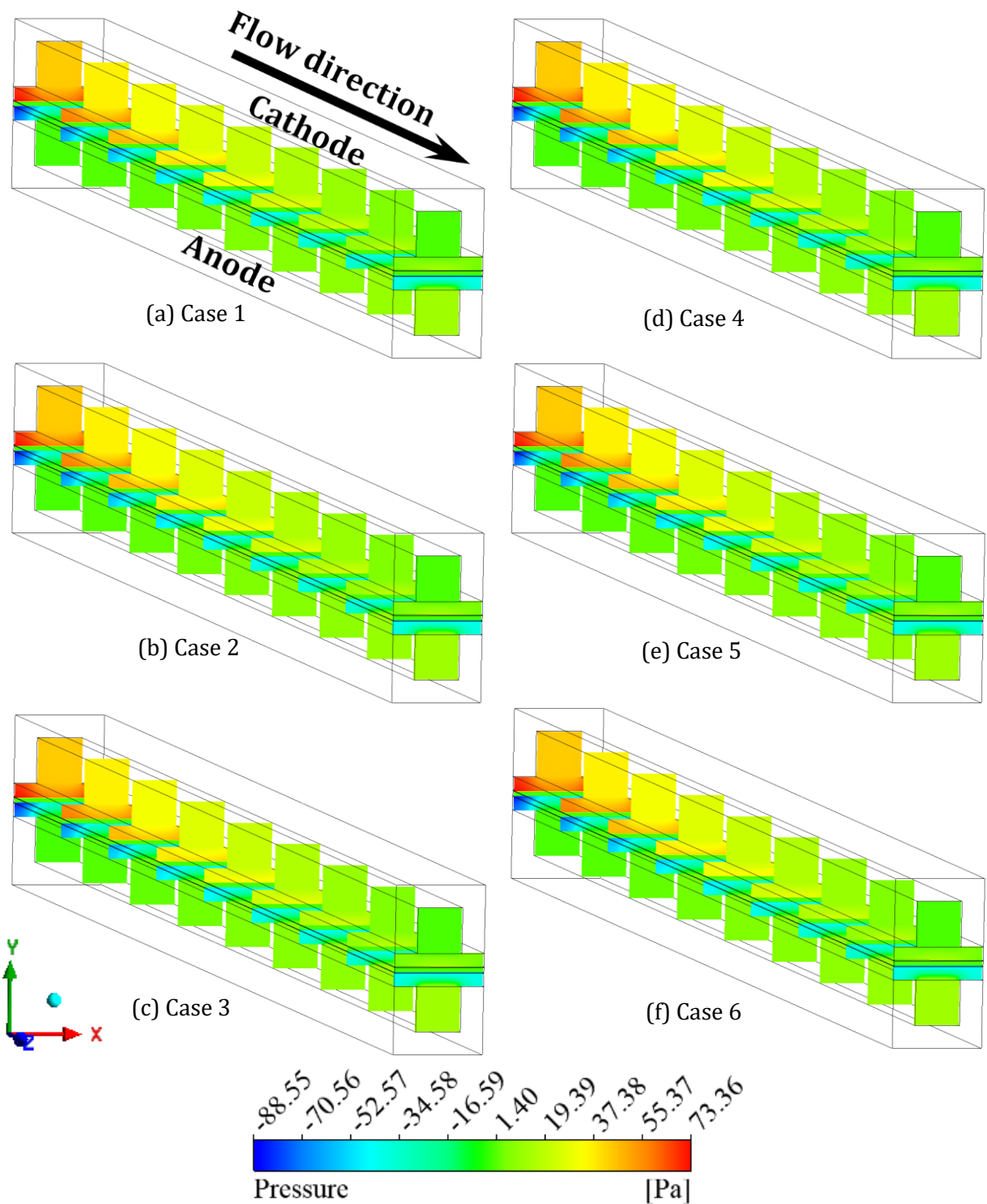


Fig. 4.16. The pressure distributions at the x-y planes inside the fuel cell through the z-axis (representing gas flow) are examined at a cell voltage of 0.4 V for six cases.

Fig. 4.16 shows the pressure profile within the fuel cell at different points along the flow channel for six distinct scenarios, all at a cell voltage of 0.4 V. Thanks to the decreased pumping work required to deliver reactants to fuel cells, a noticeable increase in pressure

can be observed near the intake CFC and CGDL. This pressure gradually decreases along the length of the channel, resulting in improved energy efficiency for fuel cells.

Furthermore, Fig. 4.17 illustrates the decrease in pressure from 55 Pa to 13 Pa along the centerline of the interface between CGDL and CFC in the cathode channel under different conditions at a cell voltage of 0.4 V. Throughout the channel, and there is a noticeable decrease in pressure drop. On the other hand, Case 1 shows the lowest pressure drop, as it does not consider GDL face permeability and TCR. In conclusion, it suggests that GDL face permeability and thermal contact resistance play a significant role in improving the performance of PEM fuel cells and optimizing the use of fuels for chemical reactions.

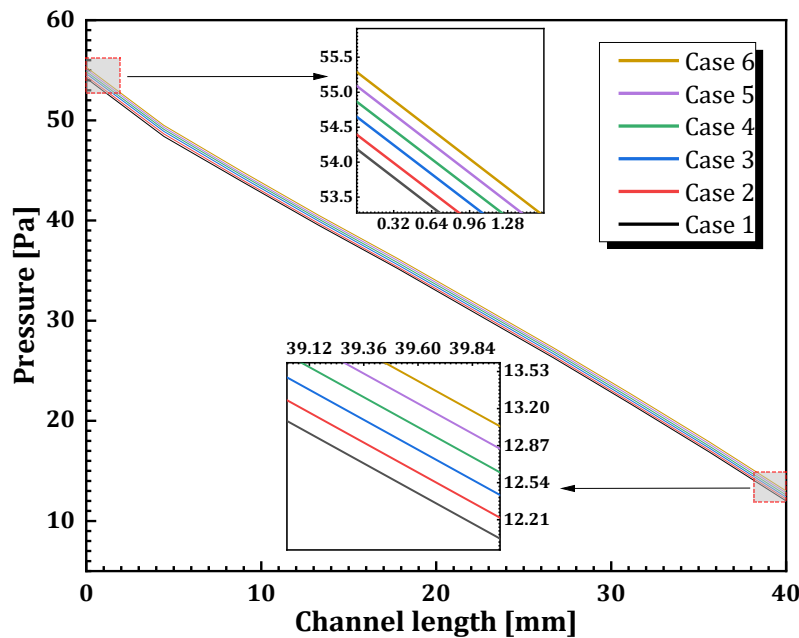


Fig. 4.17. The pressure on the centerline of the interface between CGDL and CFC along the cathode channel is examined for different scenarios at 0.4 V of a cell voltage.

4.7. Summary

This study utilizes a non-isothermal computational model for fuel cells, specifically focusing on a PEM fuel cell's temperature profiles, mass transport, and cell performance. The investigation also considers the impact of TCR and GDL face permeability on cell performance. This model's TCR and GDL face permeability is determined by comparing the calculated temperature changes between the flow plate and the cathode electrode with experimental data. This comparison results in an acceptable agreement. The numerical model is employed to examine the influence of different TCR and GDL face permeability

strategies on heat dissipation and the performance of a PEM fuel cell. From the computational results and debates presented above, we can derive the subsequent conclusions:

1. The TCR and GDL's permeability considerably impacts both the ideal temperature and the temperature distribution of the electrode. The temperature near the membrane electrolyte assembly (MEA) is elevated compared to other regions. When considering the permeability of the TCR and GDL faces, there is a noticeable increase in the ideal cell temperature by approximately 1.5°C at 0.4 V. Additionally, the temperature profiles show a characteristic "Λ" shape.
2. In order to enhance the accuracy of temperature profiles and forecasts of cell performance, it is crucial to consider the influence of thermal contact resistance (TCR) and Gas Diffusion Layer (GDL) face permeability. In the sixth scenario, the permeability values for TCR and GDL are calculated to be 1.00E-01 m²•K/W and 3.50E12 m⁻², respectively. In addition, in case 6, there was an 8.72% enhancement in cell performance compared to the original model (case 1).
3. In case 6, the thermal contact resistance and GDL face permeability influence the velocity and oxygen mass fraction. Specifically, compared to case 1, there is a 1.91% increase in velocity and a 6.58% rise in oxygen mass fraction. Furthermore, the pressure differential in example 6 is 3.11% greater than in case 1.
4. The pressure diminishes progressively as one descends the channel. Moreover, when the cell voltage is 0.4 V, the pressure in the cathode channel reduces from around 55 Pa to 13 Pa in different situations that involve CFC and CGDL at the interface.
5. The numerical investigations yielded valuable insights for enhancing fuel cells' oxygen transport and water removal. In addition, they aid in achieving a more even dispersion of oxygen and current densities by considering the TCR and chosen GDL face permeability. Furthermore, considering the thermal contact resistance (TCR) and selecting a suitable gas diffusion layer (GDL) with high permeability typically leads to lower dissolved water in the cathode catalyst layer, ultimately enhancing the cell's performance.
6. In addition, the ANN-GA approach was used to determine the maximum power densities achievable in six distinct cases. These discoveries are crucial for developing and effectively supervising fuel cell systems.

5. TAPERED FLOW FIELD CONFIGURATION TO IMPROVE MASS TRANSPORT AND PERFORMANCE OF PROTON EXCHANGE MEMBRANE FUEL CELL

In the continual effort to investigate the effect of tapered flow field configurations on bipolar plates of PEM fuel cell mass transport and cell performance enhancement, this part presents the effect of tapered flow field configuration considering the porous medium thickness (PMT) and thermal contact resistance (TCR) on overall cell performance, temperature distributions, mass transport distributions (oxygen and hydrogen mass fractions), water mass fraction, osmotic-drag coefficient, gas velocity, and pressure drop.

5.1. Effect of tapered PEM fuel cell model on overall cell performance

Through the application of a tapered flow field configuration, one can explore the optimal performance based on the chosen model. Fig. 5.1 and Fig. 5.2 showcase the polarization and power density curves for various tapered parallel flow field channels (FFCs) with different $L_{I/O}$ ratios, respectively. The figures illustrate the FFCs, considering the impact of the TCR and the PMT, without considering these effects. When comparing conventional parallel flow field channels (FFCs) with different tapered parallel FFCs, there is a significant difference in the polarization and power density curves. This is because of the variation in the $L_{I/O}$. When the $L_{I/O}$ is reduced, the output cell voltage and power density of various tapered parallel FFCs decrease, regardless of considering the TCR and PMT. This phenomenon becomes more pronounced when operating at higher current densities. The observed phenomenon can be explained by the increased interaction between the bipolar plates (BPs) and gas diffusion layers (GDLs), resulting in a decrease in the interaction between the catalyst layers (CHs) and GDLs. This, in turn, obstructs the ideal route for reactant transportation from the CHs to the GDLs. Based on the results, it seems that using a parallel flow field channel (FFC) with a tapered design, where the channel width decreases from the inlet to the outlet, negatively affects the cell's performance. When examining different tapered parallel FFCs, if we ignore the TCR and the PMT (for case number 1 $L_{I/O}$ 0.7), we can see that the cell's performance improves as $L_{I/O}$ increases. This improvement is due to the increased contact area between CHs and GDLs, resulting in enhanced reactant transport.

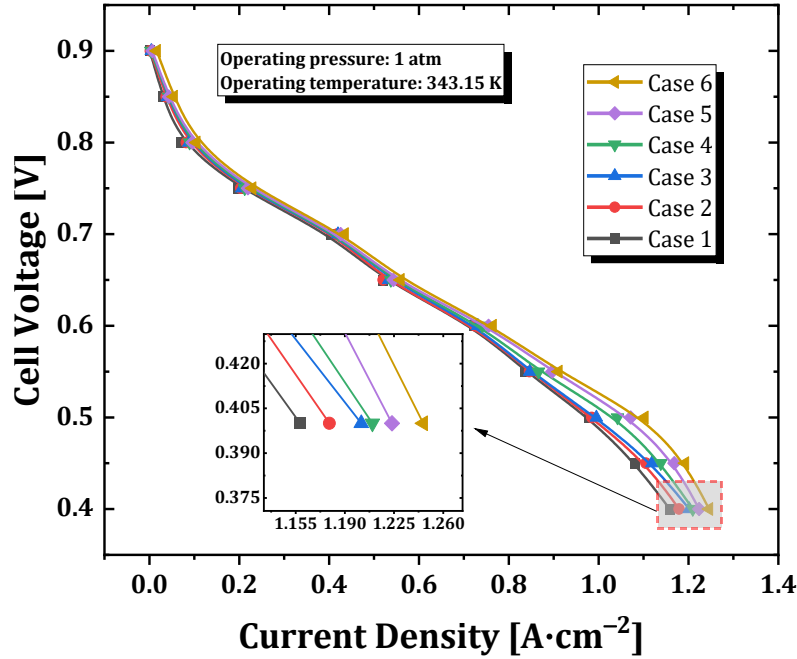


Fig. 5.1. Polarization curves for various tapered parallel FFC models.

Higher $L_{I/O}$ ratios in CN5 ($L_{I/O}$ 1.1) and CN6 ($L_{I/O}$ 1.2) lead to improved cell performance, as both the PMT and TCR are higher compared to the conventional parallel model mentioned in previous research [90]. Fig. 5.1 shows that the maximum current density of case 1 is the lowest among all the cases, measuring at 1.158 A/cm^2 . In contrast, case 6 demonstrates the highest current density outcome, measuring at 1.246 A/cm^2 . This value is 0.0877 A/cm^2 or 7.57% higher than case 1 at 0.4 V. In addition, Fig. 5.2 illustrates the power density curve for six different scenarios. Upon examination, it is evident that the lowest peak power density in case 1 is 0.489 W/cm^2 , while the highest peak power density in case 6 is 0.551 W/cm^2 . This signifies a disparity of 0.0618 W/cm^2 (equivalent to a percentage increase of 12.63%) when compared to case 1. These findings suggest that considering both the PMT and the TCR between the gas diffusion layer (GDL) and the current collector can improve the performance of PEMFC. The explanation lies in the balance between mass transport, water removal, TCR, and PMT resulting from the differences in $L_{I/O}$ for various tapered parallel FFCs. A parallel FFC with a reversed taper and a slightly higher $L_{I/O}$ ratio can positively impact cell performance. This conclusion is consistent with the mass transport characteristics, including the mass transfer as the result of the increasing flow field cross-sectional area, as previous research [67], [103], [104]. It is essential to consider the TCR and PMT between BPs and GDLs for tapered parallel FFCs in order to simulate cell performance accurately. Ignoring these factors can lead to tapered and misleading parallel FFC optimization.

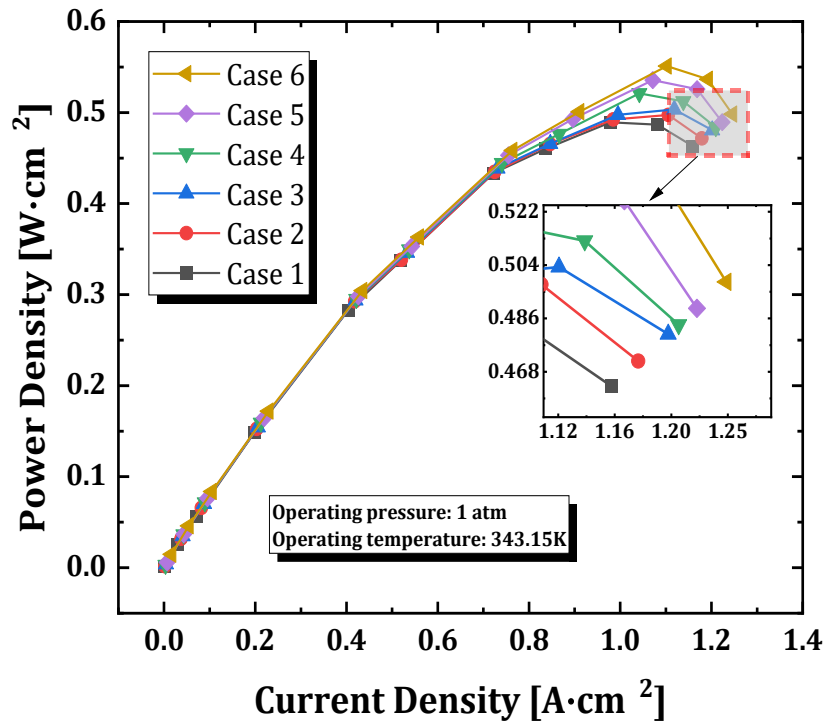


Fig. 5.2. Power density versus current density for various tapered parallel FFC models.

5.2. Temperature distributions with varying tapered flow field configuration

An output cell voltage of 0.4 V is depicted in

Fig. 5.3., showing the temperature distributions corresponding to the various case models. The rib, the channel, and the MEA regions all have distinct temperatures, with the temperature under the rib being lower than the temperature under the channel. Furthermore, the temperature beneath the channel rises when one moves further away from the channel. The heat generated in the electrode is predominantly dispersed from the rib area through heat conduction, which is made possible by the significantly low velocity present in the porous gas diffusion layer (GDL). This is the conclusion that can be drawn from this observation. In addition, it is noticed that the maximum temperature of the cell increases in parallel with the increase in the PMT and TCR values. This is something that can be witnessed visually. The increase in heat transfer resistance between the Gas Diffusion Layer (GDL) and the collector's rib due to thermal contact resistance (TCR) makes it more difficult for heat to be dissipated within the porous electrode. It has been noted that there are variations in temperature distributions with respect to the various TCR values. However, the temperature differential across the GDL and collector rib interface grows proportionally with TCR

augmentation, which has been demonstrated by works of literature [52, 53]. The study has found that the current collector is more successful at homogenizing the temperature. The TCR acts as a barrier to the dissipation of heat, which is one of the factors contributing to the behavior described above.

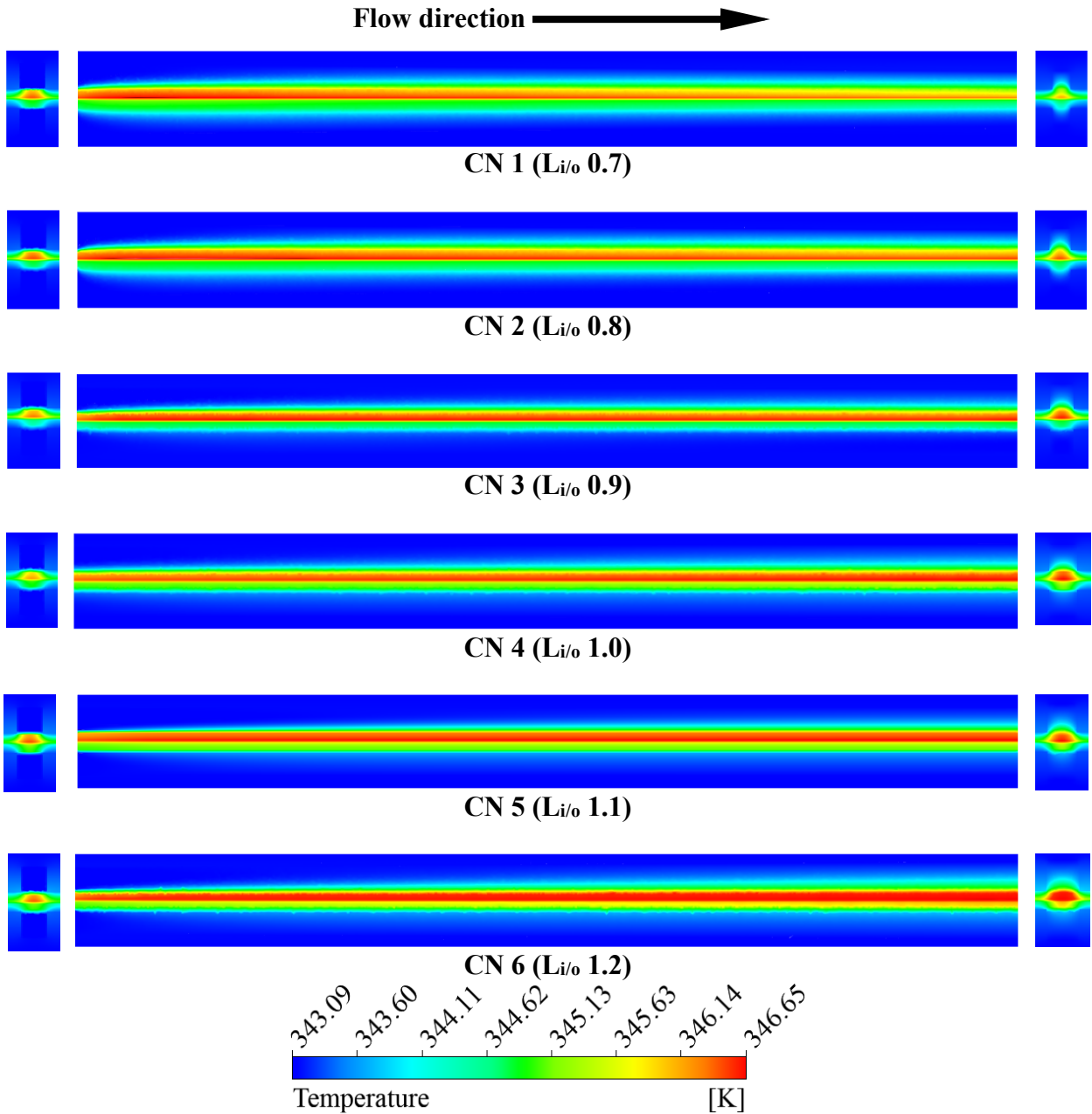


Fig. 5.3. The temperature distribution at left (inlet side), middle PEMFC (YZ-Plane), and right (outlet side) views along the CH for various cases at cell voltage 0.4 V.

5.3. Oxygen mass fraction and hydrogen mass fraction

The oxygen mass fraction distribution at the X-Y planes within the fuel cell along the Z direction (gas flow direction) are depicted in Fig. 5.4. This figure was created using a variety of tapered parallel fuel cell topologies at a cell voltage of 0.4 V. Because of the oxygen consumption that takes place as a consequence of the oxygen reduction reaction (ORR) that takes place in the CCL, the oxygen mass fraction in the X-Y planes of a fuel cell declines typically along the Z direction. This is because the CCL is responsible for the oxygen reduction reaction. As an illustration, CN6 possesses a significantly higher oxygen mass

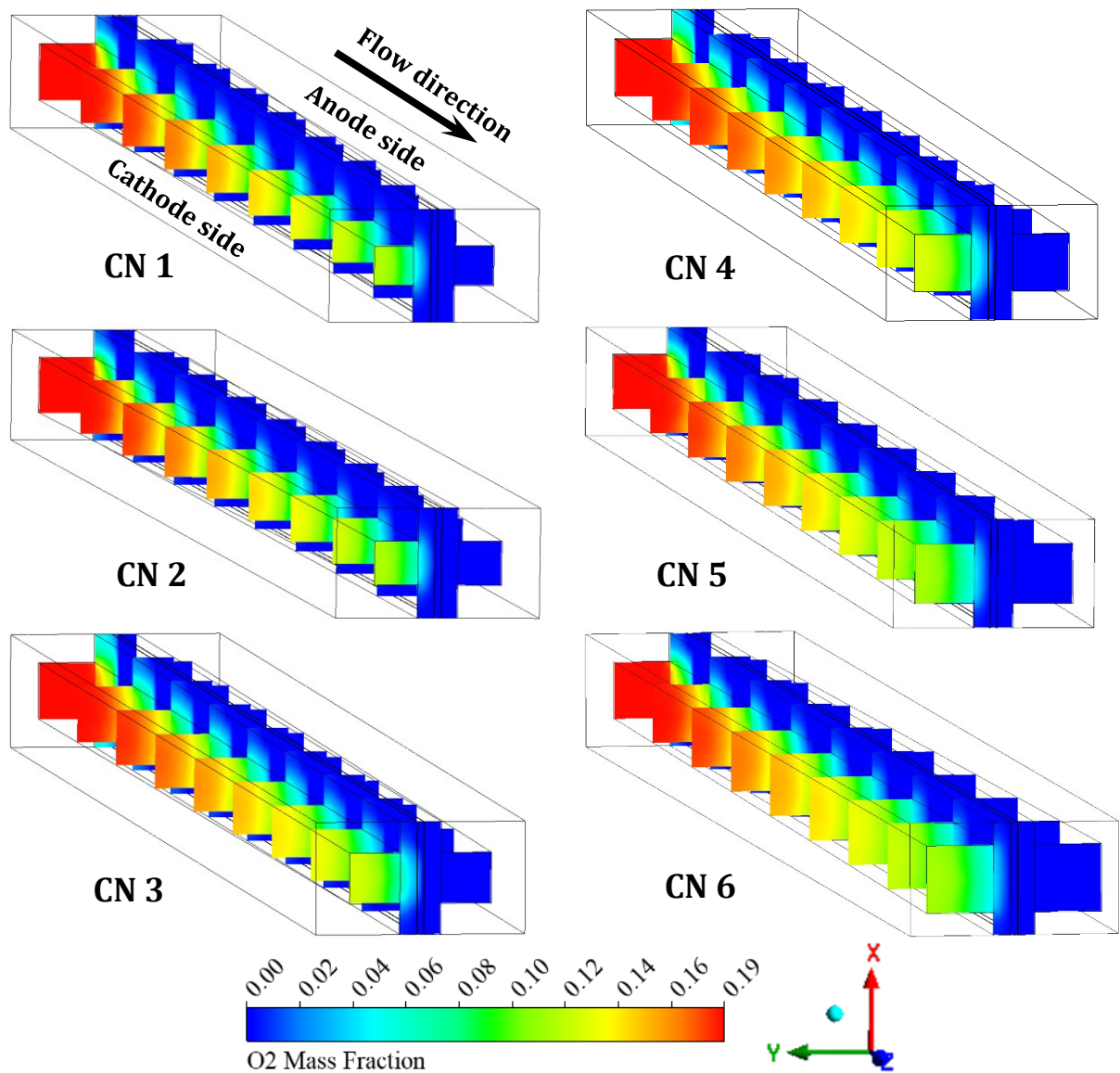


Fig. 5.4. Oxygen mass fraction distribution at the x-y planes within the fuel cell along the z (gas flow) direction for various cases at cell voltage 0.4 V.

fraction within the CGDL and CCL compared to other examples, as can be observed in Fig. 5.5. Another illustration of how a high oxygen mass fraction in the CGDL and CCL can generally be advantageous to the ORR rate in the CCL is provided by this particular instance. A more significant flow channel makes it possible for a more remarkable mass transfer of reactants, particularly oxygen, to the catalyst layer, which is one of the potential explanations for this phenomenon. Given this, there is a possibility that the restrictions of diffusion may be reduced, and the ORR rate will be accelerated. Previous studies have shown that a wider flow channel increases the likelihood that sufficient oxygen will reach the catalyst sites, which in turn leads to more effective reactions [20,21]. This phenomenon is a result of increased mass transfer. In addition, making the flow channel wider can make it simpler to remove water from the cathode side, which in turn reduces the risk of water collecting and impeding oxygen delivery pathways. A broader flow channel helps to maintain a more substantial oxygen mass fraction at the catalyst and gas diffusion layers. This is accomplished by improving water control, which in turn adds to water management.

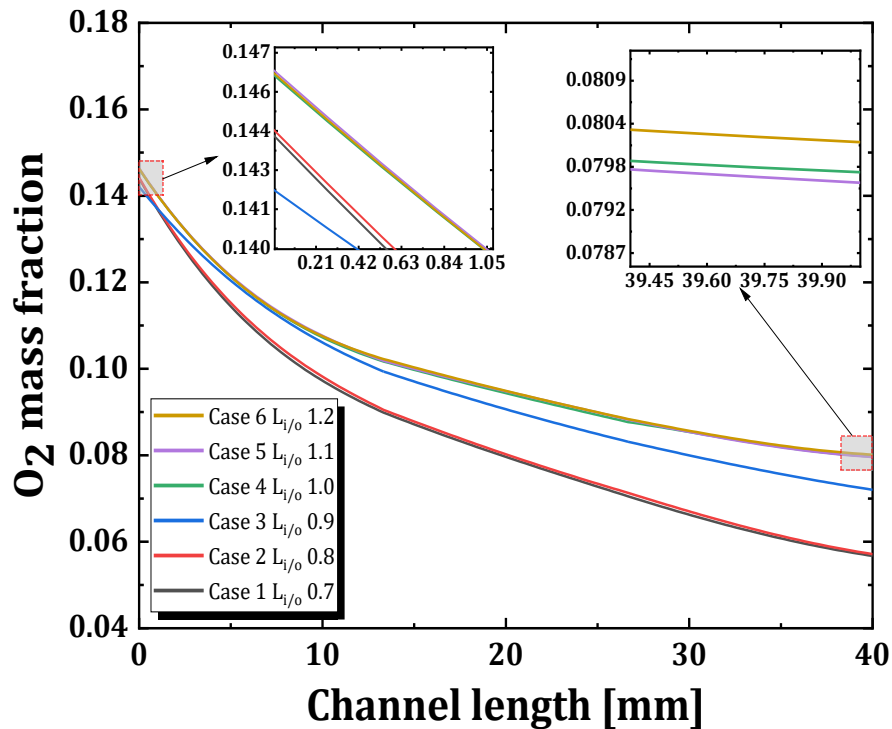


Fig. 5.5. Oxygen mass fraction on the centerline of the interface between CCL and CGDL along the cathode channel for various cases at a cell voltage of 0.4V.

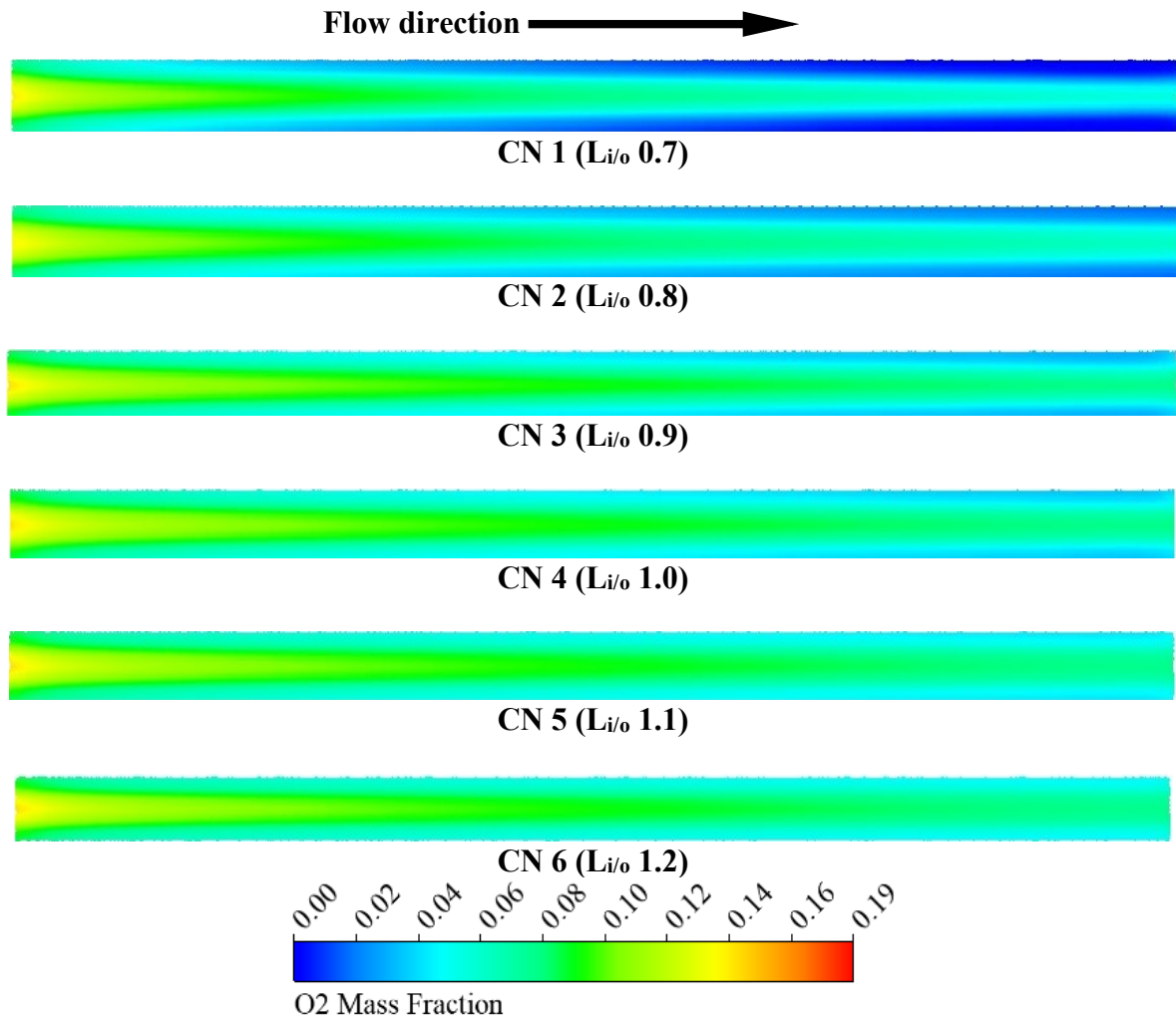


Fig. 5.6. O₂ mass fraction profiles at the interface between CCL and CGDL along the CH for various cases at cell voltage 0.4 V.

A representation of the oxygen mass fraction distribution along the channel is shown in Fig. 5.6. This illustration is located at the interface between the cathode catalyst layer (CCL) and the gas diffusion layer (CGDL). Because of the more extensive surface area at the bottom of the flow channel, a greater quantity of oxygen initially diffuses into the cathode gas diffusion layer (CGDL). This is possible because of the larger surface area. The improved convective flow in wider tapered channels, which was investigated in cases 4-6, makes it easier for more excellent oxygen to enter the cathode gas diffusion layer (CGDL). Consequently, case 6 has a superior performance compared to the other cases, which is in line with the results of simulations that have been published in the literature [13,14].

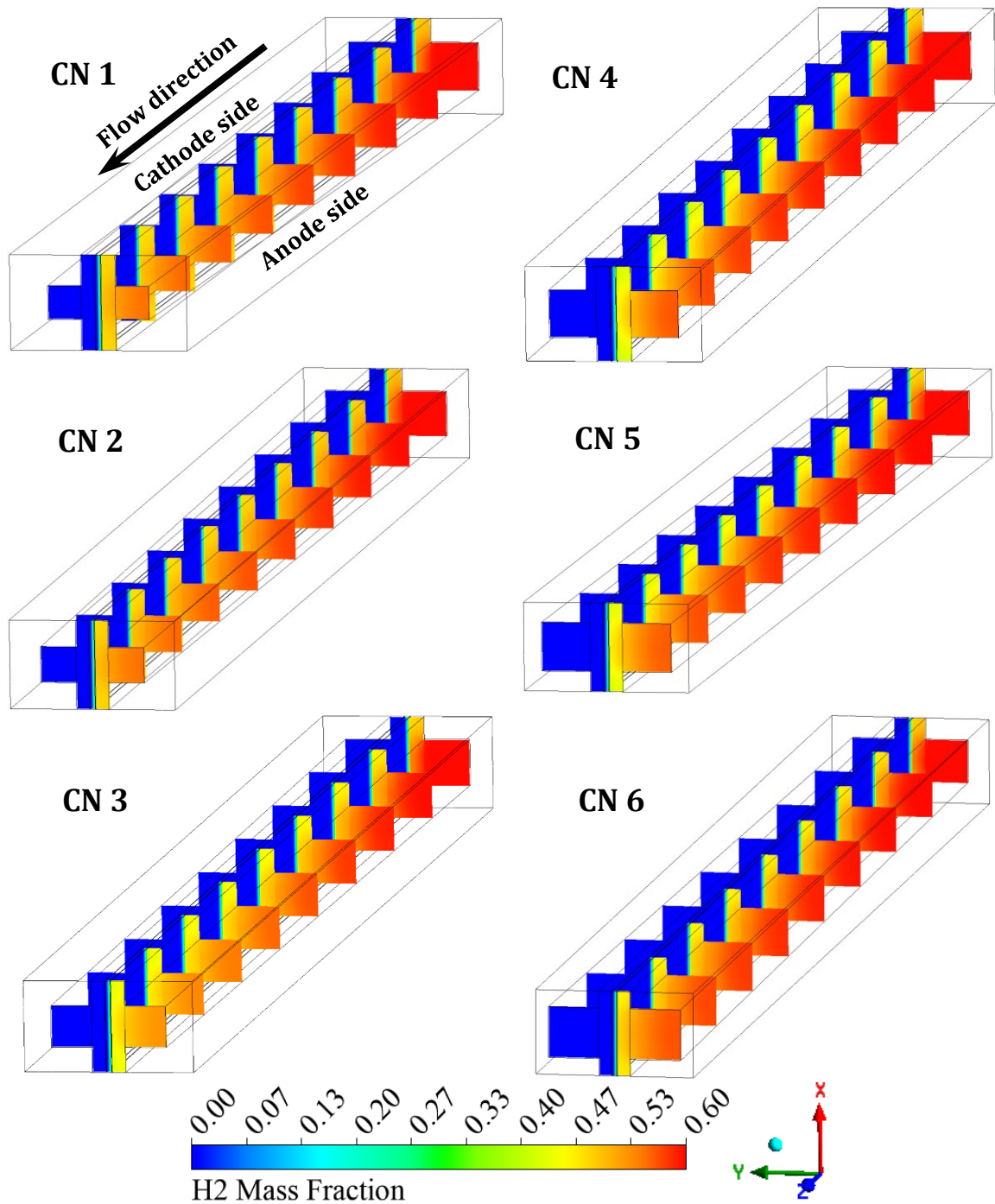


Fig. 5.7. For six distinct cases, the distributions of hydrogen mass fraction at the x-y planes within the fuel cell along the z (gas flow) at 0.4 V cell voltage.

At a cell voltage of 0.4 V, the hydrogen mass fraction profiles are depicted in Fig. 5.7. These profiles are shown at the x-y planes within the fuel cell along the z (gas flow) with six different scenarios. As a result of the hydrogen oxidation reaction (HOR) that took place within the anode catalyst layer (ACL), the hydrogen mass fraction showed a significant drop

along the gas channel in the flow direction across all of the model geometries. This is an indication that hydrogen reacted with the flow due to the decrease in the mass fraction of hydrogen detected. A more significant flow channel makes carrying hydrogen in greater quantities easier from the intake to the system's outlet. A decrease in flow resistance results from the increased cross-sectional area, making transporting hydrogen more uniformly and expediently possible. A higher proportion of hydrogen mass may be maintained at the anode catalyst layer and the gas diffusion layer due to the increased mass transportation, making it easier to keep this proportion.

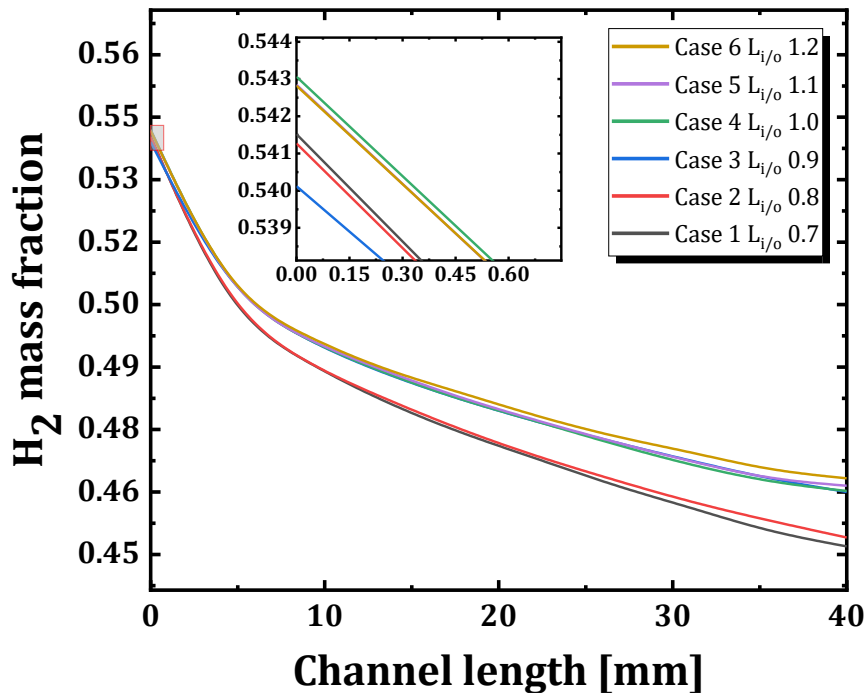


Fig. 5.8. H₂ mass fraction on the centerline of the interface between ACL and AGDL along the anode channel for various scenarios at a cell voltage of 0.4 V.

In Fig. 5.8, the hydrogen mass fraction on the centerline of the interface between the ACL and AGDL along the anode channel is depicted for a number of different scenarios where the cell voltage is only 0.4 V. The mass fraction of hydrogen was found to decrease in a linear fashion in every single instance along the anode channel. The value that is the lowest is found in case 1, and the value that is the greatest is found in case 6. This indicates that the thermal contact resistance and more prominent flow channel can have an effect on the number of mass fractions of hydrogen and offer adequate reactants to react with oxygen in order to create maximum performance, where these results can be consistent with research that has already been conducted [110].

5.4. Water mass fraction and osmotic drag coefficient

In order to keep their performance at its highest level, PEM fuel cells need to have adequate water management. This can help permit more excellent water removal from the cathode side, which in turn helps reduce flooding and enhance the transfer of protons. A wider flow channel can help support this. It is essential to have proper water management to keep the electrolyte's conductivity intact and make the ORR easier to perform. Fig. 5.9. illustrates the water mass fraction profiles at the interfaces of CCL and CGDL along the channel for a variety of scenarios, all while ensuring that the cell voltage remains at 0.4 V. It is believed that the movement of gas within the channel is responsible for the accumulation of liquid water at the interfaces that are located downstream of the channel. To be more specific, liquid

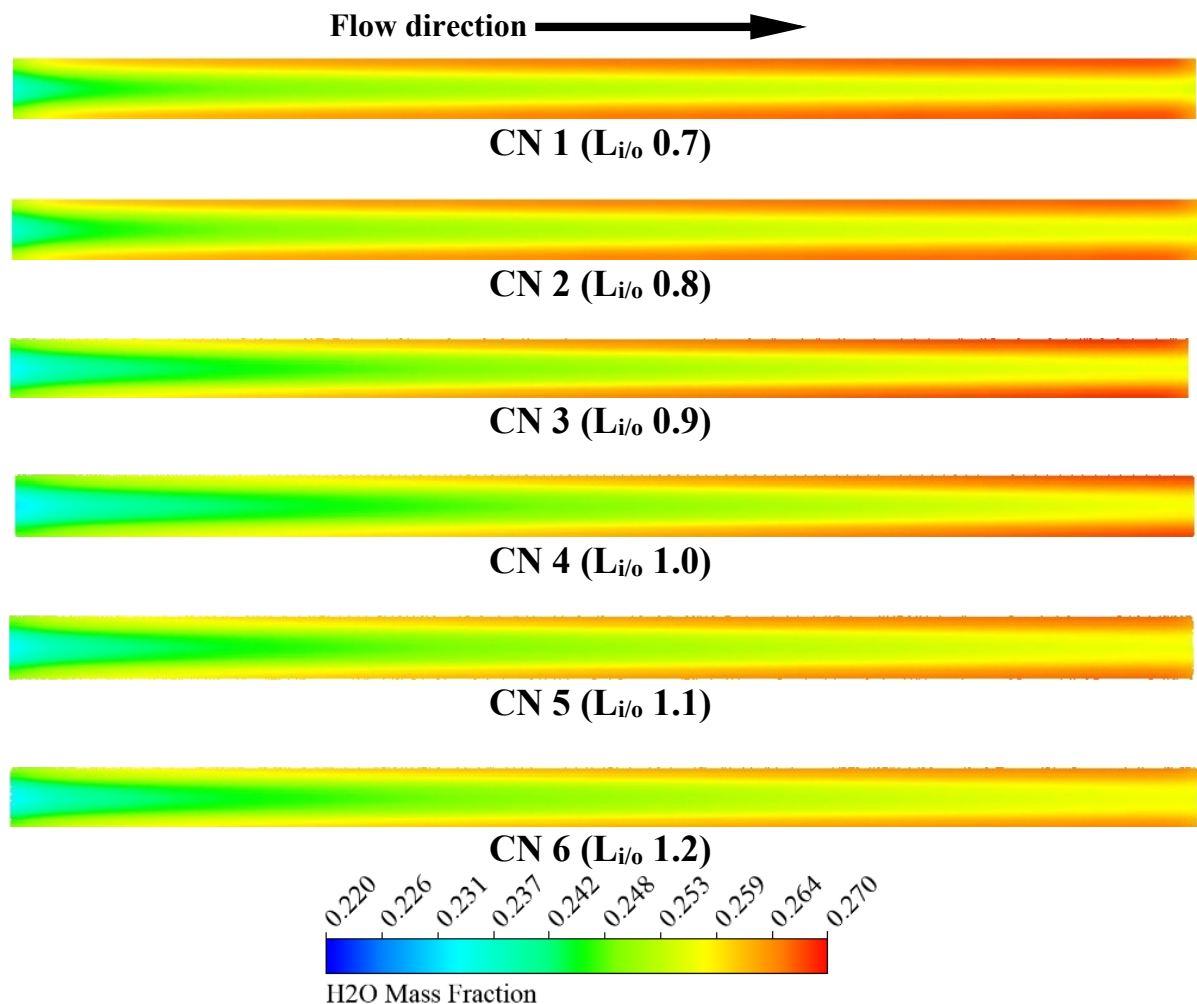


Fig. 5.9. H₂O mass fraction distribution at the interface between CCL and CGDL along the CH for various cases at cell voltage 0.4 V.

water has a tendency to build up at the interfaces between the gas diffusion layer (CGDL) and the cathode catalyst layer (CCL). In addition, it has been noted that a greater $L_{i/o}$ can be advantageous for tapered parallel FFCs, both with and without taking into consideration the

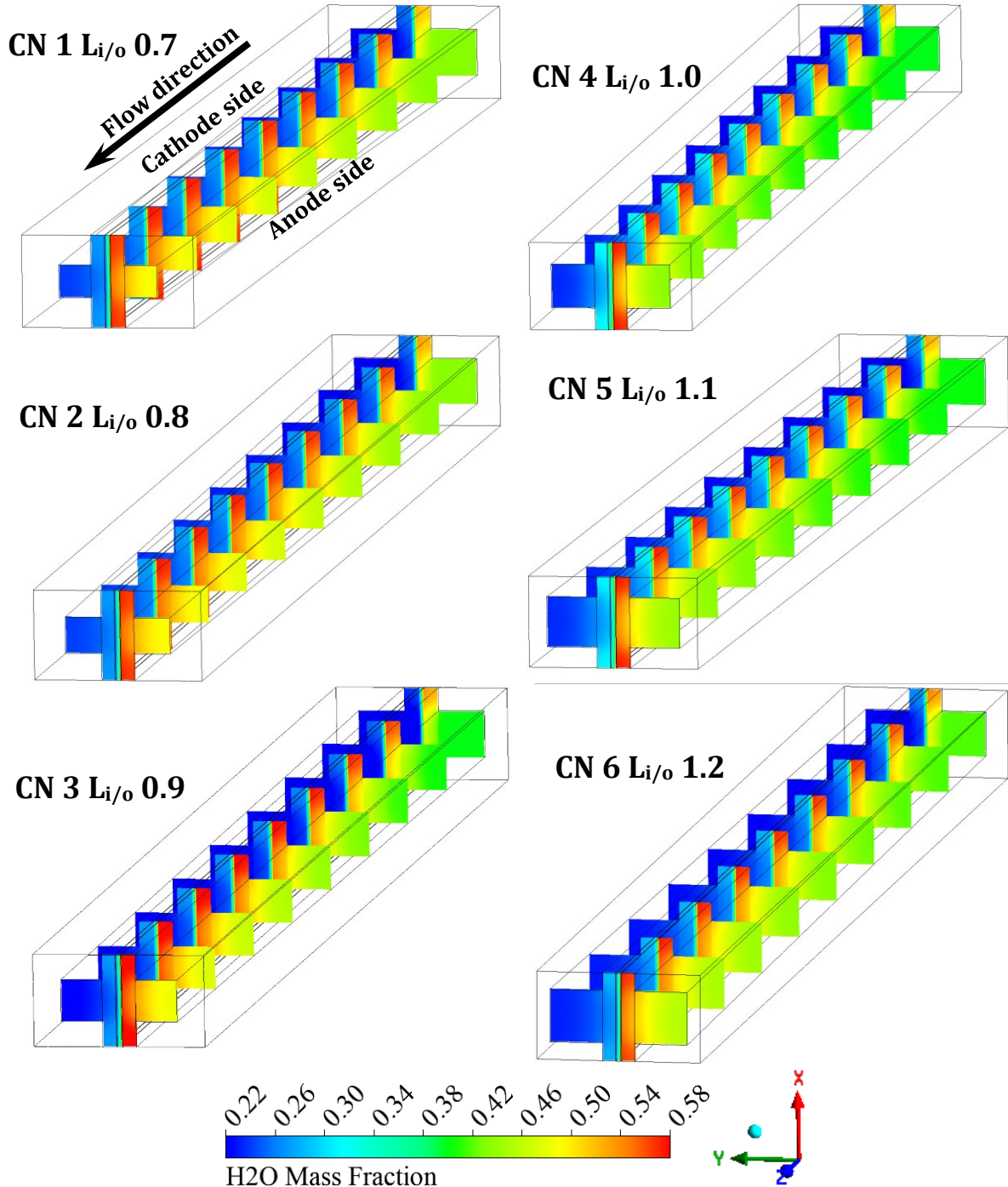


Fig. 5.10. For various cases, H₂O mass fraction distribution at X-Y planes within the fuel cell along the channel at cell voltage 0.4 V.

PMT and TCR because it results in a reduced saturation of liquid water. This is the case regardless of whether or not the PMT and TCR are taken into consideration. The investigation that Wang et al. [104] carried out shows that this result is consistent with their findings. While this is going on, Fig. 5.10. illustrates the distribution of the mass fraction of H₂O along the channels at X-Y planes for a variety of distinct scenarios when the cell voltage is 0.4 V. Since the explanation from the previous paragraph regarding the water-saturated rose as a result of the accumulation from the production result of redox reaction within the catalyst layers of the PEM fuel cell, it is essential to note that this increase occurred.

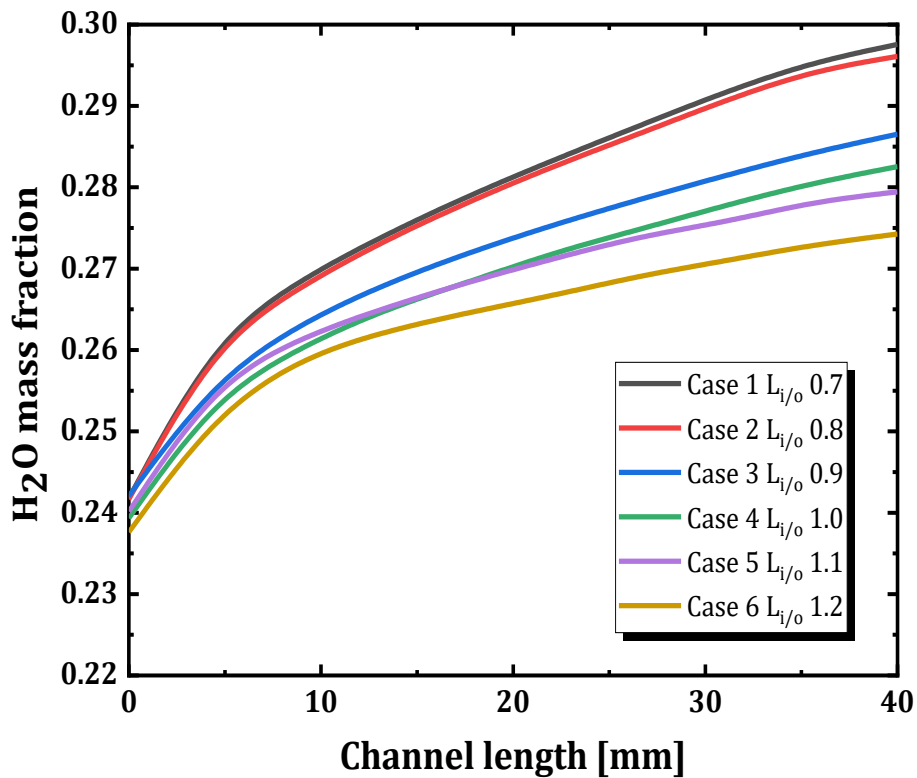


Fig. 5.11. H₂O mass fraction on the centerline of the interface between the CCL and CGDL along the cathode channel for various cases at a cell voltage of 0.4 V.

Presently, Fig. 5.11. illustrates the water mass percentage on the centerline of the interface between the CCL and the CGDL along the cathode channel for various scenarios at a cell voltage of 0.4 V. The water mass fraction is found to rise along the flow direction for all of the cases, as shown in Fig. 5.11. This is because the redox reactions created the water vapour that has accumulated. For the same reasons, case 6 has the lowest value of all the cases. Meanwhile, case 1 has the most enormous value. A broader flow channel enables improved

management within the fuel cell, which is what this signifies. Case 6 has a 5.75% improvement in water removal compared to case 1. This makes it easier to remove water from the cathode side, which in turn reduces the likelihood of water accumulation and flooding being a problem. Excessive liquid water accumulation in the cathode CL/GDL interface can block the pores and hinder the transport of oxygen to the catalyst sites, reducing the PEMFC performance [111]. Improved water management helps keep the fuel cell's water balance at its ideal level, which is essential for maintaining proton conductivity and ensuring that electrochemical processes are carried out effectively. Because of this, the water buildup has decreased, which has resulted in lower water (H₂O) mass percentage at the CCL and CGDL.

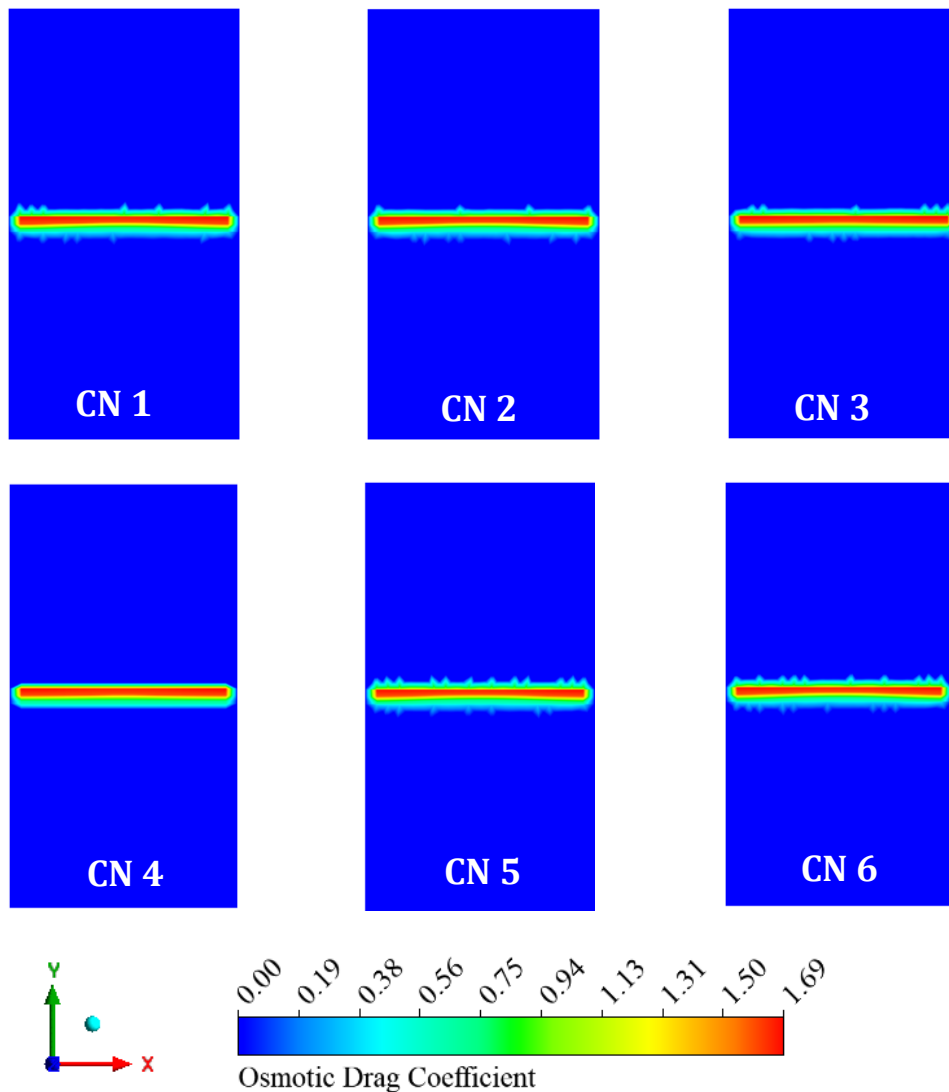


Fig. 5.12. Osmotic drag coefficient profiles at X-Y planes of the middle of the PEM fuel cell for various cases at cell voltage 0.4 V.

Fig. 5.12 illustrates the electro-osmotic drag coefficient in the central region of the X-Y planes of the PEM fuel cell. This value represents the quantity of water molecules transported per proton as protons are transferred from the anode to the cathode. The electro-osmotic drag coefficient is highly relevant as it directly affects the management of water resources. In addition, a higher thermal contact resistance might result in elevated temperature gradients and uneven heat dispersion within the fuel cell. Consequently, this can affect the amount and arrangement of water within the cell, which may have an impact on the distribution of the osmotic drag coefficient. Conversely, the MEA at the non-parallel flow model (case 6, $L_{i/o}1.2$) exhibits a marginally reduced value compared to the parallel flow (case 4) and experiences more significant fluctuations due to the flow shape. Nevertheless, the osmotic drag coefficient at the membrane electrode assembly (MEA) for tapered models remains lower than that of the parallel type.

At the middle of the X-Y planes of the PEM fuel cell, the electro-osmotic drag coefficient is depicted in Fig. 5.12. This coefficient is a measure of the number of water molecules that are transported for each proton that is transferred from the anode to the cathode during the process of proton transfer. As a result of its direct impact on the administration of water resources, the electro-osmotic drag coefficient is of extremely high significance. In addition, an enormous thermal contact resistance might result in additional temperature gradients and an uneven distribution of heat inside the fuel cell environment. This may affect the distribution of the osmotic drag coefficient, as it can affect the water content and distribution within the cell. As a result of the flow shape, the MEA at the broader taper flow model (case 6, $L_{i/o}1.2$) has a value that is somewhat lower than the value at the parallel flow model (case 4), and it fluctuates more. A lower electro-osmotic drag coefficient is generally better for performance and water management for PEM fuel cells. This is because a lower drag coefficient means fewer water molecules are transported from the anode to the cathode by the proton flux, reducing membrane dehydration at the anode side. Nevertheless, the osmotic drag coefficient at the MEA for tapered models continues to have a value that is lower than that for parallel models. Therefore, based on the findings provided, a lower electro-osmotic drag coefficient is generally better for the performance and water management in Proton Exchange Membrane fuel cells, as strengthened by the preceding study [112].

5.5. Current density, velocity magnitude, and pressure drop

Fig. 5.13. illustrates the current density profiles on the center cross-section of the CCL for various tapered parallel FFCs, both with and without the addition of TCR, PMT, and conventional parallel FFC at a cell voltage of 0.4 V. These profiles are shown for both the latter and the former. Compared to the under-rib regions located downstream of the channels, the regions located upstream of the channels have higher current densities. The occurrence of this phenomenon is most noticeable in lower $L_{i/o}$ configurations, such as CN1-CN6 and standard parallel FFC, which results in a considerable non-uniform distribution of current density in the activation area. A pertinent investigation was carried out by Wang et al. [104], in which they made the observation that raising the $L_{i/o}$, more notably CN6, results in a large

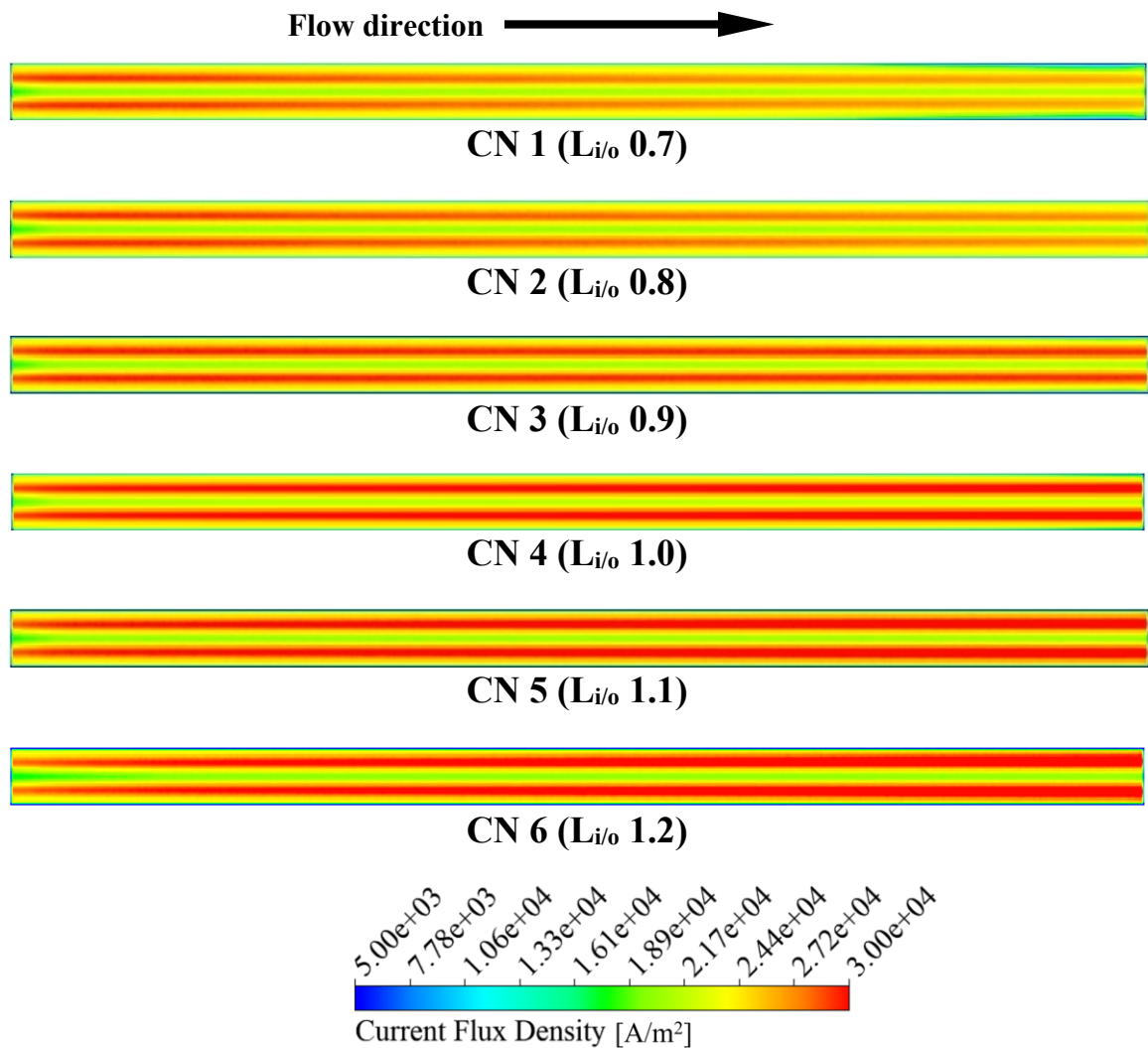


Fig. 5.13. Current density profiles at the middle cross-section of the CCL along the channel for various cases at cell voltage 0.4 V.

rise in the current density within the CCL in the under-rib regions where the channels are located. In addition, the utilization of this method results in the attainment of current densities that are more consistent throughout the CCL. Ohmic loss is a consequence of the existence of TCR in fuel cells. However, higher tapered parallel FFCs equipped with PMT and TCR display much greater current densities within the CCL than tapered parallel FFCs not provided with TCR. Consequently, ignoring the TCR will lead to errors in the optimization of tapered parallel FFCs.

Within the fuel cell, the velocity magnitude profiles at X-Y planes are displayed in Fig. 5.14. This is the case for all of the different flow channels. Based on the figures, it can be seen that the velocity in the parallel flow field is relatively lower in the core channels and displays a distribution that is not uniform. Due to the low velocity of flow, there is an accumulation of liquid water, and zones are stagnant. Moreover, the velocity on the centerline of the interface between CCL and CGDL along the cathode channel is depicted in Fig. 5.15 for a number of different scenarios at a cell voltage of exactly 0.4 V. Starting from 0, the velocity of the input flow channel climbs dramatically until it reaches $5.5E-4 \text{ m}\cdot\text{s}^{-1}$. After that, it stays rather stable until it reaches 35 mm of channel length, and then it declines dramatically until it reaches zero at the end of the channel outlet. Case 6 ($L_{i/o}$ 1.2) has the highest velocity due to the thermal contact resistance effect, which makes the energy dynamics of reactant molecules more active within the catalyst layer.

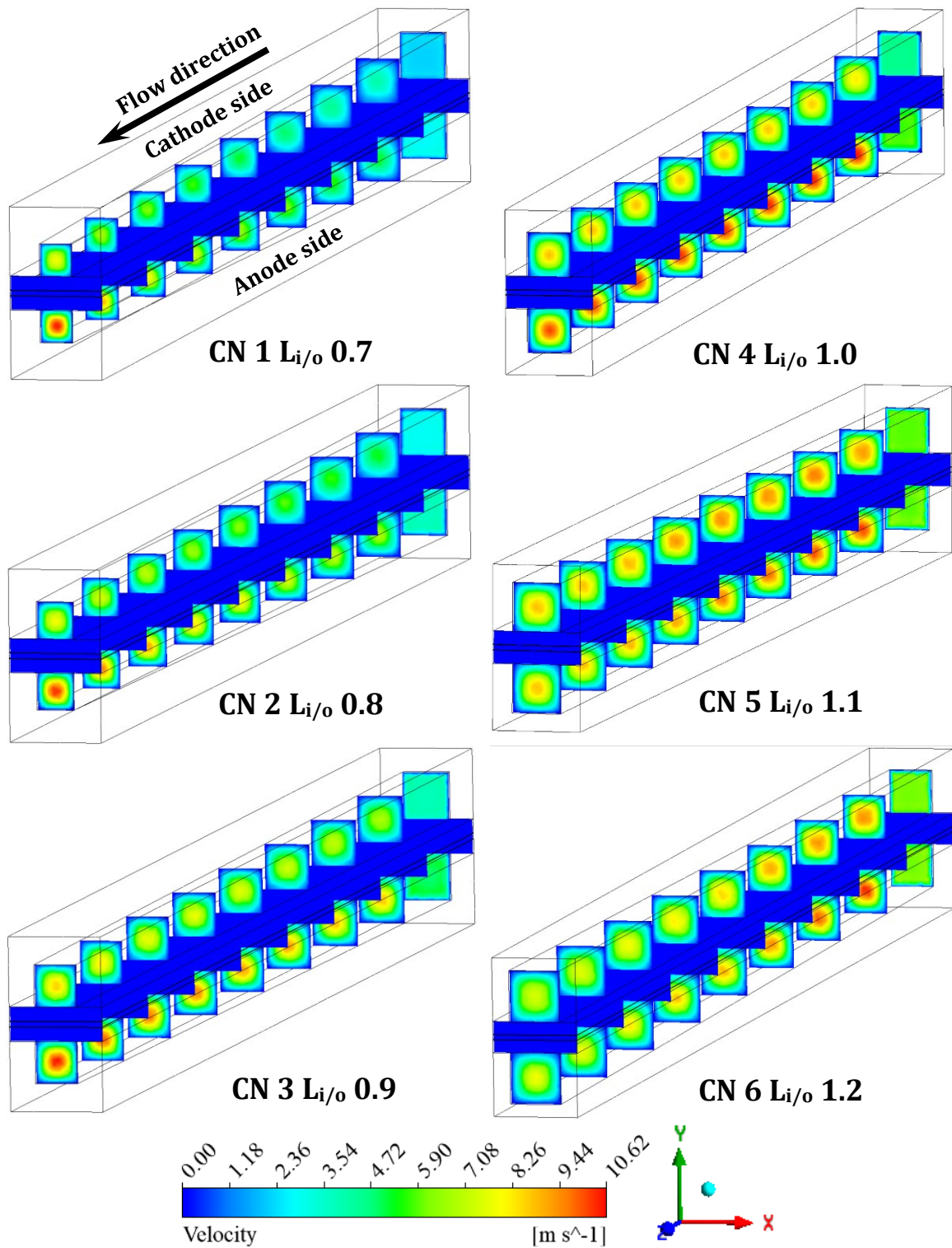


Fig. 5.14. Velocity profiles at X-Y planes within the fuel cell along the channel for various cases at cell voltage 0.4 V.

Additionally, increasing the velocity improves the mass transit of reactants to the catalyst layer. This helps to reduce concentration polarization and accelerate reaction speeds, which

could potentially improve the overall performance of the fuel cell. Furthermore, greater velocities can help reduce the amount of water removed from the gas diffusion and catalyst layers. This helps minimize floods and maintain appropriate water balance, which is essential for preserving proton conductivity and optimal performance, as demonstrated by the findings of the previous investigations [54,55].

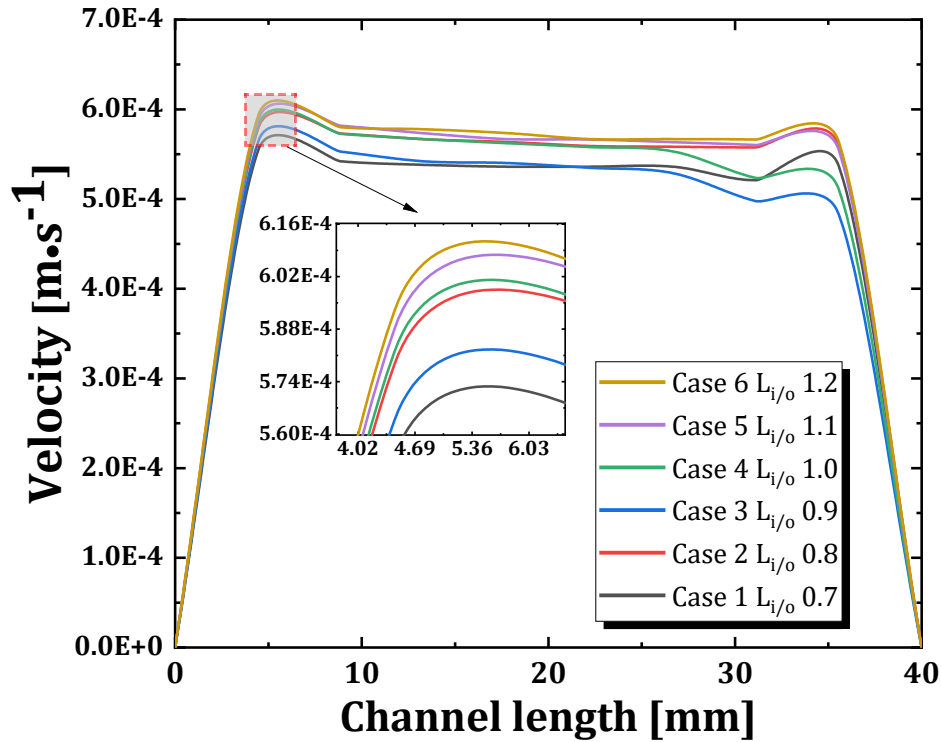


Fig. 5.15. Velocity on the centerline of the interface between CCL and CGDL along the cathode channel for various cases at a cell voltage of 0.4 V.

Fig. 5.16. depicts the pressure distribution at the X-Y planes within the channel for various scenarios while keeping the cell voltage at 0.4 V. Higher $L_{i/o}$ values for all tapered parallel FFCs result in a decrease in the pressure drop along the cathode channel. Reduced pressure in the cathode channel facilitates the delivery of reactants to fuel cells, resulting in lower pumping work and increased energy efficiency of the fuel cell. Moreover, Fig. 5.17 depicts the pressure gradient along the centerline of the interface between the cathode flow channel (CFC) and cathode gas diffusion layer (CGDL) in the cathode channel for different scenarios while keeping the cell voltage at 0.4 V. It is evident that the pressure decreases from the inlet to the outlet channel, as the transport of reactants to the catalyst layers improves. Case 6 exhibits the lowest pressure drop value among all cases due to its wider flow channel area,

which aligns with the previous study's findings [104]. In addition, efficient water removal is crucial in PEM fuel cells to prevent water flooding and maintain optimal performance.

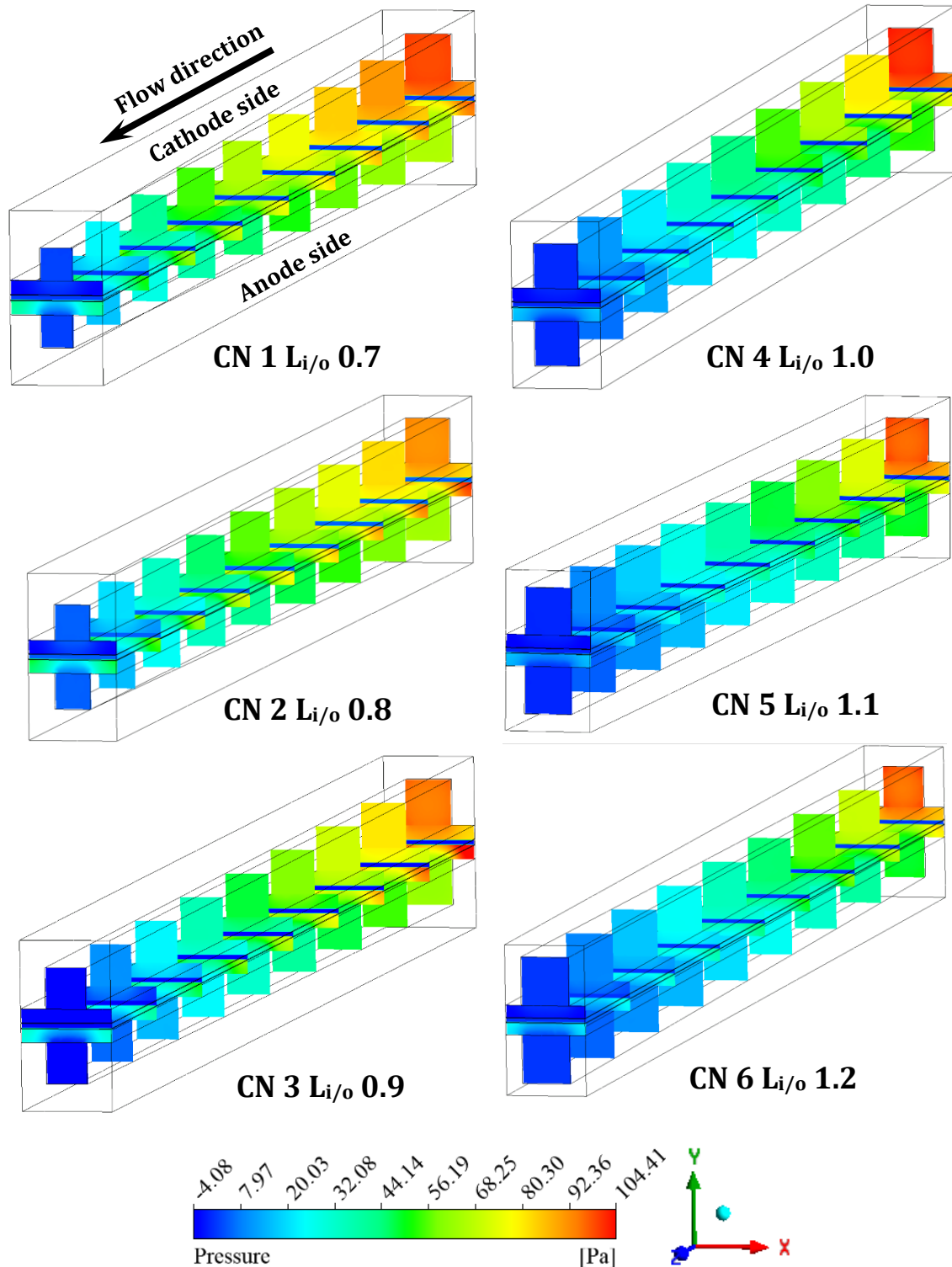


Fig. 5.16. Pressure distribution at X-Y planes along the channel for various cases at a cell voltage of 0.4 V.

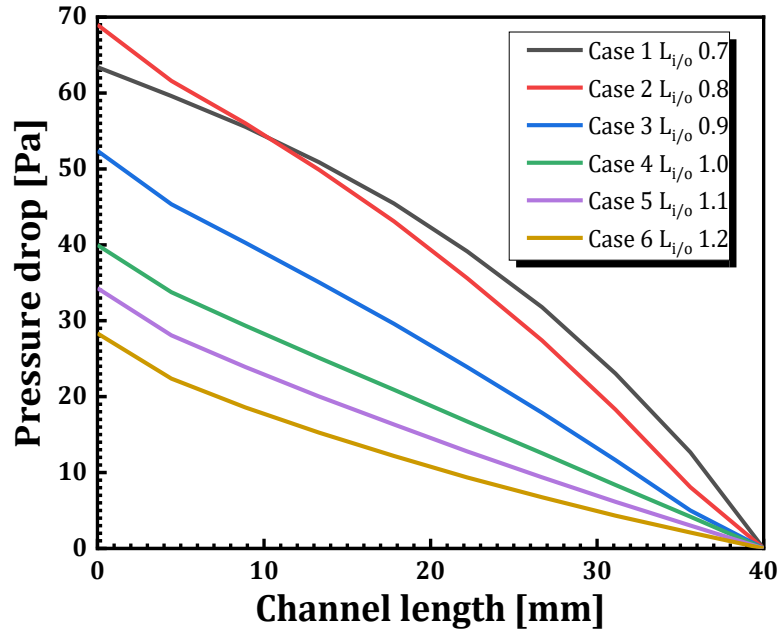


Fig. 5.17. Pressure drop on the centerline of the interface between CFC and CGDL along the cathode channel for various cases at a cell voltage of 0.4 V.

5.6. Summary

This study uses different tapered FFCs to enhance mass transport and cell performance in a PEM fuel cell by placing the TCR and PMT between bipolar plates and gas diffusion layers. Through numerical investigations, the impact of the ratio of the side length of the inlet to that of the outlet ($L_{I/O}$) on various internal physical processes in fuel cells has been studied. These processes include oxygen transport, water removal, dissolved water content, and current density distribution. The findings of this study have been confirmed by previous research [90]. A comparison is made between different tapered FFCs, both with and without the TCR and the PMT, to provide a more specific summary:

1. There is a clear relationship between the increase in the flow channel, the PMT values, the TCR values, and the rise in the maximum temperature of the cell. Due to the thermal contact resistance (TCR) between the Gas Diffusion Layer (GDL) and the bipolar plate (BP), there is an added heat transfer resistance. As a result, the dissipation of heat within the porous electrode is hindered, making it challenging to achieve the optimal working temperature.

2. The current study showcases the findings of numerical investigations, which reveal that a higher Li/o ratio in tapered FFCs with TCR and PMT can improve reactant transport, water removal, and ensure even distribution of current densities, oxygen, and hydrogen in fuel cells.
3. Case 6 (Li/o 1.2) exhibits the highest average velocity due to the impact of thermal contact resistance, which enhances the energy dynamics of reactant molecules in the catalyst layer. This is because it leads to the highest average velocity. Furthermore, increasing the speed of the reactants as they move toward the catalyst layer leads to enhanced mass transport efficiency. These factors can lead to a reduction in concentration polarization and an enhancement in reaction rates, ultimately enhancing fuel cells' overall performance.
4. When comparing case 1 with case 6, it becomes evident that the latter shows a notable enhancement in current density, power density, and pressure drop. The improvements amount to approximately 7.57%, 12.63%, and 68.74%, respectively. This development indicates a more even spread of internal physical quantities within the electrodes, leading to stable operation and increased longevity of fuel cells.

6. EFFECTS OF WATER DROP BLOCK CONFIGURATIONS ON TEMPERATURE PROFILES, MASS TRANSPORT CHARACTERISTICS, AND PERFORMANCE IN PEM FUEL CELL

In this chapter, five distinct streamlined block architectures of flow channels are considered, including interface contact resistance (ICR) and gas diffusion layer (GDL) and the face permeability effect on temperature profiles to enhance PEM fuel cell's mass transport and cell performance. The streamlined block structures of flow channels considering ICR and GDL face permeability were comparatively evaluated.

6.1. The influence of WDB models, considering interfacial contact resistance (ICR) and GDL face permeability on the temperature profiles and the cell performances

The fuel cell's temperature may deviate from optimal conditions during practical operation. This phenomenon may occur due to limitations in managing heat or specific operational procedures, such as during the initial stages. The temperature rise from ambient conditions to the optimal operating temperature of a fuel cell showcases the ignition process. The thermal properties of a passive fuel cell without an active thermal management system are mainly affected by the surrounding temperature and the waste generation rate. A deep understanding of the power output at various temperatures is essential for accurately controlling and designing fuel cell systems, as temperature plays a significant role in fuel cells' operation. Exploring the correlation between temperature and maximum power and determining the most effective operating parameters is crucial.

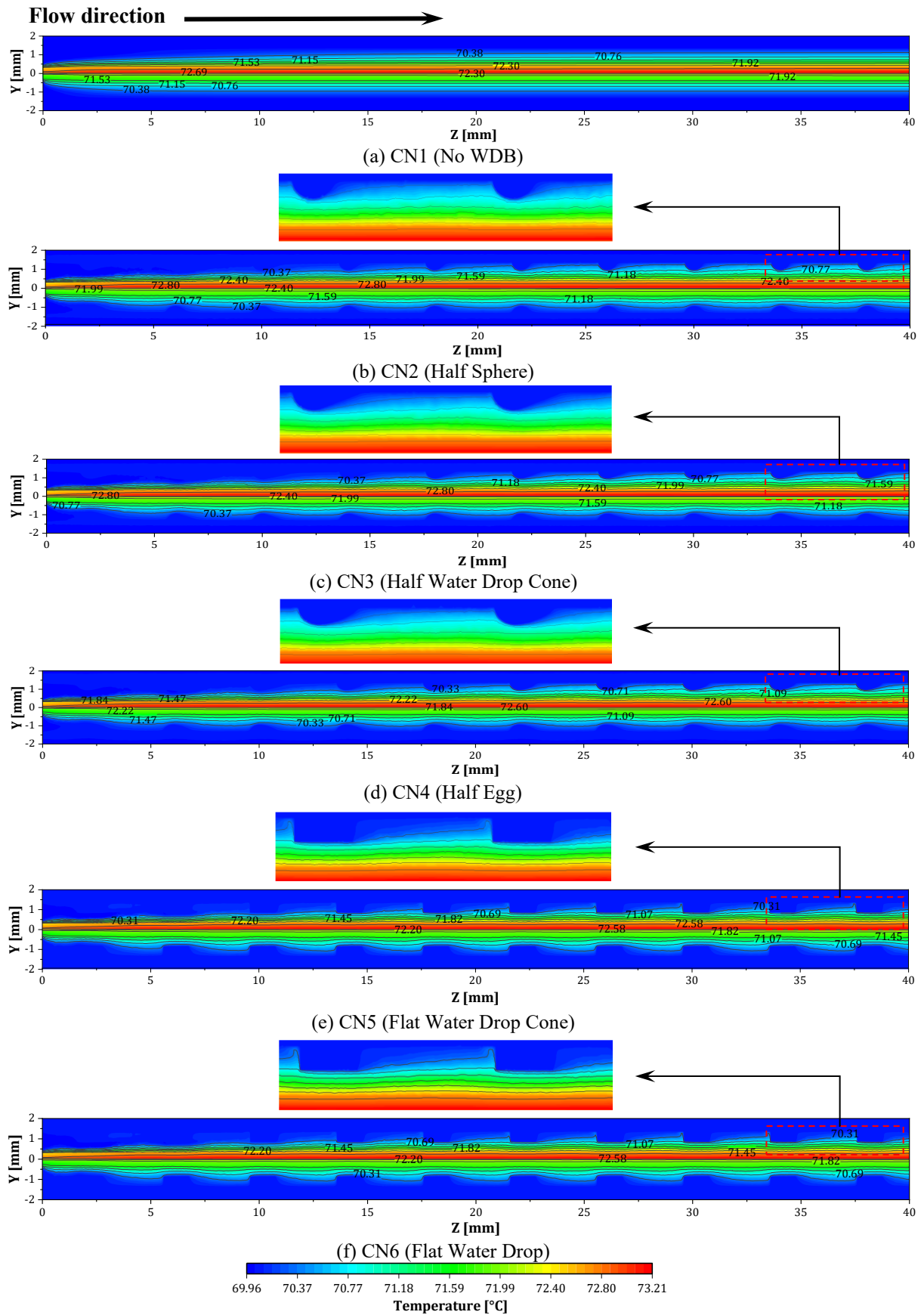


Fig. 6.1. Profiles of temperature distributions in the Z-Y planes through the fuel cell channel's midsection at 0.4 V cell voltage under various scenarios.

The influence of replicated water droplets on the temperature profile of the PEMFC at the middle of the ZY-plane, taking into account interfacial contact resistance and GDL face permeability, is illustrated in Fig. 6.1. Temperature gradients exist between the current collector (rib) and channel regions, with the rib being cooler and the channel being hotter as one moves further from it. Given the low velocity in porous GDL, it can be deduced that the rib region plays a significant role in conducting the majority of the heat dissipated by the electrode. However, the cross-sectional models show some similarities (Fig. 6.1 and Fig. 6.2), with slight variations between CN2 (half sphere), CN3 (half water drop cone), and CN4 (half egg). These differences can be observed in the shorter tail contour of CN2 compared to CN3 and CN4. These models suggest that the reactants' temperature profiles align with the WDB models.

Furthermore, CN5 (Flat Water Drop Cone) and CN6 (Flat Water Drop) possess a cross-sectional area that is relatively similar, surpassing that of CN2-CN4. In addition, researchers have found that the shapes of simulated water droplets can impact the temperature profiles. The use of suggested flow channel models has been discovered to uphold the ideal operating temperature and enhance heat transfer efficiency within the membrane electrode assembly (MEA) in comparison to straight channel configurations. In addition, these models have been observed to improve the heat dissipation rate through the bipolar plate. In addition, the strength of the argument can be bolstered by including previous studies conducted by Nitta et al. [95] and Sadeghifar et al. [96].

The temperature distributions at the xy-plane, specifically 38 mm from the origin of the z-axis, are depicted in Fig. 6.2 for various scenarios with a cell voltage of 0.4V. There is a temperature differential between the current collector (rib) and channel sections, with the rib experiencing lower temperatures. By contrast, the water-drop models that are imitated (Fig. 6.2b - Fig. 6.2f) exhibit varying temperature profiles when compared to the straight channels (Fig. 6.2a). In addition, the WDB models exhibit a more focused temperature distribution compared to traditional models. In addition, the bipolar plate can be designed with a water-drop profile that creates small channels or grooves to trap water droplets effectively. These droplets have the ability to function as heat sinks, effectively cooling the nearby MEA. This can improve heat dissipation and minimize the occurrence of hotspots in the PEMFC.

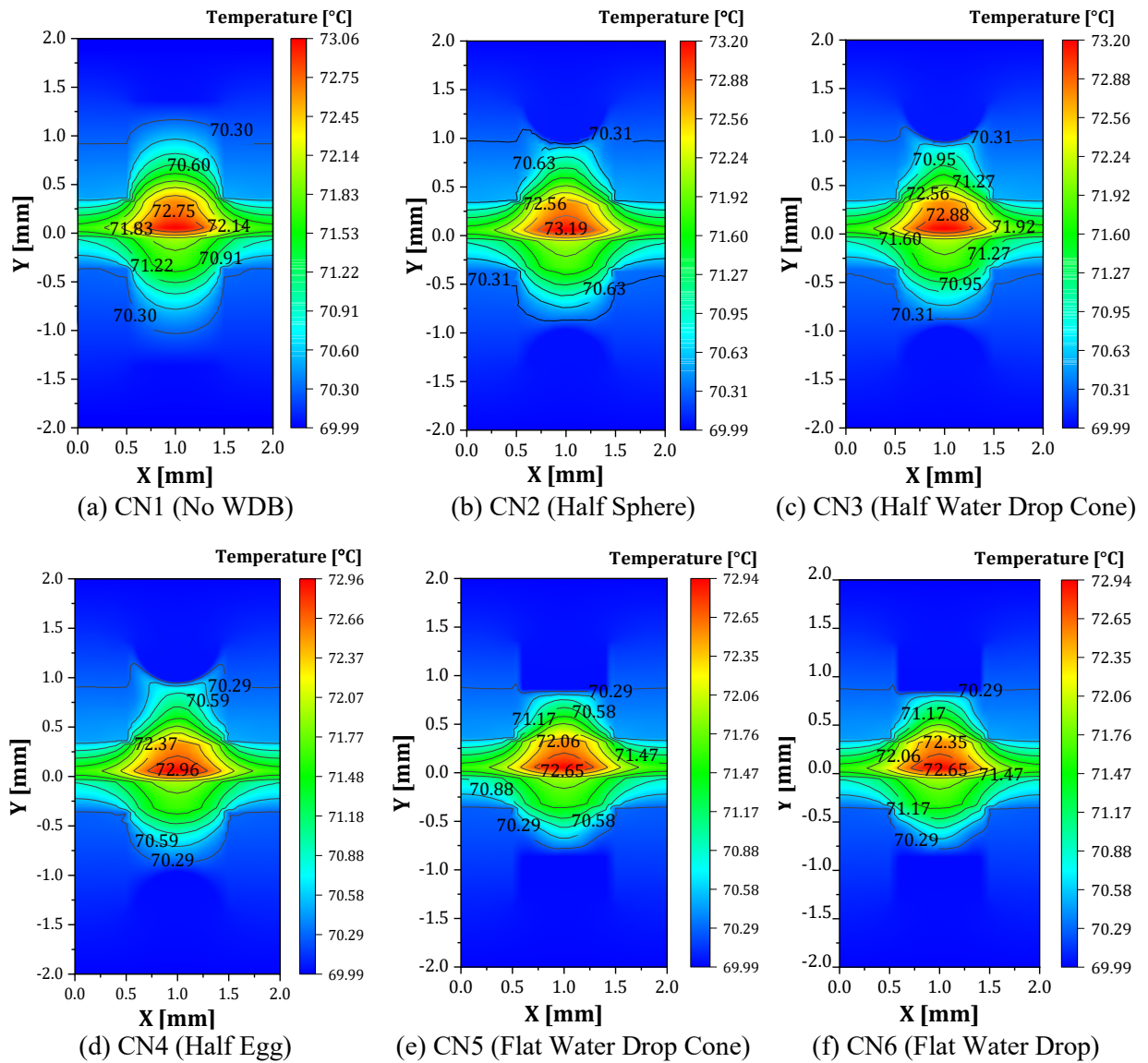


Fig. 6.2. Temperature distributions at XY-plane (38 mm from origin of Z-axis) with different cases at 0.4 V cell voltage (operating temperature, $T = 70^{\circ}\text{C}$; operating pressure, $P = 1 \text{ atm}$).

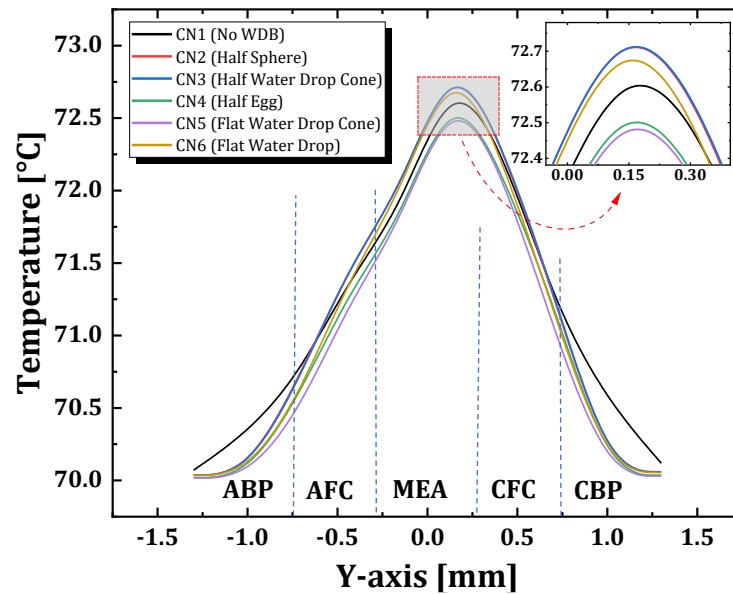


Fig. 6.3. Temperature distributions at the centerline of xy-plane (38 mm from origin of Z-axis) with different cases at 0.4 V cell voltage (operating temperature, $T = 70^{\circ}\text{C}$; operating pressure, $P = 1 \text{ atm}$).

In addition, Fig. 6.3 shows the temperature distribution at the centerline of the XY-plane, specifically 38 mm from the origin Z axis. The temperature patterns within MEA seem to form a "Λ" shape. It is evident that there is a higher occurrence of temperatures in the MEA, which gradually decrease as they flow through the channels and BPs. As depicted in Fig. 6.3, CN 5 (Flatwater drop cone) exhibited the lowest temperature peak at 72.74°C . Meanwhile, the highest recorded temperature reached 72.99°C , specifically in CN2 (Half sphere). In addition, CNN 5 (Flatwater drop cone) recorded the lowest average temperature of 70.93°C . These findings can be enhanced by referring to relevant literature [68], [97], [113], [114], which demonstrate that differences in the flow channels of PEMFCs can lead to localized heating caused by an uneven distribution of reactants or inadequate cooling. Water droplets on the bipolar plate can help address this problem by absorbing extra heat and preventing localized overheating. By mimicking a water-drop profile, the bipolar plate can enhance water distribution across the MEA. It can assist in maintaining a consistent temperature profile within the cell, which helps to prevent any fluctuations in temperature that may affect the overall performance or longevity. Given these circumstances, the performance of PEMFC can be enhanced.

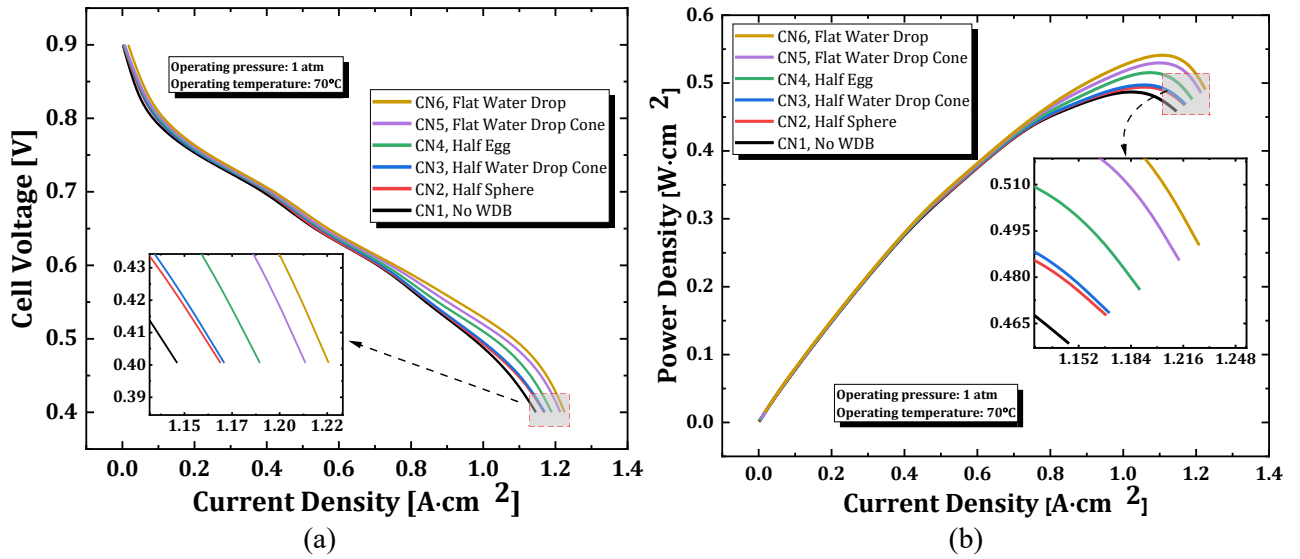


Fig. 6.4. (a) Polarization and (b) power density curves with different cases (operating pressure = 1 atm; operating temperature, $T = 70^{\circ}\text{C}$ (343.15K)).

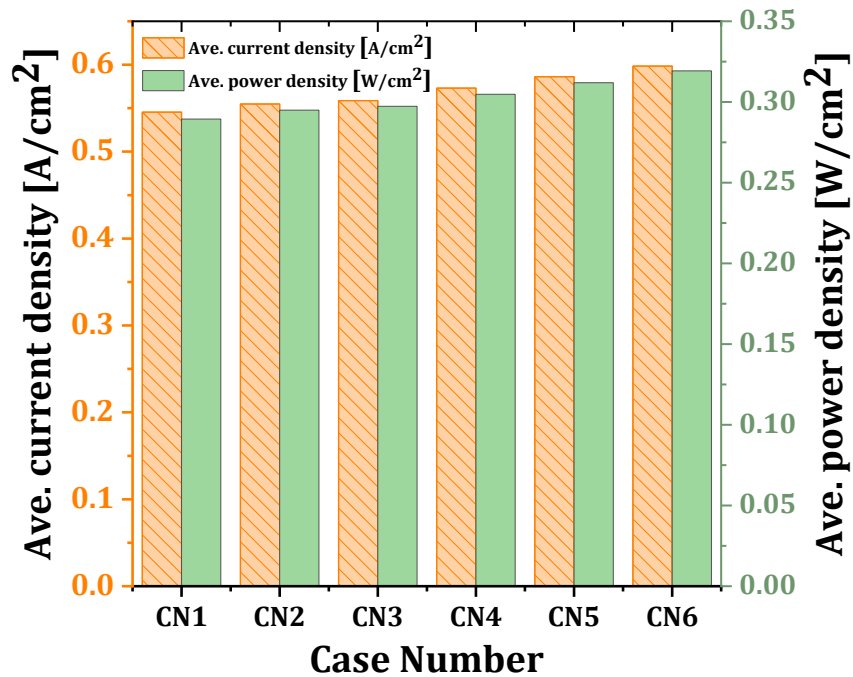


Fig. 6.5. Average current density and power density with six different cases of PEM fuel cell.

Fig. 6.4 (a) shows the polarisation curve, and Fig. 6.4 (b) shows the power density curves for six common situations with different parameters based on the simulation results for the 3D multiphysics model. Fig. 6.4 (a) illustrates the varying current density of different cases after reaching 1.146 A/cm^2 . The operation voltages were decreased, resulting in an enhanced

current density in various cases. The lowest value among all of them (1.146 A/cm^2) was found in case 1 for current density. The highest result for current density was observed in case 6 (1.226 A/cm^2), which was 0.08 A/cm^2 (6.94%) higher than that of case 1 at 0.4 V. In addition, Fig. 6.4 (b) illustrates the power density curve for six different scenarios. Based on the results of this investigation, the lowest peak power density observed in case 1 is 0.487 W/cm^2 , while the highest peak power density recorded in case 6 is 0.549 W/cm^2 . This shows a difference of 0.06 W/cm^2 or a 12.27% enhancement compared to case 1. According to the research findings, the lowest peak power density recorded in case 1 was 0.487 W/cm^2 . A similar phenomenon has been observed in previous channel designs published by Li et al. [93]. The findings suggest that incorporating certain design elements can enhance the performance of PEM fuel cells. Specifically, lower interface contact resistance (ICR) and higher GDL face permeability in ionomer-filled membrane electrode assemblies (MEA) have been shown to be beneficial.

Fig. 6.5 presents a comparison of the average current and power densities for different cases. There is a slight increase in both average current and power density from CN1 to CN6. Meanwhile, CN1 exhibits the lowest average current and power densities, measuring 0.544 A/cm^2 and 0.289 W/cm^2 , respectively. In addition, CN2 and CN3 exhibit similar values as a result of the identical cross-sectional area of WDB models. In addition, CN6 demonstrated the highest current and power density values, measuring 0.599 A/cm^2 and 0.319 W/cm^2 , respectively. Based on permeability alone, the GDL with a permeability of $3.50\text{E-}12 \text{ m}^2$ (for CN6) would be a better choice for improving PEMFC performance compared to the GDL with a permeability of $1.76\text{E-}11 \text{ m}^2$ (for CN1). Improved permeability can effectively regulate gas flow and distribution within the fuel cell, resulting in enhanced contact with the catalyst layer and increased efficiency of electrochemical reactions. In addition, the influence of the block's specific shape on overall performance is minimal in areas with low current density because of the low oxygen requirement. However, the increase in oxygen content can be attributed to various polarisation phenomena in regions with high current density. Improving oxygen utilization and optimizing reaction rates, particularly in the WDB flow channel models, is anticipated to enhance the performance of PEMFCs. This is attributed to factors such as diffusivity, lower interface contact resistance (ICR), and appropriate gas diffusion layer (GDL) face permeability.

6.2. Oxygen mass fraction distribution

Fig. 6.6 illustrates the distribution of the oxygen mass fraction at the boundary between the gas diffusion layer and the catalyst layer along the cathode channel. This distribution was measured at a cell voltage of 0.4V and is shown for six different situations. The oxygen content has a direct impact on the rate of electrochemical reactions, specifically the oxygen reduction reaction (ORR) in PEM fuel cells. During the reaction, the oxygen contained in

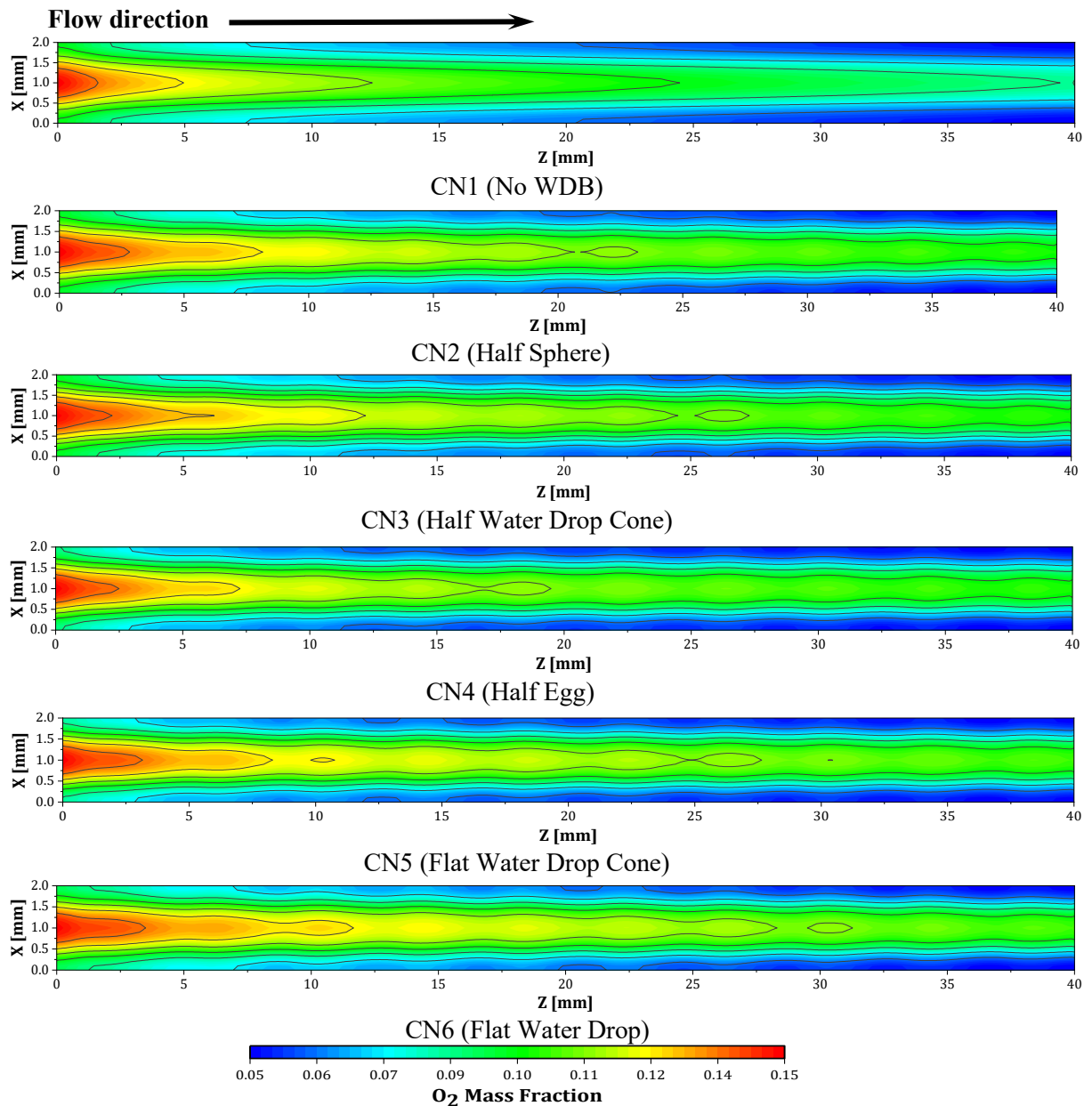


Fig. 6.6. O₂ mass fraction contours for various cases between the cathode CL/GDL interface through the channel at 0.4 V of cell voltage.

the reaction pathway is used up, resulting in a reduction in oxygen concentration from the

starting point to the ending point in the six separate flow channels. There are two possible ways that can be used to improve the even distribution of oxygen mass fraction. One method is augmenting the contact surface area between the cathode flow channel and the cathode gas diffusion layer (CGDL). The second method involves integrating blocks into the flow channel [93]. The utilization of water drop block (WDB) models has the capacity to influence the oxygen mass fraction profiles at the interface between the cathode catalyst layer (CL) and gas diffusion layer (GDL), as shown in Fig. 6.6. The CN1 (straight channel) consistently displays curved profiles. On the other hand, CN2-CN6 exhibits greater irregular arced models and a higher oxygen distribution than CN1, as reported by earlier researchers [110], [115], [116].

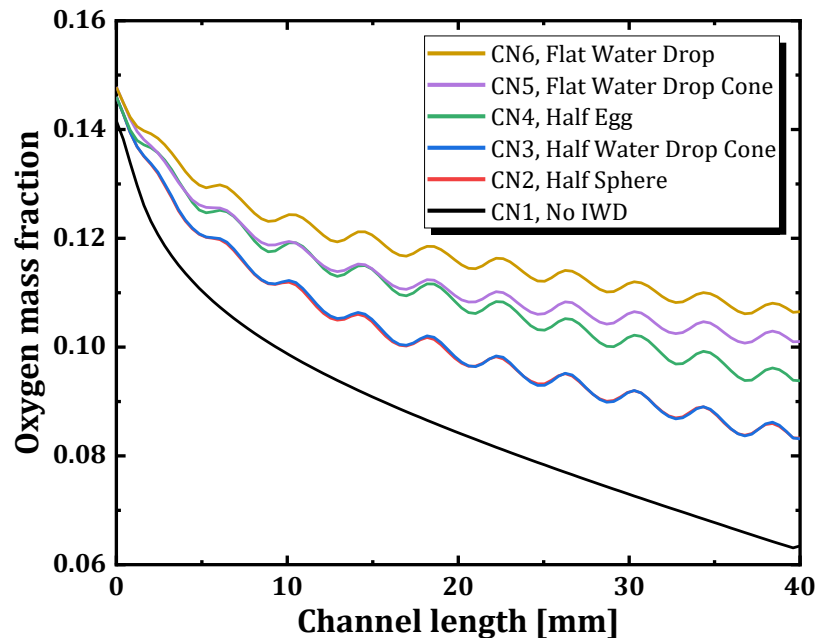


Fig. 6.7. Mass fraction of oxygen on the centerline between cathode GDL/CL interface through the cathode channel for distinct scenarios at 0.4V of a cell voltage.

The oxygen mass percentage at the center line of the interface between the gas diffusion layer and the catalyst layer in the cathode channel was determined for various scenarios at a cell voltage of 0.4 volts. The investigations' findings are illustrated in Fig. 6.7. In general, the oxygen level decreases as the reactants pass through the cathode catalyst layer during the electrochemical process. The CN1 (No WDB) exhibited the lowest mean oxygen mass fraction value, measuring at 0.088. This phenomenon can be ascribed to the lack of obstructions in the flow channel, leading to a consistent trend line across the WDB models.

When the WDB is applied, different spacing between CN2-CN6 results in fluctuating states of oxygen mass fraction. On the other hand, CN6 had an exceptionally high average mass percentage of oxygen, measuring 0.118. The trend lines at CN2 and CN3 show a strong resemblance, with values of 0.1023 and 0.1024, respectively. This similarity can be attributed to the same drag cross-sectional areas of the two things. The decrease in the distance between blocks was accompanied by an increase in the proportion of oxygen at the same location, as demonstrated in previous studies [91], [117], [75], [118].

6.3. Hydrogen mass fraction distribution

Fig. 6.8 depicts the profiles of hydrogen mass fraction along the channel on the cathode side of the fuel cell. These profiles are located at the interface between the catalyst layer and the gas diffusion layer. When the cell voltage is set to 0.4 V, the profiles are displayed for each of the different scenarios. In each of the model designs, there was a decrease in the proportion of hydrogen mass along the gas channel in the direction of flow despite the fact that the flow was in the opposite direction. Possibly, the hydrogen oxidation reaction (HOR), which takes place within the anode catalyst layer, is responsible for this phenomenon, at least in part. According to the data presented in Fig. 6.6, these events share a degree of similarity with regard to the mass percentage of oxygen. We found that the inflow flow of CN1 (straight channel) had a larger concentration of reactants than the other channels. The application of WDB in the CN2-CN6 range leads to a supply of reactants that is more equally distributed among the reaction zones. Previous research [13], [66], and [74] have uncovered the perturbation effect, which is characterized by the induction of a rapid change that ultimately results in more effective convection. This phenomenon has important repercussions for the development of improvement measures for public transportation. In particular, it makes it easier for reactants to be pushed into the anode catalyst layer (ACL), which in turn improves the performance of the PEM fuel cell by increasing the amount of mass transfer that occurs within the cell.

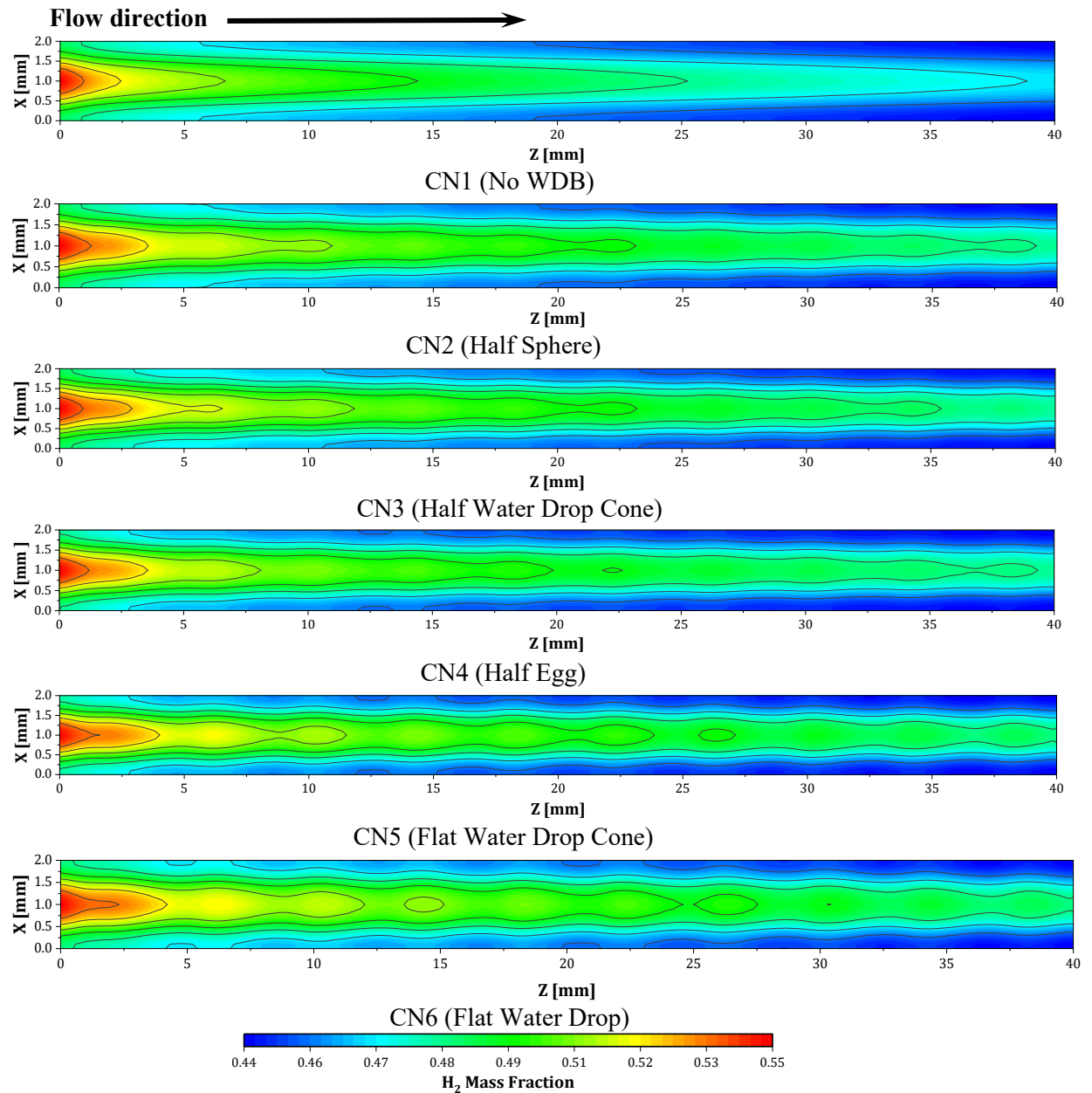


Fig. 6.8. H₂ mass fraction distribution for various cases at the anode GDL/CL interface along the channel at cell voltage 0.4 V.

An investigation into the hydrogen mass fraction in the center region between the anode CL/GDL interface in the anode channel was carried out for a number of different situations at a cell voltage of 0.4V, as shown in Fig. 6.9. When the reactants go through the anode catalyst layer (ACL) during the electrochemical reaction, such as the hydrogen oxidation reaction (HOR), the observed trend indicates that the concentration of hydrogen decreases from the first stage to the final stage. This occurs when the reaction is taking place. With a value of 0.477, the CN1 (No

WDB) demonstrates the lowest possible average gas mass fraction. The absence of obstructions in the flow channel is likely responsible for the continuity of the trend line found across all of the WDB models. In contrast, applying WDB leads to observing several hydrogen mass fraction fluctuation states for CN2-CN6 at varying intervals during the experiment. With a value of 0.504, CN6 is the compound that demonstrates the greatest average mass percentage of hydrogen. There is a striking similarity between the trend lines detected at CN2 and CN3, as stated by the values of 0.4917 and 0.4918 associated with each of these trend lines. One possible explanation for the observed similarity is that each of these entities has drag cross-sectional areas that are identical to one another. As was observed in earlier research [75], [118], the decrease in block spacing was accompanied by a concomitant increase in the hydrogen mass fraction at a position comparable to the one in which the block spacing was decreased.

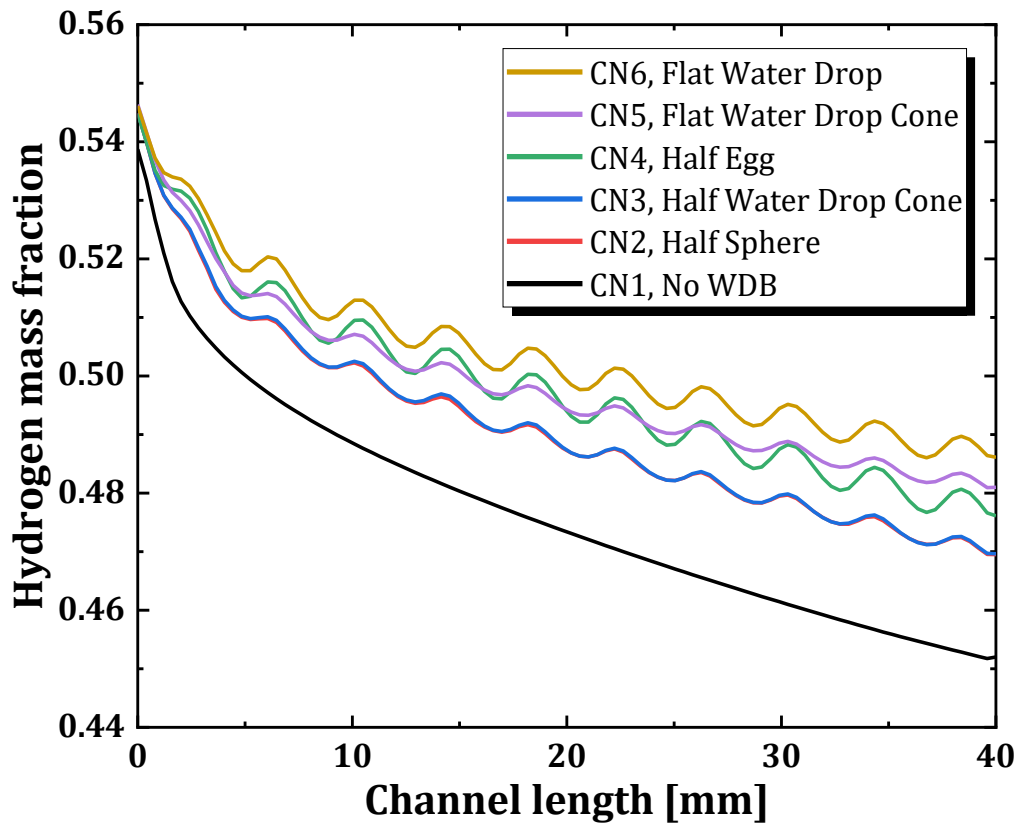


Fig. 6.9. Mass fraction of hydrogen on the centerline at the anode GDL/CL interface through the channel for six different scenarios at a cell voltage of 0.4 V.

6.4. Water mass fraction distribution

It is essential to have efficient water management in order to keep the performance of PEM fuel cells at its highest possible level. It is possible to effectively increase the efficient extraction of water from the cathode region by increasing the width of the flow channel. This will result in the reduction of floods and an improvement in the transportation of protons. In order to achieve optimal levels of electrolyte conductivity and make the oxygen reduction

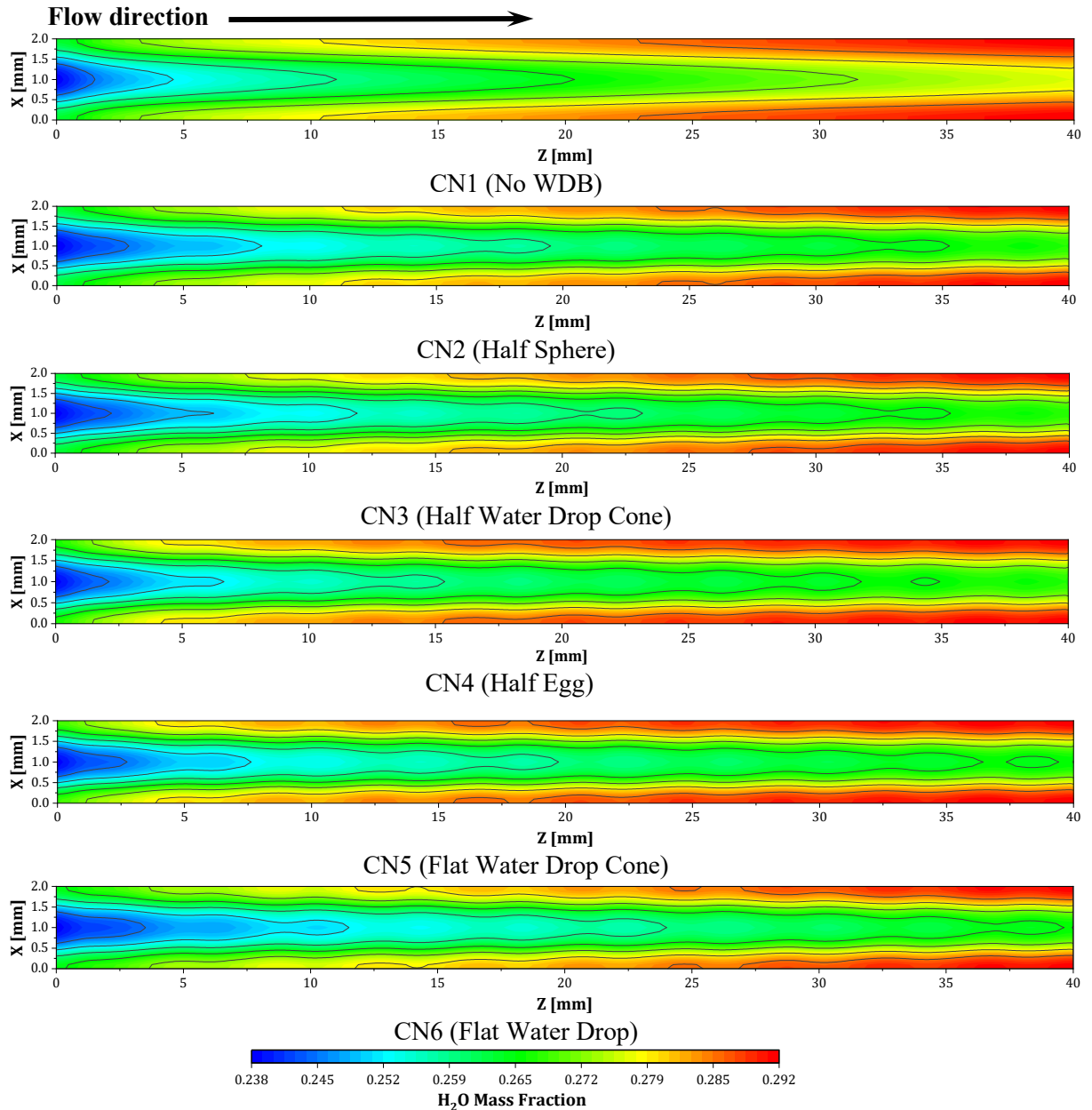


Fig. 6.10. For various cases, H₂O mass fraction profiles at the cathode GDL/CL interface throughout the channel at 0.4 V of cell voltage.

reaction (ORR) easier to carry out, it is essential to regulate the water appropriately through

proper regulation. The water mass fraction distributions that can be detected at the interfaces of the CL/GDL cathode along the channel are depicted in Fig. 6.10, which shows the distributions regardless of the circumstances. I accomplished this while maintaining a consistent cell voltage of 0.4 V. The existence of liquid water at the interfaces located further downstream of the channel may be due to the flow of gases all the way down the length of the channel. Specifically, liquid water tends to accumulate at the interfaces between the catalyst layer and the gas diffusion layer on the cathode side of the flow channel. This is because the side of the flow channel that gets lower drag forces from reactants is the preferred side. In addition, it has been found that using water drop block (WDB) models leads to a reduction in the residual amount of liquid water saturation compared to the conventional models. There is a correlation between this conclusion and the investigation that was carried out by Li et al. [93].

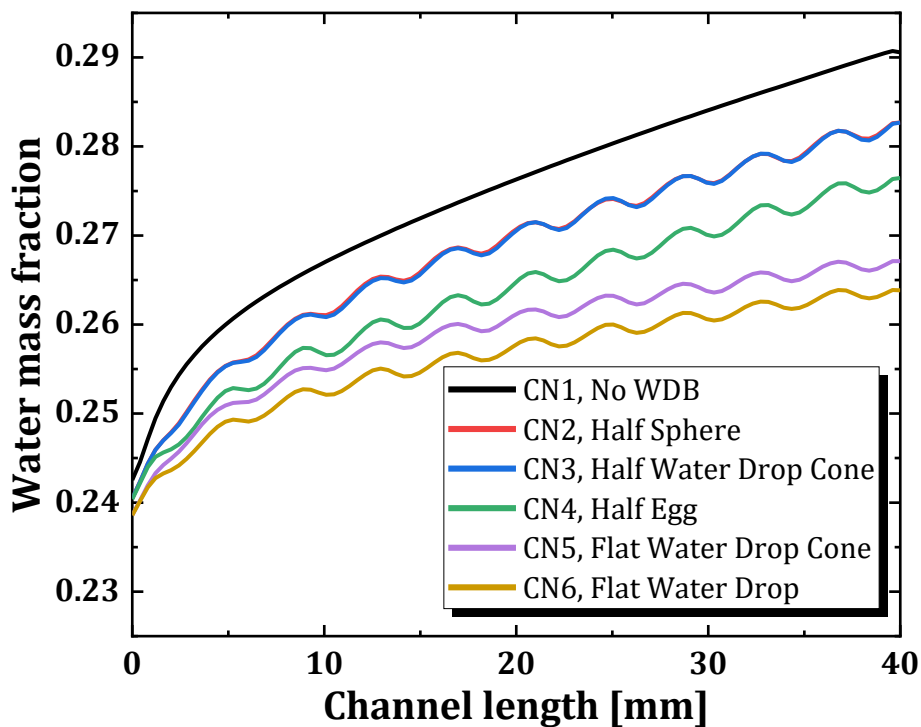


Fig. 6.11. For six cases, H₂O mass fraction comparison on the centerline within the CL/GDL interface throughout the channel at 0.4 V of cell voltage.

Fig. 6.11 illustrates the fraction of water mass that passes through the center line of the interface between the catalyst layer and the gas diffusion layer on the cathode side in a number of different scenarios when the cell voltage is 0.4 V. In accordance with the data presented in Fig. 6.11, it is possible to observe that the water mass fraction has a pattern of

growing as the flow advances. This is the case regardless of the particular example that is being investigated. The occurrence of redox reactions may be responsible for the presence of some water vapor that has been collected. Because it has a mean water mass percentage of 0.2745, the CN1 (No WDB) exhibits the most remarkable performance. When compared to this, the implementation of the mimicked water drop (WDB) makes it possible to identify discrete oscillations in the water mass percentage throughout CN2-CN6 that take place at different time intervals. CN6, on the other hand, has the lowest average mass percentage of water, which was measured at 0.2561. This represents a reduction of 7.18% in water saturation content when compared to CN1, which has the highest water saturation level. There is a significant degree of resemblance between the trend lines that were recorded at CN2 and CN3, as demonstrated by the values of 0.2682 and 0.2681, respectively, they have. It is possible that the observed similarity can be ascribed to the shared trait of having comparable drag cross-sectional areas, as demonstrated by the research that has been conducted previously [93]. The procedure helps to increase water extraction from the cathode region, which in turn reduces the likelihood of water accumulation and flooding by improving water extraction. There is a vital component in maintaining proton conductivity and optimizing electrochemical processes. Enhanced water management strategies contribute to the preservation of an optimal water balance within the fuel cell. This leads to a decrease in the water mass fraction at the cathode CL/GDL contact, which is the result of the reduced accumulation of water.

6.5. Flow velocity and pressure drops

This section presents the findings of an inquiry into the effect that a number of water-drop block (WDB) models have on the oxygen transfer process. The significance of the evaluation of the velocity magnitude and streamlines of oxygen in the cathode channel is explicit. Fig. 6.12 illustrates the analysis of the velocity magnitude profiles at ZY-planes on the center cross-section of a fuel cell across the flow channel. This analysis is performed for a variety of situations at a cell voltage of 0.4 V. After the entrance zone, it is clear that electrochemical reactions are responsible for the rise in velocity that occurs. This, in turn, leads to an increase in the kinetic energy of gas molecules, which in turn causes reactants to move at a faster speed.

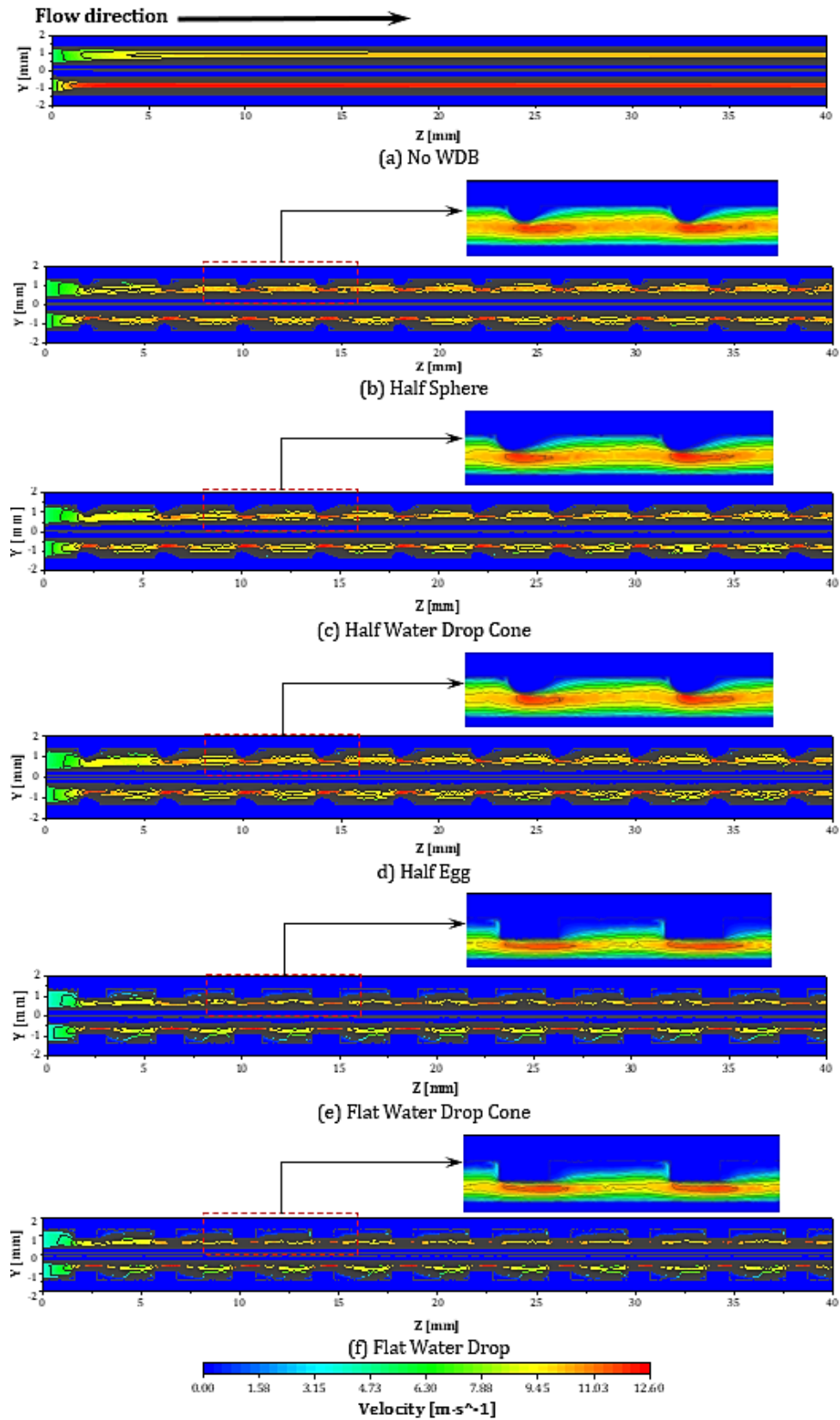


Fig. 6.12. Patterns of the velocity magnitudes at ZY planes on the center cross-section of the fuel cell passing through the channel for distinct scenarios with a 0.4 V cell voltage.

Compared to other models that use the inclined weir design (CN2-CN6), the straight channel model (CN1) displays a flow pattern that is more consistent in terms of the velocity of cathode flow. When compared to the velocities seen in the CN3 and CN4 channels, the velocities in the CN2, CN5, and CN6 channels located close to the blocks demonstrate a more significant magnitude that lasts longer. These attractive streamlined shapes that were seen in the upper portion of the block within the CN3 and CN4 channels are the key rationale that can be linked to this event. Oxygen transmission within the block is subject to frictional resistance, which impedes oxygen flow throughout the block. A relatively low level of resistance characterizes this situation. The flow lines exhibit beneficial characteristics within the CN2, CN5, and CN6 channels of the block. On the other hand, the perturbation effect causes the upper portion of the construction to hinder the transfer of oxygen. As a consequence, the CGDL receives a more remarkable supply of oxygen, which is consistent with the findings of previous studies [93], [119], [120].

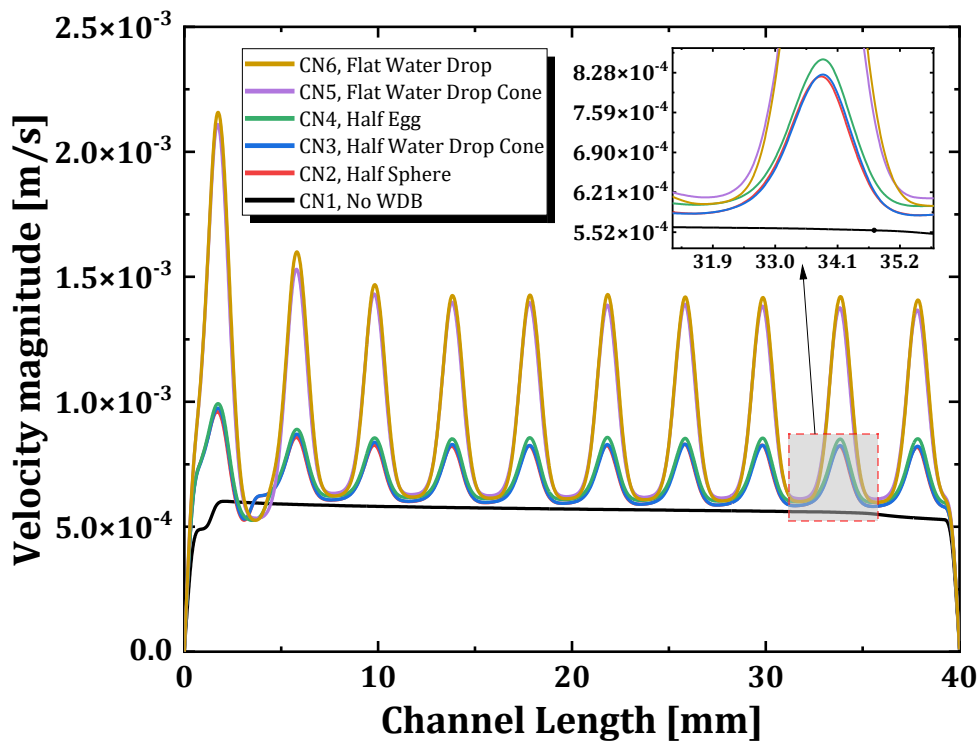


Fig. 6.13. Comparison of velocity magnitude on the center-line between cathode GDL/CL interface through the cathode channel at a cell voltage of 0.4 V for six cases.

The velocity's magnitude at the interface's centerline between the CCL and CGDL within the cathode channel is displayed in Fig. 6.13. Several cases were seen with a cell voltage of 0.4 V; the data refers to those cases. According to the information that is displayed in Fig.

6.13, the straight channel exhibits the lowest velocity of oxygen diffusion when compared to the other channels. By utilizing water-drop block (WDB) channels, which are differentiated by their spacing, it is possible to accomplish the potential improvement of oxygen participation in chemical reactions. As a consequence of this, there is a rate of increase in the utilization of oxygen within the diffusion layer, which ultimately results in an extension of its engagement period.

Furthermore, it is of the utmost importance to admit that the process in issue only results in a partial improvement in performance. It has been observed, on the basis of previous studies [93], that the rate of diffusion for the fundamental linear channel is relatively slow, which results in outcomes that are not optimal. In conclusion, it is possible to observe that the WDB (CN6) channel exhibits an excellent dispersion of oxygen mass fraction and the highest mean velocity of oxygen diffusion, which is 0.00089 meters per second compared to other examples. As a result, it is possible to draw the conclusion that the WDB (CN6) channel demonstrates considerably more outstanding performance in comparison to the other two flow channels.

A representation of the pressure distribution on the Y-Z planes at the central cross-section of the fuel cell through the channel can be seen in Fig. 6.14. Different conditions are represented by the scenarios depicted in the image, and each of these settings has a cell voltage of 0.4 V. Because of the lower amount of pumping labor and reactant consumption, it is possible to make the observation that pressure drops in the PEM fuel cell system are reduced. When compared to other varieties of water-drop block (WDB), the CN1 (straight channel) exhibits the least amount of pressure drop. As a result of blockage-induced pressure distribution and drag coefficient modifications, the pressure drop from CN2 to CN6 is significantly increased. The finding that was mentioned above, which is in line with the investigation that was carried out in the past by Zuo et al. [121], elucidates that obstruction within the flow-field channel makes the flow move in the direction of the gas diffusion layer (GDL) and increases the mass transfer from the central region of the channel to the GDL.

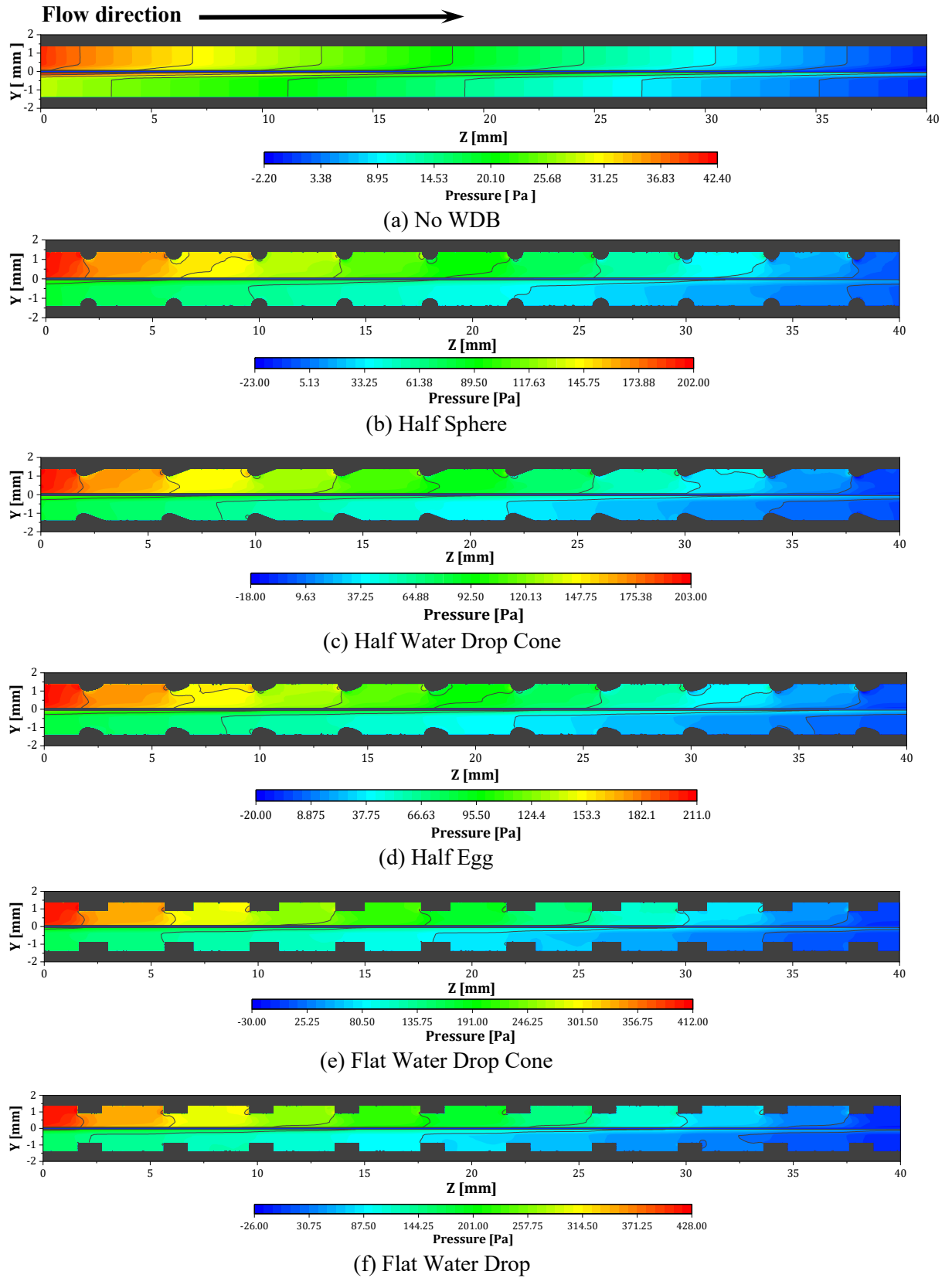


Fig. 6.14. For various cases, the pressure distributions were compared at Z-Y planes on the center cross-section of the fuel cell through the channel at 0.4 V of cell voltage.

For the electrochemical reactions that are taking place inside the fuel cell, the occurrence of pressure drop significantly impacts the reactions. There is a correlation between the fluctuation in pressure drop and the fluctuation in the voltage of the cell, which ultimately results in a decrease in the cell's overall efficiency. In light of this, this work aimed to investigate the significance of pressure drop as an essential component in flow fields that come in various configurations. A comparison of the pressure distribution at the centerline of the interface between the cathode gas diffusion layer (CGDL) and the cathode flow channel (CFC) is depicted in Fig. 6.15. This comparison is an example of how the pressure is distributed. We analyzed each of these scenarios at a cell voltage of 0.4 V, and the cases that are displayed relate to a variety of different circumstances. When compared to the other examples (CN2-CN6) that utilized WDB models, the findings indicate that the pressure in CN1 (straight channel) follows a linear trend line more closely than the other cases did. This is the case because CN1 is the highest pressure in the straight channel. Because of the different types of obstructions, the application of WDB models can result in an increase in the fluctuation of pressure between CFC and CGDL.

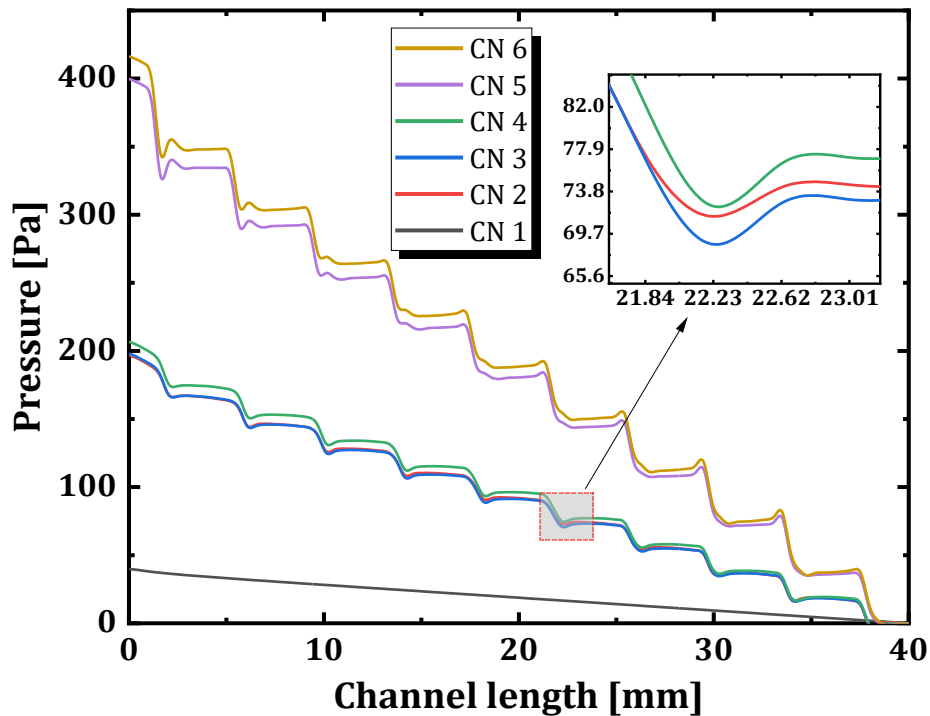


Fig. 6.15. Comparison of pressure on the middle-line of the interface between cathode GDL/FC throughout the cathode channel from inlet to outlet for various cases at a cell voltage of 0.4 V.

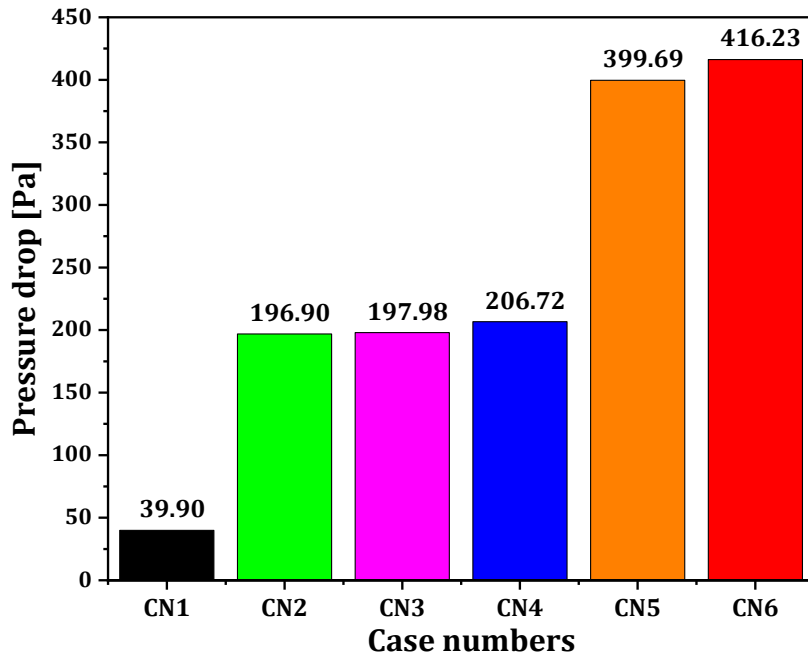


Fig. 6.16. The pressure drop comparison across the cathode channel was measured for six scenarios at a cell voltage of 0.4 V.

In addition, the pressure decrease that occurs from the entrance to the exit of the cathode channel is depicted in Fig. 6.16. This decrease occurs for various circumstances when the cell voltage is 0.4 V. Due to the use of reactants and the subsequent drop in pumping power, it is possible to see a non-linear fall in pressure across numerous different flow channels. Furthermore, as shown in Fig. 6.16, it is clear that the parallel flow fields (CN1) and the model flow fields (CN6) on the channel have the lowest and highest pressure drops, respectively, along the channels. The pressure drop observed in the CN1 model is around 39.90 Pa, equivalent to approximately one-tenth of the pressure drop recorded in the CN6 flow field structure. In accordance with Zuo et al.'s earlier findings [121], the data analysis presented in Fig. 6.16 suggests that the flat water drop (CN6) design exhibits a pressure distribution on the surface of the catalysts that are quite favorable.

6.6. Summary

This study employed a computational model of a non-isothermal fuel cell, utilizing water-drop block models in the flow channels. The objective was to examine the temperature profiles, mass transport properties, and PEM fuel cell performance. The study also investigates the impact of interface contact resistance (ICR) and gas diffusion layer (GDL) face permeability on the cell's performance. The proposed models for the (WDB) are

obtained by comparing the simulated polarisation curve with the relevant experimental data, leading to a reasonable level of agreement. From the computational findings and subsequent remarks discussed above, the following conclusions can be deduced:

1. This study examined the impact of water-drop block (WDB) models on the electrode's highest temperature and temperature distribution. Integrating the ICR and GDL face permeability into the simulated water-drop model significantly increases the maximum cell temperature. Specifically, with a cell voltage of 0.4V, there is an approximate temperature rise of 0.19°C at CN 2 compared to CN1. In addition, the temperature profiles display a characteristic "Λ" form. The increase in temperature serves to prevent the loss of heat, thereby maintaining an ideal operating temperature.
2. It is important to optimize key aspects such as ensuring sufficient and appropriate reactants on catalytic surfaces, minimizing pressure drops in flow channels, and reducing water formation at the electrode surface to increase the current and power density. The current density and power density on the CN6 are higher compared to other scenarios. At a voltage of 0.4V, the maximum current density and power density increased by 6.94% and 12.27%, respectively, compared to the conventional model CN1.
3. The flow channel should have the capability to effectively eliminate any surplus water generated on the surface of the cathode catalyst. The saturation of liquid water at the interface between the cathode gas diffusion layer (GDL) and catalyst layer (CL) decreased by approximately 7.18% in the CN6 design compared to the CN1 model with parallel channels.
4. The WDB (CN6) channel demonstrates the highest velocity of oxygen diffusion and the widest dispersion of oxygen mass fraction. Therefore, it may be inferred that the WDB channel (CN6) outperforms the straight-flow channels (CN1).
5. In summary, the goal is to find a compromise between a low interface contact resistance (ICR) and a high gas diffusion layer (GDL) face permeability in order to improve mass transport and cell performance. Hence, the selection of the WDB model case 6, with an ICR of $2.00\text{E-}06 \text{ ohm}\cdot\text{m}^2$ and a GDL face permeability of $3.50\text{E-}12 \text{ m}^2$, seems to achieve a favorable equilibrium and may be the optimal option for enhancing mass transport and cell performance in the present investigation.

7. CONCLUSIONS AND CONTRIBUTION

The objective of this study is to investigate the effect of geometry modification (tapered and water drop block models) of bipolar plate flow fields while considering some parameters such as thermal contact resistance (TCR), porous medium thickness (PMT), interface contact resistance (ICR), and GDL face permeability variations on temperature profiles, mass transport characteristics, and PEM fuel cell performances.

Chapter 1: The research background of the work undertaken is introduced. An overview of the trends and challenges of PEM fuel cell research on flow field configurations is produced by correlating the relevant literature and the recent progress of the previous author's research methods. The research objectives and scope are presented at the end of this chapter, followed by the organization of the thesis.

Chapter 2: A literature review regarding bipolar plate flow field configuration's effects on mass transport characteristics and performance of PEM fuel cells. However, all previous studies have focused on modified bipolar plate flow channels' influence on mass transport characteristics and performances of PEM fuel cells, without considering other various parameters such as porous medium thickness (PMT), thermal contact resistance (TCR), interface contact resistance (ICR), and GDL face permeability.

Chapter 3: The research methods with an explanation of the simulation modeling setup based on the ANSYS-Fluent Fuel Cell and Electrolysis Model. The simulation's validity is established by comparing the simulation's findings with the results of the experiments found in the literature concerning the polarisation curve (I-V curve). The research of the influence of variation of bipolar plate flow fields (parallel, tapered, and water drop block models) on temperature profiles, mass transport characteristics and cell performances of PEM fuel cells might be carried out using a simulated technique. This would involve taking into consideration some variable parameters.

Chapter 4: The research objective is to optimize voltage, GDL face permeability, and thermal contact resistance operating parameters on mass transport and cell performance on PEMFC. The method used in this study used six different thermal contact resistance (TCR) and GDL

face permeability variations on temperature profiles, mass transport characteristic and cell performance PEM performance with combining ANN-GA method for optimizing current and power densities. In addition, the important results in Chapter 4 are summarized below:

- Considering the TCR and GDL face permeability, there is an observed rise in the optimum cell temperature by around 1.5°C at 0.4 V, and the temperature profiles exhibit a distinctive "Λ" shape.
- The thermal contact resistance and GDL face permeability significantly impact the velocity and oxygen mass fraction in case 6, resulting in an increase of 1.91% and 6.58%, respectively, compared to case 1. In addition, the pressure drop in case 6 is 3.11% higher compared to case 1.
- The ANN-GA technique was employed to identify the highest power densities attainable in six different scenarios. These findings are important for designing and efficiently monitoring fuel cell systems.

Chapter 5: To investigate the influence of tapered flow field configurations with considering porous medium thickness and thermal contact resistance variations on improving PEM fuel cells' mass transport and cell performance. This study employed six distinct $L_{i/o}$ ratios ($L_{i/o}$ 0.7, $L_{i/o}$ 0.8, $L_{i/o}$ 0.9, $L_{i/o}$ 1.0, $L_{i/o}$ 1.1, and $L_{i/o}$ 1.2) in tapered FFCs with appropriate thermal contact resistance (TCR) and porous medium thickness (PMT) to improve mass transport and cell performance of PEM fuel cells. In addition, the important results in Chapter 5 are summarized below:

- The current study showcases the findings of numerical investigations, which reveal that a higher $L_{i/o}$ ratio in tapered FFCs with considering both suitable TCR and PMT can improve reactant transport, water removal, and ensure even distribution of current densities, oxygen, and hydrogen in fuel cells.
- Case 6 ($L_{i/o}$ 1.2) exhibits the highest average velocity due to the impact of thermal contact resistance, which enhances the energy dynamics of reactant molecules in the catalyst layer. Furthermore, increasing the speed of the reactants as they move toward the catalyst layer leads to enhanced mass transport efficiency.
- When comparing case 1 ($L_{i/o}$ 0.7) with case 6 ($L_{i/o}$ 1.2), it becomes evident that the latter shows a notable enhancement in current density, power density, and pressure drop. The improvements amount to approximately 7.57%, 12.63%, and 68.74%, respectively.

This development indicates a more even spread of internal physical quantities within the electrodes, leading to stable operation and increased longevity of fuel cells.

Chapter 6: To investigate the influence of water-block drop models on bipolar plate flow fields on mass transport characteristics, temperature profiles, and cell performances. The method integrates interface contact resistance (ICR) and GDL face permeability variations into the simulated five different water-drop block (WDB) models of PEM fuel cell. In addition, the important results in Chapter 6 are summarized below:

- The current density and power density on the CN6 are higher compared to other scenarios. At a voltage of 0.4V, the maximum current density and power density increased by 6.94% and 12.27%, respectively, compared to the conventional model CN1.
- The WDB (CN6) channel demonstrates the highest velocity of oxygen diffusion and the widest dispersion of oxygen mass fraction. Therefore, it may be inferred that the WDB channel (CN6) outperforms the straight-flow channels (CN1).
- The selection of the WDB model case 6, with an ICR of $2.00\text{E}-06$ ohm·m² and a GDL face permeability of $3.50\text{E}-12$ m², seems to achieve a favorable equilibrium and may be the optimal option for enhancing mass transport and cell performance in the present investigation.

The present work involves the following contributions:

The study discovered that optimizing operating parameters using the ANN-GA technique has a more positive impact on PEM fuel cells' mass transport and cell performance by considering the effects of thermal contact resistance (TCR) and variations in gas diffusion layer (GDL) face permeability. The study investigated the influence of tapered flow field (TFF) configurations taking into account differences in porous medium thickness (PMT) and thermal contact resistance (TCR) on temperature profiles, mass transfer, and cell performance enhancement of PEM fuel cell. In addition, a study was conducted to examine the impact of different configurations of water drop block (WDB) with considering differences in the interface contact resistance (ICR) and gas diffusion layer (GDL) face permeability on the temperature profiles, mass transfer, and performance enhancement of a PEM fuel cell.

REFERENCES

- [1] Y. Wang, B. Seo, B. Wang, N. Zamel, K. Jiao, and X. C. Adroher, “Fundamentals, materials, and machine learning of polymer electrolyte membrane fuel cell technology,” *Energy AI*, vol. 1, p. 100014, 2020, doi: 10.1016/j.egyai.2020.100014.
- [2] Kearney, “Oil consumption worldwide from 1970 to 2022 (in million metric tons),” *Energy Institute*, 2023. <https://www.statista.com/statistics/265261/global-oil-consumption-in-million-metric-tons/> (accessed Mar. 16, 2024).
- [3] M. Crippa *et al.*, “GHG emissions from all countries, JRC, Publication of the European Union,” Publications Office of the European Union, Luxembourg, 2023. doi: 10.2760/953322.
- [4] A. Fleck, “Cars Cause Biggest Share of Transportation CO₂ Emissions,” *Statista*, 2023. <https://www.statista.com/chart/30890/estimated-share-of-co2-emissions-in-the-transportation-sector/> (accessed Mar. 16, 2024).
- [5] M. S. Aygen and M. İnci, “Zero-sequence current injection based power flow control strategy for grid inverter interfaced renewable energy systems,” *Energy Sources, Part A Recover. Util. Environ. Eff.*, vol. 44, no. 3, pp. 7782–7803, 2022, doi: 10.1080/15567036.2020.1834029.
- [6] J. P. Stempien and S. H. Chan, “Comparative study of fuel cell , battery and hybrid buses for renewable energy constrained areas,” *J. Power Sources*, vol. 340, pp. 347–355, 2017, doi: 10.1016/j.jpowsour.2016.11.089.
- [7] M. W. Ellis, M. R. Von Spakovsky, and D. J. Nelson, “Fuel Cell Systems: Efficient, Flexible Energy Conversion for the 21st Century,” *Proc. IEEE*, vol. 89, no. 12, pp. 1808–1817, 2001, doi: 10.1109/5.975914.
- [8] M. İnci, “Interline fuel cell (I-FC) system with dual-functional control capability,” *Int. J. Hydrogen Energy*, vol. 45, no. 1, pp. 891–903, Jan. 2020, doi: 10.1016/J.IJHYDENE.2019.10.122.
- [9] M. İnci and M. S. Aygen, “A modified energy management scheme to support phase

- balancing in grid interfaced photovoltaic/fuel cell system,” *Ain Shams Eng. J.*, vol. 12, no. 3, pp. 2809–2822, Sep. 2021, doi: 10.1016/J.ASEJ.2020.12.018.
- [10] L. Xing *et al.*, “Membrane electrode assemblies for PEM fuel cells: A review of functional graded design and optimization,” *Energy*, vol. 177, pp. 445–464, Jun. 2019, doi: 10.1016/J.ENERGY.2019.04.084.
- [11] X. Wang, Y. Qin, S. Wu, X. Shangguan, J. Zhang, and Y. Yin, “Numerical and experimental investigation of baffle plate arrangement on proton exchange membrane fuel cell performance,” *J. Power Sources*, vol. 457, p. 228034, May 2020, doi: 10.1016/J.JPOWSOUR.2020.228034.
- [12] J. Song, Y. Huang, J. Zeng, L. Chen, and Y. Wu, “Design and numerical investigation of multi-channel cooling plate for proton exchange membrane fuel cell,” *Energy Reports*, vol. 8, pp. 6058–6067, Nov. 2022, doi: 10.1016/J.EGYR.2022.04.052.
- [13] E. Tardy, J.-P. Poirot-Crouvezier, P. Schott, C. Morel, G. Serre, and Y. Bultel, “Investigation of liquid water heterogeneities in large area proton exchange membrane fuel cells using a Darcy two-phase flow model in a multiphysics code,” *Int. J. Hydrogen Energy*, Sep. 2022, doi: 10.1016/J.IJHYDENE.2022.09.039.
- [14] J. Shen, L. Zeng, Z. Liu, and W. Liu, “Performance investigation of PEMFC with rectangle blockages in Gas Channel based on field synergy principle,” *Heat Mass Transf. und Stoffuebertragung*, vol. 55, no. 3, pp. 811–822, Mar. 2019, doi: 10.1007/S00231-018-2473-5/FIGURES/9.
- [15] C. Yang *et al.*, “Geometry optimization of a novel M-like flow field in a proton exchange membrane fuel cell,” *Energy Convers. Manag.*, vol. 228, p. 113651, Jan. 2021, doi: 10.1016/J.ENCONMAN.2020.113651.
- [16] Z. Liu, X. Zeng, Y. Ge, J. Shen, and W. Liu, “Multi-objective optimization of operating conditions and channel structure for a proton exchange membrane fuel cell,” *Int. J. Heat Mass Transf.*, vol. 111, pp. 289–298, Aug. 2017, doi: 10.1016/J.IJHEATMASSTRANSFER.2017.03.120.
- [17] X. Zeng, Y. Ge, J. Shen, L. Zeng, Z. Liu, and W. Liu, “The optimization of channels for a proton exchange membrane fuel cell applying genetic algorithm,” *Int. J. Heat*

- Mass Transf.*, vol. 105, pp. 81–89, Feb. 2017, doi: 10.1016/J.IJHEATMASSTRANSFER.2016.09.068.
- [18] H. Chen, H. Guo, F. Ye, and C. F. Ma, “ScienceDirect A numerical study of orientated-type flow channels with porous-blocked baffles of proton exchange membrane fuel cells,” *Int. J. Hydrogen Energy*, vol. 46, no. 57, pp. 29443–29458, 2020, doi: 10.1016/j.ijhydene.2020.12.178.
- [19] Q. Ding *et al.*, “Evaluation criterion of flow fields in PEM fuel cells based on entropy generation analysis,” *Int. J. Hydrogen Energy*, vol. 48, no. 6, pp. 2328–2340, Jan. 2023, doi: 10.1016/J.IJHYDENE.2022.10.112.
- [20] C. Xu, H. Wang, and T. Cheng, “Wave-shaped flow channel design and optimization of PEMFCs with a groove in the gas diffusion layer,” *Int. J. Hydrogen Energy*, vol. 48, no. 11, pp. 4418–4429, Feb. 2023, doi: 10.1016/J.IJHYDENE.2022.10.028.
- [21] M. Liu, W. Fan, and G. Lu, “Study on mass transfer enhancement of locally improved structures and the application in serpentine and parallel flow fields of PEM fuel cells,” *Int. J. Hydrogen Energy*, no. xxxx, 2023, doi: 10.1016/j.ijhydene.2023.02.030.
- [22] D. Park, S. Ham, Y. J. Sohn, Y. Y. Choi, and M. Kim, “Mass transfer characteristics according to flow field and gas diffusion layer of a PEMFC metallic bipolar plate for stationary applications,” *Int. J. Hydrogen Energy*, vol. 48, no. 1, pp. 304–317, Jan. 2023, doi: 10.1016/J.IJHYDENE.2022.09.261.
- [23] Z. Wan *et al.*, “Thermal management improvement of air-cooled proton exchange membrane fuel cell by using metal foam flow field,” *Appl. Energy*, vol. 333, no. January, p. 120642, 2023, doi: 10.1016/j.apenergy.2023.120642.
- [24] M. Sauermoser, N. Kizilova, B. G. Pollet, and S. Kjelstrup, “Flow Field Patterns for Proton Exchange Membrane Fuel Cells,” *Front. Energy Res.*, vol. 8, no. February, pp. 1–20, 2020, doi: 10.3389/fenrg.2020.00013.
- [25] X. Bai, L. Luo, B. Huang, Q. Jian, and Z. Cheng, “Performance improvement of proton exchange membrane fuel cell stack by dual-path hydrogen supply,” *Energy*, vol. 246, p. 123297, May 2022, doi: 10.1016/J.ENERGY.2022.123297.
- [26] Z. Dong, Y. Qin, J. Zheng, and Q. Guo, “Numerical investigation of novel block flow

- channel on mass transport characteristics and performance of PEMFC,” 2023, doi: 10.1016/j.ijhydene.2023.03.258.
- [27] W. Pan, X. Chen, F. Wang, and G. Dai, “Mass transfer enhancement of PEM fuel cells with optimized flow channel dimensions,” *Int. J. Hydrogen Energy*, vol. 46, no. 57, pp. 29541–29555, Aug. 2021, doi: 10.1016/J.IJHYDENE.2020.09.105.
- [28] X. Zhu *et al.*, “Performance analysis of proton exchange membrane fuel cells with traveling-wave flow fields based on Grey-relational theory,” *Int. J. Hydrogen Energy*, vol. 48, no. 2, pp. 740–756, Jan. 2023, doi: 10.1016/J.IJHYDENE.2022.09.244.
- [29] C. Xu, H. Wang, and T. Cheng, “Wave-shaped flow channel design and optimization of PEMFCs with a groove in the gas diffusion layer,” *Int. J. Hydrogen Energy*, vol. 48, no. 11, pp. 4418–4429, Feb. 2023, doi: 10.1016/J.IJHYDENE.2022.10.028.
- [30] Q. Liu, F. Lan, J. Chen, J. Wang, and C. Zeng, “Effect of anisotropic transport properties of porous layers on the dynamic performance of proton exchange membrane fuel cell,” *Int. J. Hydrogen Energy*, vol. 48, no. 29, pp. 10982–11002, Apr. 2023, doi: 10.1016/J.IJHYDENE.2022.12.161.
- [31] H. Li, B. Xu, C. Du, and Y. Yang, “Performance prediction and power density maximization of a proton exchange membrane fuel cell based on deep belief network,” *J. Power Sources*, vol. 461, no. March, p. 228154, 2020, doi: 10.1016/j.jpowsour.2020.228154.
- [32] T. D. Canonsburg, “ANSYS Fluent Fuel Cell Modules Manual,” vol. 15317, no. November, pp. 724–746, 2013.
- [33] S. Mo *et al.*, “Recent Advances on PEM Fuel Cells: From Key Materials to Membrane Electrode Assembly,” vol. 6, p. 28, 2023, doi: 10.1007/s41918-023-00190-w.
- [34] R. L. Borup *et al.*, “Recent developments in catalyst-related PEM fuel cell durability,” *Curr. Opin. Electrochem.*, vol. 21, pp. 192–200, 2020, doi: 10.1016/j.coelec.2020.02.007.
- [35] S. van Rooij, M. Magnini, O. K. Matar, and S. Haussener, “Numerical optimization of evaporative cooling in artificial gas diffusion layers,” *Appl. Therm. Eng.*, vol. 186, p. 116460, 2021, doi: 10.1016/j.applthermaleng.2020.116460.

- [36] Y. Zhang, S. He, X. Jiang, M. Xiong, Y. Ye, and X. Yang, “Three-dimensional multi-phase simulation of proton exchange membrane fuel cell performance considering constriction straight channel,” *Energy*, vol. 267, no. November 2022, p. 126544, 2023, doi: 10.1016/j.energy.2022.126544.
- [37] C. Spiegel, “Description of the Polymer Exchange Membrane,” 2019. <https://www.fuelcellstore.com/blog-section/fuel-cell-electrolyte-layer-modeling> (accessed Apr. 15, 2024).
- [38] C. Michalkowski, M. Veyskarami, C. Bringedal, R. Helmig, and V. Schleper, “Two-phase Flow Dynamics at the Interface Between GDL and Gas Distributor Channel Using a Pore-Network Model,” *Transport in Porous Media*, vol. 144, no. 2. pp. 429–458, 2022, doi: 10.1007/s11242-022-01813-4.
- [39] C. Spiegel, “Considerations for Stainless Steel Bipolar Plate Manufacturing: Part 2,” 2018. <https://www.fuelcellstore.com/blog-section/considerations-for-stainless-steel-bipolar-plate-manufacturing-part-2> (accessed Apr. 16, 2024).
- [40] D. Zhou, A. Al-durra, F. Gao, A. Ravey, I. Matraji, and M. Godoy, “Online energy management strategy of fuel cell hybrid electric vehicles based on data fusion approach,” vol. 366, pp. 278–291, 2017, doi: 10.1016/j.jpowsour.2017.08.107.
- [41] A. Kosakian, L. P. Urbina, A. Heaman, and M. Secanell, “Electrochimica Acta Understanding single-phase water-management signatures in fuel-cell impedance spectra : A numerical study,” *Electrochim. Acta*, vol. 350, p. 136204, 2020, doi: 10.1016/j.electacta.2020.136204.
- [42] M. Z. Chowdhury, O. Genc, and S. Toros, “Numerical optimization of channel to land width ratio for PEM fuel cell,” *Int. J. Hydrogen Energy*, vol. 43, no. 23, pp. 10798–10809, Jun. 2018, doi: 10.1016/J.IJHYDENE.2017.12.149.
- [43] X. Liu, R. Zhang, C. Zhang, and D. Yang, “Hydrophobic modification of flow channel surface and its effect on the performance of proton exchange membrane fuel cell,” *Int. J. Hydrogen Energy*, vol. 47, no. 68, pp. 29430–29440, Aug. 2022, doi: 10.1016/J.IJHYDENE.2022.06.272.
- [44] A. Iranzo, C. H. Arredondo, A. M. Kannan, and F. Rosa, “Biomimetic flow fields for

- proton exchange membrane fuel cells: A review of design trends,” *Energy*, vol. 190, p. 116435, Jan. 2020, doi: 10.1016/J.ENERGY.2019.116435.
- [45] T. Wilberforce *et al.*, “A comprehensive study of the effect of bipolar plate (BP) geometry design on the performance of proton exchange membrane (PEM) fuel cells,” *Renew. Sustain. Energy Rev.*, vol. 111, pp. 236–260, Sep. 2019, doi: 10.1016/J.RSER.2019.04.081.
- [46] R. Roshandel, F. Arbabi, and G. K. Moghaddam, “Simulation of an innovative flow-field design based on a bio inspired pattern for PEM fuel cells,” *Renew. Energy*, vol. 41, pp. 86–95, May 2012, doi: 10.1016/J.RENENE.2011.10.008.
- [47] Y. Zhang, S. He, X. Jiang, M. Xiong, Y. Ye, and X. Yang, “Three-dimensional multi-phase simulation of proton exchange membrane fuel cell performance considering constriction straight channel,” *Energy*, vol. 267, p. 126544, Mar. 2023, doi: 10.1016/J.ENERGY.2022.126544.
- [48] Y. Ding *et al.*, “Characterizing the two-phase flow effect in gas channel of proton exchange membrane fuel cell with dimensionless number,” *Int. J. Hydrogen Energy*, vol. 48, no. 13, pp. 5250–5265, Feb. 2023, doi: 10.1016/J.IJHYDENE.2022.09.288.
- [49] X. Yang, X. Meng, J. Sun, W. Song, S. Sun, and Z. Shao, “Study on internal dynamic response during cold start of proton exchange membrane fuel cell with parallel and serpentine flow fields,” *J. Power Sources*, vol. 561, p. 232609, Mar. 2023, doi: 10.1016/J.JPOWSOUR.2022.232609.
- [50] Q. Wang *et al.*, “Numerical analysis of static and dynamic heat transfer behaviors inside proton exchange membrane fuel cell,” *J. Power Sources*, vol. 488, no. December 2020, p. 229419, 2021, doi: 10.1016/j.jpowsour.2020.229419.
- [51] X. Chen *et al.*, “Performance investigation on a novel 3D wave flow channel design for PEMFC,” *Int. J. Hydrogen Energy*, vol. 46, no. 19, pp. 11127–11139, Mar. 2021, doi: 10.1016/J.IJHYDENE.2020.06.057.
- [52] X. Yan *et al.*, “Flow field design with 3D geometry for proton exchange membrane fuel cells,” *Appl. Therm. Eng.*, vol. 147, pp. 1107–1114, Jan. 2019, doi: 10.1016/J.APPLTHERMALENG.2018.09.110.

- [53] P. Dong, G. Xie, and M. Ni, “The mass transfer characteristics and energy improvement with various partially blocked flow channels in a PEM fuel cell,” *Energy*, vol. 206, p. 117977, Sep. 2020, doi: 10.1016/J.ENERGY.2020.117977.
- [54] L. He *et al.*, “A novel three-dimensional flow field design and experimental research for proton exchange membrane fuel cells,” *Energy Convers. Manag.*, vol. 205, p. 112335, Feb. 2020, doi: 10.1016/J.ENCONMAN.2019.112335.
- [55] W. Z. Li, W. W. Yang, N. Wang, Y. H. Jiao, Y. Yang, and Z. G. Qu, “Optimization of blocked channel design for a proton exchange membrane fuel cell by coupled genetic algorithm and three-dimensional CFD modeling,” *Int. J. Hydrogen Energy*, vol. 45, no. 35, pp. 17759–17770, Jul. 2020, doi: 10.1016/J.IJHYDENE.2020.04.166.
- [56] Y. Yin, S. Wu, Y. Qin, O. N. Otoo, and J. Zhang, “Quantitative analysis of trapezoid baffle block sloping angles on oxygen transport and performance of proton exchange membrane fuel cell,” *Appl. Energy*, vol. 271, p. 115257, Aug. 2020, doi: 10.1016/J.APENERGY.2020.115257.
- [57] V. Velisala and G. N. Srinivasulu, “Numerical Simulation and Experimental Comparison of Single, Double and Triple Serpentine Flow Channel Configuration on Performance of a PEM Fuel Cell,” *Arab. J. Sci. Eng.*, vol. 43, no. 3, pp. 1225–1234, Mar. 2018, doi: 10.1007/S13369-017-2813-7/METRICS.
- [58] M. Ghasabehi, M. Ashrafi, and M. Shams, “Performance analysis of an innovative parallel flow field design of proton exchange membrane fuel cells using multiphysics simulation,” *Fuel*, vol. 285, p. 119194, Feb. 2021, doi: 10.1016/J.FUEL.2020.119194.
- [59] C. Zhao, J. Yang, T. Zhang, D. Yan, and J. Pu, “ScienceDirect Numerical modeling of manifold design and flow uniformity analysis of an external manifold solid oxide fuel cell stack,” *Int. J. Hydrogen Energy*, vol. 45, no. 28, pp. 14440–14451, 2020, doi: 10.1016/j.ijhydene.2020.02.143.
- [60] X. W. Zhang, X. J. Wang, X. Z. Cheng, L. Jin, J. W. Zhu, and T. T. Zhou, “Numerical analysis of global and local performance variations of proton exchange membrane fuel cell with different bend layouts and flow directions,” *Energy*, vol. 207, p. 118141, Sep. 2020, doi: 10.1016/J.ENERGY.2020.118141.

- [61] G. Cai, Y. Liang, Z. Liu, and W. Liu, “Design and optimization of bio-inspired wave-like channel for a PEM fuel cell applying genetic algorithm,” *Energy*, vol. 192, p. 116670, Feb. 2020, doi: 10.1016/J.ENERGY.2019.116670.
- [62] M. Suo *et al.*, “Oxygen transport in proton exchange membrane fuel cells with metal foam flow fields,” *J. Power Sources*, vol. 521, p. 230937, Feb. 2022, doi: 10.1016/J.JPOWSOUR.2021.230937.
- [63] G. Zhang, Z. Bao, B. Xie, Y. Wang, and K. Jiao, “Three-dimensional multi-phase simulation of PEM fuel cell considering the full morphology of metal foam flow field,” *Int. J. Hydrogen Energy*, vol. 46, no. 3, pp. 2978–2989, Jan. 2021, doi: 10.1016/J.IJHYDENE.2020.05.263.
- [64] C. Yin *et al.*, “Investigation of proton exchange membrane fuel cell stack with inversely phased wavy flow field design,” *Appl. Energy*, vol. 305, p. 117893, Jan. 2022, doi: 10.1016/J.APENERGY.2021.117893.
- [65] Q. Tan, H. Lei, and Z. Liu, “Numerical simulation analysis of the performance on the PEMFC with a new flow field designed based on constructal-theory,” *Int. J. Hydrogen Energy*, vol. 47, no. 23, pp. 11975–11990, Mar. 2022, doi: 10.1016/J.IJHYDENE.2022.01.243.
- [66] Y. Wang, Z. Y. Sun, and L. Yang, “Enhancement effects of the obstacle arrangement and gradient height distribution in serpentine flow-field on the performances of a PEMFC,” *Energy Convers. Manag.*, vol. 252, p. 115077, Jan. 2022, doi: 10.1016/J.ENCONMAN.2021.115077.
- [67] H. Huang *et al.*, “Numerical simulation and visualization study of a new tapered-slope serpentine flow field in proton exchange membrane fuel cell,” *Energy*, vol. 246, p. 123406, May 2022, doi: 10.1016/J.ENERGY.2022.123406.
- [68] H. Huang *et al.*, “Effect of superior mesenteric artery branch structure-based flow field on PEMFC performance,” *Energy Convers. Manag.*, vol. 226, p. 113546, Dec. 2020, doi: 10.1016/J.ENCONMAN.2020.113546.
- [69] H. C. Kang, K. M. Jum, and Y. J. Sohn, “Performance of unit PEM fuel cells with a leaf-vein-simulating flow field-patterned bipolar plate,” *Int. J. Hydrogen Energy*, vol.

- 44, no. 43, pp. 24036–24042, Sep. 2019, doi: 10.1016/J.IJHYDENE.2019.07.120.
- [70] S. R. Badduri, G. N. Srinivasulu, and S. S. Rao, “Influence of bio-inspired flow channel designs on the performance of a PEM fuel cell,” *Chinese J. Chem. Eng.*, vol. 28, no. 3, pp. 824–831, Mar. 2020, doi: 10.1016/J.CJCHE.2019.07.010.
- [71] S. Liu, T. Chen, Y. Xie, J. Zhang, and C. Wu, “Numerical simulation and experimental study on the effect of symmetric and asymmetric bionic flow channels on PEMFC performance under gravity,” *Int. J. Hydrogen Energy*, vol. 44, no. 56, pp. 29618–29630, Nov. 2019, doi: 10.1016/J.IJHYDENE.2019.06.046.
- [72] H. Guo, H. Chen, F. Ye, and C. F. Ma, “Baffle shape effects on mass transfer and power loss of proton exchange membrane fuel cells with different baffled flow channels,” *Int. J. Energy Res.*, vol. 43, no. 7, pp. 2737–2755, 2019, doi: 10.1002/er.4328.
- [73] S. yang Zhang, Z. guo Qu, H. tao Xu, F. K. Talkhonchek, S. Liu, and Q. Gao, “A numerical study on the performance of PEMFC with wedge-shaped fins in the cathode channel,” *Int. J. Hydrogen Energy*, vol. 46, no. 54, pp. 27700–27708, Aug. 2021, doi: 10.1016/J.IJHYDENE.2021.05.207.
- [74] H. Heidary, M. J. Kermani, A. K. Prasad, S. G. Advani, and B. Dabir, “Numerical modelling of in-line and staggered blockages in parallel flowfield channels of PEM fuel cells,” *Int. J. Hydrogen Energy*, vol. 42, no. 4, pp. 2265–2277, Jan. 2017, doi: 10.1016/J.IJHYDENE.2016.10.076.
- [75] Y. Huang *et al.*, “Numerical investigation of baffle shape effects on performance and mass transfer of proton exchange membrane fuel cell,” *Energy*, vol. 266, no. July 2022, p. 126448, 2023, doi: 10.1016/j.energy.2022.126448.
- [76] Y. Wang, B. Seo, B. Wang, N. Zamel, K. Jiao, and X. C. Adroher, “Fundamentals, materials, and machine learning of polymer electrolyte membrane fuel cell technology,” *Energy AI*, vol. 1, p. 100014, Aug. 2020, doi: 10.1016/J.EGYAI.2020.100014.
- [77] B. Wang, G. Zhang, H. Wang, J. Xuan, and K. Jiao, “Multi-physics-resolved digital twin of proton exchange membrane fuel cells with a data-driven surrogate model,”

- Energy AI*, vol. 1, p. 100004, Aug. 2020, doi: 10.1016/J.EGYAI.2020.100004.
- [78] K. Y. Chang, “The optimal design for PEMFC modeling based on Taguchi method and genetic algorithm neural networks,” *Int. J. Hydrogen Energy*, vol. 36, no. 21, pp. 13683–13694, Oct. 2011, doi: 10.1016/J.IJHYDENE.2011.07.094.
- [79] A. Kheirandish, F. Motlagh, N. Shafiabady, and M. Dahari, “Dynamic modelling of PEM fuel cell of power electric bicycle system,” *Int. J. Hydrogen Energy*, vol. 41, no. 22, pp. 9585–9594, Jun. 2016, doi: 10.1016/J.IJHYDENE.2016.02.046.
- [80] Y. Pang and Y. Wang, “Water spatial distribution in polymer electrolyte membrane fuel cell: Convolutional neural network analysis of neutron radiography,” *Energy AI*, vol. 14, p. 100265, Oct. 2023, doi: 10.1016/J.EGYAI.2023.100265.
- [81] J. Wang *et al.*, “Integration of multi-physics and machine learning-based surrogate modelling approaches for multi-objective optimization of deformed GDL of PEM fuel cells,” *Energy AI*, vol. 14, p. 100261, Oct. 2023, doi: 10.1016/J.EGYAI.2023.100261.
- [82] M. Mehrpooya, B. Ghorbani, B. Jafari, M. Aghbashlo, and M. Pouriman, “Modeling of a single cell micro proton exchange membrane fuel cell by a new hybrid neural network method,” *Therm. Sci. Eng. Prog.*, vol. 7, pp. 8–19, 2018, doi: 10.1016/j.tsep.2018.04.012.
- [83] H. Lan, L. Yang, F. Zheng, C. Zong, S. Wu, and X. Song, “Analysis and optimization of high temperature proton exchange membrane (HT-PEM) fuel cell based on surrogate model,” *Int. J. Hydrogen Energy*, vol. 45, no. 22, pp. 12501–12513, Apr. 2020, doi: 10.1016/J.IJHYDENE.2020.02.150.
- [84] B. Wang, B. Xie, J. Xuan, and K. Jiao, “AI-based optimization of PEM fuel cell catalyst layers for maximum power density via data-driven surrogate modeling,” *Energy Convers. Manag.*, vol. 205, p. 112460, Feb. 2020, doi: 10.1016/J.ENCONMAN.2019.112460.
- [85] Y. Zhou, K. Jiao, Q. Du, Y. Yin, and X. Li, “Gas diffusion layer deformation and its effect on the transport characteristics and performance of proton exchange membrane fuel cell,” 2013, doi: 10.1016/j.ijhydene.2013.05.150.
- [86] Atlas Steels Australia, “Mechanical properties of 304 grade stainless steel Grade,”

Atlas Steels Aust., pp. 1–3, 2019, [Online]. Available: <https://www.dm-consultancy.com/TR/dosya/1-59/h/aisi-340-info.pdf>.

- [87] V. Mishra, F. Yang, and R. Pitchumani, “Measurement and prediction of electrical contact resistance between gas diffusion layers and bipolar plate for applications to PEM fuel cells,” *J. Fuel Cell Sci. Technol.*, vol. 1, no. 1, pp. 2–9, 2004, doi: 10.1115/1.1782917.
- [88] P. Zhou, C. W. Wu, and G. J. Ma, “Contact resistance prediction and structure optimization of bipolar plates,” *J. Power Sources*, vol. 159, no. 2, pp. 1115–1122, Sep. 2006, doi: 10.1016/J.JPOWSOUR.2005.12.080.
- [89] T. Yoshizumi, H. Kubo, and M. Okumura, “Development of High-Performance FC Stack for the New MIRAI,” *SAE Tech. Pap.*, no. 2021, Apr. 2021, doi: 10.4271/2021-01-0740.
- [90] L. Wang, A. Husar, T. Zhou, and H. Liu, “A parametric study of PEM fuel cell performances,” *Int. J. Hydrogen Energy*, vol. 28, no. 11, pp. 1263–1272, 2003, doi: 10.1016/S0360-3199(02)00284-7.
- [91] Binyamin and O. Lim, “Numerical investigation of tapered flow field configuration to improve mass transport and performance of proton exchange membrane fuel cell,” *Int. J. Hydrogen Energy*, Sep. 2023, doi: 10.1016/J.IJHYDENE.2023.08.247.
- [92] Gholam Reza Molaeimanesh and Farschad Torabi, *FUEL CELL MODELING AND SIMULATION From Microscale to Macroscale*, vol. 4, no. 1. Elsevier, 2017.
- [93] H. W. Li, J. N. Liu, Y. Yang, W. Fan, and G. L. Lu, “Research on mass transport characteristics and net power performance under different flow channel streamlined imitated water-drop block arrangements for proton exchange membrane fuel cell,” *Energy*, vol. 251, Jul. 2022, doi: 10.1016/J.ENERGY.2022.123983.
- [94] T. F. Cao, H. Lin, L. Chen, Y. L. He, and W. Q. Tao, “Numerical investigation of the coupled water and thermal management in PEM fuel cell,” *Appl. Energy*, vol. 112, pp. 1115–1125, 2013, doi: 10.1016/j.apenergy.2013.02.031.
- [95] I. Nitta, O. Himanen, and M. Mikkola, “Thermal Conductivity and Contact Resistance of Compressed Gas Diffusion Layer of PEM Fuel Cell,” *Fuel Cells*, vol. 8, no. 2, pp.

- 111–119, Apr. 2008, doi: 10.1002/FUCE.200700054.
- [96] H. Sadeghifar, N. Djilali, and M. Bahrami, “Effect of Polytetrafluoroethylene (PTFE) and micro porous layer (MPL) on thermal conductivity of fuel cell gas diffusion layers: Modeling and experiments,” *J. Power Sources*, vol. 248, pp. 632–641, 2014, doi: 10.1016/J.JPOWSOUR.2013.09.136.
- [97] T. Cao, Y. Mu, J. Ding, H. Lin, Y. He, and W. Tao, “International Journal of Heat and Mass Transfer Modeling the temperature distribution and performance of a PEM fuel cell with thermal contact resistance,” *Int. J. Heat Mass Transf.*, vol. 87, pp. 544–556, 2015, doi: 10.1016/j.ijheatmasstransfer.2015.04.010.
- [98] Z. B. Kizilkan, M. S. Sivri, I. Yazici, and O. F. Beyca, *Neural Networks and Deep Learning*. 2022.
- [99] S. E. Haupt, “Introduction to genetic algorithms,” *Artif. Intell. Methods Environ. Sci.*, pp. 103–125, 2009, doi: 10.1007/978-1-4020-9119-3_5.
- [100] L. Rostami, M. Haghshenasfard, M. Sadeghi, and M. Zhiani, “A 3D CFD model of novel flow channel designs based on the serpentine and the parallel design for performance enhancement of PEMFC,” *Energy*, vol. 258, p. 124726, Nov. 2022, doi: 10.1016/J.ENERGY.2022.124726.
- [101] J. H. Nam and M. Kaviany, “Effective diffusivity and water-saturation distribution in single- and two-layer PEMFC diffusion medium,” *Int. J. Heat Mass Transf.*, vol. 46, no. 24, pp. 4595–4611, 2003, doi: 10.1016/S0017-9310(03)00305-3.
- [102] B. Chen, Q. Liu, C. Zhang, Y. Liu, J. Shen, and Z. Tu, “Numerical study on water transfer characteristics under joint effect of placement orientation and flow channel size for PEMFC with dead-ended anode,” *Energy*, vol. 254, Sep. 2022, doi: 10.1016/J.ENERGY.2022.124365.
- [103] H. Lei *et al.*, “ScienceDirect Numerical simulation of water droplet transport characteristics in cathode channel of proton exchange membrane fuel cell with tapered slope structures,” *Int. J. Hydrogen Energy*, vol. 45, no. 53, pp. 29331–29344, 2020, doi: 10.1016/j.ijhydene.2020.07.213.
- [104] Y. Wang, X. Wang, Y. Fan, W. He, J. Guan, and X. Wang, “Numerical Investigation

- of Tapered Flow Field Configurations for Enhanced Polymer Electrolyte Membrane Fuel Cell Performance,” *Appl. Energy*, vol. 306, no. PA, p. 118021, 2022, doi: 10.1016/j.apenergy.2021.118021.
- [105] K. Shang, C. Han, T. Jiang, and Z. Chen, “Numerical study of PEMFC heat and mass transfer characteristics based on roughness interface thermal resistance model,” *Int. J. Hydrogen Energy*, vol. 48, no. 20, pp. 7460–7475, Mar. 2023, doi: 10.1016/J.IJHYDENE.2022.11.201.
- [106] J. Lee *et al.*, “Innovative cathode flow-field design for passive air-cooled polymer electrolyte membrane (PEM) fuel cell stacks,” *Int. J. Hydrogen Energy*, vol. 45, no. 20, pp. 11704–11713, 2020, doi: 10.1016/j.ijhydene.2019.07.128.
- [107] Y. Wang, C. Si, Y. Qin, X. Wang, Y. Fan, and Y. Gao, “Bio-inspired design of an auxiliary fishbone-shaped cathode flow field pattern for polymer electrolyte membrane fuel cells,” *Energy Convers. Manag.*, vol. 227, no. August 2020, p. 113588, 2021, doi: 10.1016/j.enconman.2020.113588.
- [108] X. Wang, Y. Qin, S. Wu, X. Shangguan, J. Zhang, and Y. Yin, “Numerical and experimental investigation of baffle plate arrangement on proton exchange membrane fuel cell performance,” *J. Power Sources*, vol. 457, no. March, p. 228034, 2020, doi: 10.1016/j.jpowsour.2020.228034.
- [109] Y. Yin, S. Wu, Y. Qin, O. N. Otoo, and J. Zhang, “Quantitative analysis of trapezoid baffle block sloping angles on oxygen transport and performance of proton exchange membrane fuel cell,” *Appl. Energy*, vol. 271, no. March, p. 115257, 2020, doi: 10.1016/j.apenergy.2020.115257.
- [110] J. Shen, L. Zeng, Z. Liu, and W. Liu, “Performance investigation of PEMFC with rectangle blockages in Gas Channel based on field synergy principle,” doi: 10.1007/s00231-018-2473-5.
- [111] Y. Amadane, H. Mounir, A. El Marjani, E. M. Karim, and A. Awan, “Numerical investigation of hydrogen consumption in Proton Exchange Membrane Fuel Cell by using computational fluid dynamics (CFD) simulation,” *Mediterr. J. Chem.*, vol. 7, no. 6, pp. 396–415, 2019, doi: 10.13171/mjc7618121415ya.

- [112] T. Berning, “On the Nature of Electro-Osmotic Drag,” *Energies* 2020, Vol. 13, Page 4726, vol. 13, no. 18, p. 4726, Sep. 2020, doi: 10.3390/EN13184726.
- [113] P. Dong, G. Xie, and M. Ni, “Improved energy performance of a PEM fuel cell by introducing discontinuous S-shaped and crescent ribs into flowing channels,” *Energy*, vol. 222, p. 119920, May 2021, doi: 10.1016/J.ENERGY.2021.119920.
- [114] B. Xie *et al.*, “Validation methodology for PEM fuel cell three-dimensional simulation,” *Int. J. Heat Mass Transf.*, vol. 189, p. 122705, Jun. 2022, doi: 10.1016/J.IJHEATMASSTRANSFER.2022.122705.
- [115] Y. Cai, D. Wu, J. Sun, and B. Chen, “The effect of cathode channel blockages on the enhanced mass transfer and performance of PEMFC,” *Energy*, vol. 222, p. 119951, May 2021, doi: 10.1016/J.ENERGY.2021.119951.
- [116] A. M. Dafalla, L. Wei, Z. Liao, J. Guo, and F. Jiang, “Influence of cathode channel blockages on the cold start performance of proton exchange membrane fuel cell: A numerical study,” *Energy*, vol. 263, no. PA, p. 125687, 2023, doi: 10.1016/j.energy.2022.125687.
- [117] B. Binyamin and O. Lim, “Analyzing Temperature Distribution, Mass Transport, and Cell Performance in PEM Fuel Cells with Emphasis on GDL Face Permeability and Thermal Contact Resistance Parameters,” *ACS Omega*, Jan. 2023, doi: 10.1021/ACSOMEGA.3C07932/ASSET/IMAGES/LARGE/AO3C07932_0020.JPEG.
- [118] S. yang Zhang, Z. guo Qu, H. tao Xu, F. K. Talkhonchek, S. Liu, and Q. Gao, “A numerical study on the performance of PEMFC with wedge-shaped fins in the cathode channel,” *Int. J. Hydrogen Energy*, vol. 46, no. 54, pp. 27700–27708, Aug. 2021, doi: 10.1016/j.ijhydene.2021.05.207.
- [119] A. M. Dafalla, L. Wei, Z. Liao, J. Guo, and F. Jiang, “Influence of cathode channel blockages on the cold start performance of proton exchange membrane fuel cell: A numerical study,” *Energy*, vol. 263, p. 125687, Jan. 2023, doi: 10.1016/J.ENERGY.2022.125687.
- [120] Y. Qin, Q. Guo, R. Chen, Y. Zhuang, and Y. Wang, “Numerical investigation of water

droplet impact on PEM fuel cell flow channel surface,” *Renew. Energy*, vol. 168, pp. 750–763, 2021, doi: 10.1016/j.renene.2020.12.075.

- [121] Q. Zuo *et al.*, “Optimization of blocked flow field performance of proton exchange membrane fuel cell with auxiliary channels,” *Int. J. Hydrogen Energy*, vol. 47, no. 94, pp. 39943–39960, Dec. 2022, doi: 10.1016/J.IJHYDENE.2022.09.143.
- [122] R. Baker and J. Zhang, “PROTON EXCHANGE MEMBRANE or POLYMER ELECTROLYTE MEMBRANE (PEM) FUEL CELLS,” 2011. <http://knowledge.electrochem.org/encycl/art-f04-fuel-cells-pem.htm> (accessed Apr. 16, 2024).

APPENDICES

A. List of Publications

1. **Binyamin Binyamin**, Ocktaeck Lim, "Analyzing Temperature Distribution, Mass Transport, and Cell Performance in PEM Fuel Cells with Emphasis on GDL Face Permeability and Thermal Contact Resistance Parameters", *ACS Omega*, *ACS Publications*, Volume 9, 2024, 1516-1534. **Impact Factor: 4.1, SCIE.**
<https://doi.org/10.1021/acsomega.3c07932>
2. **Binyamin**, Ocktaeck Lim, "Numerical investigation of tapered flow field configuration to improve mass transport and performance of proton exchange membrane fuel cell", *International Journal of Hydrogen Energy*, *Elsevier*, Volume 50, pp 470-491, 2024. **Impact Factor: 7.2, SCIE.**
<https://doi.org/10.1016/j.ijhydene.2023.08.247>
3. **Binyamin Binyamin**, Ocktaeck Lim, "A comparative study of streamlined flow channels with water drop block configurations and their effects on temperature profiles, mass transport characteristics, and performance in PEM fuel cell", *Energy*, *Elsevier*, 2024, **Impact Factor: 9.0, SCI.**
<https://doi.org/10.1016/j.energy.2024.131569>
4. **Binyamin Binyamin**, Ocktaeck Lim, "Numerical Analysis of the Structural and Flow Rate Characteristics of the Fuel Injection Pump in a Marine Diesel Engine", *Sustainability*, *MDPI*, Volume 15, 2023. **Impact Factor: 3.9, SCIE.**
<https://doi.org/10.3390/su15118948>
5. **Binyamin**, Ocktaeck Lim, "Performance Improvement of Proton Exchange Membrane Fuel Cells Through Numerical Investigation of a Tapered Flow Field Configuration", The 6th Mechanical Engineering, Science and Technology International Conference (MEST 2022), published in *Advances in Engineering Research*, 2023. https://doi.org/10.2991/978-94-6463-134-0_21
6. **Binyamin**, Ocktaeck Lim, "Numerical Investigation of Polymer Exchange Membrane Fuel Cell with Thermal Contact Resistance and Porous Medium Thickness Effect on Temperature Distribution and Performance", The 6th

Mechanical Engineering, Science and Technology International Conference (MEST 2022), published in *Advances in Engineering Research*, 2023. https://doi.org/10.2991/978-94-6463-134-0_19

7. **Binyamin Binyamin**, Ocktaeck Lim, “Research on Mass Transport Characteristics and Power Performance under Various Novel Baffled Block Configurations For PEM Fuel Cells”, *Applied Energy, Elsevier, Under review* (Status date 2024-05-10).

B. List of Conferences

International Conferences

1. **Binyamin** and Ocktaeck Lim, 13th International Conference of Applied Energy (ICAE) 2021, Bangkok, Thailand, 2021.
2. **Binyamin** and Ocktaeck Lim, 14th International Conference of Applied Energy (ICAE) 2022, Bochum, Germany, 2022.
3. **Binyamin** and Ocktaeck Lim, 6th International Conference of Mechanical Engineering Science and Technology (MEST) 2022, Surakarta, Indonesia.
4. **Binyamin** and Ocktaeck Lim, 15th International Conference of Applied Energy (ICAE) 2023, Doha, Qatar, 2023.

Domestic Conferences

1. **Binyamin** and Ocktaeck Lim, KSAE, Annual Spring Conference, Shinhwa World, Jeju, 2020.
2. **Binyamin** and Ocktaeck Lim, KSAE, Annual Autumn Conference, Bexco, Busan, 2022.
3. **Binyamin** and Ocktaeck Lim, KSAE, Annual Spring Conference, Shinhwa World, Jeju, 2022.
4. **Binyamin** and Ocktaeck Lim, KSAE, KSAE Spring 2023 Conference Chapter Busan, Changwon and Ulsan, Ulsan, Korea, 2023.
5. **Binyamin** and Ocktaeck Lim, KSAE, KSAE Spring 2024 Conference Chapter Gwangju, Busan, and Ulsan, Gwangju, Korea, 2024.